School of Earth and Planetary Sciences

On the Versatility of Accessory Mineral Geochronology in Addressing the Age and Provenance of Geological Material

Anthony Joseph Ian Clarke

0000-0002-0304-0484

This thesis is presented for the Degree of

Doctor of Philosophy

of

Curtin University

November 2024

Declaration

I, Anthony Joseph Ian Clarke, certify that this work contains no material that has been accepted for the award of any other degree or diploma in my name, in any university or other tertiary institution, and, to the best of my knowledge, contains no material previously published or written by another person, except where due reference has been made in the text.

In addition, I certify that no part of this work will, in the future, be used in a submission in my name for any other degree or diploma in any university or other tertiary institution without prior approval of Curtin University and, where applicable, any partner institution responsible for the joint award of this degree, the author acknowledges that the copyright of published works in this thesis resides with those works' copyright holder(s). Every reasonable effort has been made to acknowledge the owners of copyright material. I would be pleased to hear from any copyright owner who has been omitted or incorrectly acknowledged.

This thesis contains the research results I conducted within the School of Earth and Planetary Sciences at Curtin University. Except where indicated, all work and writing is my own. A list of publications arising from this work and authorship agreements for the various chapters (published and unpublished) are provided below.

Signature: .....

Date: November 29th 2024.....

Abstract

Zircon U–Pb geochronology is the principal radiometric dating technique for the Earth sciences and is used to address diverse questions, including the rate and duration of continental crust formation, paleo-geographic reconstructions, sediment flux, and the provenance of geological material. Chemical stability, physical resilience, and high U but low common Pb concentrations make zircon an exceptional geochronometer. Nonetheless, despite the proliferation of detrital and magmatic zircon studies (using U–Pb, Lu–Hf, O and trace elements), inherent geological and methodological biases associated with zircon may hamper interpretations.

Detrital zircon datasets are demonstrably biased towards elevated SiO_2 and Zr-rich intermediate-felsic igneous rocks; thus, mafic lithologies are excluded from the detrital record. Due to the 1000–900°C closure temperature of U–Pb and Lu–Hf, zircon is resilient to thermal equilibration and, therefore, has limited use in constraining mid to upper-crustal processes. Compared to other minerals, zircon incorporates a limited range of trace elements and is less sensitive to changes in fluid composition. Thus, despite its ubiquity, zircon alone may not provide a holistic picture of geological processes.

This thesis presents isotopic (U–Pb, Lu–Hf, Sm–Nd) and trace element data from accessory mineral geochronometers, including apatite and rutile, to demonstrate how analyses from other minerals can complement zircon U–Pb geochronology. Each chapter presents a case study of accessory mineral geochronology within decreasing temporal (Archean–Phanerozoic) and spatial scales (craton–single rock) using differing sample mediums, from sand, rock, thin sections, or a combination thereof.

Apatite is typically more abundant in mafic rocks than zircon and could extend the source rock envelope tracked in detrital studies. Chapter 2 presents a tandem zircon-apatite investigation using detrital grains obtained from sand atop the East Pilbara Terrane, Western Australia. Zircon provides a comprehensive record of West Australian Craton magmatism with ages spanning 200–3600 Ma, reinforcing that zircon is compositionally biased to felsic source rocks. The preservation potential of apatite during physical and chemical weathering hinders its ability to complement the zircon record entirely. As such, detrital apatite represents more mafic, first-cycle detritus. Even so, apatite (U–Pb, Lu–Hf, Sm–Nd) data reveal a history of Mesoarchean thermal overprinting absent from the zircon record. Combining zircon (magmatic processes and crustal evolution) and apatite (timing of metamorphism and cooling) insights yielded a comprehensive picture of Archean crust formation in the Pilbara Craton.

Detrital minerals can be the only extant record of now destroyed, heavily modified, or concealed lithologies and thus give insight into an otherwise inaccessible archive. In Chapter 3, we present isotopic data for detrital zircon (U–Pb, Lu–Hf and trace element data) and apatite (U–Pb) from the Proterozoic Woodline Formation in the Barren Basin of the Albany Fraser Orogen (AFO), Western Australia. Detrital zircon grains match the age and Hf isotopic signatures of the adjacent Nornalup, Biranup, and Frazer Zone magmatic suites of the AFO. However, the provenance of 2300–2000 Ma zircon detritus remains unresolved as such dates are not accounted for by known tectonomagmatic activity in the Western Australian Craton. Based on age, chemical and Hf isotopic signatures, some of our detrital apatite and zircon are derived from the recently defined 2030–2010 Ma felsic-igneous Moonyoora Suite. However, zircon trace element data also help characterise an earlier ca. 2250 Ma episode of mafic A-type, enigmatic rift-related magmatism, offering an important glimpse into the earliest stages of rifting within this highly prospective margin of the Yilgarn Craton.

Chapter 4 presents a case study of the multi-mineral approach for constraining smaller-scale, mid to upper crustal igneous processes within the crystalline basement of southern Britain. Zircon and apatite from the Johnston Complex, south Wales, yield a 570 ± 3 Ma coeval crystallisation age. Zircon inheritance in S-type granitoids, such as the Johnston Complex, can complicate primary crystallisation age determinations. Given solubility considerations, apatite is less likely to become inherited during crustal reworking. Thus, in situations where the closure temperature of U–Pb in apatite has not been exceeded, combined zircon-apatite geochronology can mitigate age ambiguity due to zircon inheritance. Coeval crystallisation ages for zircon and apatite imply rapid cooling through the Pb-closure temperatures ≥900°C to ≥350°C of both minerals, respectively. Furthermore, zircon and apatite trace elements provide a more holistic picture of melt evolution within complex magmatic terranes. Apatite trace elements reveal a sedimentary component within the melt, whereas zircon demonstrates an oxidised calc-alkaline source magma. Our data necessitate that calc-alkaline magmatism was ongoing until ca. 570 Ma, prior to the oblique convergence of East Avalonia with Laurentia and the detachment of coherent geology into tectonic slivers and subsequent terrane dispersal.

Radiometric determinations are essential in constraining and correlating fossiliferous horizons throughout geological time. Indeed, zircon U–Pb ages have revealed that Ediacaran biota emerged and proliferated within the final ca. 30 Ma of the Neoproterozoic. However, low zircon abundance (e.g., from limited sample material or ultramafic rocks) can hinder paleontological dating studies. Chapter 5 explores the Llangynog Inlier of south Wales, which

contains an assemblage of Ediacaran macrofossils, including *Aspidella*, *Hiemalora*, *Palaeopascichnus*, and *Yelovichnus*. However, the lack of absolute age constraints has hampered direct comparison with other assemblages. The data presented in Chapter 5 demonstrate that multi-mineral isochrons can enable more precise age determinations. Specifically, rutile U–Pb analyses with higher common lead concentrations than zircon were used to constrain the initial Pb composition of the isochron, resulting in a 25% improvement of zircon age uncertainties (562.8 ± 7.7 Ma, n = 3) improved to 563.1 ± 6.2 Ma by incorporating rutile analyses. Moreover, the discordant zircon component lies along the same regression line as the rutile common–radiogenic mixing array, implying a shared initial Pb source that was comparatively unradiogenic, like other peri-Gondwanan terranes. Thus, the zircon-rutile approach can give more precise U–Pb ages and insight into source composition. An ID-TIMS zircon U–Pb age of 564.09 ± 0.70 Ma corroborates previous *in-situ* ages and helps establish the biota of the Llangynog Inlier as a lateral equivalent to the similarly shallow-marine, tidally influenced ecosystem of the upper Fermeuse Formation in Newfoundland.

Chapter 6 represents a culmination of techniques developed throughout this thesis. We demonstrate that more holistic provenance interpretations can be made when implementing a multi-mineral and isotopic system strategy, which benefits from each phase's different chemical and physical properties. To that end, we answer an outstanding archaeological question: where did the Altar Stone, the central, six-tonne megalith of Stonehenge, come from? Using a combined zircon, apatite, and rutile (U–Pb, Lu–Hf and trace elements) approach, we show that the Orcadian Basin of northern Scotland represents the ultimate source of the Altar Stone. Statistical analysis of zircon U–Pb ages and apatite Lu–Hf ages fingerprint the megalith to the Orcadian Basin, while apatite and rutile U–Pb ages show derivation from an ultimate Laurentian crystalline source region that was overprinted by Grampian magmatism. Thus, the Altar Stone was sourced at least 750 km from its current location on the Salisbury Plain in southern England. The difficulty of long-distance overland transport of such massive cargo from Scotland, navigating topographic barriers, suggests marine shipping. Such routing points towards extraordinary societal organisation with intra-Britain transport during the Neolithic.

The diverse findings from this thesis demonstrate that perceived deficiencies in zircon U–Pb geochronology can be mitigated by incorporating isotopic analyses from other accessory phases. Apatite U–Pb (± Lu–Hf) extends the compositional envelope tracked in detrital studies, revealing mafic components or first-cycle detritus absent from the zircon record. Moreover, incorporating apatite and rutile with lower U–Pb closure temperatures gives insight into mid-

crustal processes occurring over 600–300°C. Hence, a more complete picture of processes over geological time can be obtained from a multi-mineral and isotopic system approach to geochronology.

Acknowledgements

An Australian Research Council Discovery Project Grant (DP200101881) funded this research. The Institute of Geoscience Research at Curtin University, the Geological Society of Australia-Western Australia Division, and the Specialist Group in Economic Geology provided additional funding for conference attendance.

Looking back over the past three years, I can confidently say that spending a month in quarantine was worth it. My supervisors, Chris, Stijn, Pete, and Jack, encouraged and challenged me to deliver the best research possible. Thank you for allowing me to explore various fascinating topics under the guise of apatite. I was fortunate to work with the Timescales of Mineral Systems Group, who fostered a collaborative environment that meant an answer to a question was only ever a knocked door away.

I have been lucky to have exceptional mentors growing up, including Dr. Elizabeth Richards from Coleg Sir Gâr and Professor Adrian Finch of St. Andrews, who both inspired my love of geology. Thank you for everything. Curtis, you shared this PhD with me in 2020, triggering my move to Australia. We have come far since those never-ending days in Greenland.

Throughout this experience, seeing people come and go has been bittersweet. So, I thank my inspirational officemates, past and present, for bringing much-needed smiles to the workday. You know who you are, wherever you are in the world.

Without the help of my brothers, Trevor and Gavin, this PhD would not have been possible. Thanks to Trev and Anisa for making Adelaide feel like a second home during my “work” trips. Trevor, you came to Australia to have a better life. Thank you for showing me a better future. Every weekend, I could count on Gavin and Charlotte’s scepticism, humour, and support whenever I mentioned my research. I thank my mother for her consistent encouragement throughout my academic career in Scotland, Cornwall, and Australia.

Denosha, you came into my life halfway through this journey. From then on, my time became filled with love, fun, and adventure.

Finally, I dedicate this entire endeavour to my father, Ian. I often thought about you during those days crossing the Nullarbor.

Diolch i bawb am eich cefnogaeth.

Publication List

Published Journal Articles

Clarke, A.J.I., Kirkland, C.L., Glorie, S., 2023. A detective duo of apatite and zircon geochronology for East Avalonia, Johnston Complex, Wales. Journal of the Geological Society 180.

Clarke, A.J.I., Kirkland, C.L., Glorie, S., Gillespie, J., Kinny, P.D., 2023. The unroofing of Archean crustal domes as recorded by detrital zircon and apatite. Precambrian Research 395, 107132.

Clarke, A.J.I., Kirkland, C.L., Menon, L.R., Condon, D.J., Cope, C.W.J., Bevins, R.E., Glorie, S., 2024. U–Pb zircon–rutile dating of the Llangynog Inlier, Wales: constraints on an Ediacaran shallow-marine fossil assemblage from East Avalonia. Journal of the Geological Society 181.

Clarke, A.J.I., Kirkland, C.L., Bevins, R.E., Pearce, N.J.G., Glorie, S., Ixer, R.A., 2024. A Scottish Provenance for the Altar Stone of Stonehenge. Nature 623 (8025): 570-575.

Clarke, A.J.I., Kirkland, C.L., Glorie, S., Quentin de Gromard, R., Tucker, M.N. Detrital zircon and apatite reveal Paleoproterozoic rifting along the eastern margin of the Yilgarn Craton. Precambrian Research 414, 107602.

Conference Presentations

Clarke, A.J.I., Kirkland, C.L., Glorie, S., Gillespie, J., Kinny, P.D., 2022. The unroofing of Archean crustal domes as recorded by detrital zircon and apatite. 'Earth, Sea and Sky' Specialist Group in Geochemistry, Mineralogy & Petrology Biennial Conference 2022, Yallingup. ***Highly Commended Student Presentation Award.***

Clarke, A.J.I., Kirkland, C.L., Glorie, S., Gillespie, J., Kinny, P.D., 2022. The unroofing of Archean crustal domes as recorded by detrital zircon and apatite. GESSS-WA 2022 Symposium, Perth. ***Best Presentation in Isotope Geochemistry and Provenance.***

Clarke, A.J.I., Kirkland, C.L., Glorie, S., 2023. A detective duo; an apatite–zircon case study of the Johnston Complex, Wales. European Geosciences Union 2023, Vienna.

Clarke, A.J.I., Kirkland, C.L., Glorie, S., 2023. Detrital zircon and apatite trace enigmatic Yilgarn Craton rift-magmatism – where did all the 2 Ga grains go? Australian Earth Science Convention 2023, Perth.

Clarke, A.J.I., Kirkland, C.L., Glorie, S., 2023. Detrital zircon and apatite trace enigmatic Yilgarn Craton rift-magmatism – where did all the 2 Ga grains go? 6th International Archean Symposium 2023, Perth.

Clarke, A.J.I., Kirkland, C.L., Menon, L.R., Condon, D.J., Cope, C.W.J., Bevins, R.E., Glorie, S., 2023. U–Pb dating of the Llangynog Inlier, Wales: A glimpse into an early shallow marine ecosystem. GESSS-WA 2023 Symposium, Perth. ***Best Talk – Isotope Geochemistry and Geochronology.***

Clarke, A.J.I., Kirkland, C.L., Menon, L.R., Condon, D.J., Cope, C.W.J., Bevins, R.E., Glorie, S., 2024. U–Pb zircon–rutile dating of the Llangynog Inlier, Wales: Constraints on an Ediacaran shallow-marine fossil assemblage from East Avalonia. Goldschmidt 2024, Chicago.

Other Contributions

Clarke, A.J.I., September 2022, The Rise and Fall of Dome: Insights into continental crust formation from isotopes in detrital minerals. Geological Survey of Western Australia GeoChat #26 (Invited Talk).

Clarke, A.J.I., June 2023, What ancient rocks in Pembrokeshire tell us about Wales' past: Nation. Cymru (Online Article).

Clarke, A.J.I., October 2023, An appetite for apatite: Perth Gem and Mineral Show, Western Australia (Invited Talk).

Clarke, A.J.I., Kirkland, C.L., January 2024, 565-million-years-old, some of the oldest UK fossils are eerily similar to famous Australian ones: The Conversation (Online Article).

Clarke, A.J.I., Kirkland, C.L., Glorie, S., August 2024, The Altar Stone of Stonehenge came from an unexpectedly distant place; new study reveals: The Conversation (Online Article).

Clarke, A.J.I., September 2024, A Scottish Provenance for the Altar Stone of Stonehenge. Scottish Geology Festival 2024 (Invited Talk).

Authorship Agreement Form

The Curtin University Authorship, Peer Review and Publication of Research Findings Policy and Procedures, which references the Australian Code for the Responsible Conduct of Research, provides clear guidelines regarding attribution of authorship. This form assists researchers in capturing discussions around intended publications arising from joint work. It does not replace copyright or certification forms required by publishers.

Research Summary

Project Title:	On the Versatility of Accessory Mineral Geochronology in Addressing the Age and Provenance of Geological Material
Project identifier	DP200101881
Principal Investigators	Professor Christopher Kirkland Associate Professor Stijn Glorie

Publications

Publication	Description	Publication Type
1	The unroofing of Archean crustal domes as recorded by detrital zircon and apatite	Journal article (published)
2	A detective duo of apatite and zircon geochronology for East Avalonia, Johnston Complex, Wales	Journal article (published)
3	U–Pb zircon–rutile dating of the Llangynog Inlier, Wales: constraints on an Ediacaran shallow-marine fossil assemblage from East Avalonia	Journal article (published)
4	A Scottish provenance for the Altar Stone of Stonehenge	Journal article (published)
5	Detrital zircon and apatite reveal Paleoproterozoic rifting along the eastern margin of the Yilgarn Craton	Journal article (published)

Attribution Table

Publication 1	**Conception and Design**	**Acquisition of Data and Method Development**	**Data Conditioning and Manipulation**	**Analysis and Statistical Method**	**Interpretation and Discussion**
Anthony Clarke		✓	✓	✓	✓
I acknowledge that these represent my contribution to the above research output, and I have approved the final version.				Signed:	
Christopher Kirkland	✓		✓	✓	✓
I acknowledge that these represent my contribution to the above research output, and I have approved the final version.				Signed:	
Stijn Glorie			✓	✓	
I acknowledge that these represent my contribution to the above research output, and I have approved the final version.				Signed:	
Jack Gillespie			✓		✓
I acknowledge that these represent my contribution to the above research output, and I have approved the final version.				Signed:	
Pete Kinny					✓
I acknowledge that these represent my contribution to the above research output, and I have approved the final version.				Signed:	

Publication 2	**Conception and Design**	**Acquisition of Data and Method Development**	**Data Conditioning and Manipulation**	**Analysis and Statistical Method**	**Interpretation and Discussion**
Anthony Clarke		✓	✓	✓	✓
I acknowledge that these represent my contribution to the above research output, and I have approved the final version.				Signed:	
Christopher Kirkland	✓	✓	✓	✓	✓
I acknowledge that these represent my contribution to the above research output, and I have approved the final version.				Signed:	
Stijn Glorie			✓	✓	✓
I acknowledge that these represent my contribution to the above research output, and I have approved the final version.				Signed:	

Publication 3	**Conception and Design**	**Acquisition of Data and Method Development**	**Data Conditioning and Manipulation**	**Analysis and Statistical Method**	**Interpretation and Discussion**
Anthony Clarke	✓	✓	✓	✓	✓
I acknowledge that these represent my contribution to the above research output, and I have approved the final version.				Signed:	
Christopher Kirkland	✓		✓	✓	✓
I acknowledge that these represent my contribution to the above research output, and I have approved the final version.				Signed:	
Latha Menon					✓
I acknowledge that these represent my contribution to the above research output, and I have approved the final version.				Signed:	
Daniel Condon		✓	✓	✓	
I acknowledge that these represent my contribution to the above research output, and I have approved the final version.				Signed:	
John Cope	✓				✓
I acknowledge that these represent my contribution to the above research output, and I have approved the final version.				Signed:	
Richard Bevins	✓				✓
I acknowledge that these represent my contribution to the above research output, and I have approved the final version.				Signed:	
Stijn Glorie					✓
I acknowledge that these represent my contribution to the above research output, and I have approved the final version.				Signed:	

Publication 4	**Conception and Design**	**Acquisition of Data and Method Development**	**Data Conditioning and Manipulation**	**Analysis and Statistical Method**	**Interpretation and Discussion**
Anthony Clarke	✓	✓	✓	✓	✓
I acknowledge that these represent my contribution to the above research output, and I have approved the final version.				Signed:	
Christopher Kirkland	✓	✓	✓	✓	✓
I acknowledge that these represent my contribution to the above research output, and I have approved the final version.				Signed:	
Richard Bevins	✓				✓
I acknowledge that these represent my contribution to the above research output, and I have approved the final version.				Signed:	
Nick Pearce	✓				✓
I acknowledge that these represent my contribution to the above research output, and I have approved the final version.				Signed:	
Stijn Glorie	✓	✓	✓	✓	✓
I acknowledge that these represent my contribution to the above research output, and I have approved the final version.				Signed:	
Rob Ixer					✓
I acknowledge that these represent my contribution to the above research output, and I have approved the final version.				Signed:	

Publication 5	**Conception and Design**	**Acquisition of Data and Method Development**	**Data Conditioning and Manipulation**	**Analysis and Statistical Method**	**Interpretation and Discussion**
Anthony Clarke		✓	✓	✓	✓
I acknowledge that these represent my contribution to the above research output, and I have approved the final version.				Signed:	
Christopher Kirkland	✓				✓
I acknowledge that these represent my contribution to the above research output, and I have approved the final version.				Signed:	
Stijn Glorie					✓
I acknowledge that these represent my contribution to the above research output, and I have approved the final version.				Signed:	
Raphael Quentin de Gromard					✓
I acknowledge that these represent my contribution to the above research output, and I have approved the final version.				Signed:	
Naomi Tucker					✓
I acknowledge that these represent my contribution to the above research output, and I have approved the final version.				Signed:	

Table of Contents

List of Tables

List of Figures

Chapter 1. Introduction

1.1. The Age of the Earth

"The result, therefore, of our present enquiry is that we find no vestige of a beginning — no prospect of an end".

Two hundred years after James Hutton's closing line in *Theory of the Earth*, we now know that Earth formed about 4.54 billion years ago from a collapsing cloud of dust and gas, and in five billion years, the Sun, as a red giant, will engulf our planet. Thus, we are neatly positioned halfway through this planetary saga to understand the past and future. Geological processes write epic chapters of mountain building, collapse, flooding, continental movement, and ore formation – the tale of the Earth is written in the rocks and their mineral constituents. To add page numbers to the story, we need temporal constraints.

Aristotle observed gradual river sediment deposition and speculated that the thickness of strata could indicate the total accumulation time or the age of sedimentary rocks (Dimas et al., 2022). The ancient Egyptians carefully studied alternating bands of silt and sandstone left each year by the flooding Nile. By measuring these varve deposits, they developed the Nilometer, an intricate structure used to measure the river’s water level and clarity (Mays, 2010). In their most essential form, these efforts are conceptualisations of physical processes that measure time – geochronology. Now an established science, geochronology is the discipline of determining the history of geological material, from entire rocks to μm-scale areas within a crystal.

Relative geochronology uses simple logic like cross-cutting relationships, correlating fossils between strata, and superposition to determine relative ages for rocks. Absolute ages, however, within a specific degree of uncertainty, provide a quantitative temporal framework for geoscientists to interpret Earth's history. Calculated ages can represent various events, from magmatic crystallisation to metamorphism, which are connected to grand narratives such as subduction, ore mineralisation, or even meteorite impacts.

In 1862, Lord Kelvin published "*On the Age of the Earth,"* where he calculated the age of the Earth to be between 20 and 400 million years (Burchfield, 1975; Kelloway et al., 2014). Kelvin's ages were far older than any earlier scripture-based estimates. Nevertheless, these thermodynamic calculations were out by an order of magnitude, for he had not considered a key variable: radioactive decay. The radioactive decay of elements such as uranium, thorium, and potassium help maintain the Earth's heat budget and is the primary driving force behind mantle convection.

Pioneering geochronologists of the 20th century include Ernest Rutherford and Bertram Boltwood, who were the first to measure the age of rocks using radioactive decay. In 1907, Boltwood analysed a thorianite sample from Sri Lanka, which yielded an age of 2.2 billion years – an age older than most imagined possible for the Earth. The theoretical framework for modern geochronology was now set (Boltwood, 1907).

Inspired by Boltwood's work, Arthur Holmes published "*The Association of Lead with Uranium in Rock-Minerals, and its Application to the Measurement of Geological Time"* three months after his graduation in 1910. Later, in 1913, he published *"The Age of the Earth,"* where he showed evidence for billions of years of geological history from radioactive elements in minerals (Holmes, 1913). Holmes persisted and meticulously calibrated his dating methods, considering factors like variations in mineral compositions and potential contamination. He laid the foundation for future work and established radiometric geochronology as a viable tool for dating samples, paving the way for further refinements and applications (Holmes, 1947).

By the 1940s, the Holmes-Houterman model for Pb–Pb dating was developed, and the accepted age of the Earth was about 4.5 billion years. These advances coincided with the establishment of plate tectonic theory; geological processes now had the mechanism and, importantly, the ***time*** to operate (Holmes, 1947). Those efforts bring us to today, where collecting thousands of dates from geological materials is a routine process conducted in laboratories worldwide. Scientists can now date samples to within 0.1% of their true age. Indeed, one might presume James Hutton and Arthur Holmes would be delighted to learn that Earth's beginning is now well constrained to 4.543 ± 0.05 Ga (Dalrymple, 2001).

Geochronology is not merely limited to Earthly timescales, however, as basalt angrites, a rare type of meteorite, have yielded an age of 4.56 ± 0.0001 Ga (Baker et al., 2005). Peering further back, silicon carbide particles within the Murchison Meteorite formed over seven billion years ago during a cosmic interval of increased star formation (Heck et al., 2020). With plans for Mars and asteroid (Ribeiro et al., 2023) sample return missions in the coming decades (Kminek et al., 2021), geochronology, or now rather “chronological” sciences, are set to answer fundamental questions regarding the formation of our Solar System.

1.2. Zircon, Earth's Time Capsule

Absolute ages are obtained from radiometric dating, which uses the principle of nuclear decay, in which unstable parent radionuclides will, over time, decay to at least one lower-mass daughter nuclide. Although it is impossible to determine when an individual atom may decay, the overall decay rate for a quantity of radioactive material can be expressed via a half-life and associated decay constant. One can, therefore, determine the age of a given sample by measuring the ratio of parent to daughter isotopes coupled with a knowledge of the decay constant(s), which are known from laboratory and empirical studies (Schoene et al., 2006; Söderlund et al., 2004). However, essential conditions must be met for a sample to be accurately dated, including:

1. The sample must incorporate sufficient amounts of parent isotope(s) to allow the necessary ingrowth of measurable decay products over time.
2. A closed system must be maintained following crystallisation, ensuring that the parent-daughter isotope ratio accurately reflects the passage of time rather than some secondary, ratio-altering process.
3. Daughter decay products must accumulate within a reservoir where the initial component can be accurately modelled. For ease and lowest uncertainties, a volume in which no daughter product exists at the beginning is ideal. Large amounts of non-radiogenic component without an adequate model to account for this can make samples undatable.

The U–Pb dating method uses the parallel decay chains of ^{238}U to ^{206}Pb, with a half-life of 4.47 billion years, and ^{235}U to ^{207}Pb, with a half-life of 710 million years. Age determinations from each decay system function as a quality check on the other. Given this in-built redundancy and the duration of both half-lives, events occurring over geological timescales, typically 1 – 4500 million years, can be precisely constrained. For example, the oldest terrestrial material dated is zircon from the Jack Hills of Western Australia at 4.404 ± 0.008 Ga (Wilde et al., 2001). Conversely, geologically young zircon (typically < 5 Ma) can be challenging to date due to low concentrations of radiogenic Pb, which results in elevated common to radiogenic Pb ratios. Despite these challenges, Quaternary zircon are able to be reliably dated but are towards the lower limit (for beam-based analytical techniques) of the U–Pb method, including zircon from the Whakamaru Ignimbrite of New Zealand at 449 ± 20 ka (Brown and Fletcher, 1999), Kos-Nisyros volcanics at 124 ± 35 ka (Guillong et al., 2014) and basaltic rocks in Pailin, Cambodia at 1.017 ± 0.067 Ma (Kirkland et al., 2020b). Alternatively, the U–Th/He decay scheme can be used for young zircon where U and Th decay to different isotopes of Pb via α-

emission to produce ^{4}He gas. One can calculate the sample's age by measuring the concentrations of parental ^{238}U, ^{232}Th, and accumulated ^{4}He within the zircon crystal.

In addition to temporal limitations for young samples, geochronology becomes increasingly challenging at smaller spatial scales. For example, due to the high spatial resolution of atom probe tomography (sub-nanometre), parent and daughter isotopes may not be in the same unitised analytical volume due to disequilibrium effects (Gault et al., 2021).

The mineral zircon ($ZrSiO_4$) is the primary target of U–Pb radiometric dating studies (Figure 1.1) as it incorporates appreciable U and negligible Pb concentrations into its crystal lattice during crystallisation. Therefore, all measured Pb within zircon is usually considered radiogenic and not an inherited or “common” component. Zircon is a ubiquitous accessory mineral present in granitoids to sandstones and is exceptionally durable and chemically inert, enabling the storage of valuable information throughout Earth's history (Morton and Hallsworth, 1999).

Despite the widespread use of zircon geochronology, one should consider what zircon U–Pb dates represent. Different minerals from the same igneous rock may give different U–Pb dates, so what is the actual age of that rock? To answer this question, we must understand closure or blocking temperature, a crucial concept in geochronology (Dodson, 1973). Above the closure temperature, daughter isotopes of a given decay chain can freely diffuse out of the crystal lattice. As the system cools, diffusion of daughter isotopes out of the crystal lattice becomes negligible due to decreased atomic mobility. Below the closure temperature, the parent-daughter system can be considered “locked”, and the isotopic clock can start accumulating time. Daughter isotopes produced from radioactive decay will be trapped within the crystal lattice. Thus, if the system remains closed or undisturbed (i.e. below the closure temperature), the measured isotopic ratios will record when the system within the mineral passes below its closure temperature.

Besides being mineral-dependent, the diffusion of daughter isotopes out of a crystal lattice is a volume-controlled process. Small grains have a larger surface area to volume ratio, facilitating the outward diffusion of daughter isotopes at lower temperatures. Furthermore, crystal imperfections such as microfractures, dislocations, and metamict zones can lower closure temperatures by providing fast-diffusion pathways for daughter isotopes (Chew and Spikings, 2021; Glorie et al., 2023; Kirkland et al., 2018). As a result of these complexities for minerals and isotopic systems, closure temperatures are best described as a range rather than a definitive value. For example, the closure temperature of zircon U–Pb is 1000–900°C (Cherniak and Watson, 2001; Lee et al., 1997).

Given the high closure temperature for Pb diffusion in zircon, U–Pb ages from this phase typically represent primary, igneous crystallisation that can help trace processes at lower to mid-crustal levels. Conversely, the (U–Th)/He system in zircon has a closure temperature of 100–200°C, allowing for low-temperature processes such as orogenic uplift, denudation, and low-grade metamorphism to be constrained (Danišík et al., 2017; Reiners, 2005). Coupling different isotopic systems within zircon or other phases could help trace the thermal history of a rock from primary crystallisation to upper-crustal cooling (Campbell et al., 2005; Kirkland et al., 2020a; Reiners, 2005).

When dating igneous rocks using zircon, it is essential to consider the influence of inherited zircon grains, which often complicate the determination of the “true” magmatic crystallisation age of the rock. Antecrysts, zircons formed earlier in the same magmatic system, can be recycled into later magmatic pulses, while xenocrysts are crystals introduced from external sources, such as the assimilation of older crustal material. Ultimately, both types of inheritance can result in dates unrelated to the rock's final crystallisation. These complexities require careful evaluation of zircon through petrographic contexts, U–Pb concordance diagrams, trace element compositions, and isotopic data (e.g., Lu–Hf) to differentiate between inherited versus primary dates.

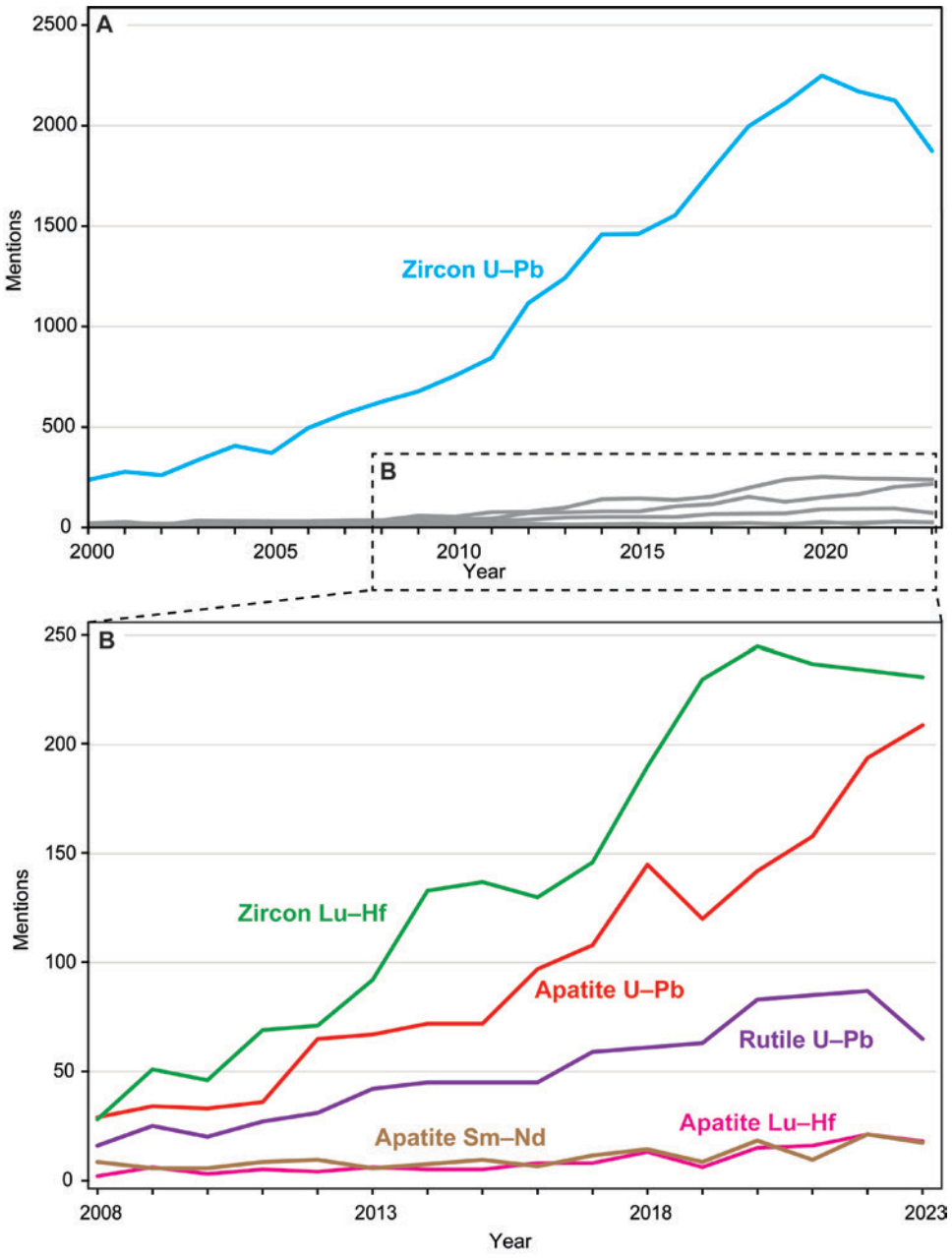

Figure 1.1. Mentions of select geochronometers in title, keywords, and abstracts of published research articles from 2000 to 2023. ***A)*** *The dominance of zircon U–Pb over other geochronometers.* ***B)*** *A magnified view of other geochronometers and isotopic systems. Publication data was sourced from Scopus, 2024.*

1.3. Zircon Lu–Hf: Time-Constrained Chemical Information

The continental crust constitutes less than 1% of the Earth's volume yet is the fundamental geochemical reservoir that modulates the atmosphere, biosphere, and ore deposit formation (Cawood et al., 2013; Hawkesworth et al., 2020). The crust has served as a vital recycling pathway for a wide range of chemicals, important in establishing and maintaining a habitable planet. Despite the importance of the continental crust to civilisation, the timing of formation and subsequent evolution of the crust are contested and remain unresolved in the Earth sciences (Cawood et al., 2013; Hawkesworth et al., 2020). Continental crust results from a dynamic interplay of processes, including partial melting, differentiation, and crustal recycling, all driven by plate tectonics (Hawkesworth et al., 2019). As these processes create and destroy crust, the record of continental crust becomes increasingly fragmented over time. Therefore, zircon, which persists through geological time, is frequently targeted to help unravel continental crust evolution.

Lutetium–hafnium (Lu–Hf) signatures in zircon can give insight into crust-mantle differentiation processes, i.e. continental crust formation and evolution (Spencer et al., 2020). Lutetium is a naturally occurring element, of which 97.4% is stable ^{175}Lu and the remainder radioactive ^{176}Lu. The Lu–Hf technique utilises the radioactive decay of ^{176}Lu to ^{176}Hf through β−decay, with a 37.8-billion-year half-life (Söderlund et al., 2004). During mantle-melting, Hf is more incompatible than Lu; therefore, Hf becomes concentrated in the magma's melt phase, hence its enrichment in the continental crust. This fractionation process produces comparatively radiogenic (depleted mantle or DM) and non-radiogenic ^{176}Hf/^{177}Hf reservoirs (continental crust). Thus, Lu–Hf measurements are increasingly coupled to zircon U–Pb ages to give a time-constrained understanding of crustal evolution. Moreover, the Lu–Hf signature of zircon can track the rate, duration, and timing of the formation and reworking of the continental crust from which it formed (Spencer et al., 2020).

To facilitate comparisons of zircon crystallising melts to a reference frame, we assume that the Hf isotopic composition of the bulk Earth evolved from the Lu–Hf composition of chondritic meteorites, also known as the chondritic uniform reservoir (CHUR). To allow easy comparison, measured Lu–Hf isotopic values are frequently normalised to CHUR, and deviations are expressed in epsilon notation (ƐHf). A positive ƐHf value indicates that the measured zircon has a higher ratio of ^{176}Hf to ^{177}Hf compared to CHUR and, therefore, enrichment in Lu relative to Hf. Such a positive ƐHf > 0 trend may point towards interaction with a more radiogenic, mantle-derived melt for the zircon crystallising magma or mantle-

derived melts with negligible crustal contamination. Conversely, a negative ƐHf < 0 trend can demonstrate the continued reworking of continental crust with an already low Hf/Lu ratio or the assimilation of older crustal material with distinct Lu–Hf ratios compared to mantle-derived magma (Spencer et al., 2020).

1.4. Zircon Trace Elements: An Information Repository

The crystal lattice of zircon can incorporate a diverse trace element cargo, which is sensitive to conditions during crystallisation and thus reflects the geodynamic environment of formation. In addition to U, Th, Pb, Hf, and Lu, zircon includes trace concentrations of rare earth elements (REEs), Ti, Nb, Y, Sc, Fe, and Ta. In conjunction with isotopic analyses, the trace element profile of zircon is a useful petrogenetic tool that provides insight into magmatic evolution and later metamorphism (Bell and Kirkpatrick., 2021; Grimes et al., 2015; Kohn and Kelly, 2018). Indeed, the chemistry of detrital zircon can help characterise the composition of the source rock. For example, the discrimination scheme of Belousova et al. (2002a) classifies detrital zircon (where geological context is lost) using bivariate and multivariate plots to assign source rock types using the concentrations of 26 trace elements.

REEs fractionate and partition within zircon during various geological processes, including partial melting, differentiation, assimilation, metamorphism, and metasomatism (Kohn and Kelly, 2018). Minerals growing alongside zircon compete for the same element budget in the surrounding melt or fluid. For example, due to metamorphic reactions such as the growth of REE incorporating garnet, high-grade metamorphic zircon shows a depletion in those trace elements compared to igneous zircon (Warren et al., 2019). Alternatively, monazite and apatite readily incorporate LREEs, leading to a lower LREE within zircon (Belousova et al., 2002a).

Much like Hf isotopic signatures, zircon REE analyses are normalised to values from chondrites or another reservoir, such as the depleted mantle, to facilitate comparison. REE signatures can fingerprint the tectonic setting (e.g., subduction zone versus volcanic arc) within which the zircon crystallised (Bell and Kirkpatrick, 2021; Grimes et al., 2015; Kohn and Kelly, 2018). In subduction zones, fluids released from the subducting oceanic slab enrich the melt and zircon in light REEs and Th. Conversely, zircon from volcanic arcs shows a depletion in light REEs, as minerals at depth, such as garnet, preferentially extract light REEs from a melt, leaving a depleted melt to rise and form volcanic arcs (Warren et al., 2019). Continental rift zones impart characteristic chemical signatures on zircon, including distinct Ti and Nb enrichments. Zircon trace element profiles from upwelling continental rift melt are primarily

left intact from modifying minerals (Grimes et al., 2015). However, such discrimination diagrams have overlapping compositional fields, reflecting the various variables that work together to dictate the zircon trace element budget (Belousova et al., 2002a; Grimes et al., 2015).

Ti in zircon can be a proxy for the temperature conditions during crystallisation. Ti is incorporated in place of Zr and Si atoms within zircon in a highly temperature-dependent process. Therefore, the measurement of Ti within zircon growth rings could constrain the thermodynamic history of the entire crystal from initial crystallisation to later neoblastic growth. This technique can yield uncertainty within 10–20°C; however, uncertainties surrounding Ti activation energy are unclear; nevertheless, this method can help determine the thermal history of zircon (Fu et al., 2008). Indeed, this method has been applied to Hadean zircon and returned relatively low-temperature crystallisation temperatures consistent with meteoric water interaction and, thus, oceans on the early Earth (Fu et al., 2008).

1.5. Detrital Zircon

Sedimentary rocks cover approximately 75% of Earth's land surface yet only constitute 8% of the volume of the continental crust (Cawood et al., 2013; Hawkesworth et al., 2020). Within this thin veneer of sediments, often from a now-destroyed hinterland, detrital grains offer tantalising clues into Earth's history. Although the immediate geological context in which zircon grows is lost after the grain erodes from its host rock, detrital zircon retains a wealth of source and transport history information. Detrital zircon has been studied to address a wide range of questions in the geosciences, including the rate and duration of continental crust formation (Cawood et al., 2013), sediment flux (source to sink pathways) (Dröllner et al., 2023), and quantifying orogenesis (Spencer et al., 2015). Indeed, detrital grains may provide a more holistic picture of Earth's evolution than the crystalline record alone, as the latter can be poorly preserved, heavily modified, concealed and thus inaccessible.

Attempts to reconstruct the original context of detrital grains are becoming increasingly advanced. For instance, detrital zircon grain morphology holds promise as a provenance tool, offering insight into initial growth conditions, including silica content (mafic versus felsic) and the presence of certain co-crystallising phases such as feldspar (Scharf et al., 2023). Secondary processes, such as the degree of hydraulic sorting through reworking and abrasion, can be discerned from the quantitative analysis of detrital zircon shape parameters (Gartmair et al., 2022; Markwitz and Kirkland, 2018).

Furthermore, in tandem with age information, trace element profiles can provide a unique chemical fingerprint that allows detrital grains to be matched with potential source regions. The combined trace element and Hf-isotopic approach can remove some ambiguity and help discern magmatic sources when determining the provenance of detrital zircon.

Beyond more conventional geological applications, detrital zircon can be used in archaeological fields and has helped locate the source for clay artifacts and building materials (Kelloway et al., 2014; Shewan et al., 2021), giving insights into ancient trade networks and cultures. Furthermore, zircon U–Pb ages have been used as a fingerprint to link the dolerite bluestones of Stonehenge to specific Neolithic quarrying sites in the Mynydd Preseli, Wales (Bevins et al., 2017). Yet the potential for a multi-mineral and isotopic system approach in archaeological provenance studies is yet to be fully explored.

1.6. Zircon – A Biased Tool?

Zircon undoubtedly has an exceptional combination of desirable chemical properties, including high U and negligible common Pb concentrations, high (>900°C) U–Pb closure temperature, and a useful trace element cargo. Combined with its physical properties, such as its durability and ubiquity within lithologies, zircon is the go-to mineral for understanding geological processes over time. Given the variety of techniques applicable to zircon, much of our understanding of geological processes is underpinned by zircon (Figure 1.1) – however, can our tool be biased?

Let us first consider detrital studies. Zircon tends to crystallise from evolved (SiO_2-rich), high-temperature magmas, which undoubtedly biases the geological interpretations towards more Zr and silica-rich, felsic lithologies. Entire orogenies characterised by low-volume magma or terranes composed of mafic rocks might be missed from the detrital zircon record (Hietpas et al., 2011; Krippner and Bahlburg, 2013). Importantly, robust models for the evolution of the continental crust need to include time-constrained information from less evolved (SiO_2-poor) rock types. Estimates for the time of new crust generation suggest that between 60 – 70% of the current volume of continental crust was generated between ~3.0 and 3.5 Ga when the crust may have been largely mafic (low SiO_2) in composition (Belousova et al., 2010; Dhuime et al., 2015).

Although the durability of zircon lends itself to detrital studies since it will survive multiple cycles of reworking, the tendency of zircon to remain in sedimentary systems as multi-cycle grains can complicate the interpretation of the detrital zircon record (Barham et al., 2021). A similar difficulty is encountered when attempting to definitively identify neoblastic growth in S-type granitoids or metamorphic zircon growth, where zircon inheritance is entirely possible. Detrital studies exclusively using zircon may have a limited scope due to these biases.

Analyses of zircon Lu–Hf and U–Pb typically reflect high-temperature processes>800°C; thus, these isotopic systems in zircon do not record low to medium-temperature events. Information on metamorphism below granulite facies, shearing, and associated hydrothermal alteration are typically absent from zircon. Therefore, entire tectonic and magmatic regimes (i.e. mid to upper-crustal processes) are frequently overlooked by zircon Lu–Hf and U–Pb analyses. Nonetheless, zircon fission track dating provides a thermochronological method within a lower temperature regime of 300–200°C. This temperature range corresponds to the partial annealing zone of fission tracks in zircon and can

make this a valuable technique for studying processes, such as cooling related to exhumation, basin evolution, or shallow crustal heating events (Kohn et al., 2024).

Compared to other more chemically diverse phases, the trace element profile of zircon is limited by its restricted trace element cargo, which typically includes U, Pb, Th, Hf, and HREE and, importantly, zircon trace elements are less responsive to variations in melt composition and fractionation processes.

1.7. Alternative Geochronometers

There are about 300 naturally occurring U-bearing minerals, and in theory, any U-bearing phase can be the target of U–Pb geochronology, assuming that some mechanism can be devised to account for any common Pb component. Improvements in precision and spatial resolution from advances in laser ablation systems and ion microprobes have fuelled a surge in the *in-situ* analysis of minerals other than zircon, including apatite and rutile.

Sometimes, zircon can be absent or too small to analyse, e.g., in silica-poor systems or limited sample material, highlighting the importance of apatite and rutile, which may be the only U-bearing minerals present that are amenable to dating.

1.7.1. Apatite

Apatite, $Ca_5(PO_4)_3(X)$, describes a diverse range of phosphate-bearing minerals with three end-member compositions defined by the dominant halogen ion (X) present: hydroxyapatite (OH^-), fluorapatite (F^-), and chlorapatite (Cl^-). Due to the low solubility of P_2O_5 in silicate melts, phosphorus is not readily incorporated in the crystal lattices of major silicate rock-forming minerals. Hence, phosphorus crystallizes phosphates, of which apatite is the most common. Apatite is a ubiquitous accessory mineral found in most rock types and can be a primary phase in ultramafic rocks such as carbonatites and lamprophyres and sedimentary rocks, like phosphorites, as a precipitate. In addition, late-stage apatite found within Lunar basalts and meteorites has been used to match extraterrestrial regolith volatile abundances to terrestrial material and constrain meteorite genesis (Boyce et al., 2010; Brounce et al., 2022).

Given these applications, apatite is a powerful and versatile tool in the Earth sciences able to constrain a diverse range of processes, from tracking the tectonic history of continental crust (Glorie et al., 2020), unravelling shear zone fluid dynamics (Prent et al., 2020; Ribeiro et al., 2020) to dating bioapatite within fossils (Herwartz et al., 2013). Moreover, apatite has vital biological functions, as hydroxyapatite is the primary inorganic component of tooth enamel and bone material. Apatite is the most abundant phosphate mineral, the basis of the phosphorus cycle and is essential to sustaining life (Filippelli, 2008).

Despite often containing lower concentrations of U and elevated concentrations of non-radiogenic common lead compared to zircon, apatite geochronology is achievable through the U–Pb system. In addition to being a U–Pb geochronometer, apatite is also amenable to Sm–Nd or Lu–Hf geochronology through the isochron method. The half-life of ^{147}Sm to ^{143}Nd is 107 Ga, which allows its use as a geochronometer and has seen use in dating ancient mafic rocks

and meteorites (LaFlamme et al., 2017). Lu–Hf can be deployed similarly to the Sm–Nd system to record time-constrained magmatic differentiation (Barfod et al., 2002; Debaille et al., 2017). To summarise, apatite can be dated using several radioactive decay systems:

1. U–Pb, with a closure temperature of ca. 375–600°C (Chew and Spikings, 2021; Cochrane et al., 2014; Kirkland et al., 2018). This system is typically considered both a geo- and thermo-chronometer in apatite, as the relatively low closure temperature may preserve cooling or thermal resetting during mid to upper-crustal processes.
2. Lu–Hf dating. This system has a closure temperature of 660 – 730°C (Barfod et al., 2002; Chew and Spikings, 2015; Glorie et al., 2023) and thus typically constrains the timing of primary crystallisation or high-grade metamorphism.
3. Sm–Nd. The closure temperature is similar to that of Lu-Hf, around 600°C to 700°C; thus, this system is primarily used to date high-temperature processes such as magmatic crystallisation or later hydrothermal processes.

Laboratory and empirical studies report diverse apatite U–Pb closure temperatures (Chew and Spikings, 2021; Cochrane et al., 2014; Kirkland et al., 2018). However, natural apatite likely closes to Pb-U diffusion at approximately 375 to 600°C (Chew and Spikings, 2015), but the specific temperature is influenced by grain size and fast diffusion pathways (Kirkland et al., 2018). Therefore, apatite's U–Pb system is susceptible to thermal disturbance following initial crystallisation (Glorie et al., 2019). Apatite U–Pb dates may correspond to relatively lower temperature tectonic events other than primary crystallisation than zircon, such as regional metamorphism at mid-to-shallow crustal levels (Kirkland et al., 2018). Thus, measured apatite U–Pb and Sm–Nd ratios may not represent thermally activated volume diffusion from magmatic crystallisation but recrystallisation.

Compared to zircon, apatite incorporates a far more heterogenous trace element cargo, including REEs, Y, Mn, Sr, U, Th, halogens, and ions such as Si, S, and V. Primary geological factors such as host rock composition, magma temperature and oxygen fugacity and secondary processes such as hydrothermal fluid overprinting can influence the chemical composition of apatite (Belousova et al., 2002b Mao et al., 2016; O'Sullivan et al., 2018). Thus, apatite's ability to host a wide range of condition-sensitive trace elements combined with radiometric age determinations makes it an extremely powerful tracer for a range of geological phenomena to locating ore-mineralisation (Mao et al., 2016) to detrital studies and understanding sediment flux (O'Sullivan et al., 2018).

In-situ laser ablation Lu–Hf dating of apatite is a new tool (Glorie et al., 2023; Kharkongor et al., 2023; Simpson et al., 2021) that is potentially more robust to isotopic resetting than the U–Pb. Traditionally, apatite Lu–Hf dating required sample digestion via the dissolution and chemical separation of ^{176}Lu, ^{176}Yb on ^{176}Hf prior to mass spectrometry (Larsson and Söderlund, 2005), resulting in the loss of geological context, whereas *in-situ* Lu–Hf geochronology has a spatial resolution of 100—60 μm (Simpson et al., 2021). Apatite in mafic rocks typically has low U concentrations, leading to a low ratio of radiogenic Pb to common Pb, increasing the uncertainty of age determinations. Fortunately, the Lu–Hf geochronology can reliably date apatite within mafic-ultramafic rocks (Kharkongor et al., 2023).

Apatite Sm–Nd may not always be a robust geochronometer due to later modification, i.e. open system disruptions from fluid interaction. High-temperature fluids rich in ligands (e.g. CO_2, F^-) typical of hydrothermal processes can change the $^{147}Sm/^{144}Nd$ ratio, with both elements becoming mobilised out of the crystal lattice of apatite (Gillespie et al., 2022; Li et al., 2022). Therefore, the present ratio could not reflect the apatite's crystallisation age.

1.7.2. Rutile

Rutile (TiO_2) is the most abundant titanium oxide polymorph (anatase, akaogiite, and brookite) and is typically an accessory phase in high-pressure metamorphic rocks, and metasomatised peridotites. Less commonly, rutile is found in plutonic igneous rocks and mafic extrusive rocks such as kimberlites and lamproites. Furthermore, rutile is a ubiquitous heavy mineral found in clastic sedimentary rocks due to its stability during weathering, transport, and diagenesis (Zack and Kooijman, 2017).

Rutile incorporates trace concentrations of U and Pb and a diverse suite of other elements, including Fe, Cr, Nb Ta, and HFSE. However, compared to zircon, rutile U–Pb dating is complicated by its low U concentrations (as low as <0.01 ppm) and high common Pb to radiogenic Pb ratios. Compared to apatite and zircon, rutile is a comparatively underutilised geochronometer (Santos et al., 2020). An advantage of rutile is low Th/U ratios (<0.003) that allow for a common Pb correction via ^{208}Pb due to negligible radiogenic ^{208}Pb from ^{232}Th decay (Zack and Kooijman, 2017). However, rutile can be elevated in Th (up to 35 ppm), as reported from diagenetically grown rutile from Oman (Dunkl and von Eynatten, 2009).

The closure temperature of U–Pb in rutile is highly dependent on grain size but typically ranges between 500 – 600°C (Cherniak, 2000); therefore, like apatite, rutile U–Pb analyses are often used in thermochronology (Li et al., 2003; Liebmann et al., 2023). Furthermore, given the lower closure temperature of rutile U–Pb, hydrothermal vein emplacement has also been accurately dated using rutile. To that end, hydrothermal rutile can constrain the formation of porphyry Cu deposits at a precision of 2% despite the variable incorporation of common Pb (Schirra and Laurent, 2021).

1.8. Problems and Solutions Associated with Alternative Geochronometers

1.8.1. Common Pb

U-bearing geochronometers such as zircon, rutile, and apatite each variably incorporate common Pb into their crystal lattice during magmatic formation or subsequent metamorphism and fluid interaction (Figure 1.2) (Chew et al., 2014). Common or non-radiogenic isotopes of Pb must be accounted for to produce robust radiometric dates. For this contribution, the primary concern was the accurate correction of non-radiogenic Pb within rutile and apatite to give meaningful ages. Pb has four stable isotopes, of which ^{204}Pb is primordial or non-radiogenic and makes up 1.4% of natural lead. Thus, ^{204}Pb can provide a baseline for the initial Pb composition (i.e. the concentration of other Pb isotopes present) during the formation of a rock or mineral. Critically, if common Pb is **not** accounted for, calculated U–Pb ages can become skewed, potentially leading to erroneous interpretation.

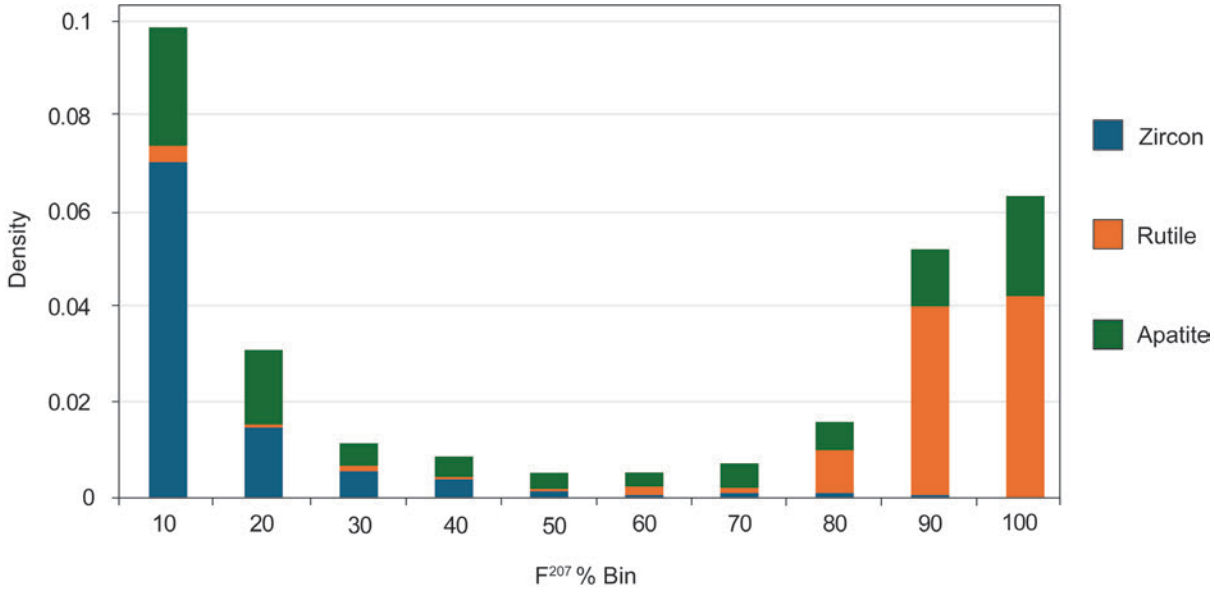

Figure 1.2. A probability density stacked bar chart of F^{207} % values (in 10% bins) for zircon, rutile, and apatite analysed in this thesis. Note the elevated common Pb content of apatite and rutile compared to zircon.

The problem of common Pb can be accounted for by using the following three techniques:

1. This method involves constraining the common Pb composition at the time of crystallisation. This technique is typically performed by conducting multiple U–Pb analyses of common Pb-bearing minerals such as apatite or rutile and then plotting results on a Tera-Wasserburg diagram, which is a plot of ^{207}Pb/^{206}Pb versus ^{238}U/^{206}Pb. Such analyses represent binary mixtures of common Pb and radiogenic Pb and will generally form a straight line in Tera-Wasserburg space, known as an isochron, from which a date can be calculated. The degree of mixing between the initial and radiogenic

Pb composition can expressed as an F^{207} %, where a higher % implies a greater component of common Pb. The upper isochron intercept corresponds to the common $^{207}Pb/^{206}Pb$ ratio composition during crystallisation, and the lower Tera-Wasserburg intercept defines the timing of radiogenic Pb incorporation. Benefits of this approach include the direct assessment and, thus, correction of Pb isotopic heterogeneity within single mineral grains; however, loss or gain during later alteration can complicate the interpretation of the initial common Pb composition. Furthermore, when F^{207} % is insufficiently variable, no robust isochron regressions can be calculated, resulting in poorly defined dates.

2. Another common Pb correction method uses a model-based Pb isotopic composition using the measured concentration of ^{204}Pb or another Pb isotope. Following the measurement of ^{204}Pb, a model of Pb isotopic composition is used to derive the initial Pb ratios. The Pb isotope model chosen can vary from the two-stage Stacey and Kramers (1975) model of terrestrial Pb isotopic evolution within the entire continental crust to localised models, such as that proposed for the Yilgarn Craton (Zametzer et al., 2022). The benefits of a model-based approach include its applicability to a wide range of minerals with varying common Pb concentrations in diverse geological settings. Furthermore, in cases where ^{204}Pb is unmeasurable, a model-based approach still allows for common Pb correction using ^{207}Pb or ^{208}Pb. However, this method fails when the initial Pb composition of the analysed material differs from that of the model, for example, due to local radiogenic Pb reservoirs from the breakdown of a high-Pb-producing precursor phase such as zircon or monazite.
3. A final method includes measuring the Pb isotopic composition in a co-existing low U–Th phase, such as feldspar, to constrain the U-bearing common Pb composition. However, areas pervasively altered by hydrothermal fluids, e.g., orebodies, may not exhibit a primary common Pb signature. Furthermore, this technique cannot be applied to detrital samples with lost geological context.

An important note is that directly measuring ^{204}Pb composition during LA-ICP-MS is challenging due to low natural abundances combined with isobaric interference and contamination from ^{204}Hg, which shares the same mass-to-charge ratio as ^{204}Pb. Such contamination can come from a persistent source, such as the carrier gases (He, Ar), or transient contamination, such as the accidental ablation of a Hg-bearing phase (e.g., cinnabar or gold). Recent work has demonstrated the potential of using collision cell technology to remove ^{204}Hg

interference to allow the accurate measurement of ^{204}Pb using ICP-MS/MS instruments. Such instruments are fitted with a reaction cell, wherein NH_3 gas can eliminate the interference from ^{204}Hg on ^{204}Pb. Subsequently, the $^{206}Pb/^{204}Pb$ and $^{207}Pb/^{204}Pb$ ratios can be used for accurate, common Pb corrections (Gilbert and Glorie, 2020).

While common Pb is often considered a hindrance to geochronology, common Pb signatures are a useful tool that provides insight into the magmatic source from which the mineral originated (Zametzer et al., 2022) and are an indicator of crustal recycling (Halla, 2018), formation (Hartnady et al., 2022), or fluid-rock interaction (Ishizuka et al., 2003; Krmíčková et al., 2020). Furthermore, common Pb isotopic compositions can serve as geological fingerprints that help identify the sources of archaeological remains (Evans et al., 2022) and the extent of reworking that sedimentary rocks and detrital minerals have experienced (Tyrrell et al., 2006; Zutterkirch et al., 2023).

1.9. Research Objectives

The primary objective of this thesis is to integrate analyses and insights from often underutilised or overlooked geochronometers with conventional zircon U–Pb analysis to gain a more complete understanding of geological processes occurring at various locations within the crust. This thesis also focuses on fingerprinting material provenance using isotopic signatures. Each chapter uses a different sample medium, including sand, rock, thin and thick -sections (or a combination thereof), to illustrate how additional minerals in diverse geological contexts can be incorporated into the workflow of typical zircon-based geochronology studies. As is often the case, despite the availability of other minerals, geochronological studies frequently target zircon alone.

This thesis comprises several case studies of decreasing temporal (Archean to Phanerozoic) and spatial scales (craton to a single stone). Each chapter explores how interpretations from "routine" zircon geochronology can be complemented by analysing additional mineral phases.

Individual objectives include:

1. Detrital zircon (U–Pb and Lu–Hf) studies of sedimentary rock and unconsolidated sediment are a staple of the earth sciences. However, detrital zircon datasets are demonstrably biased towards high-temperature felsic crystalline source rocks. Compared to zircon, apatite and rutile are typically more abundant in mafic and

metamorphic rocks. Can compositional biases in detrital zircon datasets be mitigated by incorporating apatite and rutile?

2. In the case of zircon U–Pb studies, age determinations may not be as robust due to a low number of analyses (e.g. little sample material or an ultramafic rock). To what extent can other minerals, such as apatite and rutile, lead to improved age determinations in situations with deficient zircon?
3. Apatite U–Pb analyses are increasingly used in geosciences (Figure 1.1). However, other decay systems within apatite, including Lu–Hf and Sm–Nd are comparatively underutilised. Given the varying closure temperature of each system within apatite and the different propensity to common isotope contamination, can a multi-isotopic system yield more holistic insights into the thermal history of a rock than U–Pb alone? Moreover, are apatite U–Pb and Lu–Hf ages comparable in a detrital dataset, and do they provide a more specific fingerprint of the source region?
4. A multi-mineral and isotopic system approach can yield more precise provenance determinations than zircon U–Pb analyses alone. Accordingly, what are the novel applications of multi-mineral provenance interpretations from isotopic analysis of multiple minerals? What enhanced source interpretations are possible with zircon Lu–Hf measurements?

1.9.1 Thesis Structure

This thesis comprises five chapters of research work, all published in peer-reviewed international journals as standalone papers. Consequently, there is some unavoidable repetition of method sections between each chapters.

Each chapter addresses the outlined thesis objectives at different spatial and temporal scales (Figure 1.3). Chapter 2 begins at a cratonic scale and investigates detrital zircon and apatite from ephemeral streams draining Paleoarchean crust in the East Pilbara Terrane, Western Australia. In Chapter 3, we deploy a similar detrital zircon and apatite approach to study Proterozoic rocks along the southeast margin of the Yilgarn Craton. Chapters 4 and 5 decrease the scale further to a single granitoid pluton and rhyolitic tuff layer from the Neoproterozoic basement of southern Britain. Finally, Chapter 6 studies zircon, apatite, and rutile using a variety of techniques (U–Pb, Lu–Hf, and trace element analysis) to answer a fundamental question in the archaeological sciences: where did the central six-tonne megalith at the centre of Stonehenge, the Altar Stone, come from?

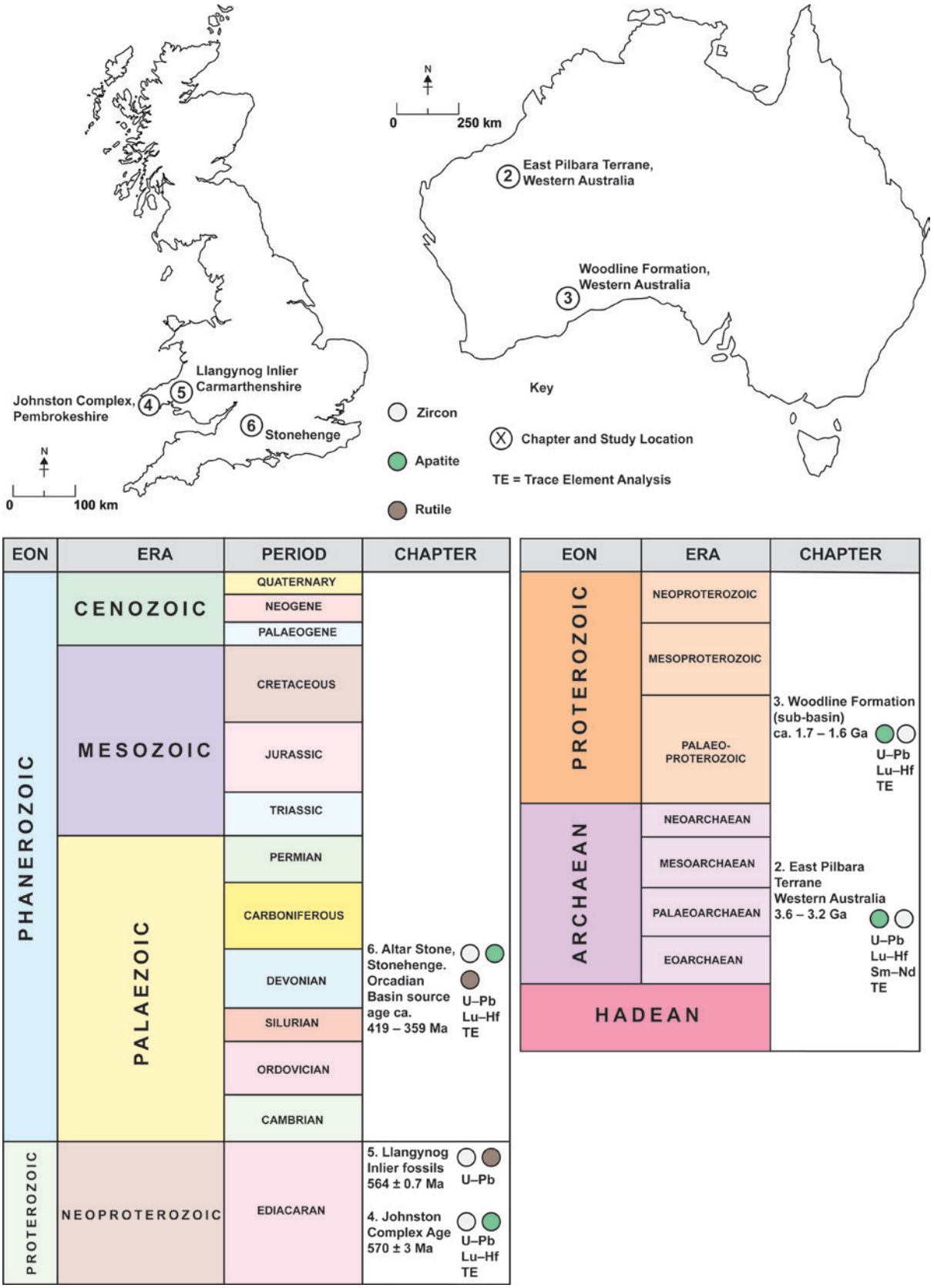

Figure 1.3. The locations and geological time covered by each chapter of this thesis. The mineral and isotopic systems analysed within each chapter are shown within the geological timescale. The mineral dates obtained in this theis comprise nearly 75% of Earth's history.

Chapter 2: **The unroofing of Archean crustal domes as recorded by detrital zircon and apatite.** This work presents *in-situ* U–Pb, Lu–Hf, and Sm–Nd isotopic data for detrital zircon and apatite collected from ephemeral streams of the East Pilbara Terrane, Western Australia. Both minerals offered distinct insights into Archean crustal evolution. Zircon U–Pb ages span 3.6. – 0.2 Ga, representing an archive of magmatism throughout the West Australian Craton, but are compositionally biased towards felsic crust. Apatite show a unimodal Pilbara U–Pb age at ca. 2.9 Ga, consistent with regional cooling following prograde metamorphism and magmatic crystallisation at 3.2 Ga from Lu-Hf and Sm-Nd isochron ages. Time-resolved zircon ƐHf tracks the unroofing of evolved (unradiogenic) detrital components consistent with the unroofing of dome cores. Ultimately, compared to zircon, detrital apatite in the Pilbara Craton does not provide a comprehensive record of crustal evolution due to its lability, but highlights the importance of certain events that can be underappreciated by zircon alone.

Chapter 3: **Detrital zircon and apatite reveal Paleoproterozoic rifting along the eastern margin of the Yilgarn Craton.** Using the workflow developed in Chapter 2, we analyse zircon (U–Pb, Lu–Hf, and trace elements) and apatite (U–Pb) from sand and rock to identify the earliest expression of rifting during the Albany-Fraser Orogeny along the eastern margin of the Yilgarn Craton. Our data from the Woodline Formation show that rifting commenced along the southeast margin of the Yilgarn Craton at ca. 2225 Ma, some 200 Ma earlier than what is currently recognised from the crystalline record. Detrital zircon trace element analyses characterise the ca. 2225 Ma detritus originating from more mafic, A-type granitoids, whilst Paleoproterozoic apatite points towards a proximal source for rift-related lithologies. In this case study, the holistic zircon-apatite approach allowed for detailed characterisation of source geology where the only extant archive of lithology was detrital grains.

Chapter 4: **A detective duo of apatite and zircon geochronology for East Avalonia, Johnston Complex, Wales.** This work implements a tandem zircon-apatite U–Pb and trace element analytical approach to unravel the crustal evolution of Neoproterozoic rocks from the crystalline basement of southern Britain. In the case of the Johnston Complex of southwest Wales, coeval zircon-apatite U–Pb ages give greater confidence in magmatic age determination when the Pb-closure temperature in apatite has not been exceeded. Due to solubility considerations, apatite is unlikely to represent an inherited component within S-type granitoids; thus, the combined zircon-apatite method can help discern primary versus inherited phases. This work necessitates a revised timeline of magmatism in East Avalonia during the assembly of Gondwana.

Chapter 5: **U–Pb zircon-rutile dating of the Llangynog Inlier, Wales: constraints on an Ediacaran shallow marine fossil assemblage from East Avalonia.** In this case study, we demonstrate that zircon age determinations can be enhanced by incorporating U–Pb analyses from rutile, an often-overlooked geochronometer. The precision of a zircon concordia age of 563 ± 8 Ma (n = 3) is improved by 25 % to 563 ± 6 Ma (n = 97) when a regression through rutile and zircon U–Pb analyses is calculated. ID-TIMS of zircon yielded an age of 564.09 ± 0.75 Ma, the precision required for biostratigraphic comparisons. We demonstrate the cosmopolitan distribution of organisms in shallow and deep marine environments across Avalonia during the mid-Ediacaran.

Chapter 6: **A Scottish Provenance for the Altar Stone of Stonehenge**. Stonehenge is Europe's most famous prehistoric monument, yet its construction history remains cryptic. The building blocks of Stonehenge have varied provenances: The sarsen stones were sourced locally, ~25 km away the monument from the West Woods, Marlborough, whereas the "bluestones" were transported from the Mynydd Preseli, southwest Wales, ~225 km away from the Salisbury Plain. However, the provenance of the central six-tonne sandstone megalith, the Altar Stone, remained unknown. In this chapter, we implement a multi-mineral (zircon, apatite and rutile) and isotopic system (U–Pb and Lu–Hf) to answer a crucial question in the Stonehenge saga: where did the Altar Stone come from? Our results show that the Altar Stone was sourced from the Old Red Sandstone of Scotland's Orcadian Basin. A Scottish provenance thus necessitates a transport route of at least 750 km, an unprecedented distance for Neolithic construction. These findings point towards a Neolithic marine transport spanning the entire length of Britain.

1.10. References

Baker, J., Bizzarro, M., Wittig, N., Connelly, J., and Haack, H., 2005, Early planetesimal melting from an age of 4.5662 Gyr for differentiated meteorites: Nature, v. 436, no. 7054, p. 1127-1131.

Barfod, G., Frei, R., and Krogstad, E. J., 2002, The closure temperature of the Lu-Hf isotopic system in apatite: Geochimica et Cosmochimica Acta, v. 66, p. A51-A51.

Bell, E. A., and Kirkpatrick, H. M., 2021, Effects of crustal assimilation and magma mixing on zircon trace element relationships across the Peninsular Ranges Batholith: Chemical Geology, v. 586, p. 120616.

Belousova, E., Griffin, W., O'Reilly, S. Y., and Fisher, N., 2002a, Igneous zircon: trace element composition as an indicator of source rock type: Contributions to Mineralogy and Petrology, v. 143, no. 5, p. 602-622.

Belousova, E. A., Griffin, W. L., O'Reilly, S. Y., and Fisher, N. I., 2002b, Apatite as an indicator mineral for mineral exploration: trace-element compositions and their relationship to host rock type: Journal of Geochemical Exploration, v. 76, no. 1, p. 45-69

Belousova, E., Kostitsyn, Y. A., Griffin, W. L., Begg, G. C., O'Reilly, S. Y., and Pearson, N. J., 2010, The growth of the continental crust: Constraints from zircon Hf-isotope data: Lithos, v. 119, no. 3-4, p. 457-466.

Bevins, R., Atkinson, N., Ixer, R., and Evans, J., 2017, U–Pb zircon age constraints for the Ordovician Fishguard Volcanic Group and further evidence for the provenance of the Stonehenge bluestones: Journal of the Geological Society, v. 174, no. 1, p. 14-17.

Boltwood, B. B., 1907, ART. VII.--On the Ultimate Disintegration Products of the Radio-active Elements. Part II. The Disintegration Products of Uranium: American Journal of Science (1880-1910), v. 23, no. 134, p. 77.

Boyce, J. W., Liu, Y., Rossman, G. R., Guan, Y., Eiler, J. M., Stolper, E. M., and Taylor, L. A., 2010, Lunar apatite with terrestrial volatile abundances: Nature, v. 466, no. 7305, p. 466-469.

Brounce, M., Boyce, J. W., and McCubbin, F. M., 2022, Sulfur in apatite from the Nakhla meteorite record a late-stage oxidation event: Earth and Planetary Science Letters, v. 595, p. 117784.

Brown, S. J. A., and Fletcher, I. R., 1999, SHRIMP U-Pb dating of the preeruption growth history of zircons from the 340 ka Whakamaru Ignimbrite, New Zealand: Evidence for >250 k.y. magma residence times: Geology, v. 27, no. 11, p. 1035-1038.

Burchfield, J. D., 1975, Kelvin and the Physics of Time, *in* Burchfield, J. D., ed., Lord Kelvin and the Age of the Earth: London, Macmillan Education UK, p. 21-56.

Campbell, I. H., Reiners, P. W., Allen, C. M., Nicolescu, S., and Upadhyay, R., 2005, He–Pb double dating of detrital zircons from the Ganges and Indus Rivers: Implication for quantifying sediment recycling and provenance studies: Earth and Planetary Science Letters, v. 237, no. 3, p. 402-432.

Cawood, P. A., Hawkesworth, C. J., and Dhuime, B., 2013, The continental record and the generation of continental crust: GSA Bulletin, v. 125, no. 1-2, p. 14-32.

Cherniak, D. J., 2000, Pb diffusion in rutile: Contributions to Mineralogy and Petrology, v. 139, no. 2, p. 198-207.

Cherniak, D. J., and Watson, E. B., 2001, Pb diffusion in zircon: Chemical Geology, v. 172, no. 1, p. 5-24.

Chew, D. M., Petrus, J. A., and Kamber, B. S., 2014, U–Pb LA–ICPMS dating using accessory mineral standards with variable common Pb: Chemical Geology, v. 363, p. 185-199.

Chew, D. M., and Spikings, R. A., 2015, Geochronology and Thermochronology Using Apatite: Time and Temperature, Lower Crust to Surface: Elements, v. 11, no. 3, p. 189-194.

Chew, D. M., and Spikings, R. A., 2021, Apatite U-Pb Thermochronology: A Review: Minerals, v. 11, no. 10.

Cochrane, R., Spikings, R. A., Chew, D. M., Wotzlaw, J. F., Chiaradia, M., Tyrrell, S., Schaltegger, U., and Van der Lelij, R., 2014, High temperature (>350°C) thermochronology and mechanisms of Pb loss in apatite: Geochimica et Cosmochimica Acta, v. 127, p. 39-56.

Dalrymple, G. B., 2001, The age of the Earth in the twentieth century: a problem (mostly) solved: Geological Society, London, Special Publications, v. 190, no. 1, p. 205-221.

Danišík, M., McInnes, B. I. A., Kirkland, C. L., McDonald, B. J., Evans, N. J., and Becker, T., 2017, Seeing is believing: Visualization of He distribution in zircon and implications for thermal history reconstruction on single crystals: Science Advances, v. 3, no. 2, p. e1601121.

Debaille, V., Van Orman, J., Yin, Q.-Z., and Amelin, Y., 2017, The role of phosphates for the Lu–Hf chronology of meteorites: Earth and Planetary Science Letters, v. 473, p. 52-61.

Dhuime, B., Wuestefeld, A., and Hawkesworth, C. J., 2015, Emergence of modern continental crust about 3 billion years ago: Nature Geoscience, v. 8, no. 7, p. 552-555.

Dimas, P., Falcon, A., and Kelsey, S., 2022, Aristotle: On Generation and Corruption Book II, *in* Dimas, P., Falcon, A., and Kelsey, S., eds., Aristotle: On Generation and Corruption Book II: Introduction, Translation, and Interpretative Essays: Cambridge, Cambridge University Press, p. i-ii.

Dodson, M. H., 1973, Closure temperature in cooling geochronological and petrological systems: Contributions to Mineralogy and Petrology, v. 40, no. 3, p. 259-274.

Dröllner, M., Barham, M., and Kirkland, C. L., 2023, Reorganization of continent-scale sediment routing based on detrital zircon and rutile multi-proxy analysis: Basin Research, v. 35, no. 1, p. 363-386.

Dunkl, I., and von Eynatten, H., 2009, Anchizonal-hydrothermal growth and (U-Th)/He dating of rutile crystals in the sediments of Hawasina window, Oman.

Evans, J. A., Pashley, V., Mee, K., Wagner, D., Parker Pearson, M., Fremondeau, D., Albarella, U., and Madgwick, R., 2022, Applying lead (Pb) isotopes to explore mobility in humans and animals: PLOS ONE, v. 17, no. 10, p. e0274831.

Filippelli, G. M., 2008, The global phosphorus cycle: past, present, and future: Elements, v. 4, no. 2, p. 89-95.

Fu, B., Page, F. Z., Cavosie, A. J., Fournelle, J., Kita, N. T., Lackey, J. S., Wilde, S. A., and Valley, J. W., 2008, Ti-in-zircon thermometry: applications and limitations: Contributions to Mineralogy and Petrology, v. 156, no. 2, p. 197-215.

Gartmair, G., Barham, M., and Kirkland, C. L., 2022, Detrital Zircon Perspectives on Heavy Mineral Sand Systems, Eucla Basin, Australia: Economic Geology, v. 117, no. 2, p. 383-399.

Gault, B., Chiaramonti, A., Cojocaru-Mirédin, O., Stender, P., Dubosq, R., Freysoldt, C., Makineni, S. K., Li, T., Moody, M., and Cairney, J. M., 2021, Atom probe tomography: Nature Reviews Methods Primers, v. 1, no. 1, p. 51.

Gilbert, S. E., and Glorie, S., 2020, Removal of Hg interferences for common Pb correction when dating apatite and titanite by LA-ICP-MS/MS: Journal of Analytical Atomic Spectrometry, v. 35, no. 7, p. 1472-1481.

Gillespie, J., Kirkland, C. L., Kinny, P. D., Simpson, A., Glorie, S., and Rankenburg, K., 2022, Lu–Hf, Sm–Nd, and U–Pb isotopic coupling and decoupling in apatite: Geochimica et Cosmochimica Acta, v. 338, p. 121-135.

Glorie, S., Hand, M., Mulder, J., Simpson, A., Emo Robert, B., Kamber, B., Fernie, N., Nixon, A., and Gilbert, S., 2023, Robust laser ablation Lu–Hf dating of apatite: an empirical

evaluation: Geological Society, London, Special Publications, v. 537, no. 1, p. SP537-2022-2205.

Glorie, S., Jepson, G., Konopelko, D., Mirkamalov, R., Meeuws, F., Gilbert, S., Gillespie, J., Collins, A. S., Xiao, W., Dewaele, S., and De Grave, J., 2019, Thermochronological and geochemical footprints of post-orogenic fluid alteration recorded in apatite: Implications for mineralisation in the Uzbek Tian Shan: Gondwana Research, v. 71, p. 1-15.

Glorie, S., March, S., Nixon, A., Meeuws, F., O'Sullivan, G. J., Chew, D. M., Kirkland, C. L., Konopelko, D., and De Grave, J., 2020, Apatite U–Pb dating and geochemistry of the Kyrgyz South Tian Shan (Central Asia): Establishing an apatite fingerprint for provenance studies: Geoscience Frontiers, v. 11, no. 6, p. 2003-2015.

Grimes, C. B., Wooden, J. L., Cheadle, M. J., and John, B. E., 2015, "Fingerprinting" tectono-magmatic provenance using trace elements in igneous zircon: Contributions to Mineralogy and Petrology, v. 170, no. 5, p. 46.

Guillong, M., von Quadt, A., Sakata, S., Peytcheva, I., and Bachmann, O., 2014, LA-ICP-MS Pb–U dating of young zircons from the Kos–Nisyros volcanic centre, SE Aegean arc: Journal of Analytical Atomic Spectrometry, v. 29, no. 6, p. 963-970.

Halla, J., 2018, Pb isotopes – A multi-function tool for assessing tectonothermal events and crust-mantle recycling at late Archaean convergent margins: Lithos, v. 320-321, p. 207-221.

Hartnady, M. I. H., Kirkland, C. L., Smithies, R. H., Johnson, S. P., and Johnson, T. E., 2022, Pb isotope insight into the formation of the Earth's first stable continents: Earth and Planetary Science Letters, v. 578.

Hawkesworth, C., Cawood, P. A., and Dhuime, B., 2019, Rates of generation and growth of the continental crust: Geoscience Frontiers, v. 10, no. 1, p. 165-173.

Hawkesworth, C., Cawood, P. A., and Dhuime, B., 2020, The evolution of the continental crust and the onset of plate tectonics: Front Earth Sci (Lausanne), v. 8.

Heck, P. R., Greer, J., Kööp, L., Trappitsch, R., Gyngard, F., Busemann, H., Maden, C., Ávila, J. N., Davis, A. M., and Wieler, R., 2020, Lifetimes of interstellar dust from cosmic ray exposure ages of presolar silicon carbide: Proceedings of the National Academy of Sciences, v. 117, no. 4, p. 1884-1889.

Herwartz, D., Münker, C., Tütken, T., Hoffmann, J. E., Wittke, A., and Barbier, B., 2013, Lu–Hf isotope systematics of fossil biogenic apatite and their effects on geochronology: Geochimica et Cosmochimica Acta, v. 101, p. 328-343.

Hietpas, J., Samson, S., and Moecher, D., 2011, A direct comparison of the ages of detrital monazite versus detrital zircon in Appalachian foreland basin sandstones: Searching for the record of Phanerozoic orogenic events: Earth and Planetary Science Letters, v. 310, no. 3, p. 488-497.

Holmes, A., 1913, The Age of the Earth, Harper & Brothers.

Holmes, A., 1947, A Revised Estimate of the Age of the Earth: Nature, v. 159, no. 4030, p. 127-128.

Ishizuka, O., Taylor, R. N., Milton, J. A., and Nesbitt, R. W., 2003, Fluid–mantle interaction in an intra-oceanic arc: constraints from high-precision Pb isotopes: Earth and Planetary Science Letters, v. 211, no. 3, p. 221-236.

Kelloway, S., Craven, S., Pecha, M., Dickinson, W., Gibbs, M., Ferguson, T., and Glascock, M., 2014, Sourcing Olive Jars Using U-Pb Ages of Detrital Zircons: A Study of 16th Century Olive Jars Recovered from the Solomon Islands: Geoarchaeology, v. 29, p. 47-60.

Kharkongor, M. B. K., Glorie, S., Mulder, J., Kirkland, C. L., Chew, D., Kohn, B., and Simpson, A., 2023, Apatite laser ablation Lu–Hf geochronology: A new tool to date mafic rocks: Chemical Geology, v. 636, p. 121630.

Kirkland, C. L., Barham, M., and Danišík, M., 2020a, Find a match with triple-dating: Antarctic sub-ice zircon detritus on the modern shore of Western Australia: Earth and Planetary Science Letters, v. 531.

Kirkland, C. L., Danišík, M., Marsden, R., Piilonen, P., Barham, M., and Sutherland, L., 2020b, Dating young zircon: A case study from Southeast Asian megacrysts: Geochimica et Cosmochimica Acta, v. 274, p. 1-19.

Kirkland, C. L., Yakymchuk, C., Szilas, K., Evans, N., Hollis, J., McDonald, B., and Gardiner, N. J., 2018, Apatite: a U-Pb thermochronometer or geochronometer?: Lithos, v. 318-319, p. 143-157.

Kminek, G., Meyer, M. A., Beaty, D. W., Carrier, B. L., Haltigin, T., and Hays, L. E., 2021, Mars Sample Return (MSR): Planning for Returned Sample Science: Astrobiology, v. 22, no. S1, p. S-1-S-4.

Kohn, M. J., and Kelly, N. M., 2018, Petrology and Geochronology of Metamorphic Zircon, Microstructural Geochronology, p. 35-61.

Kohn, B. P., Ketcham, R. A., Vermeesch, P., Boone, S. C., Hasebe, N., Chew, D., Bernet, M., Chung, L., Danišík, M., Gleadow, A. J. W., and Sobel, E. R., 2024, Interpreting and

reporting fission-track chronological data: GSA Bulletin, v. 136, no. 9-10, p. 3891-3920.

Krippner, A., and Bahlburg, H., 2013, Provenance of Pleistocene Rhine River Middle Terrace sands between the Swiss–German border and Cologne based on U–Pb detrital zircon ages: International Journal of Earth Sciences, v. 102, no. 3, p. 917-932.

Krmíčková, S., Krmíček, L., Romer, R. L., and Ulrych, J., 2020, Lead isotope evolution of the Central European upper mantle: Constraints from the Bohemian Massif: Geoscience Frontiers, v. 11, no. 3, p. 925-942.

LaFlamme, C., McFarlane, C. R. M., Fisher, C. M., and Kirkland, C. L., 2017, Multi-mineral geochronology: insights into crustal behaviour during exhumation of an orogenic root: Contributions to Mineralogy and Petrology, v. 172, no. 2-3.

Larsson, D., and Söderlund, U., 2005, Lu–Hf apatite geochronology of mafic cumulates: An example from a Fe–Ti mineralization at Smålands Taberg, southern Sweden: Chemical Geology, v. 224, no. 4, p. 201-211.

Lee, J. K. W., Williams, I. S., and Ellis, D. J., 1997, Pb, U and Th diffusion in natural zircon: Nature, v. 390, no. 6656, p. 159-162.

Li, Q., Li, S., Zheng, Y.-F., Li, H., Massonne, H. J., and Wang, Q., 2003, A high precision U–Pb age of metamorphic rutile in coesite-bearing eclogite from the Dabie Mountains in central China: a new constraint on the cooling history: Chemical Geology, v. 200, no. 3-4, p. 255-265.

Li, X.-C., Harlov, D. E., Zhou, M.-F., and Hu, H., 2022, Experimental investigation into the disturbance of the Sm-Nd isotopic system during metasomatic alteration of apatite: Geochimica et Cosmochimica Acta, v. 330, p. 191-208.

Liebmann, J., Barham, M., and Kirkland, C. L., 2023, Rutile Ages and Thermometry Along a Grenville Anorthosite Pathway: Geochemistry, Geophysics, Geosystems, v. 24, no. 2, p. e2022GC010330.

Mao, M., Rukhlov, A. S., Rowins, S. M., Spence, J., and Coogan, L. A., 2016, Apatite Trace Element Compositions: A Robust New Tool for Mineral Exploration*: Economic Geology, v. 111, no. 5, p. 1187-1222.

Markwitz, V., and Kirkland, C. L., 2018, Source to sink zircon grain shape: Constraints on selective preservation and significance for Western Australian Proterozoic basin provenance: Geoscience Frontiers, v. 9, no. 2, p. 415-430.

Mays, L. W., 2010, Water Technology in Ancient Egypt, *in* Mays, L., ed., Ancient Water Technologies: Dordrecht, Springer Netherlands, p. 53-65.

Morton, A. C., and Hallsworth, C. R., 1999, Processes controlling the composition of heavy mineral assemblages in sandstones: Sedimentary Geology, v. 124, no. 1, p. 3-29.

O'Sullivan, G. J., Chew, D. M., Morton, A. C., Mark, C., and Henrichs, I. A., 2018, An Integrated Apatite Geochronology and Geochemistry Tool for Sedimentary Provenance Analysis: Geochemistry, Geophysics, Geosystems, v. 19, no. 4, p. 1309-1326.

Prent, A. M., Beinlich, A., Raimondo, T., Kirkland, C. L., Evans, N. J., and Putnis, A., 2020, Apatite and monazite: An effective duo to unravel superimposed fluid-flow and deformation events in reactivated shear zones: Lithos, v. 376-377.

Reiners, P. W., 2005, Zircon (U-Th)/He Thermochronometry: Reviews in Mineralogy and Geochemistry, v. 58, no. 1, p. 151-179.

Ribeiro, B. V., Mulder, J. A., Faleiros, F. M., Kirkland, C. L., Cawood, P. A., O'Sullivan, G., Campanha, G. A. C., Finch, M. A., Weinberg, R. F., and Nebel, O., 2020, Using apatite to resolve the age and protoliths of mid-crustal shear zones: A case study from the Taxaquara Shear Zone, SE Brazil: Lithos, v. 378-379.

Ribeiro, T. M., D'Ambrosio, A., Dominguez Calabuig, G. J., Athanasopoulos, D., Bates, H., Riegler, C., Gassot, O., Gerig, S.-B., Gómez-González, J. L., Huber, N., Seton, R., and Magalhães, T. E. C., 2023, CARINA: A near-Earth D-type asteroid sample return mission: Acta Astronautica, v. 212, p. 213-225.

Santos, M. M., Lana, C., Scholz, R., Buick, I. S., Kamo, S. L., Corfu, F., and Queiroga, G., 2020, LA-ICP-MS U–Pb dating of rutiles associated with hydrothermal mineralization along the southern Araçuaí Belt, SE Brazil: Journal of South American Earth Sciences, v. 99, p. 102502.

Scharf, T., Kirkland, C. L., Barham, M., Yakymchuk, C., and Puzyrev, V., 2023, Does Zircon Shape Retain Petrogenetic Information?: Geochemistry, Geophysics, Geosystems, v. 24, no. 10, p. e2023GC011018.

Schirra, M., and Laurent, O., 2021, Petrochronology of hydrothermal rutile in mineralized porphyry Cu systems: Chemical Geology, v. 581, p. 120407.

Schoene, B., Crowley, J. L., Condon, D. J., Schmitz, M. D., and Bowring, S. A., 2006, Reassessing the uranium decay constants for geochronology using ID-TIMS U–Pb data: Geochimica et Cosmochimica Acta, v. 70, no. 2, p. 426-445.

Shewan, L., O'Reilly, D., Armstrong, R., Toms, P., Webb, J., Beavan, N., Luangkhoth, T., Wood, J., Halcrow, S., Domett, K., Van Den Bergh, J., and Chang, N., 2021, Dating the megalithic culture of Laos: Radiocarbon, optically stimulated luminescence and U/Pb zircon results: PLOS ONE, v. 16, no. 3.

Simpson, A., Gilbert, S., Tamblyn, R., Hand, M., Spandler, C., Gillespie, J., Nixon, A., and Glorie, S., 2021, In-situ Lu Hf geochronology of garnet, apatite and xenotime by LA ICP MS/MS: Chemical Geology, v. 577.

Söderlund, U., Patchett, P. J., Vervoort, J. D., and Isachsen, C. E., 2004, The 176Lu decay constant determined by Lu–Hf and U–Pb isotope systematics of Precambrian mafic intrusions: Earth and Planetary Science Letters, v. 219, no. 3-4, p. 311-324.

Spencer, C. J., Cawood, P. A., Hawkesworth, C. J., Prave, A. R., Roberts, N. M. W., Horstwood, M. S. A., and Whitehouse, M. J., 2015, Generation and preservation of continental crust in the Grenville Orogeny: Geoscience Frontiers, v. 6, no. 3, p. 357-372.

Spencer, C. J., Kirkland, C. L., Roberts, N. M. W., Evans, N. J., and Liebmann, J., 2020, Strategies towards robust interpretations of in situ zircon Lu–Hf isotope analyses: Geoscience Frontiers, v. 11, no. 3, p. 843-853.

Stacey, J. S., and Kramers, J. D., 1975, Approximation of terrestrial lead isotope evolution by a two-stage model: Earth and Planetary Science Letters, v. 26, no. 2, p. 207-221.

Tyrrell, S., Haughton, P. D. W., Daly, J. S., Kokfelt, T. F., and Gagnevin, D., 2006, The Use of the Common Pb Isotope Composition of Detrital K-Feldspar Grains as a Provenance Tool and Its Application to Upper Carboniferous Paleodrainage, Northern England: Journal of Sedimentary Research, v. 76, no. 2, p. 324-345.

Wilde, S., Valley, J., Peck, W., and Graham, C., 2001, Evidence from detrital zircons for the existence of continental crust and oceans on the Earth 4.4 Gyr ago: Nature, v. 409, p. 175-178.

Zack, T., and Kooijman, E., 2017, Petrology and Geochronology of Rutile: Reviews in Mineralogy and Geochemistry, v. 83, no. 1, p. 443-467.

Zametzer, A., Kirkland, C. L., Hartnady, M. I. H., Barham, M., Champion, D. C., Bodorkos, S., Smithies, R. H., and Johnson, S. P., 2022, Applications of Pb isotopes in granite K-feldspar and Pb evolution in the Yilgarn Craton: Geochimica et Cosmochimica Acta, v. 320, p. 279-303.

Zutterkirch, I. C., Barham, M., Kirkland, C. L., and Elders, C., 2023, Contrasting Detrital Feldspar Pb Isotope Ratios and Zircon Geochronology to Distinguish Proximal versus Distal Transport: The Journal of Geology, v. 131, no. 1, p. 25-73.

Chapter 2. The unroofing of Archean crustal domes as recorded by detrital zircon and apatite

This chapter is published as:

Clarke, A. J. I., Kirkland, C. L., Glorie, S., Gillespie, J., and Kinny, P. D., 2023, The unroofing of Archean crustal domes as recorded by detrital zircon and apatite: Precambrian Research, v. 395, p. 107132

Doi: 10.1016/j.precamres.2023.107132.

Minor post-publication changes and clarifications have been made.

This study presents *in-situ* U–Pb, Lu–Hf, and Sm–Nd isotopic data for detrital zircon and apatite collected from ephemeral streams of the East Pilbara Terrane, Western Australia. Given their disparate abundances in felsic versus mafic lithologies, a tandem apatite-zircon approach may offer more holistic insights into crust formation. Apatite U–Pb data define a single age peak at c. 2.9 Ga, consistent with labile, proximal, and first-cycle detritus from the Pilbara Craton. Conversely, zircon, a more refractory and durable mineral, records a more diverse geological history with U–Pb ages spanning from 3.6 to 0.2 Ga. The apatite U-Pb age of c. 2.9 Ga records the timing through the Pb closure temperature during regional cooling following prograde metamorphism, while the Lu–Hf and Sm–Nd isotopic systems in the same grains yield c. 3.2 Ga isochrons, consistent with magmatic crystallisation at that time. Crystallisation age, initial $^{143}Nd/^{144}Nd$ and trace element geochemistry (Eu/Eu*) imply a chondritic or mixed (more radiogenic plus a less radiogenic component) source for the apatite grains locally derived from the East Pilbara Terrane. Conversely, zircon ƐHf data reveal a broadly chondritic Paleoarchean proto-crust undergoing continual isotopic evolution punctuated by the input of juvenile, more radiogenic material on a quasiperiodic basis. Previous workers have invoked a crust-mantle overturn model triggered by stagnant-lid cooling and the episodic (re)fertilisation of the upper mantle to account for the periodic nature of crust formation in the East Pilbara Terrane. Detrital zircon grains track this process from a c. 3.8 Ga component that may have acted as a nucleus for subsequent crust formation. The oldest detrital zircon, on average, encompasses less radiogenic (-ve ƐHf) components, suggesting that the oldest grains preserve the unroofing of an ancient reworked crustal nucleus. Thus, the detrital zircon load arguably provides a more holistic record of the older crust in the region than the crystalline domes alone. Specifically, the less radiogenic dome cores are preferentially eroded due to their structural position and their mineral cargo lost into the detrital archive. We demonstrate that the apatite-

zircon approach can be limited by the ability of apatite to be retained through crustal denudation.

2.1. Introduction

The continental crust is arguably the fundamental geochemical reservoir that shaped the evolution of Earth's atmosphere, oceans, biosphere, and ore deposits (Hawkesworth et al., 2020). With increasing age, the record of crustal evolution becomes increasingly fragmented due to an inevitable preservation bias in the rock record (Cawood et al., 2012, 2013; Hawkesworth et al., 2019). Hence, the detrital mineral archive may be an important store of information poorly retained in the crystalline rock record (Belousova et al., 2010; Cawood et al., 2012, 2013; Dhuime et al., 2017; Hawkesworth et al., 2019; Taylor and McLennan, 1985). Accordingly, detrital studies of resistive minerals have become commonplace in resolving questions regarding crustal formation (Cawood et al., 2013), orogenesis (Spencer et al., 2015), and source-to-sink relationships (Moecher and Samson, 2006).

The Lu–Hf signature in U–Pb dated zircon is an established tool to constrain crust-mantle differentiation and aids understanding of the timing, rate, and duration of continental crust formation and reworking (Belousova et al., 2010; Cawood et al., 2013). Although zircon crystals provide a wealth of information, they tend to crystallise from relatively evolved (SiO_2-rich) magmas (Moecher and Samson, 2006). This compositional effect has the potentially undesirable consequence of biasing the zircon crustal growth record towards more silica-rich (felsic) lithologies (Malusà et al., 2016). Furthermore, each tectonic environment has a different degree of grain preservation potential, which may further bias the detrital zircon record (Barham et al., 2022; Cawood et al., 2013; Spencer et al., 2015). Rather than simply representing episodes of crust formation, peaks in the detrital zircon U–Pb record could instead be a function of the preservation potential of different tectonic environments (Barham et al., 2022; Cawood et al., 2013).

Apatite is increasingly used to complement the zircon record as it extends the source rock compositional envelope that is tracked and can be dated by a range of established [U–Pb; e.g. Chew et al. (2014)] and more novel [Lu–Hf; e.g. Simpson et al. (2021) and Glorie et al. (2022), Sm–Nd; e.g. Fisher et al. (2020)] isotopic systems. Apatite is more labile than zircon during physical and chemical weathering processes and is, therefore, more likely to represent first-cycle detritus, potentially including from more mafic sources than zircon (Chew and Spikings, 2021; Chew et al., 2011; Gillespie et al., 2018; Glorie et al., 2022). Hence,

combinations of detrital zircon and apatite may, in some respects, complement each other, where zircon retains an encompassing (multi-cycle) history of felsic crust, whereas apatite provides a more restricted (first-cycle) view of crust, including more mafic components. However, interpreting apatite ages may not be so straightforward given its relatively low U–Pb closure temperature of ~ 375 to 600°C compared to zircon (> 900°C) (Chew and Spikings, 2015). Therefore, the apatite U–Pb system is more susceptible to disturbance/recrystallisation post-magmatic crystallisation (Chew and Spikings, 2021; Kirkland et al., 2018; Schoene and Bowring, 2007).

This work reports time-constrained isotopic data from detrital zircon (U–Pb, Lu–Hf) and apatite (U–Pb, Lu–Hf, Sm–Nd), collected from ephemeral streams draining the East Pilbara Terrane. These results from detrital grains demonstrate continental-scale sediment dispersal across Western Australia and inform on the early construction and recycling of the Pilbara Craton. Using these data, we develop a model of dome unroofing, incorporating previous isotopic (Gardiner et al., 2017; Kemp et al., 2015; Kemp et al., 2023; Petersson et al., 2020; Petersson et al., 2019a; Salerno et al., 2021) and geological mapping (GSWA, 2024; Hickman, 1990; Van Kranendonk et al., 2007a; Wiemer et al., 2018), which may be applicable to some other Archean granite-greenstone terranes.

2.2. Geological Background

The Pilbara Craton represents a rare occurrence of extensively exposed Paleo to Mesoarchean crust and offers important insights into early crustal evolution. Some workers infer that crust production within the Pilbara Craton began at c. 3.8 Ga as implied by ages of inherited zircon and Pb and Hf isotope systematics of Eoarchean gneisses (Gardiner et al., 2017; Hartnady and Kirkland, 2019; Petersson et al., 2019b). During the protracted (c. 3.8 – 3.0 Ga) construction of the Pilbara Craton, mafic lithologies may have dominated crust production globally (Dhuime et al., 2015). Some workers have argued that this period encompasses the transition from an earlier, hotter, and more vertical tectonic regime to the more modern style of horizontal plate tectonics (Dhuime et al., 2012; Dhuime et al., 2015; Hartnady and Kirkland, 2019; Hawkesworth et al., 2020; Korenaga, 2013). Conversely, other workers maintain that subduction-type settings with mobile lid dynamics were operational from the Eoarchean (Nutman et al., 2021; Windley et al., 2021).

Unconformable Neoarchean and Proterozoic metasedimentary rock units overlie much (> 80%) of the Pilbara Craton, and only the northern (60,000 km^2) portion is exposed as an

inlier (Hickman and Van Kranendonk, 2012). The exposed geology is classified into three tectonic components: the De Grey Superbasin (3.1–2.9 Ga), the West Pilbara Superterrane (3.3–3.1 Ga) and the East Pilbara Terrane (3.8–3.1 Ga) (Figure 2.1) (Van Kranendonk et al., 2004).

The East Pilbara Terrane represents the classic example of a dome and basin granite-greenstone terrane (Hickman and Van Kranendonk, 2012; Jahn et al., 1981; Myers, 1993; Van Kranendonk et al., 2007b). The granitoid domes of the East Pilbara Terrane are composite intrusions formed from several generations of variably metamorphosed and deformed felsic igneous rocks (tonalite-trondhjemite-granodiorite — TTGs). The domes exhibit a spatial zonation from younger, less radiogenic (-ve ƐHf and ƐNd) cores to juvenile, more radiogenic (+ve ƐHf and ƐNd) rims (Gardiner et al., 2017). Greenstone belts bound the granitoid domes and exhibit lower amphibolite to greenschist and prehnite-pumpellyite facies metamorphism with increasing distance from domes (Bickle et al., 1985). Such greenstone successions predominantly comprise weakly metamorphosed ultramafic to mafic extrusive volcanic sequences intercalated with sedimentary package (Hickman, 1990; Myers, 1993; Petersson et al., 2020). The dome and basin terrane of the East Pilbara Terrane is interpreted to have formed from episodic granitoid intrusion, with associated deformation of the overlying greenstone within the mid to lower crust from c. 3.60 – 3.25 Ga (Hickman and Van Kranendonk, 2012; Sandiford et al., 2004; Van Kranendonk et al., 2004).

Ephemeral river systems of unconsolidated clay, silt, sand, gravel, and localised calcrete dominate the lowland drainage basins of the Pilbara Craton (Hocking et al., 2001). These recent sediments were used as the sampling medium in this study (Table 2.1; Figure 2.1).

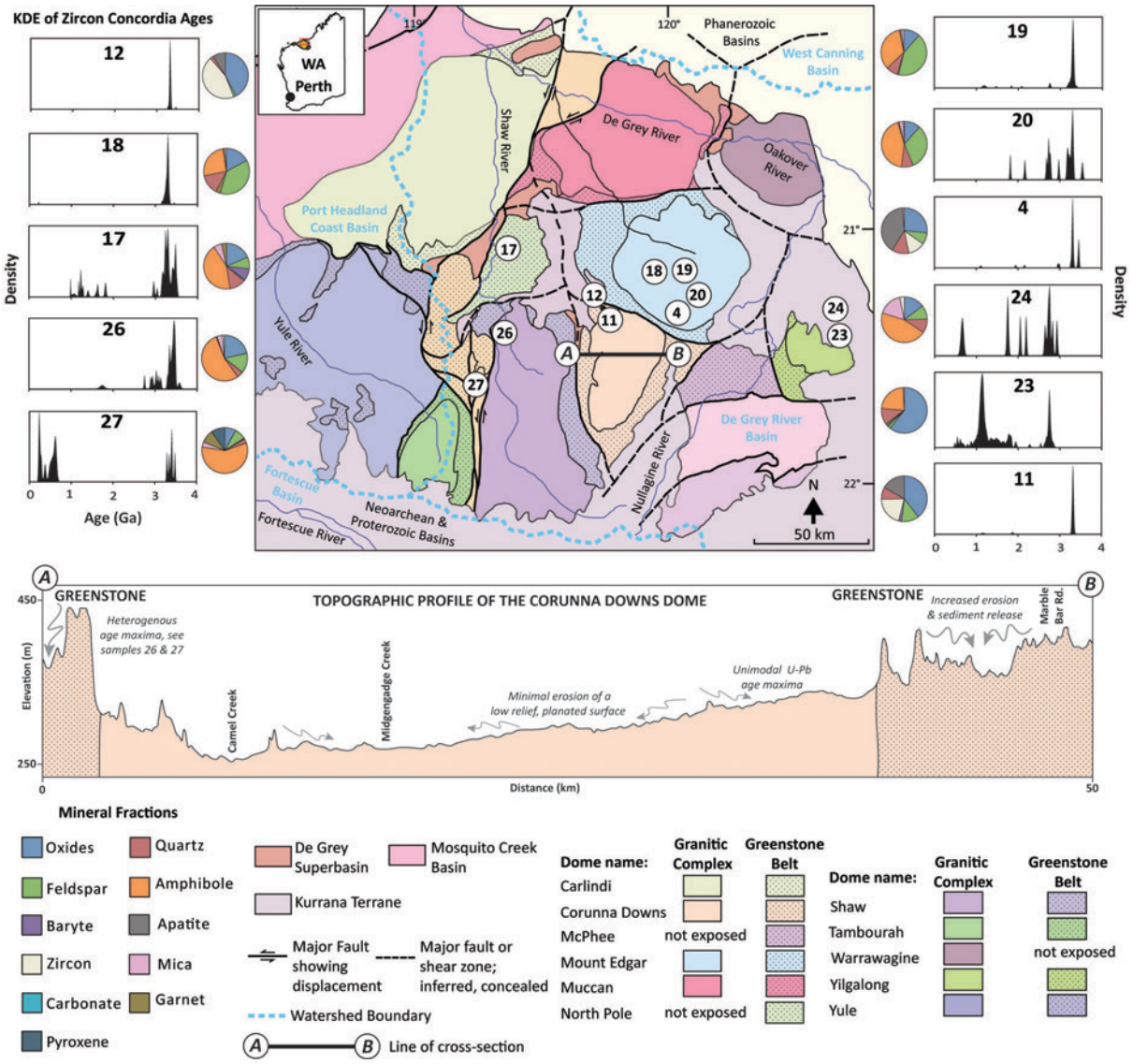

*Figure 2.1. A simplified geological map of the East Pilbara Terrane showing major drainage systems. To the sides are kernel density estimates of zircon concordia ages (filtering for > 10% discordance) and mineral fraction pie charts. Line **A-B** shows an illustrative topographic profile of the Corunna Downs Dome and surrounding greenstone belts; note the vertical exaggeration. The geodetic system used is WGS 84. Geological map of the East Pilbara Terrane adapted after Hickman (2021).*

Sample	Latitude	Longitude	UTM	Analysis	Local Drainage	Unit	Age* (Ma)
4	-21.3504	120.0559	51K 194649 7636214	Zircon U–Pb, Lu–Hf	House Creek	Kennell Granodiorite	3315 ± 2
11	-21.3718	119.8159	50K 792017 7634084	Zircon U–Pb, Lu–Hf	Camel & Sandy Creeks	Apex Basalt	3459 – 3434
12	-21.3364	119.7898	50K 789372 7638051	Zircon U–Pb, Lu–Hf	Camel Creek	Euro Basalt	3350 – 3335
17	-21.0486	119.3918	50K 748550 7670608	Zircon U–Pb, Lu–Hf	Shaw River	Mount Ada Basalt	3470 – 3469
18	-21.1836	120.0225	51K 190824 7654631	Zircon U–Pb, Lu–Hf. Apatite U–Pb, Sm–Nd, Lu–Hf	Yandicoogina Creek	Fig Tree Gneiss	3448 – 3416
19	-21.1931	120.1282	51K 201835 7653786	Zircon U–Pb, Lu–Hf. Apatite U–Pb, Sm–Nd, Lu–Hf	Mount Creek	Bishop Creek Monzonite	3246 – 3223
20	-21.2112	120.262	51K 215768 7652024	Zircon U–Pb, Lu–Hf	Talga River	Bishop Creek Monzonite	3246 – 3223
23	-21.3213	120.8689	51K 278957 7640802	Zircon U–Pb, Lu–Hf	Garrigan Creek	Carawine Dolomite	2629 – 2565
26	-21.5304	119.3427	50K 742651 7617329	Zircon U–Pb, Lu–Hf. Apatite U–Pb, Sm–Nd, Lu–Hf	Mulgandinnah River	Callina Supersuite	3484 – 3462
27	-21.6203	119.1943	50K 727132 7607600	Zircon U–Pb	Mulgandinnah River	Euro Basalt	3350 – 3335

*Table 2.1. A summary table of sample localities, analyses performed (Appendix A) and the underlying geological unit is provided. *Ages reported are zircon U-Pb weighted mean crystallisation dates of the crystalline basement (GSWA, 2024).*

2.3. Methods

2.3.1. Location and Sampling

Eleven 1–2 kg sand samples from ephemeral streams were collected across the East Pilbara Terrane, broadly centred around the Marble Bar town site (Table 2.1; Figure 2.1). Tributaries of the Oakover, Fortescue, Shaw, and Nullagine rivers were sampled. For detailed location information, see Appendix B.

2.3.2. Sample Processing

The collected sands were concentrated for apatite and zircon via conventional heavy mineral processing steps at Curtin University. A riffle splitter was used to ensure subsequent concentrates were representative. For each sample, initial sieving at < 425 μm yielded fractions of c. 500 g, which underwent heavy mineral separation via a Jasper Canyon Research shaking platform (Dumitru, 2016) and lithium heteropolytungstate heavy liquid (2.85 g/cm^3). A handheld neodymium magnet was first used to remove coarse ferric fragments. Following coarse fragment removal, three rounds of Frantz isodynamic magnetic separation using a constant side-slope angle of 10° but varying amperages (~0.4, 1 and 1.7 A) were implemented to retrieve three separates of varying magnetic susceptibility (Strong and Driscoll, 2016). The final non-magnetic fraction (> 0.5 g) was then bulk-mounted into 25 mm diameter epoxy rounds.

Polishing (to a 1 μm finish) ensured that grains were sufficiently flat and exposed. Minerals were mapped using a TESCAN Integrated Mineral Analyser (TIMA). Additional imaging, including cathodoluminescence and backscatter electron, was undertaken using a Clara FE-SEM. The imaging process identified internal textures and crystal morphologies, aiding analysis positioning. Target apatite and zircon grains for isotopic analysis were chosen based on TIMA phase identification and SEM images.

2.3.3. Zircon U–Pb and Lu–Hf

Four split-stream U–Pb / Lu–Hf sessions were undertaken at the GeoHistory Facility, JdLC, Curtin University. Zircon U–Pb data was collected using an Agilent 8900 ICP-MS, whereas Hf isotopes were collected contemporaneously via a Nu Plasma II MC-ICP-MS. Ablations used a RESOlution LE193 nm ArF laser and a Lauren Technic S155 cell. A relatively small spot of 38 microns was used for split-stream laser analyses, necessitated by the zircon grain size and internal complexity. For further analytical details, see Appendix A.

Session 1									
Reference	**Primary Reference**	**Reported Age (Ma)**	**2σ**	**Age Ma***	**2SD**	**2σ**	**MSWD**	**p**	**n**
Plešovice	GJ1	337.13 (Sláma et al., 2008)	0.37	332	8	4	0.52	0.96	22
GJ1	Plešovice	601.95 (Jackson et at., 2004)	0.40	596	12	6	0.42	1.00	37
OG1	Maniitsoq	3465.4 (Stern et al., 2009)	0.60	3465	11	3	1.40	0.07	33
Maniitsoq	OG1	3008.7 (Marsh et al., 2019)	0.72	3005	8	5	0.68	0.76	12
Session 2									
Reference	**Primary Reference**	**Reported Age (Ma)**	**2σ**	**Age Ma***	**2SD**	**2σ**	**MSWD**	**p**	**n**
Plešovice	GJ1	337.13 (Sláma et al., 2008)	0.37	334	3	1	1.20	0.28	8
GJ1	Plešovice	601.95 (Jackson et at., 2004)	0.40	606	3	3	0.50	0.88	11
OG1	Maniitsoq	3465.4 (Stern et al., 2009)	0.60	3466	7	3	1.00	0.43	17
Maniitsoq	OG1	3008.7 (Marsh et al., 2019)	0.72	3014	14	6	1.40	0.15	12
Session 3									
Reference	**Primary Reference**	**Reported Age (Ma)**	**2σ**	**Age Ma***	**2SD**	**2σ**	**MSWD**	**p**	**n**
Plešovice	GJ1	337.13 (Sláma et al., 2008)	0.37	341	4	2	1.20	0.26	10
GJ1	Plešovice	601.95 (Jackson et at., 2004)	0.40	596	4	5	0.19	1.00	14
OG1	Maniitsoq	3465.4 (Stern et al., 2009)	0.60	3465	5	5	0.40	0.95	11
Maniitsoq	OG1	3008.7 (Marsh et al., 2019)	0.72	3008	6	4	0.50	1.00	16
Session 4									
Reference	**Primary Reference**	**Reported Age (Ma)**	**2σ**	**Age Ma***	**2SD**	**2σ**	**MSWD**	**p**	**n**
Plešovice	GJ1	337.13 (Sláma et al., 2008)	0.37	339	4	2	2.10	0.02	12
GJ1	Plešovice	601.95 (Jackson et at., 2004)	0.40	599	6	4	0.66	0.84	18
OG1	Maniitsoq	3465.4 (Stern et al., 2009)	0.60	3467	8	4	0.88	0.57	14
Maniitsoq	OG1	3008.7 (Marsh et al., 2019)	0.72	3004	6	4	1.20	0.29	17

*Table 2.2. Summary table of U–Pb zircon secondary reference material. * Weighted Mean 95% confidence $^{207}Pb/^{206}Pb$ ages for zircons OG1 and Maniitsoq whereas $^{206}Pb/^{238}U$ ages are reported for all other reference material.*

Zircon downhole fractionation can vary with the zircon crystal state; hence, zircons with $^{207}Pb/^{206}Pb$ ages > 2.4 Ga were reduced using OG1 as the primary reference, whereas < 2.4 Ga zircon were reduced using GJ1, so the reference material best matched unknown ablation responses. For all sessions, the following (primary or secondary) reference materials were used: Plešovice 337.13 ± 0.37 Ma (Sláma et al., 2008), GJ1 601.95 ± 0.40 (Jackson et al., 2004), Maniitsoq 3008.70 ± 0.72 Ma (Marsh et al., 2019) and OG1 3465.4 ± 0.6 Ma (Stern et al., 2009). Secondary reference material yielded weighted mean ages within 2σ or 2SD uncertainty of the expected value when reduced using an appropriate primary reference material (Table 2.2).

For zircon Lu–Hf analyses, secondary reference materials included Plešovice $^{176}Hf/^{177}Hf$ 0.282482 ± 0.000013 (Sláma et al., 2008), R33 0.282764 ± 0.000014 (Fisher et al., 2014a), GJ1 0.282000 ± 0.000025 (Morel et al., 2008) and FC1 0.282184 ± 0.000016 (Woodhead and Hergt, 2005) and OG1 0.280633 ± 0.000034 (Coyner et al., 2004; Kemp et al., 2017). Secondary reference materials were 2D uncertainty of reported $^{176}Hf/^{177}Hf$ ratios (Table 2.3), and the stable ratio of $^{178}Hf/^{177}Hf$ was within 2σ error of reported values (Fisher et al., 2014b; Sláma et al., 2008). Fixed ratios of $^{176}Yb/^{173}Yb = 0.7962$ and $^{176}Lu/^{175}Lu = 0.02655$ were used to correct for isobaric interferences on ^{176}Hf (Chu et al., 2002; Hartnady et al., 2019). The contributions of ^{176}Yb and ^{176}Lu were then subtracted from the total ^{176} mass signal to obtain the interference-corrected $^{176}Hf/^{177}Hf$.

Session 1

Reference	Primary Reference	Expected $^{176}Hf/^{177}Hf$	2SD	$^{176}Hf/^{177}Hf$*	2σ	MSWD	$^{176}Hf/^{177}Hf$ **	2SD	*n*
Plešovice	Mudtank	0.282482 (Sláma et al., 2008)	0.000013	0.282494	0.000022	1.1	0.282491	0.000078	12
R33	Mudtank	0.282764 (Fisher et al., 2014)	0.000014	0.282770	0.000017	1.2	0.282769	0.000083	20
GJ1	Mudtank	0.282000 (Morel et al., 2008)	0.000025	0.282012	0.000027	1.7	0.282013	0.000116	20
OG1	Mudtank	0.280633 (Kemp et al., 2017)	0.000034	0.280664	0.000018	0.9	0.280665	0.000073	19

Session 2

Reference	Primary Reference	Expected $^{176}Hf/^{177}Hf$	2SD	$^{176}Hf/^{177}Hf$*	2σ	MSWD	$^{176}Hf/^{177}Hf$**	2SD	*n*
Plešovice	Mudtank	0.282482 (Sláma et al., 2008)	0.000013	0.282487	0.00002	0.5	0.282488	0.000045	12
R33	Mudtank	0.282764 (Fisher et al., 2014)	0.000014	0.282761	0.000017	0.7	0.282762	0.000053	15
GJ1	Mudtank	0.282000 (Morel et al., 2008)	0.000025	0.282018	0.000021	1.0	0.280019	0.000082	16
Maniitsoq	Mudtank	0.280862 (Marsh et al., 2019)	0.000021	0.280889	0.000018	0.5	0.280887	0.000047	16

Session 3

Reference	Primary Reference	Expected $^{176}Hf/^{177}Hf$	2SD	$^{176}Hf/^{177}Hf$*	2σ	MSWD	$^{176}Hf/^{177}Hf$**	2SD	*n*
Plešovice	GJ1	0.282482 (Sláma et al., 2008)	0.000013	0.282463	0.000022	0.3	0.282463	0.000042	12
R33	GJ1	0.282764 (Fisher et al., 2014)	0.000014	0.282754	0.000016	0.6	0.282752	0.000048	16
FC1	GJ1	0.282184 (Woodhead & Hergt, 2005)	0.000012	0.282177	0.000022	0.7	0.282180	0.000070	12
OG1	GJ1	0.280633 (Kemp et al., 2017)	0.000034	0.280594	0.000018	0.9	0.280596	0.000071	18

Session 4

Reference	Primary Reference	Expected $^{176}Hf/^{177}Hf$	2SD	$^{176}Hf/^{177}Hf$*	2σ	MSWD	$^{176}Hf/^{177}Hf$**	2SD	*n*
Plešovice	GJ1	0.282482 (Sláma et al., 2008)	0.000013	0.282461	0.000023	1.0	0.282466	0.000077	12
R33	GJ1	0.282764 (Fisher et al., 2014)	0.000014	0.282756	0.000016	0.9	0.282754	0.000060	17
FC1	GJ1	0.282184 (Woodhead & Hergt, 2005)	0.000012	0.282204	0.000024	1.2	0.282205	0.000080	10
OG1	GJ1	0.280633 (Kemp et al., 2017)	0.000034	0.280637	0.000021	1.0	0.280626	0.000080	17

*Table 2.3. Summary table of Hf results for zircon secondary reference material. * Weighted Mean 95% confidence. ** Arithmetic Mean.*

2.3.4. Apatite U–Pb

U–Pb analyses of apatite were undertaken using the LA–ICP–MS at the JdLC at Curtin University utilising a RESOlution 193 nm excimer laser ablation system connected to an Agilent 8900 ICP–MS with a RESOlution LE193 nm ArF and a Lauren Technic S155 cell ICP–MS. A 38 µm spot size, fluence of 2 J/cm^{2,} and a 5 Hz repetition were used. The primary reference material used for U–Pb analysis was Madagascar (MAD2) apatite (Thomson et al., 2012). Secondary reference materials included the Mt. McClure apatite (MMC) 523.51 ± 1.47 (Schoene and Bowring, 2006) and Duluth Complex (FC) apatite 1099.1 ± 0.2 Ma (Schmitz et

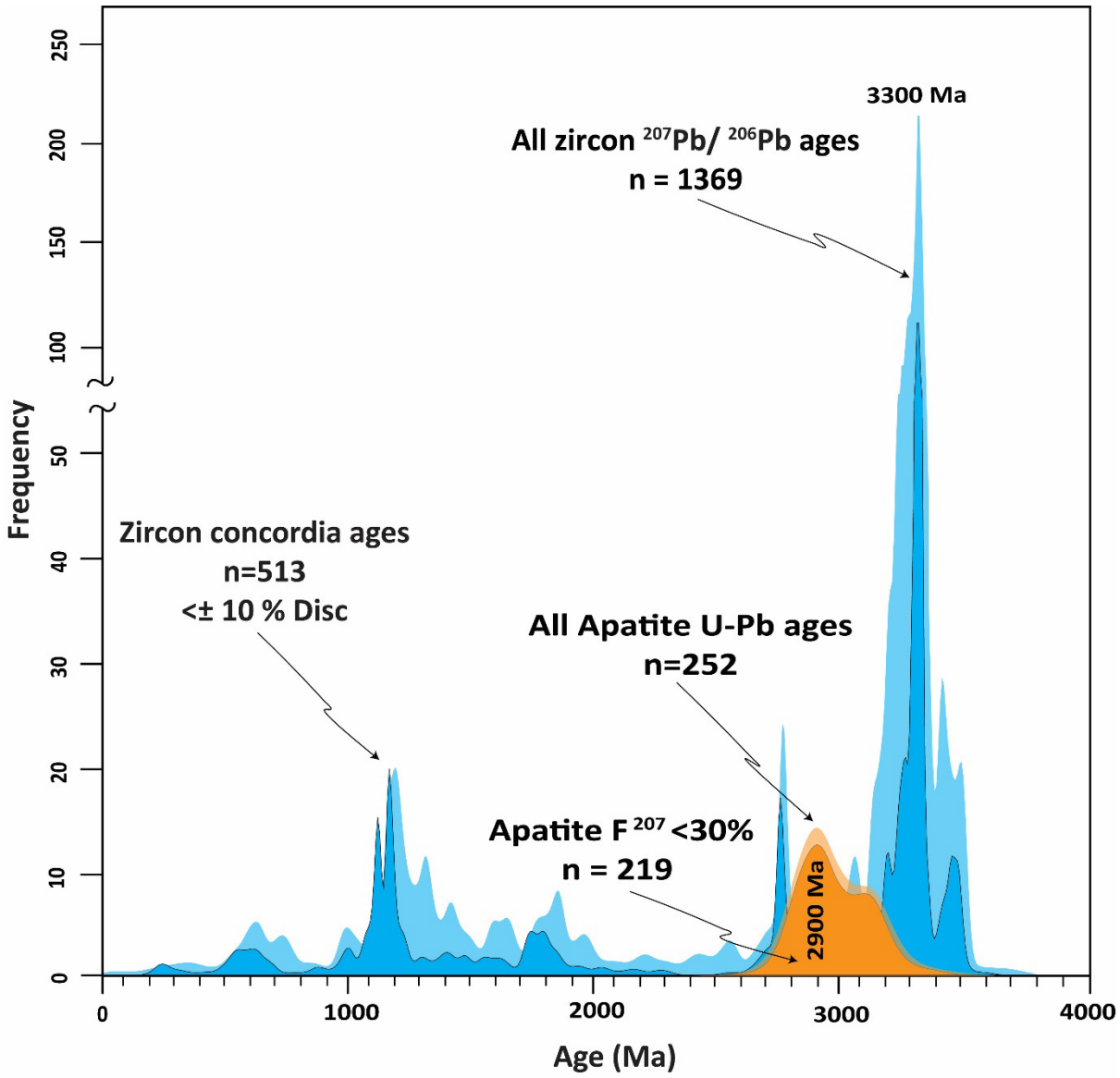

Figure 2.2. Stacked adaptive kernel density estimates for ages obtained from detrital apatite and zircon. The light orange KDE represents all ^{207}Pb corrected U-Pb apatite ages, whilst the solid orange KDE is filtered for < 30% F^{207}. The light blue KDE is unfiltered ^{207}Pb/ ^{206}Pb zircon ages, and the solid blue KDE represents zircon concordia ages within ± 10% of concordance. Note the scale break in the Y-axis.

al., 2003). Ages obtained from the secondary reference materials via anchored regressions are within 2σ uncertainty of the expected results (e.g. FC1, Duluth Complex 1079 ± 22 Ma, MSWD = 0.66; n = 19; Mt. McClure 522 ± 11 Ma, MSWD = 0.93; n = 14).

2.3.5. Apatite Sm–Nd and Lu–Hf

Sm–Nd and trace element geochemistry analyses of apatite were undertaken using the LA–ICP–MS at the JdLC at Curtin University. A RESOlution 193 nm excimer laser ablation system was connected to the Agilent 8900 ICP–MS with a RESOlution LE193 nm ArF and a Lauren Technic S155 cell ICP–MS. A 50 µm spot size, fluence of 2 J/cm^{2,} and a 5 Hz repetition were used. Sm–Nd data for apatite was collected during a single session. Durango apatite was the matrix-matched primary reference material for Sm–Nd and trace element analysis. Secondary standards included the Otter Lake apatite $^{143}Nd/^{144}Nd_i$ = 0.511447 (Yang et al., 2014) along with the Durango Apatite $^{143}Nd/^{144}Nd_i$ = 0.512472 (Yang et al., 2014), reduced against Otter Lake. All analyses fell within the 2SD uncertainty of previously reported values. Durango apatite yielded a mean $^{143}Nd/^{144}Nd$ initial ratio of 0.512483 ± 0.000094 2SD and Otter Lake 0.511452 ± 0.000043 2SD.

Apatite Lu–Hf isotope analyses were performed at the University of Adelaide. Due to the isobaric interference of ^{176}Lu and ^{176}Yb on ^{176}Hf, dissolution and chemical separation are conventionally required for high Lu–Hf phases prior to mass spectrometry, resulting in the loss of spatial context for isotopic information and necessitating time-consuming wet-chemical separation. However, the Simpson et al. (2021) approach allows for in situ Lu–Hf isotopic analysis using laser ablation. A RESOlution 193 nm excimer laser ablation system coupled to an Agilent 8900 ICP–MS/MS was used with analytical conditions identical to those in Glorie et al. (2022). In-house reference apatite Bamble with a corrected Lu–Hf age of 1097 ± 5 Ma (Simpson et al., 2021) was monitored as an accuracy check and is consistent with previously published data (Glorie et al., 2022). The resulting apatite Lu–Hf ages were calculated both as inverse isochron (Li and Vermeesch, 2021) intercept ages as well as common Hf-corrected weighted mean ages (excluding data with $^{177}Hf/^{176}Hf$ ratios > 2).

2.4. Results

2.4.1. Zircon

Zircon concordia ages are interpreted as the ages of zircon-crystallising rocks within the detrital source region(s) or as the ages of detrital components within sediments that have been reworked into ephemeral stream sediment (Figure 2.2). The samples covered a large geographic area (Figure 2.1) and, therefore, may represent a variety of Pilbara lithologies and potentially distal non-Pilbara sources.

Some samples yield large percentages of discordant zircon U–Pb analyses. For example, of the 116 U–Pb analyses undertaken on Sample 26, 77% are > 10% discordant (Appendix B). However, the basement geology underlying the stream sediment samples appears to have little control over the degree to which the detrital grains have lost radiogenic Pb (Appendix B). Instead, a combination of factors appear to have acted in unison to yield discordant grains; namely, the antiquity of many grains means they would have accumulated variable radiation damage, dependent on age, U, and Th content, and access to fluids (Figure 2.2). The prolonged subaerial exposure would have facilitated access to hydrothermal/meteoric fluids that would have stripped Pb in susceptible grains with fluid pathways (Pidgeon et al., 2017). Additionally, as demonstrated for Archean zircon grains, prolonged exposure to low-temperature environments would have inhibited structural recovery in any damaged zircon grains (Herrmann et al., 2021; Pidgeon et al., 2017). Moreover, we adopted a bulk mounting and random spot-picking strategy to minimise zircon selection bias during LA–ICP–MS analysis (Dröllner et al., 2021); it could be reasonably expected to incorporate more discordant analyses, more representative of actual zircon load. Concordia ages provide optimum use of the U–Pb and Pb–Pb systems and, importantly, give an objective measure of concordance, with data being filtered for greater than ± 10% discordance. The zircon grains separated from the sand samples represent a diverse population of crystal morphologies and were therefore categorised based on age. The youngest concordant zircon grain is 221 Ma, whilst the oldest is 3586 Ma (Figure 2.2).

2.4.2. Zircons with Ages 2.6 – 3.6 Ga

Over 70% of zircon grains are between 3.6 – 2.6 Ga. Zircon grains of this category are generally well-rounded (with aspect ratios of c. 1:1), transparent to opaque brown, anhedral, equant and small, with typical lengths of only up to 40 μm (Figure 2.3). Sector zoning is the dominant texture but is often truncated at grain margins. The surface pitting and the highly

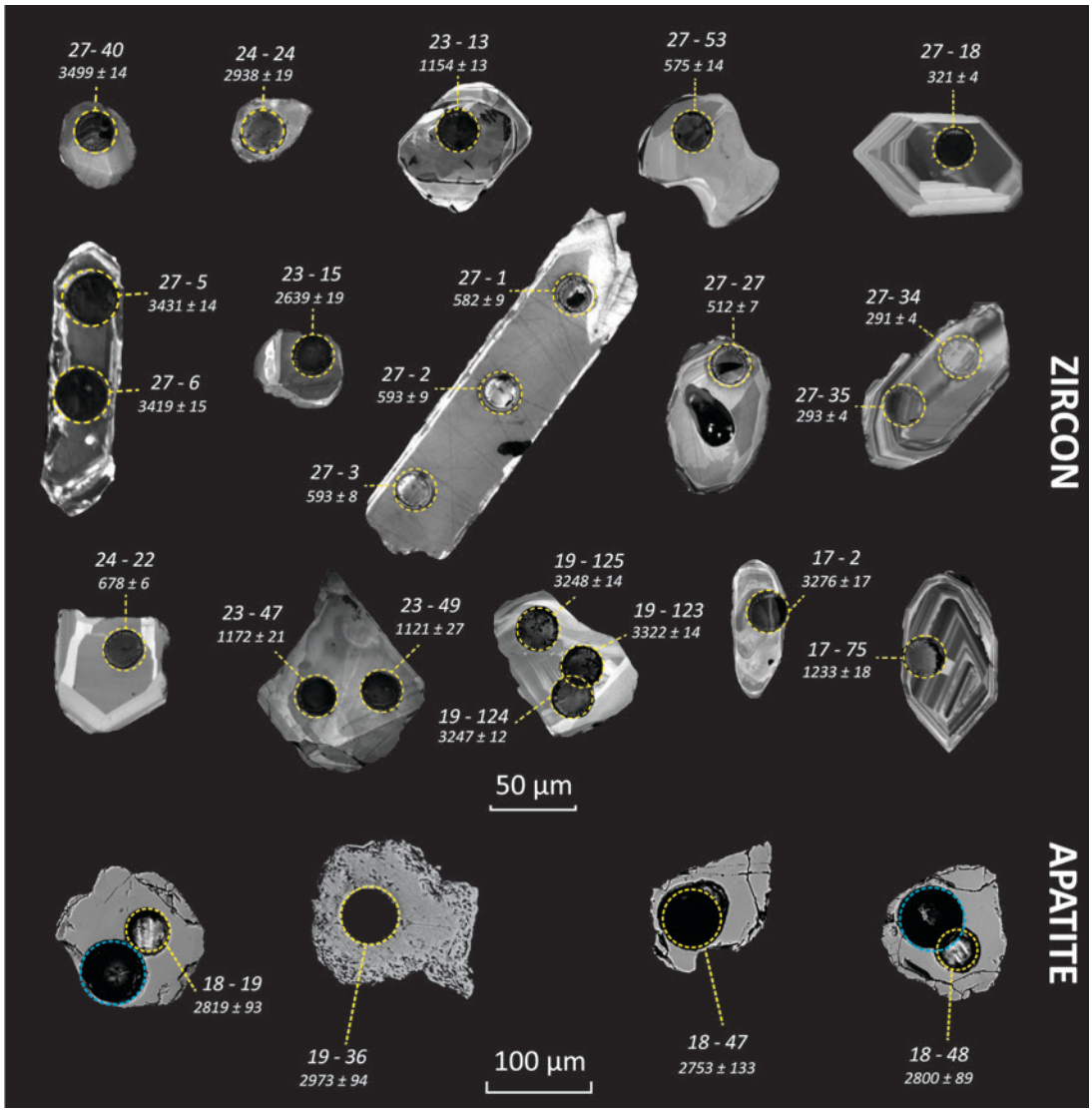

Figure 2.3. ***Top rows:*** *Cathodoluminescence images of representative zircon grains showing sample and spot number, laser spot location (38 µm) and concordia age (Ma ± 2σ). Only grains ≤ 10 % discordant are shown.* ***Bottom row:*** *A compilation of backscatter electron images of representative apatite. The smaller spot is a 38µm U-Pb ablation, whereas the larger spot is a 50 µm ablation.*

rounded nature of these grains indicate high degrees of mechanical abrasion during sedimentary reworking. 3.6 – 2.6 Ga zircon grains largely constitute samples with simple unimodal age populations (Figure 2.1); such age distributions suggest direct derivation from the underlying crystalline basement.

2.4.3. Zircon with Ages 2.6 – 1.2 Ga

Twelve per cent of concordant analyses are in this age group. These grains are primarily euhedral to sub-euhedral, opaque light brown to cloudy transparent, with variable lengths of 50 – 120 µm (Figure 2.3). Most of these zircons have simple concentric zoning, often truncated at grain margins. Grains of this category show less physical damage than older zircons, with

larger and better-preserved prismatic crystal shapes with aspect ratios generally of 2:1. Rare apatite inclusions form small (< 10 μm) anhedral grains within the cores of concentrically zoned > 40 μm zircon crystals.

2.4.4. Zircon with Ages < 1.2 Ga

Twenty-five per cent of zircon ages are younger than 1.2 Ga. In this age group, zircon grains are predominantly euhedral, showing tabular to prismatic crystals with minor abrasion compared to older grains. Sharp concentric oscillatory zoning is common, and grain lengths are generally over 50 μm (Figure 2.3). These zircon grains are generally transparent to opaque light brown, with aspect ratios exceeding 3:1.

2.4.5. Apatite Morphology

Apatites typically occur as anhedral to sub-euhedral rounded grains with crystals generally exceeding 100 μm in length. Apatite is opaque pale brown to transparent, usually homogenous with no pronounced zoning; however, faint magmatic zoning is apparent in some of the largest (> 100 μm) grains (Figure 2.3).

2.4.6. Apatite Geochronology

Apatite can host significant concentrations of common lead (Pb_c), and U–Pb data typically sit along two (or more) Pb mixing lines that generally stretch between a time-significant radiogenic and initial Pb_c component(s). On a Tera-Wasserburg plot, such data generally reveal lower intercepts representing the timing of radiogenic Pb accumulation. A

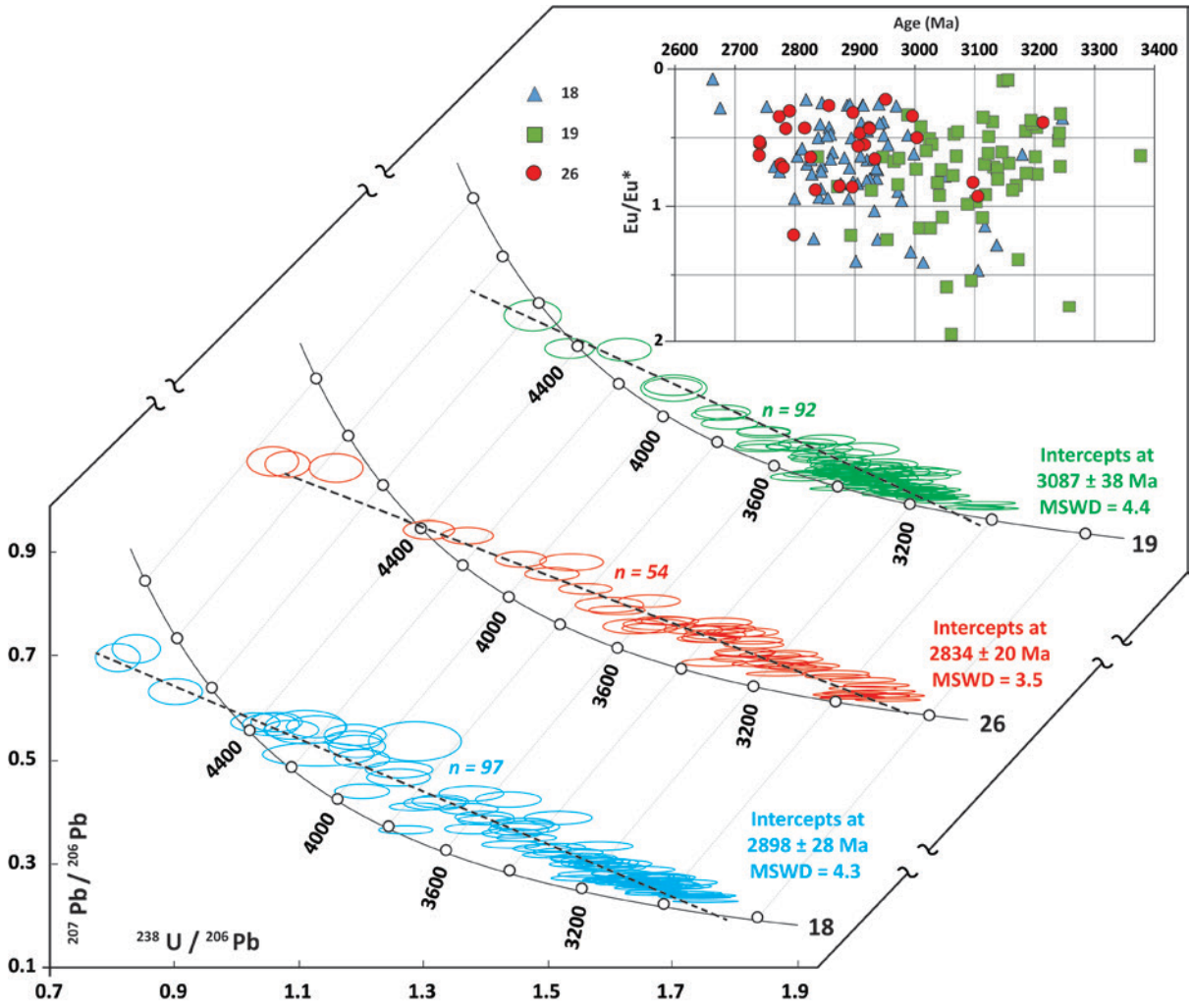

Figure 2.4. Stacked Tera-Wasserburg concordia diagrams for apatite U–Pb analyses, colour coded by sample. Error ellipses and intercept uncertainties are shown at 2σ. A best fit Model-1 regression from Isoplot R (Vermeesch, 2018). Analyses with ^{238}U / ^{206}Pb < 0.7 are not presented graphically but are included in regression calculations. The inset plot shows apatite Eu/Eu anomalies against F^{207} corrected ages (< 30%).*

^{207}Pb correction (Compston, 1999) can be performed using an initial Pb_c composition first estimated from the apparent U/Pb age and an appropriate Pb model (Stacey and Kramers, 1975). This initial ^{207}Pb corrected age can then be used to recalculate an apparent $^{207}Pb/^{206}Pb_i$, and the procedure iterated until no subsequent change in corrected age occurs. This method converges towards a mean $^{207}Pb/^{206}Pb_i$ of 1.10 for the detrital apatite population. To verify the results of this approach, we also calculated internal, individual apatite isochrons, where up to six analyses on the same crystal were performed. This technique yielded $^{207}Pb/^{206}Pb_i$ upper intercepts of 1.10 ± 0.20, consistent with the Stacey and Kramers (1975) terrestrial Pb model for c. 3.0 Ga crust. The detrital apatite U–Pb ages are more temporally restricted than the zircon ages, with apatite ^{207}Pb corrected ages implying a near unimodal population at c. 2.9 Ga (Figure 2.2) (Figure 2.4).

A total of 261 Sm–Nd apatite analyses were undertaken on samples 18, 19, and 26. All analyses yield a 3157 ± 66 Ma isochron with an initial $^{143}Nd/^{144}Nd$ of 0.508504 ± 0.000084 (MSWD = 2.3) (Figure 2.5). A further 83 apatite Lu–Hf analyses were also undertaken on samples 18, 19, and 23, which yielded a 3181 ± 33 Ma isochron, with an initial $^{177}Hf/^{176}Hf$ of 3.566 ± 0.037 (MSWD = 1.2) (Figure 2.5).

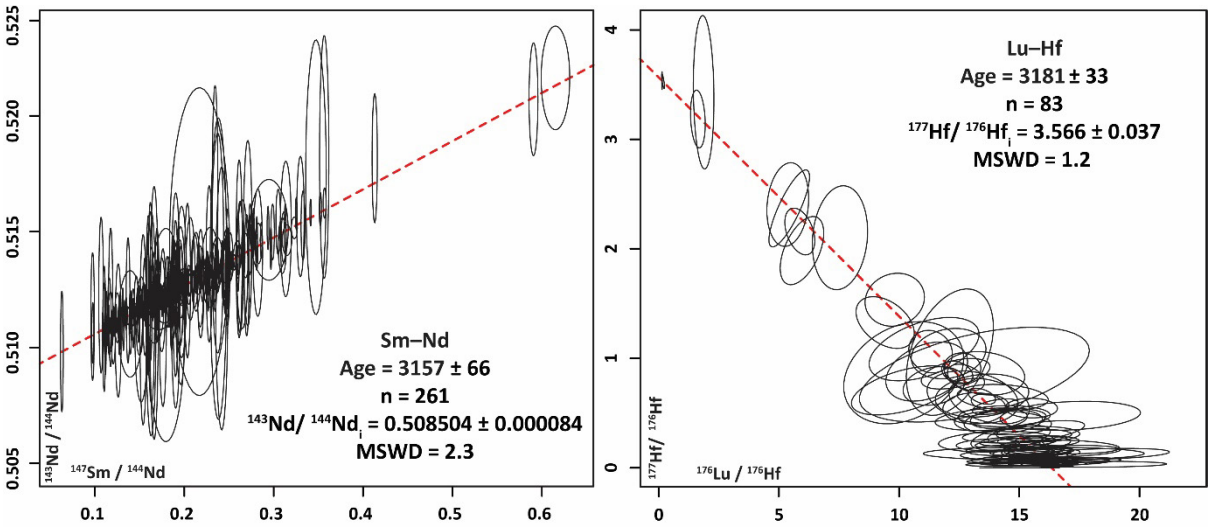

Figure 2.5. ***Left:*** *apatite Sm–Nd isochron for all apatite samples using the maximum likelihood model (Vermeesch, 2018).* ***Right:*** *Inverse apatite Lu–Hf isochron for apatite using the maximum likelihood of fit. All uncertainty ellipses are reported at 2σ.*

2.5. Discussion

2.5.1. Pilbara Provenance

The detrital zircon ages offer a broad snapshot of Paleoarchean to early Triassic magmatism throughout Western Australia (Figure 2.2). The oldest zircon age component (3.6 – 2.6 Ga) comprises 70% of zircon analyses and is predominantly made up of highly rounded, small (≤ 50 μm) grains consistent with a multi-cycle history of reworking from the crystalline basement of the Pilbara Craton (Figure 2.3). Extensive basement zircon U–Pb geochronology has shown that magmatism in the Pilbara Craton occurred in major episodes, each contributing to the formation of the granitoid domes (Hickman and Van Kranendonk, 2012; Nelson, 2005). The Archean detrital zircon reflects the timing of this magmatism, with distinct age peaks at 3.45, 3.30, 3.14, and 2.95 Ga defined by 38, 80, 136, and 11 grains, respectively. The c. 3.45 Ga zircon grains are likely derived from the Callina Supersuite, a voluminous intrusion of TTG magmas that partially occurs as a sheeted dyke complex in the North Shaw Suite (Van Kranendonk, 2008). The emplacement of the Callina Supersuite led to localised crustal thickening, which commenced the intrusion of granitoid domes (Hickman and Van Kranendonk, 2012). The Cleland and Emu Pool Supersuite have contributed to the most significant age peak at c. 3.30 Ga, and both suites predominantly comprise the Mount Edgar dome (GSWA, 2024; Roberts and Tikoff, 2021) (Figure 2.1). The c. 2.9 – 2.8 Ga zircon population is consistent with a Cutinduna and Split Rock Supersuite source. Both magmatic supersuites occur in the west to northwestern portion of the EPT and consist of granitoids emplaced during the Mosquito Creek Orogeny (Figure 2.1) (Hickman and Van Kranendonk, 2012).

The zircon U–Pb age populations have a pronounced geographical influence, with ephemeral stream sediment samples collected atop granitoid domes predominantly recording discrete, unimodal age components (Figure 2.1). The felsic granitoid domes have a higher intrinsic zircon load than surrounding greenstones, thus dominating age components with their locally derived magmatic zircon. For instance, the Mt. Edgar dome was assembled over 3.46 to 2.83 Ga (Van Kranendonk et al., 2004) and samples 18, 19, 20 and 4 were collected from streams atop the dome (Table 2.1) (Figure 2.1). Of the concordant ages obtained from those samples, 89% fall within the dome-forming period. Conversely, samples collected from greenstones show a more heterogenous zircon U–Pb age distribution (Figure 2.1), reflecting input from sources outside the Pilbara Craton, likely compounded by a lack of intrinsic zircon

load from the predominantly mafic (zircon-poor) geology (Hickman, 2021; Myers, 1993; Van Kranendonk et al., 2007a).

Another control on the detrital load of contemporaneous sediment is the present-day physiography of the East Pilbara Terrane. The flat, low-lying granitoid domes are bound by supracrustal greenstone belts and sedimentary successions, forming areas of comparatively high topographic relief (Figure 2.1) (Hickman and Van Kranendonk, 2012). Steep, unvegetated hills have increased erosion rates and thus, sediment release would be elevated from greenstone successions and overlaying regolith (Riebe et al., 2015). Coupled with the concept of intrinsic zircon load, the erosion of greenstones would rapidly release a diverse cargo of zircon grains into stream sediment. Conversely, the stream sediment of granitoid domes represents the product of slow, *in-situ* erosion of expansive outcrops of homogenous (unimodal age maxima) granitoid (Figure 2.1).

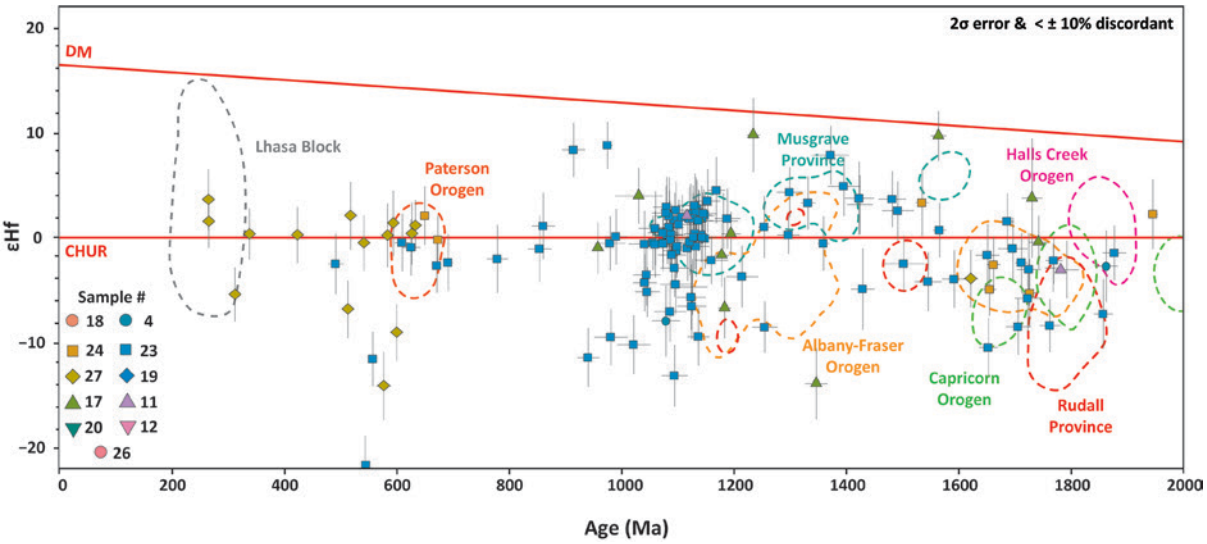

Figure 2.6. ℰHf versus concordia age for Proterozoic and Phanerozoic detrital zircon from this study compared to crystalline basement samples compiled from previous work. Dashed areas represent 75% peak density using fixed KDE bandwidth of ℰHf = 1.5 and age = 25 Ma. Data compiled from Gardiner et al. (2018); Johnson et al. (2017); Kirkland et al. (2013a); Kirkland et al. (2013b); Martin et al. (2017); Tucker et al. (2018). Error bars are at 2σ uncertainty.

2.5.2. Zircon from Outside the Pilbara Craton

Thirty per cent of concordant zircon grains in this work are younger than 2.6 Ga and represent detritus ultimately derived from crystalline sources outside the Pilbara Craton. Given the localised catchment areas and the ephemeral nature of the streams sampled, they are unlikely to be the mechanism by which exotic zircons have been delivered to the Pilbara. Kinny et al. (2022) reported zircon U–Pb geochronology from ephemeral streams draining the metasediments at Jack Hills and found a suite of Neoarchean and younger grains. In both that

study and this work, the distance to Proterozoic or younger lithologies and the widespread distribution of < 2.6 Ga zircon within streams (e.g., samples 23 and 27 are 170 km apart, overlay Archean geology, yet both contain Palaeozoic zircon) are consistent with Mesozoic continental scale sediment movement systems (Craddock et al., 2019; Morón et al., 2019).

There is a general paucity of zircon ages between 2.6 – 2.0 Ga, consistent with a general lack of large-scale magmatism identified in WA during this period (GSWA, 2024). Discerning the provenance of < 2.6 Ga zircon grains remains somewhat speculative based on age signature alone due to several potential sources having overlapping crystallisation ages (e.g., Albany-Fraser Orogen (AFO), Musgrave Province, Rudall Province, Capricorn Orogen). Zircon Lu–Hf signatures allow the refinement of such provenance interpretations. At c. 1.8 Ga, zircon ƐHf data ranges from -12 to +5 and is broadly sub-chondritic, much like signatures from the Capricorn Orogen, Halls Creek Orogen, the Biranup Zone or Rudall Province (Figure 2.6). These magmatic complexes girdling the Yilgarn Craton likely supplied the Paleoproterozoic zircon grains to the Pilbara sediments. Additional detrital input was perhaps derived from granitoid plutons in the Northern Yilgarn craton and the Capricorn Orogen, Ashburton Basin, and Glenburgh Terrane, which are associated with c. 1750 Ma magmas and ƐHf signatures of -12 – +3.3 (Figure 2.6) (Jahn et al., 2021).

The Rudall Province, on the eastern margin of the Pilbara Craton, is characterised by several episodes of Paleoproterozoic felsic magmatism with sub-chondritic ƐHf signatures, consistent with the prolonged reworking of an Archean Pilbara basement (Gardiner et al., 2018). Supracrustal material within the province is intruded by three generations of granitoid plutons (1. Kalkan Supersuite 1804 – 1762 Ma, 2. Krackatinny Supersuite 1589 – 1549 Ma and 3. Camel Suite 1310 – 1286 Ma) (Gardiner et al., 2018; GSWA, 2024). Some Pilbara stream detrital zircon ƐHf data (see samples 23 and 24) reveal a broadly sub-chondritic signature consistent with a Rudall Province source (Figure 2.6).

Detrital age components at 1.3 Ga and 1.2 Ga (Figure 2.2) may correspond to felsic magmatism during Stages 1 and 2 of the AFO (Figure 2.6) (Spaggiari et al., 2014). However, ƐHf values between +2 and +10 are more radiogenic than typical AFO magmas and are, therefore, better correlated with the juvenile magmas of similar age and closer proximity in the Musgrave Province (Figure 2.6) (Kirkland et al., 2013b).

The aforementioned source regions imply an extensive mechanism to transport detritus from the south while minimising damage to zircon grains (Figure 2.3). During the late

Palaeozoic, the Pilbara Craton, as part of the West Australian Craton, was a component of the Gondwana supercontinent and was situated north of Antarctica (Wopfner and Jin, 2009). Prior to the breakup of Gondwana, continental ice sheets flowing from the paleo-south pole carried and deposited an extensive covering of Permian to Carboniferous sediment (Morón et al., 2019). The ice sheets presumably contained a cargo of zircon collected from lithologies en route to the Pilbara Craton, which were ultimately deposited in Phanerozoic basins bounding the Pilbara Craton (Craddock et al., 2019). Within the post-glacial period, continental-scale fluvial systems originating from the south of East Gondwana continued transporting detritus (Morón et al., 2019). The detrital zircons from such fluvial systems within the Officer, Canning, Northern Carnarvon, and Roebuck Basin have age spectra that show a close similarity to those obtained from the East Pilbara Terrane (Figure 2.2) (Haines et al., 2013; Morón et al., 2019; Zutterkirch et al., 2021). We conclude that the Palaeozoic paleo-continental configuration of Gondwana enabled the delivery of well-preserved zircon grains into the Pilbara Craton.

The youngest zircon population at c. 200 – 300 Ma is enigmatic, post-dating the Gondwana sedimentation episode, and likely represents exotic material, given that no igneous rocks of this age range crop out in the Pilbara Craton or the West Australian Craton more generally. Zircon grains within this component have a distinct morphology, being larger (≥ 150 μm), euhedral with high aspect ratios exceeding 3.0, consistent with minimal abrasion during their transport (Figure 2.3).

The Lhasa Terrane, an east-west trending tectonic belt in the Tibetan Plateau, represents a plausible provenance for young zircons. From the early Triassic onwards, southwards subduction beneath the Lhasa Terrane formed a backarc basin with felsic magmatism (Zhu et al., 2011a). During the early Jurassic break up of Gondwana, the Lhasa Terrane is believed to have rifted away from northwest Australia and collided with the Qiangtang terrane during the Himalayan orogeny (Zhu et al., 2011a). Using detrital zircon ages and Hf isotope data, Zhu et al. (2011b) invoked a shared paleo-drainage system whereby detritus flowed between the sub-aerially exposed Lhasa Terrane and the Western Australia Craton. Detrital U–Pb zircon ages of c. 200 – 300 Ma and positive ƐHf signatures of −5.0 – +16.2 are reported for the Lhasa Terrane, tentatively correlating to those recorded in Figure 2.6. (Zhu et al., 2011a; Zhu et al., 2011b). Furthermore, detrital zircon studies within the North West Shelf oil field off the coast of the Pilbara Craton area have reported Mesozoic zircon grains (Lewis and Sircombe, 2013; Morón et al., 2019; Zutterkirch et al., 2021).

Surficial deposits of the East Pilbara Terrane consist of isolated Cenozoic successions of iron-rich alluvial duricrust and pisolite (Hocking et al., 2001). These diverse but often fragmentary layers occur throughout the West Australian Craton (Hocking et al., 2001) and represent the remnants of a once extensive northwards-flowing Mesozoic fluvial system (Morón et al., 2019). Despite a period of stability and restricted sediment input following the breakup of Gondwana, exotic detrital zircons are abundant within the ephemeral streams sampled (Figure 2.1). U–Pb zircon datasets for this unconsolidated cover in Western Australia support the widespread distribution of Proterozoic detritus atop the Archean basement (Hocking et al., 2001; Kinny et al., 2022; Veevers et al., 2005). Salama et al. (2022) reported a well-preserved population of c. 1000 – 2000 Ma zircon grains from regolith in the Yamarna Terrane, Eastern Yilgarn. Veevers et al. (2005) also demonstrated that various contemporaneous sands and regolith along the southern margin of the Yilgarn Craton contain a cargo of zircon consistent with sources from the Pinjarra and Albany-Fraser Orogens. Large detrital loads of similarly Proterozoic-aged zircon grains are found across the northern margin of the Pilbara Craton (Dröllner et al., 2023; Zutterkirch et al., 2021). Hence, we posit that the Cenozoic strata of the Pilbara hold a reserve of far-transported Proterozoic zircon, which was periodically eroded, releasing grains into contemporary sediment.

2.5.3. Apatite Provenance and Thermal History

A diverse range of apatite U–Pb closure temperatures have been reported from laboratory and empirical studies (Chew and Spikings, 2021; Cochrane et al., 2014; Kirkland et al., 2018), with natural apatite likely closing to Pb diffusion over a temperature range of ~ 375 to 600°C (Chew and Spikings, 2015). Grain size and fast diffusion pathways, such as fractures within apatite, highly influence specific closure temperatures. In addition, the U–Pb system of apatite is vulnerable to thermal disturbance and recrystallisation following initial formation (Chew and Spikings, 2021; Chew et al., 2011; Kirkland et al., 2018).

The closure temperature for Sm–Nd diffusion in apatite has been inferred to be as high as c. 950°C (Cherniak, 2000) and the Lu–Hf system in apatite has a likely closure temperature of ~675 – 750 °C (Barfod et al., 2005; Glorie et al., 2022). Both isotope systems are, therefore, seemingly less susceptible to thermal resetting than the U–Pb system (Gillespie et al., 2022). The apatite Sm–Nd isochron (n= 261, an aggregate of all samples) yielded an age of 3157 ± 66 Ma. The inverse Lu–Hf isochron for apatite from all samples (n= 83) yielded an age of 3181 ± 33 Ma (MSWD = 1.2) (Figure 2.5), which is strikingly similar to the Sm–Nd isochron. The matching isochrons for these different systems support an interpretation of a c. 3.2 Ga crystallisation age for an essentially unimodal apatite primary age component (Figure 2.7).

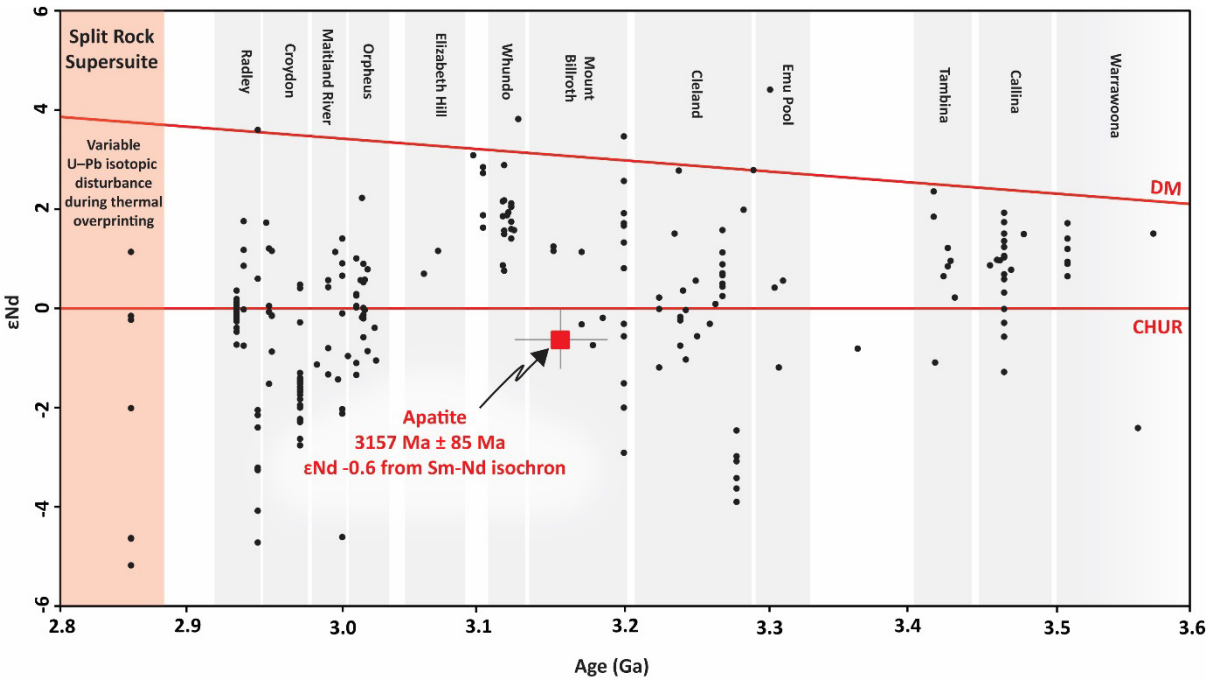

Figure 2.7. ℰNd evolution plot versus indicated age. The red overlaid square is derived from detrital apatite Sm/Nd analysis. Whole-rock Nd values (black circles) were collected from crystalline basement lithologies of the Pilbara Craton (GSWA, 2024). Magmatic supersuites are labelled. Error bars are reported at 2σ uncertainty.

By surface area, the Bishop Creek Monzonite is the largest constituent component of the Mt. Edgar Dome and has a crystallisation age of c. 3.24 Ga (GSWA, 2024). However, the assembly of the Mt. Edgar Dome was a protracted process and occurred over c. 3.4 – 2.8 (GSWA, 2024; Roberts and Tikoff, 2021). Further, the constituent supersuites of the Mt. Edgar Dome are variable in granitic composition from TTG to monzogranite (Bickle et al., 1985; Gardiner et al., 2017). Given its labile nature, apatite is unlikely to survive multiple reworking cycles (O'Sullivan et al., 2020) and, on average, can represent a more proximal detrital source than zircon. Samples 18 and 19 yielded 76% of apatite U–Pb analyses, and both were collected from stream sediment atop the Bishop Creek Monzonite. Accordingly, the supersuites of the Mt. Edgar Dome likely represent the predominant source of detrital apatite analysed, representing the unimodal age signature from a restricted source seen in the Sm–Nd and Lu–Hf isochrons (Figure 2.2) (Figure 2.4).

There is a difference between the apatite ages obtained by the U–Pb and Sm–Nd/Lu–Hf isotopic systems (Figure 2.7). Previous work has demonstrated that apatite U–Pb ages may record thermotectonic events at lower temperatures than magmatic crystallisation, such as cooling at mid-to-shallow crustal levels (Chew and Spikings, 2021). Alternatively, apatite U–-Pb ages can represent prograde metamorphic processes within the U–Pb closure temperature range, thus resetting or recrystallising a primary age to a metamorphic age (Chew and Spikings, 2021; Kirkland et al., 2018).

The Moolyella monzogranite is part of the Split Rock Supersuite and forms a series of irregular stock-like outcrops between the Nullagine and Shaw Rivers (de Laeter and Blockley, 1972) and has been dated via zircon U–Pb to c. 2.83 Ga, thus representing some of the youngest magmatism in the East Pilbara Terrane (GSWA, 2024). The Moolyella monzogranite intrudes the Bishop Creek monzonite, while the related 2.83 Ga Cooglegong monzogranite intrudes the Shaw granitic complex (from where Sample 26, which gave 21% of apatite U–Pb analyses, was collected) (de Laeter and Blockley, 1972). We conclude that the ^{207}Pb-corrected age probability maximum at c. 2912 Ma likely records the thermal overprinting of various apatite populations, resetting their Pb isotopic system during the discontinuous c. 2.89 to 2.83 (Hickman, 2021) emplacement of the Split Rock Supersuite. Such thermal disturbance of apatite is reflected in the U–Pb regression lines calculated for each sample (Figure 2.4). MSWD values of > 1 imply that a single age population does not define the calculated U–Pb mean age. The older lower intercept age obtained from sample 19 of 3087 ± 38, along with its more heterogenous Eu* signature, is distinct compared to samples 18 and 26 (Figure 2.4). The latter

two samples (18 and 26) share similar lower intercept ages of 2898 ± 28 Ma and 2834 ± 20 Ma, respectively, with similar Eu* values despite being over 80 km apart and located on distinct underlying lithologies (Figure 2.4; Table 2.1). Based on Lu–Hf and Sm–Nd ratios that imply crystallisation ages that match the underlying crystalline basement, we interpret the detrital apatite to represent material derived from proximal granitoids (Figure 2.5). Consequently, the various isotopic signatures retained within the detrital apatite should reflect the thermal history of its source rock, consistent with the variable degrees of U–Pb resetting in these grains. Samples 18 and 26 are ~ 1.6 and 2.2 km from the Split Rock Supersuite plutons, whereas sample 19 is over 12 km from the nearest outcrop. Hence, we posit that the younger U–Pb lower intercept ages and more homogeneous Eu*signatures in samples 18 and 26 reflect higher degrees of thermal overprinting and recrystallisation (Berger et al., 2022; Kirkland et al., 2018).

Trace element geochemistry undertaken during Sm–Nd analysis can help enhance provenance interpretations (Figure 2.7). Apatites from more felsic magmas typically have larger Eu anomalies, reflecting co-crystallisation with plagioclase (Mao et al., 2016). The mean Eu anomaly ($Eu/Eu^* = Eu_{CN}/ (Sm_{CN} * Gd_{CN})^{-0.5}$) of the detrital apatite population is 0.73 (Figure 2.4), a weakly negative signature, consistent with an intermediate melt source where the Eu^{2+} budget was not significantly depleted during prolonged plagioclase fractionation (Belousova et al., 2002; Buzenchi et al., 2022). The constituent lithologies of the Mt. Edgar Dome all demonstrate a negative Eu anomaly (Buzenchi et al., 2022). We interpret the Eu anomalies obtained for each sample (Figure 2.4) to reflect the composition of the underlying granitoids variably modified by thermal/fluid overprinting during Split Rock granitoid emplacement (Figure 2.4). Further, apatite ƐNd values define a normal distribution (Shapiro-Wilk = 0.85 and Anderson-Darling = 9.57 normality tests) about a CHUR-like composition with a mean of -0.6. This mean apatite Nd isotopic composition is similar to the average for granitoids within the EPT, which during the Mesoarchean have whole rock ƐNd values that range between -8 – +3 (Figure 2.7) (GSWA, 2023).

2.5.4. The Detrital Record of Archean Crustal Evolution

The detrital Hf pattern is generally very similar to that seen in the crystalline igneous record (Figure 2.8C). ƐHf signatures for dominant detrital pulses at 3.45 and 3.30 Ga appear to reflect on average, a greater degree of mixing with a radiogenic component than the earlier 3.60 Ga event, as preserved by zircon xenocrysts (Kemp et al., 2015; Petersson et al., 2019b). Such a mixing process could occur during pulses of magmatism associated with granitoid dome emplacement and greenstone subsidence (Figure 2.8C; Figure 2.9) (Roberts and Tikoff, 2021). The isotopic pattern for the Archean detrital grains is consistent with an autochthonous source, given that all data seem to originate from a common isotopic precursor compositionally indistinguishable from CHUR (based on Hf and Nd) at ≤ 3.8 Ga, consistent with the known crystalline igneous record (Gardiner et al., 2017; Petersson et al., 2019b) (Figure 2.8C).

The crustal evolution of the Pilbara Craton is marked by magmatic events at c. 3.50, c. 3.43, 3.31, and 3.20 Ga, associated with the voluminous emplacement of granitoid domes (GSWA, 2024; Kemp et al., 2023; Petersson et al., 2020). One scenario to account for the quasiperiodic nature of crust formation, with an approximate rejuvenation period of 100 Ma, seen in the East Pilbara Terrane, is that of early-Archean crust formation being controlled by a series of gravitationally driven crustal overturns (François et al., 2014; Wiemer et al., 2018). In this model, high geothermal gradients in the Archean encouraged vertical material flow whereby denser mafic volcanics and lighter felsic crust could overturn on a quasiperiodic basis (Wiemer et al., 2018). Such vertical tectonic process is reflected in the architecture of the East Pilbara Terrane, where buoyant granitoid domes are bounded by denser keels of coeval komatiite successions in the greenstone belts (Petersson et al., 2020). Alternative tectonomagmatic scenarios are, however, proposed (Van Kranendonk et al., 2004), including initial crust formation in the East Pilbara Terrane as early as the Hadean (Tessalina et al., 2010), although this appears inconsistent with recent isotopic studies (Hartnady et al., 2022; Kemp et al., 2015; Kemp et al., 2023; Petersson et al., 2020).

A c. 100 Ma interval for rejuvenation events has been observed in the geology of other Archean terranes, such as the Kaapvaal Craton (Bédard, 2018) and the North Atlantic Craton, as expressed in West Greenland (Kirkland et al., 2021) (Figure 2.8D). We propose that this cyclicity could appear as a characteristic feature of continental crust formation within the East Pilbara Terrane during the early Archean and may typify proto-crust development prior to modern-style plate tectonics (Wiemer et al., 2018). The c. 100 Ma interval may represent the

time required for heat and volatiles to accumulate beneath stagnant lids to trigger voluminous magmatism associated with overturns events (Bédard, 2018).

Hence, our detrital zircon ƐHf data appears to reflect the quasiperiodic nature of crust formation on an approximate 100 Ma frequency (Figure 2.8D). Whilst a c. 100 Ma frequency may characterise early Earth overturn processes, it need not be expected to be globally synchronous (e.g. the periodicity is the same across different cratons, but the specific initiation timing is distinct). We interpret the isotopic arrays to represent evolution with discrete periods of crustal reworking precipitated by a magmatic component with more radiogenic compositions, as marked by vertical ƐHf mixing arrays at 3.45 and 3.30 Ga, which, in both cases, extended into unradiogenic compositions similar to 3.6 Ga magmatism. These magmatic episodes define periods of crust generation (Hickman and Van Kranendonk, 2012; Van Kranendonk et al., 2004; Wiemer et al., 2018) (Figure 2.8C).

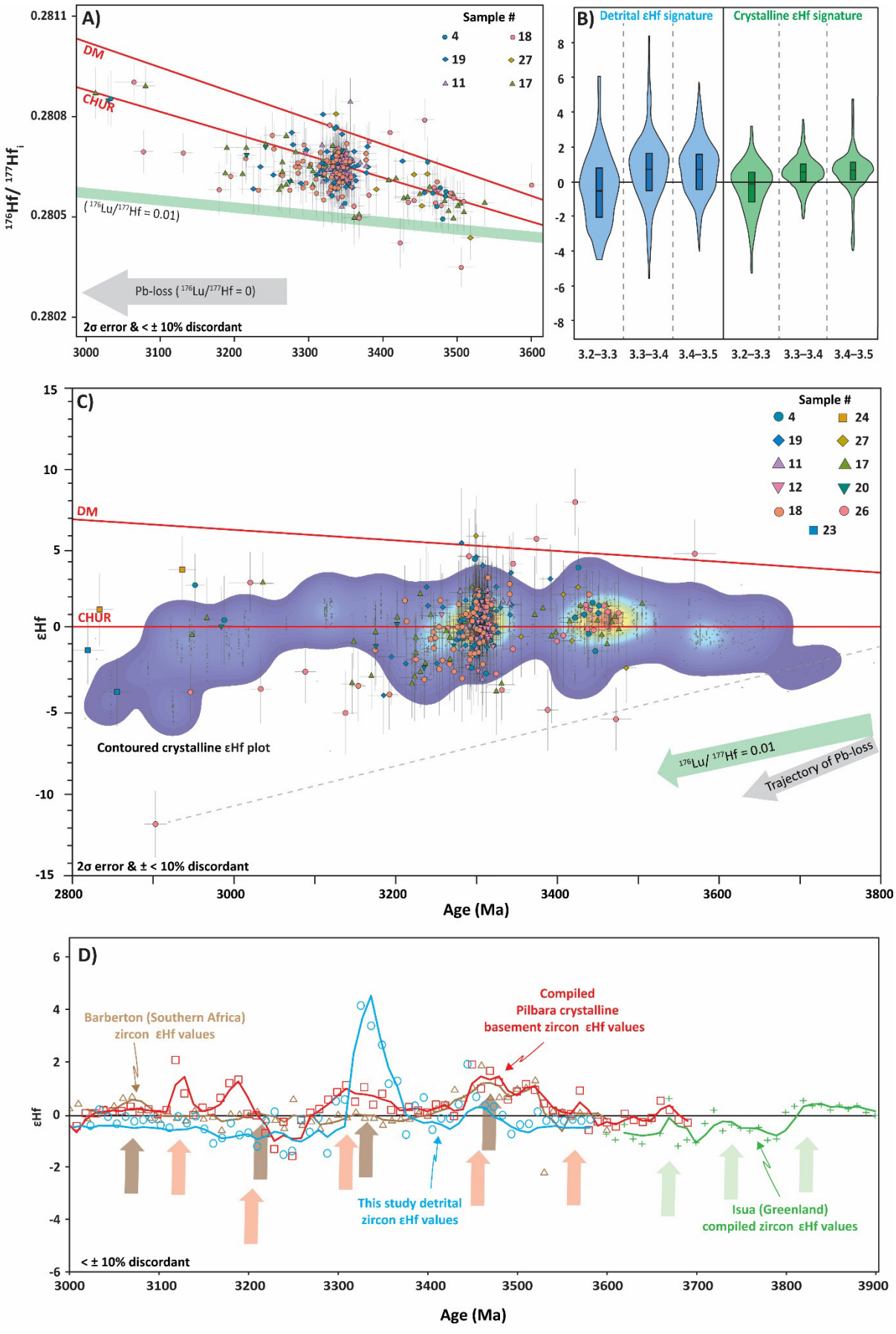
A)
Sample #
4
18
19
27
11
17
DM
CHUR
(176Lu/177Hf = 0.01)
Pb-loss (176Lu/177Hf = 0)
2σ error & < ± 10% discordant
176Hf/ 177Hfi
B)
Detrital εHf signature
Crystalline εHf signature
3.2–3.3
3.3–3.4
3.4–3.5
C)
Sample #
4
24
19
27
11
17
12
20
18
26
23
DM
CHUR
Contoured crystalline εHf plot
176Lu/ 177Hf = 0.01
Trajectory of Pb-loss
2σ error & ± < 10% discordant
εHf
Age (Ma)
D)
Barberton (Southern Africa)
zircon εHf values
Compiled
Pilbara crystalline
basement zircon εHf values
This study detrital
zircon εHf values
Isua (Greenland)
compiled zircon εHf values
< ± 10% discordant
εHf
Age (Ma)

Figure 2.8. ***A)*** *Initial $^{176}Hf/^{177}Hf$ versus concordia age of Archean detrital zircons (this study) with the expected trajectory for Pb-loss shown. A $^{176}Lu/^{177}Hf$ ratio of 0.01 for average Archean TTGs composition is also shown. (Blichert-Toft and Albarède, 2008; Taylor and McLennan, 1985).* ***B)*** *Violin plots for the detrital ƐHf signatures compared to crystalline values from the East Pilbara Terrane.* ***C)*** *ƐHf versus concordia age for detrital zircon. At least two vertical Hf mixing arrays (3.45 and 3.30 Ga) punctuate evolution slopes ($^{176}Lu/^{177}Hf$ = 0.01). Hafnium data for contoured plot from Amelin et al. (2000); Gardiner et al. (2017); Kemp et al. (2015); Kemp et al. (2023); Petersson et al. (2020); Petersson et al. (2019b); Salerno et al. (2021)* ***D)*** *A compilation of ƐHf values from various Archean terranes (interpolated on a 10 Ma interval with a 3-period moving average). Significant juvenile input events are highlighted. Hf data compiled from Puetz et al. (2021).*

2.5.5. Ancient Crust Unroofing

The granitoid domes of the East Pilbara Terrane are composite structures (Figure 2.1) (Figure 2.9) (Hickman, 2021; Roberts and Tikoff, 2021), in which pre-existing lithologies were destroyed (consumed/assimilated within new melts and also uplifted and eroded) during later granitoid emplacement – hence there is a progressively more limited igneous archive of early crust preserved in the Pilbara Craton. A consequence of this process is a trend from more radiogenic ƐHf positive values at the margins to less radiogenic, negative ƐHf values in the cores of the granitoid domes of the East Pilbara Terrane (Figure 2.9) (Gardiner et al., 2017). The spatial zonation of ƐHf reflects this multi-stage formation of domes whereby the source melts become less radiogenic through the Archean, reflecting the increased incorporation of earlier reworked crust over more radiogenic melts (Figure 2.8C) (Buzenchi et al., 2022; Gardiner et al., 2017).

Previous work in the East Pilbara Terrane has supported the existence of a poorly resolved and perhaps locally reworked (+ve ƐHf) proto-crust with an age of at least 3.55 – 3.80 Ga (Collins et al., 1998; Gardiner et al., 2017; Hickman, 1990; Hickman and Van Kranendonk, 2012; Petersson et al., 2019b). Indeed, recent insights from Pb isotopes in the Pilbara have demonstrated that continental nuclei derived from a CHUR-like source were preserved for up to 500 Ma following their formation during the Eoarchean to Paleoarchean, but not Hadean (Hartnady et al., 2022). This earlier crust has been studied indirectly through Nd and Hf model ages; however, direct insights have been limited to xenocrystic zircon crystals inherited within granitic gneiss or mafic enclaves within granitoids (Petersson et al., 2019a). Our ƐHf data may help resolve an earlier (≥ 3.8 Ga) crustal evolution array, as suggested in Hickman and Van Kranendonk (2012), Petersson et al. (2019a), and Hartnady et al. (2022). The fit of the lowermost isotopic evolution array through ƐHf data in Figure 2.8C, using a $^{176}Lu/^{177}Hf$ of 0.01, appears to represent a preserved remnant of the continued isotopic evolution of an extraction event at c. 3.8 Ga (Petersson et al., 2019a) (Figure 2.8C). Despite some of the less radiogenic ƐHf values in Petersson et al. (2019a) being interpreted as modified by radiogenic

Pb-loss, the detrital data here and the K-feldspar Pb isotopic modelling of Hartnady et al. (2022) imply a real source component of up to 3.8 Ga. Such a 3.8 Ga source appears to coincide with more widespread crustal extraction or the better preservation of this isotopic legacy of fractionation after a putative late heavy bombardment (Drabon et al., 2022; Dröllner et al., 2022).

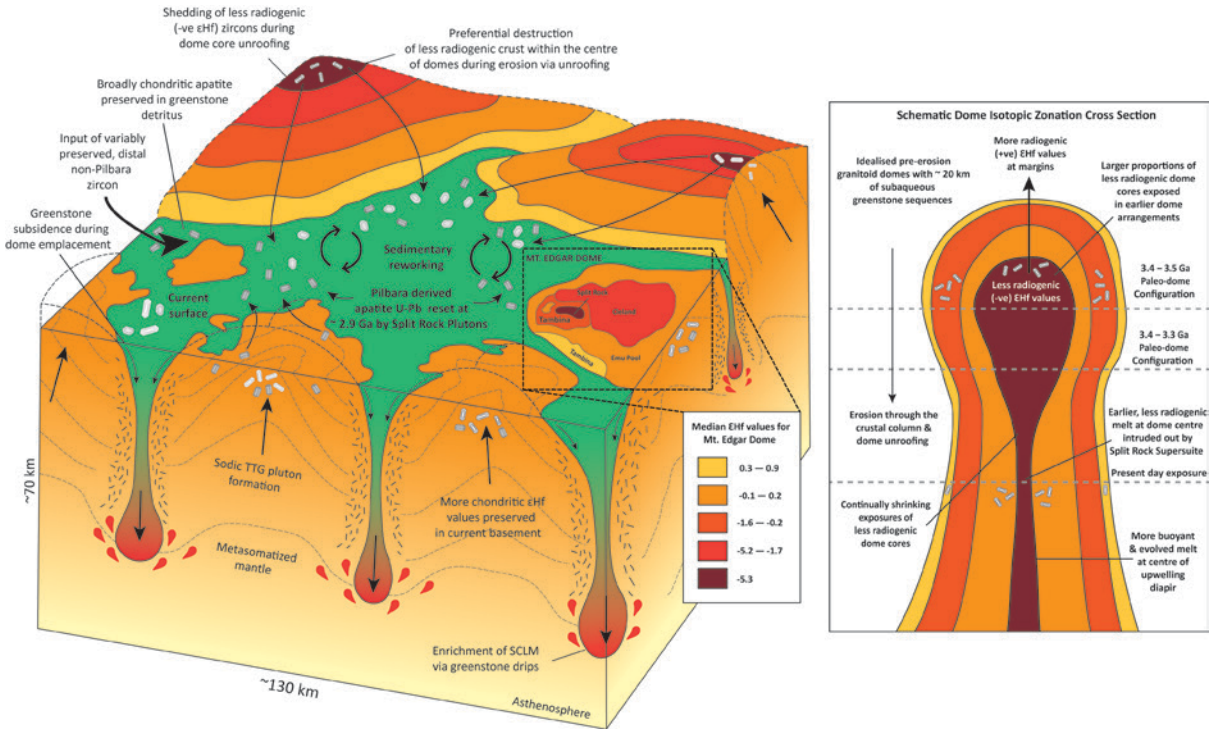

Figure 2.9. Schematic block diagram of the East Pilbara Terrane showing the present surface and the hypothesised pre-erosion surface. Inputs of apatite and zircon off the denuded craton are indicated. A simplified ƐHf map of the Mount Edgar Dome, subdivided by magmatic supersuite and coloured by median ƐHf signature, highlights the general rim-core trend from more to less radiogenic compositions. Inset is a schematic cross-section of a granitoid dome showing isotopic zonation. The ƐHf map was adapted after Gardiner et al. (2017). Block diagram adapted after Smithies et al. (2021).

The Split Rock Suite (2.89–2.83 Ga) (Hickman, 2021) is the least radiogenic (-ve ƐHf) constituent of the Mt. Edgar dome (Gardiner et al., 2017) and is presently the least exposed supersuite by surface area (Figure 2.9). Granitoid domes are multi-generational features whose younger cores extend from more radiogenic values into the same evolution array as the surrounding granitoid supersuites (Gardiner et al., 2017). The emplacement of granitoid domes in the EPT occurred via the upwelling of buoyant melt diapirs (Roberts and Tikoff, 2021; Wiemer et al., 2018) (Figure 2.9). A 3-dimensional spatial isotopic arrangement within the paleo-domes could explain salient features within the detrital record. Specifically, if the paleo-domes had a proportionally greater volume of less radiogenic material higher within the crustal column, this would be preferentially eroded relative to more radiogenic and lower in the crustal

column margins (Figure 2.9). Such a process would result in zircon shed from central paleo-dome components having a bias towards less radiogenic (-ve) ƐHf, whilst zircons preserved within the crystalline basement would, on average, retain a more radiogenic (+ve) signature (Figure 2.8B;9). Despite similar median ƐHf values between detrital and magmatic zircons, the oldest detrital grains show a wider compositional range and encompass less radiogenic (-ve) ƐHf values. Critically, the interquartile range for the 3.5 – 3.4 Ga time interval encompasses proportionally more negative ƐHf values than the contemporaneous crystalline basement, supporting the described unroofing model (Figure 2.8B).

The scattering of Archean zircon to lower ƐHf values due to radiogenic Pb-loss has been documented by previous workers (Petersson et al., 2019b; Spencer et al., 2020). Such a process could conceivably result in ƐHf trends that resemble those produced from the unroofing dome model presented (e.g. more unradiogenic signatures dominating the oldest detrital component). Some samples in this work yield a high percentage of discordant zircon grains (sample 26, 77% are > 10 % discordant), which we interpret as a function of grain antiquity, prolonged surficial exposure, bulk mounting and representative sampling. However, the % of discordant grains (i.e. increased radiogenic Pb-loss) does not increase over the 2.8 – 3.6 Ga interval and remains at a mean of ~ 22 % discordance.

Furthermore, Pb-loss is mitigated by filtering analyses with ± 10% discordance, and no radiogenic Pb-loss trend is evident in ƐHf versus age plots where such a process yields a distinct vector (ƐHf/Ma = 0.022), which contrast to the observed trend in the data (Figure 2.8). Hence, we attribute the distribution of data towards lower ƐHf values in old grains (Figure 2.8B) as a function of a detrital process, whereby less radiogenic zircon grains in the dome cores are preferentially lost into the detrital archive following granitoid unroofing, given their concentric Hf (and Nd) isotopic zonation (Figure 2.9).

The less radiogenic (-ve ƐHf) zircon shed from now-destroyed dome cores has been preserved proximally within basins to the East Pilbara Terrane (Figure 2.9). Thus, the detrital record of the Pilbara may be a more extensive archive of the earlier, more evolved crust of the Pilbara Craton, in contrast to what the contemporary crystalline exposures offer.

2.6. Conclusions

New (U–Pb) time-constrained *in-situ* isotopic signatures (Lu–Hf, Sm–Nd) from detrital zircon and apatite grains collected from ephemeral streams offer insights into the construction and subsequent erosion of Archean continental crust. Zircon ages record a history of sediment flux into and within the Pilbara Craton.

Detrital zircon and apatite offer two distinct insights. The refractory and durable nature of zircon allows it to persist through multiple cycles of reworking. Detrital zircon grains record Pilbara magmatism but also represent an archive of Proterozoic and Phanerozoic geological history within Western Australia (e.g., Capricorn, Albany-Fraser, Paterson Orogens). The occurrence of young ≤ 500 Ma zircon grains also implies a detrital source into the Pilbara Craton from the Lhasa Block.

The labile nature of apatite is not conducive to prolonged transport, leading to a less diverse primary and, indeed, secondary age signature retained in this mineral. We record a unimodal apatite U–Pb age population at 2.9 Ga, interpreted as the time of thermal resetting due to heating from granitoids of the Split Rock Supersuite. While the Lu–Hf, (Eu/Eu*), and Sm–Nd isochrons constrain primary crystallisation primarily from the Bishop Creek Monzonite at c. 3.2 Ga and other granitoids of the EPT granitoid domes. This work highlights a substantial geospatial control on zircon U–Pb age signatures, with samples collected directly atop granitoid domes showing a largely felsic mineral profile and unimodal age signatures, broadly corresponding to the dome's crystallisation (Figure 2.1). Samples collected from greenstone terranes show a more heterogeneous age profile, retaining a greater number of younger grains, likely due to their lower intrinsic zircon load of the underlying basement.

Our detrital zircon ƐHf signatures, on average, stretch to more evolved values than previous data sets from crystalline samples of the domes (Figure 2.8B). This observation supports an unroofing model, critically dependent on the observed age and isotopic zonation of the domes (youngest and least radiogenic in the dome cores). Detrital zircon potentially preserves information about lost components in the primary magmatic record and complements the crystalline record. However, the proportions of such ancient grains need not reflect volumetric proportions in the crystalline basement due to a plethora of geological (and analytical) biases imparted onto the detrital zircon record.

The detrital zircon data (U–Pb, Lu–Hf) implies the continued reworking of earlier crustal components punctuated by the input of juvenile material on an approximate 100 Ma

frequency, similar to some other ancient cratons (Figure 2.8D). This reworking and periodic rejuvenation appear to occur quasiperiodically, perhaps during crust-mantle overturns. This work shows that detrital apatite from the ancient crust, due to its preservation potential and compositional growth affinity, will unlikely provide as extensive a crustal evolution record as detrital zircon. Nonetheless, detrital apatite in the Pilbara Craton offers important insights into thermal/fluid overprinting in the EPT, which is poorly represented in the zircon record.

2.7. Acknowledgments

This work was funded by an Australian Research Council Discovery Project (DP200101881). SG was supported by an Australian Research Council Future Fellowship (FT210100906). AC acknowledges helpful discussions with M. Dröllner, S. Makin and H. Olierook during data reduction and visualisation. GeoHistory Facility instruments in the JdLC, Curtin University, were funded via an Australian Geo-physical Observing System grant provided to AuScope Pty Ltd. by the AQ44 Australian Education Investment Fund program. AuScope and the Australian Government support the JdLC GeoHistory laser ablation facility through the National Collaborative Research Infrastructure Strategy. Bradley McDonald and Noreen Evans are thanked for their help with LA–ICP–MS analysis. This research was undertaken using the Tescan Mira3 TIMA with four PulsTor SDD X-ray detectors (ARC LE140100150) and Tescan Clara FESEM with Oxford Instruments Ultim Max 170 SDD X-ray detector, Symmetry EBSD detector and AZtec Synergy software (ARC LE190100176). We thank Wilson Teixeira and Elson Oliveira for their expeditious editorial handling. Tony Kemp, Allen Nutman and an anonymous reviewer gave comments that significantly improved the quality of this work.

2.8. Data Availability

Isotopic data for zircon (U–Pb, Lu–Hf) and apatite (U–Pb, Lu–Hf, Sm–Nd) are available online as Supplementary data 2 – 4 via *DOI: 10.1016/j.precamres.2023.107132.*

2.9. References

Amelin, Y., Lee, D. C., and Halliday, A. N., 2000, Early-middle archaean crustal evolution deduced from Lu-Hf and U-Pb isotopic studies of single zircon grains: Geochimica et Cosmochimica Acta, v. 64, no. 24, p. 4205-4225.

Barfod, G. H., Krogstad, E. J., Frei, R., and Albarède, F., 2005, Lu-Hf and PbSL geochronology of apatites from Proterozoic terranes: A first look at Lu-Hf isotopic closure in metamorphic apatite: Geochimica et Cosmochimica Acta, v. 69, no. 7, p. 1847-1859.

Barham, M., Kirkland, C. L., and Handoko, A. D., 2022, Understanding ancient tectonic settings through detrital zircon analysis: Earth and Planetary Science Letters, v. 583, p. 117425.

Belousova, E., Griffin, W. L., O'Reilly, S. Y., and Fisher, N., 2002, Apatite as an indicator mineral for mineral exploration: Trace-element compositions and their relationship to host rock type: Journal of Geochemical Exploration, v. 76, p. 45-69.

Belousova, E., Kostitsyn, Y. A., Griffin, W. L., Begg, G. C., O'Reilly, S. Y., and Pearson, N. J., 2010, The growth of the continental crust: Constraints from zircon Hf-isotope data: Lithos, v. 119, no. 3-4, p. 457-466.

Berger, A., Egli, D., Glotzbach, C., Valla, P. G., Pettke, T., and Herwegh, M., 2022, Apatite low-temperature chronometry and microstructures across a hydrothermally active fault zone: Chemical Geology, v. 588, p. 120633.

Bédard, J. H., 2018, Stagnant lids and mantle overturns: Implications for Archaean tectonics, magmagenesis, crustal growth, mantle evolution, and the start of plate tectonics: Geoscience Frontiers, v. 9, no. 1, p. 19-49.

Bickle, M., Morant, P., Bettenay, L., Boulter, C., Blake, T., and Groves, D., 1985, Archaean tectonics of the Shaw Batholith, Pilbara Block, Western Australia: structural and metamorphic tests of the batholith concept: Evolution of Archean Supracrustal Sequences, v. 28, p. 325-341.

Blichert-Toft, J., and Albarède, F., 2008, Hafnium isotopes in Jack Hills zircons and the formation of the Hadean crust: Earth and Planetary Science Letters, v. 265, no. 3, p. 686-702.

Buzenchi, A., Moreira, H., and Dhuime, B., 2022, Evidence for Protracted Intracrustal Reworking of Palaeoarchaean Crust in the Pilbara Craton (Mount Edgar Dome, Western Australia): Lithosphere, v. 2022.

Cawood, P. A., Hawkesworth, C. J., and Dhuime, B., 2012, Detrital zircon record and tectonic setting: Geology, v. 40, no. 10, p. 875-878.

-, 2013, The continental record and the generation of continental crust: GSA Bulletin, v. 125, no. 1-2, p. 14-32.

Cherniak, D. J., 2000, Rare earth element diffusion in apatite: Geochimica et Cosmochimica Acta v. 64, no. 22, p. 3871-3885.

Chew, D. M., Petrus, J. A., and Kamber, B. S., 2014, U–Pb LA–ICPMS dating using accessory mineral standards with variable common Pb: Chemical Geology, v. 363, p. 185-199.

Chew, D. M., and Spikings, R. A., 2015, Geochronology and Thermochronology Using Apatite: Time and Temperature, Lower Crust to Surface: Elements, v. 11, no. 3, p. 189-194.

-, 2021, Apatite U-Pb Thermochronology: A Review: Minerals, v. 11, p. 1095.

Chew, D. M., Sylvester, P. J., and Tubrett, M. N., 2011, U–Pb and Th–Pb dating of apatite by LA-ICPMS: Chemical Geology, v. 280, no. 1-2, p. 200-216.

Chu, N. C., Taylor, R. N., Chavagnac, V., Nesbitt, R. W., Boella, R. M., Milton, J. A., German, C. R., Bayon, G., and Burton, K., 2002, Hf isotope ratio analysis using multi-collector inductively coupled plasma mass spectrometry: an evaluation of isobaric interference corrections: Journal of Analytical Atomic Spectrometry, v. 17, no. 12, p. 1567-1574.

Cochrane, R., Spikings, R. A., Chew, D. M., Wotzlaw, J. F., Chiaradia, M., Tyrrell, S., Schaltegger, U., and Van der Lelij, R., 2014, High temperature (>350°C) thermochronology and mechanisms of Pb loss in apatite: Geochimica et Cosmochimica Acta, v. 127, p. 39-56.

Collins, W. J., Van Kranendonk, M. J., and Teyssier, C., 1998, Partial convective overturn of Archaean crust in the east Pilbara Craton, Western Australia: driving mechanisms and tectonic implications: Journal of Structural Geology, v. 20, no. 9, p. 1405-1424.

Compston, W., 1999, Geological age by instrumental analysis: the 29th Hallimond Lecture: Mineralogical Magazine, v. 63, no. 3, p. 297-311.

Coyner, S., Kamenov, G., Mueller, P., Rao, V., and Foster, D., 2004, FC1: a Zircon Reference Standard for the Determination of Hf Isotopic Compositions via Laser Ablation ICP-MS: AGU Fall Meeting Abstracts.

Craddock, J. P., Ojakangas, R. W., Malone, D. H., Konstantinou, A., Mory, A., Bauer, W., Thomas, R. J., Affinati, S. C., Pauls, K., Zimmerman, U., Botha, G., Rochas-Campos, A., Santos, P. R. d., Tohver, E., Riccomini, C., Martin, J., Redfern, J., Horstwood, M., and Gehrels, G., 2019, Detrital zircon provenance of Permo-Carboniferous glacial diamictites across Gondwana: Earth-Science Reviews, v. 192, p. 285-316.

de Laeter, J. R., and Blockley, J. G., 1972, Granite ages within the Archaean Pilbara Block, Western Australia: Journal of the Geological Society of Australia, v. 19, no. 3, p. 363-370.

Dhuime, B., Hawkesworth, C. J., Cawood, P. A., and Storey, C. D., 2012, A change in the geodynamics of continental growth 3 billion years ago: Science, v. 335, no. 6074, p. 1334-1336.

Dhuime, B., Hawkesworth, C. J., Delavault, H., and Cawood, P. A., 2017, Continental growth seen through the sedimentary record: Sedimentary Geology, v. 357, p. 16-32.

Dhuime, B., Wuestefeld, A., and Hawkesworth, C. J., 2015, Emergence of modern continental crust about 3 billion years ago: Nature Geoscience, v. 8, no. 7, p. 552-555.

Drabon, N., Byerly, B. L., Byerly, G. R., Wooden, J. L., Wiedenbeck, M., Valley, J. W., Kitajima, K., Bauer, A. M., and Lowe, D. R., 2022, Destabilization of Long-Lived Hadean Protocrust and the Onset of Pervasive Hydrous Melting at 3.8 Ga: AGU Advances, v. 3, no. 2, p. e2021AV000520.

Dröllner, M., Barham, M., and Kirkland, C. L., 2023, Reorganization of continent-scale sediment routing based on detrital zircon and rutile multi-proxy analysis: Basin Research, v. 35, no. 1, p. 363-386.

Dröllner, M., Kirkland, C. L., Barham, M., Evans, N. J., and McDonald, B. J., 2022, A persistent Hadean–Eoarchean protocrust in the western Yilgarn Craton, Western Australia: Terra Nova, v. n/a, no. n/a.

Dumitru, T. A., 2016, A New Zircon Concentrating Table Designed for Geochronologists, American Geophysical Union, Volume 2016: San Francisco, AGU Fall Meeting Abstracts, p. 23-2956.

Fisher, C. M., Bauer, A. M., Luo, Y., Sarkar, C., Hanchar, J. M., Vervoort, J. D., Tapster, S. R., Horstwood, M., and Pearson, D. G., 2020, Laser ablation split-stream analysis of the Sm-Nd and U-Pb isotope compositions of monazite, titanite, and apatite – Improvements, potential reference materials, and application to the Archean Saglek Block gneisses: Chemical Geology, v. 539.

Fisher, C. M., Vervoort, J. D., and DuFrane, S. A., 2014a, Accurate Hf isotope determinations of complex zircons using the “laser ablation split stream” method: Geochemistry, Geophysics, Geosystems, v. 15, no. 1, p. 121-139.

Fisher, C. M., Vervoort, J. D., and Hanchar, J. M., 2014b, Guidelines for reporting zircon Hf isotopic data by LA-MC-ICPMS and potential pitfalls in the interpretation of these data: Chemical Geology, v. 363, p. 125-133.

François, C., Philippot, P., Rey, P., and Rubatto, D., 2014, Burial and exhumation during Archean sagduction in the East Pilbara Granite-Greenstone Terrane: Earth and Planetary Science Letters, v. 396, p. 235-251.

Gardiner, N. J., Hickman, A. H., Kirkland, C. L., Lu, Y., Johnson, T., and Zhao, J.-X., 2017, Processes of crust formation in the early Earth imaged through Hf isotopes from the East Pilbara Terrane: Precambrian Research, v. 297, p. 56-76.

Gardiner, N. J., Maidment, D. W., Kirkland, C. L., Bodorkos, S., Smithies, R. H., and Jeon, H., 2018, Isotopic insight into the Proterozoic crustal evolution of the Rudall Province, Western Australia: Precambrian Research, v. 313, p. 31-50.

Gillespie, J., Glorie, S., Khudoley, A., and Collins, A. S., 2018, Detrital apatite U-Pb and trace element analysis as a provenance tool: Insights from the Yenisey Ridge (Siberia): Lithos, v. 314-315, p. 140-155.

Gillespie, J., Kirkland, C. L., Kinny, P. D., Simpson, A., Glorie, S., and Rankenburg, K., 2022, Lu–Hf, Sm–Nd, and U–Pb isotopic coupling and decoupling in apatite: Geochimica et Cosmochimica Acta, v. 338, p. 121-135.

Glorie, S., Gillespie, J., Simpson, A., Gilbert, S., Khudoley, A., Priyatkina, N., Hand, M., and Kirkland, C. L., 2022, Detrital apatite Lu–Hf and U–Pb geochronology applied to the southwestern Siberian margin: Terra Nova, v. 34, p. 201-209.

GSWA, 2024, Compilation of WAROX data : [Western Australia] / Government of Western Australia, Geological Survey of Western Australia, *in* Peng, J., and White, S. R., eds.: East Perth, Western Australia, Geological Survey of Western Australia.

Haines, P. W., Wingate, M., and Kirkland, C. L., 2013, Detrital Zircon U–Pb Ages from the Paleozoic of the Canning and Officer Basins, Western Australia: Implications for Provenance and Interbasin Connections.

Hartnady, M. I. H., and Kirkland, C. L., 2019, A gradual transition to plate tectonics on Earth between 3.2 to 2.7 billion years ago: Terra Nova, v. 31, no. 2, p. 129-134.

Hartnady, M. I. H., Kirkland, C. L., Martin, L., Clark, C., Smithies, R. H., and Spaggiari, C. V., 2019, Zircon oxygen and hafnium isotope decoupling during regional metamorphism: implications for the generation of low $\delta^{18}O$ magmas: Contributions to Mineralogy and Petrology, v. 175, no. 1, p. 9.

Hartnady, M. I. H., Kirkland, C. L., Smithies, R. H., Johnson, S. P., and Johnson, T. E., 2022, Pb isotope insight into the formation of the Earth's first stable continents: Earth and Planetary Science Letters, v. 578.

Hawkesworth, C., Cawood, P. A., and Dhuime, B., 2019, Rates of generation and growth of the continental crust: Geoscience Frontiers, v. 10, no. 1, p. 165-173.

Hawkesworth, C., Cawood, P. A., and Dhuime, B., 2020, The evolution of the continental crust and the onset of plate tectonics: Front Earth Sci (Lausanne), v. 8.

Herrmann, M., Söderlund, U., Scherstén, A., Næraa, T., Holm-Alwmark, S., and Alwmark, C., 2021, The effect of low-temperature annealing on discordance of U–Pb zircon ages: Scientific Reports, v. 11, no. 1, p. 7079.

Hickman, A. H., 1990, Geology of the Pilbara Craton, *in* Glover, J. S., Myers, J. R., and Ho, J. E., eds., Third International Archaean Symposium Excursion Guidebook Volume 21: Perth, University of Western Australia, p. 1-13.

-, 2021, East Pilbara Craton: a record of one billion years in the growth of Archean continental crust, Perth, Geological Survey of Western Australia, 187 p.:

Hickman, A. H., and Van Kranendonk, M. J., 2012, Early Earth evolution: Evidence from the 3.5-1.8 Ga geological history of the Pilbara region of Western Australia: Episodes, v. 35, p. 283-297.

Hocking, R. M., Langford, R. L., Thorne, A. M., Sanders, A. J., Morris, P. A., Strong, C. A., Gozzard, J. R., and Riganti, A., 2001, A classification system for regolith in Western Australia, Perth, Geological Survey of Western Australia, 22 p.:

Jackson, S. E., Pearson, N. J., Griffin, W. L., and Belousova, E. A., 2004, The application of laser ablation-inductively coupled plasma-mass spectrometry to in situ U–Pb zircon geochronology: Chemical Geology, v. 211, no. 1, p. 47-69.

Jahn, B. M., Glikson, A. Y., Peucat, J. J., and Hickman, A. H., 1981, REE geochemistry and isotopic data of Archean silicic volcanics and granitoids from the Pilbara Block, Western Australia: implications for the early crustal evolution: Geochimica et Cosmochimica Acta, v. 45, no. 9, p. 1633-1652.

Jahn, I., Clark, C., Reddy, S., and Taylor, R. J. M., 2021, Zircon U–Pb Geochronology and Hf–O Isotope Characteristics of Granitoids from the Capricorn Orogen, Western Australia: Journal of Petrology, v. 62, no. 11.

Johnson, S. P., Korhonen, F. J., Kirkland, C. L., Cliff, J. B., Belousova, E. A., and Sheppard, S., 2017, An isotopic perspective on growth and differentiation of Proterozoic orogenic crust: From subduction magmatism to cratonization: Lithos, v. 268-271, p. 76-86.

Kemp, A. I. S., Hickman, A. H., Kirkland, C. L., and Vervoort, J. D., 2015, Hf isotopes in detrital and inherited zircons of the Pilbara Craton provide no evidence for Hadean continents: Precambrian Research, v. 261, p. 112-126.

Kemp, A. I. S., Vervoort, J. D., Bjorkman, K. E., and Iaccheri, L. M., 2017, Hafnium Isotope Characteristics of Palaeoarchaean Zircon OG1/OGC from the Owens Gully Diorite, Pilbara Craton, Western Australia: Geostandards and Geoanalytical Research, v. 41, no. 4, p. 659-673.

Kemp, A. I. S., Vervoort, J. D., Petersson, A., Smithies, R. H., and Lu, Y., 2023, A linked evolution for granite-greenstone terranes of the Pilbara Craton from Nd and Hf isotopes, with implications for Archean continental growth: Earth and Planetary Science Letters, v. 601, p. 117895.

Kinny, P. D., Clark, C., Kirkland, C. L., Hartnady, M., Gillespie, J., Johnson, T. E., and McDonald, B., 2022, How old are the Jack Hills metasediments really?: The case for contamination of bedrock by zircon grains in transported regolith: Geology, v. 50, no. 6, p. 721-725.

Kirkland, C. L., Hartnady, M. I. H., Barham, M., Olierook, H. K. H., Steenfelt, A., and Hollis, J. A., 2021, Widespread reworking of Hadean-to-Eoarchean continents during Earth's thermal peak: Nat Commun, v. 12, no. 1, p. 331.

Kirkland, C. L., Johnson, S. P., Smithies, R. H., Hollis, J. A., Wingate, M. T. D., Tyler, I. M., Hickman, A. H., Cliff, J. B., Tessalina, S., Belousova, E. A., and Murphy, R. C., 2013a, Not-so-suspect terrane: Constraints on the crustal evolution of the Rudall Province: Precambrian Research, v. 235, p. 131-149.

Kirkland, C. L., Smithies, R. H., Woodhouse, A. J., Howard, H. M., Wingate, M. T. D., Belousova, E. A., Cliff, J. B., Murphy, R. C., and Spaggiari, C. V., 2013b, Constraints and deception in the isotopic record; the crustal evolution of the west Musgrave Province, central Australia: Gondwana Research, v. 23, no. 2, p. 759-781.

Kirkland, C. L., Yakymchuk, C., Szilas, K., Evans, N., Hollis, J., McDonald, B., and Gardiner, N. J., 2018, Apatite: a U-Pb thermochronometer or geochronometer?: Lithos, v. 318-319, p. 143-157.

Korenaga, J., 2013, Initiation and Evolution of Plate Tectonics on Earth: Theories and Observations: Annual Review of Earth and Planetary Sciences, v. 41, no. 1, p. 117-151.

Lewis, C., and Sircombe, K., 2013, Use of U-Pb geochronology to delineate provenance of North West Shelf Sediments, Australia.

Li, Y., and Vermeesch, P., 2021, Short communication: Inverse isochron regression for Re–Os, K–Ca and other chronometers: Geochronology, v. 3, no. 2, p. 415-420.

Malusà, M. G., Resentini, A., and Garzanti, E., 2016, Hydraulic sorting and mineral fertility bias in detrital geochronology: Gondwana Research, v. 31, p. 1-19.

Mao, M., Rukhlov, A. S., Rowins, S. M., Spence, J., and Coogan, L. A., 2016, Apatite Trace Element Compositions: A Robust New Tool for Mineral Exploration: Economic Geology, v. 111, p. 1187-1222.

Marsh, J. H., Jørgensen, T. R. C., Petrus, J. A., Hamilton, M. A., and Mole, D. R., 2019, U-Pb, trace element, and hafnium isotope composition of the Maniitsoq zircon: A potential new Archean zircon reference material, Goldschmidt: Barcalona.

Martin, E. L., Collins, W. J., and Kirkland, C. L., 2017, An Australian source for Pacific-Gondwanan zircons: Implications for the assembly of northeastern Gondwana: Geology, v. 45, no. 8, p. 699-702.

Moecher, D., and Samson, S., 2006, Differential zircon fertility of source terranes and natural bias in the detrital zircon record: Implications for sedimentary provenance analysis: Earth and Planetary Science Letters, v. 247, no. 3-4, p. 252-266.

Morel, M. L. A., Nebel, O., Nebel-Jacobsen, Y., Miller, J., and Vroon, P. Z., 2008, Hafnium isotope characterization of the GJ-1 zircon reference material by solution and laser-ablation MC-ICPMS: Chemical Geology, v. 255, p. 231-235.

Morón, S., Cawood, P. A., Haines, P. W., Gallagher, S. J., Zahirovic, S., Lewis, C. J., and Moresi, L., 2019, Long-lived transcontinental sediment transport pathways of East Gondwana: Geology, v. 47, no. 6, p. 513-516.

Myers, J. S., 1993, Precambrian History of the West Australian Craton and Adjacent Orogens: Annual Review of Earth and Planetary Sciences, v. 21, no. 1, p. 453-485.

Nelson, D., 2005, Compilation of geochronology data, June.

Norris, C., Ashley, and Danyushevsky, L., Towards Estimating the Complete Uncertainty Budget of Quantified Results Measured by LA-ICP-MS, *in* Proceedings Goldschmidt, Boston, 2018.

Nutman, A. P., Bennett, V. C., Friend, C. R. L., Polat, A., Hoffmann, E., and Van Kranendonk, M., 2021, Fifty years of the Eoarchean and the case for evolving uniformitarianism: Precambrian Research, v. 367, p. 106442.

O'Sullivan, G., Chew, D. M., Kenny, G., Henrichs, I., and Mulligan, D., 2020, The trace element composition of apatite and its application to detrital provenance studies: Earth-Science Reviews, v. 201.

Paton, C., Hellstrom, J. C., Paul, B., Woodhead, J. D., and Hergt, J. M., 2011, Iolite: Freeware for the visualisation and processing of mass spectrometric data: Journal of Analytical Atomic Spectrometry, v. 26, p. 2508-2518.

Petersson, A., Kemp, A. I. S., Gray, C. M., and Whitehouse, M. J., 2020, Formation of early Archean Granite-Greenstone Terranes from a globally chondritic mantle: Insights from igneous rocks of the Pilbara Craton, Western Australia: Chemical Geology, v. 551, p. 119757.

Petersson, A., Kemp, A. I. S., Hickman, A. H., Whitehouse, M. J., Martin, L., and Gray, C. M., 2019a, A new 3.59 Ga magmatic suite and a chondritic source to the east Pilbara Craton: Chemical Geology, v. 511, p. 51-70.

Petersson, A., Kemp, A. I. S., and Whitehouse, M. J., 2019b, A Yilgarn seed to the Pilbara Craton (Australia)? Evidence from inherited zircons: Geology, v. 47, no. 11, p. 1098-1102.

Pidgeon, R., Nemchin, A., and Whitehouse, M. J., 2017, The effect of weathering on U–Th–Pb and oxygen isotope systems of ancient zircons from the Jack Hills, Western Australia: Geochimica et Cosmochimica Acta, v. 197, p. 142-166.

Puetz, S. J., Spencer, C. J., and Ganade, C. E., 2021, Analyses from a validated global UPb detrital zircon database: Enhanced methods for filtering discordant UPb zircon analyses and optimizing crystallization age estimates: Earth-Science Reviews, v. 220, p. 103745.

Riebe, C. S., Sklar, L. S., Lukens, C. E., and Shuster, D. L., 2015, Climate and topography control the size and flux of sediment produced on steep mountain slopes: Proceedings of the National Academy of Sciences, v. 112, no. 51, p. 15574-15579.

Roberts, N. M., and Tikoff, B., 2021, Internal structure of the Paleoarchean Mt Edgar dome, Pilbara Craton, Western Australia: Precambrian Research, v. 358.

Salama, W., Anand, R. R., Tunmer, W., and Aspandiar, M., 2022, Regolith characterization and landscape evolution for geochemical exploration of the covered Yamarna Terrane, Western Australia: Journal of Geochemical Exploration, v. 232, p. 106881.

Salerno, R., Vervoort, J., Fisher, C., Kemp, A., and Roberts, N., 2021, The coupled Hf-Nd isotope record of the early Earth in the Pilbara Craton: Earth and Planetary Science Letters, v. 572.

Sandiford, M., Van Kranendonk, M. J., and Bodorkos, S., 2004, Conductive incubation and the origin of dome-and-keel structure in Archean granite-greenstone terrains: A model based on the eastern Pilbara Craton, Western Australia: Tectonics, v. 23, no. 1, p. n/a-n/a.

Schmitz, M. D., Bowring, S. A., and Ireland, T. R., 2003, Evaluation of Duluth Complex anorthositic series (AS3) zircon as a U-Pb geochronological standard: new high-

precision isotope dilution thermal ionization mass spectrometry results: Geochimica et Cosmochimica Acta, v. 67, no. 19, p. 3665-3672.

Schoene, B., and Bowring, S., 2006, U-Pb systematics of the McClure Mountain syenite: Thermochronological constraints on the age of the $^{40}Ar/^{39}Ar$ standard MMhb: Contributions to Mineralogy and Petrology, v. 151, p. 615-630.

Schoene, B., and Bowring, S. A., 2007, Determining accurate temperature–time paths from U–Pb thermochronology: An example from the Kaapvaal craton, southern Africa: Geochimica et Cosmochimica Acta, v. 71, no. 1, p. 165-185.

Simpson, A., Gilbert, S., Tamblyn, R., Hand, M., Spandler, C., Gillespie, J., Nixon, A., and Glorie, S., 2021, In-situ Lu Hf geochronology of garnet, apatite and xenotime by LA ICP MS/MS: Chemical Geology, v. 577.

Sláma, J., Košler, J., Condon, D. J., Crowley, J. L., Gerdes, A., Hanchar, J. M., Horstwood, M. S. A., Morris, G. A., Nasdala, L., Norberg, N., Schaltegger, U., Schoene, B., Tubrett, M. N., and Whitehouse, M. J., 2008, Plešovice zircon — A new natural reference material for U–Pb and Hf isotopic microanalysis: Chemical Geology, v. 249, no. 1, p. 1-35.

Smithies, R. H., Lu, Y., Kirkland, C. L., Johnson, T. E., Mole, D. R., Champion, D. C., Martin, L., Jeon, H., Wingate, M. T. D., and Johnson, S. P., 2021, Oxygen isotopes trace the origins of Earth's earliest continental crust: Nature, v. 592, no. 7852, p. 70-75.

Spaggiari, C., Kirkland, C., Smithies, R., Occhipinti, S., and Wingate, M., 2014, Geological framework of the Albany-Fraser Orogen, p. 12-27.

Spencer, C. J., Cawood, P. A., Hawkesworth, C. J., Prave, A. R., Roberts, N. M. W., Horstwood, M. S. A., and Whitehouse, M. J., 2015, Generation and preservation of continental crust in the Grenville Orogeny: Geoscience Frontiers, v. 6, no. 3, p. 357-372.

Spencer, C. J., Kirkland, C. L., Roberts, N. M. W., Evans, N. J., and Liebmann, J., 2020, Strategies towards robust interpretations of in situ zircon Lu–Hf isotope analyses: Geoscience Frontiers, v. 11, no. 3, p. 843-853.

Stacey, J. S., and Kramers, J. D., 1975, Approximation of terrestrial lead isotope evolution by a two-stage model: Earth and Planetary Science Letters, v. 26, no. 2, p. 207-221.

Stern, R. A., Bodorkos, S., Kamo, S. L., Hickman, A. H., and Corfu, F., 2009, Measurement of SIMS Instrumental Mass Fractionation of Pb Isotopes During Zircon Dating: Geostandards and Geoanalytical Research, v. 33, no. 2, p. 145-168.

Strong, T. R., and Driscoll, R. L., 2016, A process for reducing rocks and concentrating heavy minerals, 2016-1022.

Taylor, S. R., and McLennan, S. M., 1985, The continental crust: Its composition and evolution, United States, Blackwell Scientific Pub.,Palo Alto, CA.

Thomson, S. N., Gehrels, G. E., Ruiz, J., and Buchwaldt, R., 2012, Routine low-damage apatite U-Pb dating using laser ablation–multicollector–ICPMS: Geochemistry, Geophysics, Geosystems, v. 13, no. 2.

Tucker, N. M., Morrissey, L. J., Payne, J. L., and Szpunar, M., 2018, Genesis of the Archean–Paleoproterozoic Tabletop Domain, Rudall Province, and its endemic relationship to the West Australian Craton: Australian Journal of Earth Sciences, v. 65, no. 6, p. 739-768.

Van Kranendonk, M. J., 2008, Structural geology of the central part of the Lalla Rookh – Western Shaw structural corridor, Pilbara Craton,: Geological Suvery of Western Australia.

Van Kranendonk, M. J., Collins, W. J., Hickman, A., and Pawley, M. J., 2004, Critical tests of vertical vs. horizontal tectonic models for the Archaean East Pilbara Granite–Greenstone Terrane, Pilbara Craton, Western Australia: Precambrian Research, v. 131, no. 3-4, p. 173-211.

Van Kranendonk, M. J., Smithies, R. H., Hickman, A. H., and Champion, D. C., 2007a, Chapter 4.1 Paleoarchean Development of a Continental Nucleus: the East Pilbara Terrane of the Pilbara Craton, Western Australia, *in* Van Kranendonk, M. J., Smithies, R. H., and Bennett, V. C., eds., Developments in Precambrian Geology, Volume 15, Elsevier, p. 307-337.

Van Kranendonk, M. J., Smithies, R. H., Hickman, A. H., and Champion, D. C., 2007b, Review: secular tectonic evolution of Archean continental crust: interplay between horizontal and vertical processes in the formation of the Pilbara Craton, Australia: Terra Nova, v. 19, no. 1, p. 1-38.

Veevers, J. J., Saeed, A., Belousova, E. A., and Griffin, W. L., 2005, U–Pb ages and source composition by Hf-isotope and trace-element analysis of detrital zircons in Permian sandstone and modern sand from southwestern Australia and a review of the paleogeographical and denudational history of the Yilgarn Craton: Earth-Science Reviews, v. 68, no. 3-4, p. 245-279.

Vermeesch, P., 2018, IsoplotR: A free and open toolbox for geochronology: Geoscience Frontiers, v. 9, no. 5, p. 1479-1493.

Wiemer, D., Schrank, C. E., Murphy, D. T., Wenham, L., and Allen, C. M., 2018, Earth's oldest stable crust in the Pilbara Craton formed by cyclic gravitational overturns: Nature Geoscience, v. 11, no. 5, p. 357-361.

Windley, B. F., Kusky, T., and Polat, A., 2021, Onset of plate tectonics by the Eoarchean: Precambrian Research, v. 352, p. 105980.

Woodhead, J. D., and Hergt, J. M., 2005, A Preliminary Appraisal of Seven Natural Zircon Reference Materials for In Situ Hf Isotope Determination: Geostandards and Geoanalytical Research, v. 29, no. 2, p. 183-195.

Wopfner, H., and Jin, X., 2009, Pangea Megasequences of Tethyan Gondwana-margin reflect global changes of climate and tectonism in Late Palaeozoic and Early Triassic times--A review: Palaeoworld, v. 18, p. 169-192.

Yang, Y. H., Wu, F. Y., Yang, J. H., Chew, D. M., Xie, L. W., Chu, Z. Y., Zhang, Y. B., and Huang, C., 2014, Sr and Nd isotopic compositions of apatite reference materials used in U–Th–Pb geochronology: Chemical Geology, v. 385, p. 35-55.

Zhu, D. C., Zhao, Z. D., Niu, Y., Dilek, Y., and Mo, X. X., 2011a, Lhasa terrane in southern Tibet came from Australia: Geology, v. 39, no. 8, p. 727-730.

Zhu, D. C., Zhao, Z. D., Niu, Y., Mo, X. X., Chung, S. L., Hou, Z., Wang, L. Q., and Wu, F. Y., 2011b, The Lhasa Terrane: Record of a microcontinent and its histories of drift and growth: Earth and Planetary Science Letters, v. 301, p. 241-255.

Zutterkirch, I. C., Kirkland, C. L., Barham, M., and Elders, C., 2021, Thin-section detrital zircon geochronology mitigates bias in provenance investigations: Journal of the Geological Society, v. 179.

2.10. Appendix A

2.10.1 Zircon U–Pb

Analyses of reference zircon were conducted every ~15 unknowns to account for instrumental and mass fraction drift. High-purity Ar with a flow rate of 0.98 L min^{-1} was used as the carrier gas. On sample energy of ~2.3, J cm^{-2} with a repetition rate of 5 Hz was used to create ~38 µm diameter ablations. Two cleaning pulses preceded each analysis, and the signal from zircon grains and background were analysed for 30 seconds. Sample cells were cleansed by ultra-high purity He (0.4 L min^{-1}). Zircon U-Pb ratios were reduced in Iolite 4 using the U-Pb geochronology DRS (Paton et al., 2011).

2.10.2 Zircon Lu–Hf

Over 1300 zircon Lu-Hf analyses were obtained along with U-Pb data over four split-stream sessions. Data reduction was performed in Iolite 4 using the Hf Isotopes Nu Plasma DRS (Paton et al., 2011). The Mud Tank Zircon was the primary reference for the first two sessions, whilst GJ1 was used for the last two.

2.10.3 Apatite U–Pb

Data reduction was performed in Iolite 4 using the VisualAge UcomPbine DRS (Paton et al., 2011), following the procedure detailed by Chew et al. (2014). The primary reference material used for matrix matching was the Madagascar (MAD) apatite standard (Thomson et al., 2012). Secondary reference materials included the Mt. McClure apatite (MMC) 523.51 ± 1.47 Ma (Schoene and Bowring, 2006) and Duluth Complex (FC) apatite (U-Pb zircon age of 1099.1 ± 0.2 Ma; (Schmitz et al., 2003).

2.10.4 Apatite Sm–Nd

Each analysis consisted of a 40 s baseline measurement followed by 60 s ablation. Data reduction to account for background, instrumental drift, mass bias, and interference corrections was performed in Iolite 4 using the Nd Isotopes Nu Plasma (Paton et al., 2011) following the procedure detailed by Fisher et al., 2017.

2.10.5 Apatite Lu–Hf

Laser beam diameters were variable between 43 – 100 µm. Isotope ratios were calculated in LADR (Norris and Danyushevsky, 2018) using NIST 610 as the primary reference material and corrected for matrix-induced fractionation (correction factor of 0.967 ± 0.008)

using OD306 apatite (1597 ± 7 Ma). A mixture of $NH_3$and He, within a collision cell situated between the two quadrupole mass analysers, reacts with analyte isotopes to produce measurable reaction products, thus allowing for the quantification of interference-free $^{176}Lu/^{176}Hf$ and $^{177}Hf/^{176}Hf$ ratios.

2.11. Appendix B

2.11.1 Sample 4

Sample 4 was collected along the Marble Bar Road, 20m north of a crossing over the ephemeral House Creek, a tributary of the Yandicoogina Creek. The bedrock geology is mapped as the boundary between the Kenell Granodiorite and the Fig Tree Gneiss, dated at 3315 and 3448 Ma, respectively (GSWA, 2024). The Kenell Group includes metamorphosed hornblende-biotite-bearing granitoid and mafic xenoliths, and the Fig Tree Gneiss includes granitoid, syenites, and migmatites. Over a single session, 83 Zircon U-Pb analyses were undertaken, of which 33 were within ± 10% of concordia. Concordant zircon U-Pb ages ranged from 1110 — 3465 Ma, and age peaks at 3310 and 3432 Ma were defined by 17 and 6 grains, respectively.

2.11.2 Sample 11

This sample was collected 30m east of the Corunna Downs Road on the confluence of the Camel and Sandy Creeks. Sample 11 was collected atop the Apex Basalt and Nangingarra Granodiorite, dated at 3459 – 3434 and 3313 – 3300 Ma (GSWA, 2024). The Apex Basalt comprises komatiitic mafics, minor felsic volcaniclastics, and peridotite, while the Nangingarra Granodiorite is formed from hornblende-biotite felsics with inclusions of the Tambina Supersuite. During a single session, 93 U-Pb analyses were obtained, of which 32 were within ± 10% of concordia. Concordant ages spanned from 1162 to 3351 Ma, and a single age peak at 3320 Ma, defined by 21 grains.

2.11.3 Sample 12

Sample 12 was collected 100m northeast of an unnamed track on the Camel Creek. The sample was collected at the abandoned North Shaw Mine site. The underlying geology is the Euro Basalt, dated at 3350 – 3335 Ma (GSWA, 2024).

Over a single session, 108 zircon U-Pb analyses were obtained, and 38 were within ± 10% of concordia. Concordant ages spanned from 3266 to 3454 Ma, and 34 grains defined an age peak at 3320 Ma.

2.11.4 Sample 17

Sample 17 was gathered along the North Pole Road, 20m west of a crossing of an unnamed tributary of the Shaw River. The sand was collected atop the boundary of two lithological units, the Mount Ada Basalt and the Antarctic Creek, dated at 3470 Ma. 100m to the east is a north-south trending Black Range Dolerite dyke, dated at 2772 Ma (GSWA, 2024). 193 U-Pb analyses were performed on Sample 17 over two sessions, and 106 were within ± 10% of concordia. Concordant values ranged from 981 to 3519 Ma. The concordant ages formed peaks at 3188, 3238, 3271 and 3476, defined by 11, 13, 11 and 10 grains, respectively.

2.11.5 Sample 18

This sample was collected on the Yandicoogina stream feeding the Oakover River, 10m south of the Rippon Hills Road. This sample sits atop the Fig Tree Gneiss unit belonging to the Tambina Supersuite. Two hundred thirty-one zircon U-Pb analyses were undertaken, of which 66 were within ± 10% of concordia. Concordant ages range from 221 – 3452 Ma, with significant age populations defined at 3258 and 3308 Ma by 8 and 30 grains, respectively. Ninety-seven apatite U-Pb analyses were performed, of which 79 had an f^{207} of less than 30%. The filtered analyses yielded f^{207} corrected ages of 2663 – 3632 Ma, with a single age peak of 2882 Ma formed from 61 analyses. All 97 analyses yielded a regression intersecting concordia at 2897 +/- 27.6 (MSWD = 4.3) with a $^{207}Pb/^{206}Pb_i$ of 1.13. 125 Sm-Nd spots were analysed on apatite. All sample 18 analyses yielded a 3208 ± 120 Ma isochron, with an initial $^{143}Nd/^{144}Nd$ of 0.050846 ± 0.00016 (MSWD = 2.1). 48 Lu-Hf apatite analyses were undertaken on grains already analysed via U-Pb. Sample 18 analyses produced an inverse isochron equal to 3183 ± 32 Ma, with an initial $^{177}Hf/^{176}Hf$ of 3.563 ± 0.045 (MSWD = 0.92).

2.11.6 Sample 19

This sample was collected along the Rippon Hills Road, 15m southeast of the Mount Creek track, a tributary of the Yilgalong River. The sample was collected from within the Bishop Creek Monzonite, comprised of granodiorite, syenogranite and uncommon pegmatitic dykes. Bishop Creek is monzonite, dated to between 3246 – 3223 Ma (GSWA, 2024). Over two sessions, 144 zircon U-Pb analyses were performed, and 59 were within ± 10% of concordia. Concordant zircon yielded 1160 – 3403 Ma ages, with a single age peak of 3315 Ma defined by 27 grains.

Ninety-two apatite U-Pb analyses were performed, of which 88 had <30% f^{207}. Filtered ^{207}Pb corrected ages (f^{207} < 30%) ranged from 2838 – 3623 Ma, with a single age peak defined at 3109 Ma by 64 analyses. All 92 analyses yield a regression intersecting concordia at 3087 ± 37.8 (MSWD = 4.4) with a $^{207}Pb/^{206}Pb_i$ of 1.12. Such a scatter about this regression may imply a slightly different closure to the radiogenic-Pb blocking temperature in different crystals. 93 Sm-Nd spots were created. All analyses produced an isochron equal to 3246 ± 100 Ma, with an initial $^{143}Nd/^{144}Nd$ of 0.050842 ± 0.00013 (MSWD = 1.5). 30 Lu-Hf apatite analyses were obtained on grains already analysed via U-Pb, and analyses yielded an isochron equal to 3194 ± 48 Ma with an initial $^{177}Hf/^{176}Hf$ of 3.574 ± 0.066 (MSWD = 1.8).

2.11.7 Sample 20

Sample 20 was collected along the Rippon Hills Road, 20m south of a crossing of the Talga River. The underlying geology is the Bishop Creek monzogranite, consisting of biotite granodiorite and syenogranite. 300m to the northwest is a northeast-southeast trending Bamboo Creek member rhyolitic dyke, dated at 2766 Ma (GSWA, 2024). Across two sessions, 88 zircon U-Pb analyses were undertaken, of which 20 were within ± 10% of concordia. Concordant ages range between 1454 – 3339 Ma, with a single age peak of 3315 Ma represented by three analyses.

2.11.8 Sample 23

Sample 23 was collected from the Rippon Hills area from a minor tributary stream of the Gingarrigan Creek. The area is 700m north of the Rippon Hills Road at the end of a minor road. To the west is an area of unnamed hills from which the stream drains. The sample was collected atop the Carawine Dolomite Formation, dated 2629 – 2565 Ma. 200m to the east is the Paterson Formation, a conglomeration of sandstone and siltstones with ages between 305 – 295 Ma (GSWA, 2024). 500m to the north is the Jeerinah Formation, a package of siliciclastic sedimentary rocks and intercalated dolerite sills dated between 2713 – 2629 Ma (GSWA, 2024). Two hundred-five zircon U-Pb analyses were performed, of which 132 were within ± 10% of concordia. Concordant ages range between 484 – 2902 Ma, and 23, 22, 21, and 15 grains define age populations at 1122, 1159, 1177, and 2753 Ma, respectively.

2.11.9 Sample 24

Sample 24 was collected along the Rippon Hills Road 30m south of the crossing over the Yigalong Creek. The sample was collected atop the Jeerinah Formation. Forty-one zircon

U-Pb analyses were performed, and 15 are within ± 10% of concordia. Concordant ages range from 653 to 3137 Ma, with no significant age peak defined. Eight apatite U-Pb analyses were obtained, and four were <30% f^{207}. F^{207} corrected ages ranged from 1892 to 3158 Ma, and no age peak was established. Given the low number of analyses, a regression line cannot be fitted with confidence.

2.11.10 Sample 26

The sample was collected 20m south of the Woodstock - Marble Bar road crossing over the De Gray River in the Rocky Island area. The underlying geology is the Calina Supersuite, formed of metamorphosed diorite and syenogranite, dated at 3484 – 3462 Ma (GSWA, 2024). One hundred sixteen zircon U-Pb analyses were undertaken, and 27 were within ± 10% of concordia. Concordant ages range from 1743 – 3586 Ma, with four age peaks at 3354, 3402, 3451 and 3475 Ma defined by 3, 3, 4 and 3 analyses. Fifty-four apatite U-Pb analyses were obtained with 47 <30% f^{207}. The low f^{207} analyses yield 207 corrected ages that range from 2738 – 3214 Ma. 26 analyses define a single ^{207} corrected age peak at 2805 Ma. All 54 analyses yield a regression intersecting concordia at 2834 ± 19.9 (MSWD = 3.5) with a $^{207}Pb/^{206}Pb_i$ of 1.10. 51 Sm-Nd spots were created, and three were performed on pristine apatite grains without previous U-Pb analyses. All analyses produced an isochron equal to 3001 ± 180 Ma, with an initial $^{143}Nd/^{144}Nd$ of 0.050851 ± 0.00024 (MSWD = 1.9). Five apatite Lu-Hf analyses were obtained on grains already dated via U-Pb. Analyses produced a 3137 ± 88 Ma isochron equal to, with an initial $^{177}Hf/^{176}Hf$ of 3.61 ± 0.68 (MSWD = 1.8).

2.11.11 Sample 27

Sample 27 was collected from the alluvial river sediments of the Mulgandinnah River at the confluence of a minor stream. The Woodstock Road is 600m to the southeast, leading to the FMG Railway Camp 145 to the east. The underlying geology is the Euro Basalt Formation, comprising basalt, komatiitic, minor dolerite, and peridotite. The formation is dated from 3350 to 3335 Ma. 300m to the southwest is the Strelley Pool formation of silicified carbonate rocks at 3246 – 3350 Ma. The sample was collected directly over an exposed fault within the Euro Basalt Formation (GSWA, 2024). One hundred forty-one zircon U-Pb grains were analysed, and 24 were within ± 10% of concordia. Concordant ages range from 243 to 3499 Ma, with a single age peak at 3433 Ma formed from 3 grains.

Chapter 3. Detrital zircon and apatite reveal Paleoproterozoic rifting along the eastern margin of the Yilgarn Craton

This chapter is published as:

Clarke, A. J. I., Kirkland, C. L., Glorie, S., Quentin de Gromard, R., Tucker, M.N. Detrital zircon and apatite reveal Paleoproterozoic rifting along the eastern margin of the Yilgarn Craton. Precambrian Research, v. 414, p. 107602.

Doi.org/10.1016/j.precamres.2024.107602.

Minor post-publication changes and clarifications have been made.

Detrital minerals within Proterozoic basins are commonly an extant record of now-destroyed crust and provide valuable constraints on ancient paleogeography and tectonic processes. However, reconstructing basin histories depends on discriminating potentially exotic, far-travelled (allochthonous) versus locally sourced (autochthonous) detritus. Detrital zircon from the Woodline Formation, a component of the Proterozoic Barren Basin at the margin of the Yilgarn Craton, Western Australia, closely matches the age and Hf isotopic signatures of magmatic units in the Paleo- to Mesoproterozoic Albany–Fraser Orogen (AFO). However, the provenance of some 2300–2000 Ma zircon detritus is not readily accounted for by known magmatism in the AFO nor the wider Western Australian Craton. To help resolve this enigmatic source, we present isotopic data (U–Pb, Lu–Hf) and trace element geochemistry for zircon and limited U–Pb data for scarce apatite collected from sand and rocks of the Woodline Formation. Based on Hf isotopic signatures, some of the detritus appears to be derived from the recently identified 2030–2010 Ma felsic-igneous Moonyoora Suite, representing the oldest known magmatic components of the AFO. Moreover, the isotopic data imply an earlier ca. 2250 Ma episode of mafic rift-related magmatism, potentially offering a glimpse into the earliest rifting stages along the Yilgarn Craton's eastern margin. While Paleoproterozoic detritus is omnipresent in Woodline rocks, it is conspicuously absent from overlaying regolith, demonstrating that cover atop the Woodline Formation is imported and not locally derived. This disparity is important as it highlights that ongoing exploration efforts analysing unconsolidated regolith may not fully capture basement signatures.

3.1. Introduction

Sedimentary basins, through their detrital mineral cargo, can represent comprehensive archives of regional geology and offer insights into a region's tectonic-magmatic and metamorphic history (Cawood et al., 2012; Chew et al., 2020; Dhuime et al., 2017). Detrital grains, such as zircon and apatite, often retain an imperfect record of paleogeography and sediment flux (Cawood et al., 2012; Dröllner et al., 2022). Different tectonic settings will have varying preservation potentials for crystalline basement and overlying basin components (Barham et al., 2022; Cawood et al., 2013; Hawkesworth et al., 2009). Biases in the detrital record are further compounded by the dissimilar preservation potential of different minerals, which is a function of their physical and chemical durability and their duration within source-to-sink transport systems (Barham et al., 2022; Cawood et al., 2012; Glorie et al., 2020).

In some terranes, detrital minerals are commonly the only extant archive of now-destroyed, heavily modified, or concealed rocks. For example, detrital zircon within metasediments of the Lhasa and Qiantang Terranes of the Himalayas preserve evidence of sediment exchange with Western Australia, which is not retained within the exposed crystalline rocks (Bhattacharya et al., 2020; Gehrels et al., 2011). Source-to-sink relationships for sedimentary packages are often deciphered using detrital zircon age (U–Pb dating) and composition (e.g. trace elements and Lu–Hf) (Clarke et al., 2023; Strachan et al., 2021). However, more nuanced interpretations are possible when multiple detrital minerals are investigated from the same sample, as this may mitigate source fertility and mineral-specific biases (Chew et al., 2020; Dröllner et al., 2023; Gillespie et al., 2018).

The resistive mineral cargo contained within modern sands can complement the conventional crystalline record via U–Pb and Lu–Hf studies (Clarke et al., 2023; Dröllner et al., 2022; Kirkland et al., 2021). Nevertheless, the relationship between unconsolidated cover and underlying geology may not be straightforward, and detrital grain ages obtained from both need not be congruent, as distal inputs into the cover sequences are possible (Kinny et al., 2022). This potential disparity becomes especially important in highly prospective regions, such as the southeastern margin of the Yilgarn Craton, where exploration efforts target unconsolidated cover material as a proxy for basement mineralisation. This approach is predicated on the cover representing the underlying geology, which is not always the case. Moreover, using detrital grains to understand basement geology comes with important considerations, such as the varying properties of minerals. Compared to zircon, apatite is more labile during chemical weathering and can often characterise mafic, first-cycle detritus

(O'Sullivan et al., 2020). Moreover, apatite increasingly accompanies zircon studies to offer alternative insights via its combined U–Pb, Sm–Nd, and Lu–Hf systems (Gillespie et al., 2022; Glorie et al., 2024; Kharkongor et al., 2023).

The Albany–Fraser Orogen (AFO) in Western Australia is one example of a study area where detrital zircon provenance and source-to-sink pathways are relatively well understood (Kuper et al., 2024; Morrissey et al., 2017; Spaggiari et al., 2014a; Spaggiari et al., 2015; Waddell et al., 2015). The AFO is a Paleo- to Mesoproterozoic orogenic belt along the southeastern margin of the Archean Yilgarn Craton that records periods of prolonged extension, crustal reworking, and new juvenile magmatic additions into the edge of one of the Archean nuclei of the West Australian Craton (WAC) (Clark et al., 2000; Kirkland et al., 2011; Spaggiari et al., 2014a).

Detrital zircon data from basins in the AFO closely match the age and Hf-isotopic signature of magmatic suites in the orogen (Morrissey et al., 2017; Spaggiari et al., 2014b; Spaggiari et al., 2015). Such detrital relationships have been used to support reconstructions of the orogen as it oscillated from periods of hyperextension and basin formation into periods of compression and inversion (Adams, 2012; Dawson et al., 2002; Hall et al., 2008). Still, the provenance of some distinct detrital zircon age components in the AFO basins remains enigmatic. For example, previous studies document Paleoproterozoic (2300–2000 Ma) detrital zircon ages, which are not readily accounted for by known tectonomagmatic activity in the AFO, nor the WAC more broadly (Hall et al., 2008; Rasmussen et al., 2002; Spaggiari et al., 2014a; Spaggiari et al., 2015). Nonetheless, given the unconstrained source for some of the oldest Palaeoproterozoic detritus in the AFO, the geodynamic setting of the earliest magmatism along the southeast margin of the Yilgarn Craton remains an open question.

Recent zircon isotopic analysis has revealed evidence for an earlier magmatic event in the AFO, resulting in the emplacement of the ca. 2030–2010 Ma Moonyoora Suite (Tucker et al., 2023). These rocks are A-type granitoids that appear to have isotopic links to ca. 2060 Ma rift-related ultramafic rocks in the eastern Yilgarn Craton (Choi et al., 2021; Fiorentini et al., 2020; Tucker et al., 2023). Thus, the Moonyoora Suite implies that extension and associated magmatism commenced ca. 200 Ma earlier in the AFO than was previously recognised from exposed crystalline lithologies (Tucker et al., 2023). These Paleoproterozoic rocks provide important insights into a period in Earth's evolution that was otherwise characterised by a global tectonic-magmatic lull from ca. 2300–2200 Ma (Spencer et al., 2018). The ca. 2300–

2000 Ma detrital record may also offer insights into this poorly represented period in the geological record.

To account for the Paleoproterozoic detrital zircon ages recorded from the AFO, previous workers have speculated that the source rock(s) (1) no longer exist, (2) are presently unidentified, (3) do not crop out, or (4) that they come from an allochthonous terrane, exotic to the WAC (Hall et al., 2008; Spaggiari et al., 2014b). Johnson et al. (2011) and Spaggiari et al. (2015) favoured an autochthonous WAC source, whereby ca. 2300–2000 detritus in the Barren Basin was derived from rocks of the Capricorn Orogen. However, this interpretation is complicated by the long transport distance (> 800 km northwest of the AFO) that it implies. Moreover, the detrital zircon ages from the AFO are not entirely coeval to those in the Capricorn Orogen (Hall et al., 2008). Thus, the ultimate provenance of ca. 2300—2000 Ma detritus throughout the AFO remains unresolved yet important in constraining the orogen's formative history.

This study presents isotopic and chemical data for detrital zircon and apatite collected from rocks and sand of the Woodline Formation, Western Australia (Figures 3.1;3.2). We use this combined dataset to illustrate the disparate detrital mineral cargos between in situ rocks and unconsolidated cover sequences in the Woodline Formation. We characterise enigmatic Paleoproterozoic zircon through Lu–Hf and trace element signatures, which reveal distinct rift-related mafic signatures based on reworking the Yilgarn Craton crust. In addition, we propose a rift geometry model along the Yilgarn Craton's southeast margin to account for the limited temporal supply of Paleoproterozoic detritus. Our data place the Paleoproterozoic detritus within the contemporary understanding of WAC magmatism.

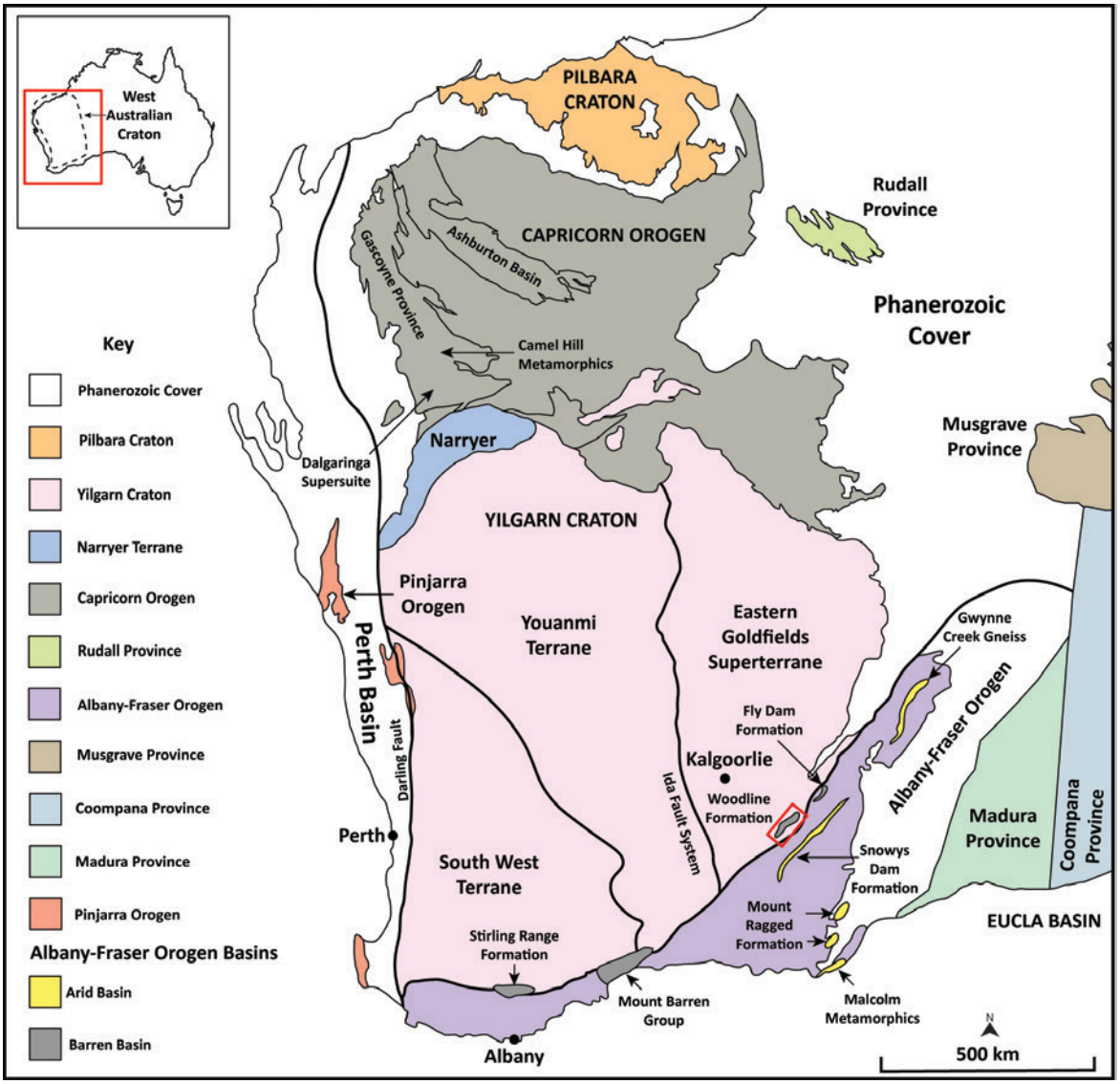

Figure 3.1. A simplified geological map of the West Australian Craton showing major tectonic units. The locations of the Barren Basin (Woodline Formation) and Arid Basin are highlighted. Map adapted after GSWA, 2024 and Tucker et al., 2023.

3.2. Geological Background

3.2.1. Yilgarn Craton

The 3730–2600 Ma Yilgarn Craton is one of the largest exposures of Archean continental crust globally, spanning more than 650,000 km^2 (Cassidy et al., 2006; Mole et al., 2019). By area, over 70% of the craton is composed of granitoids, gneisses, and felsic volcanics; mafic to ultramafic metavolcanics and metasedimentary "greenstone belts" constitute the remaining lithologies (Champion and Cassidy, 2007; Mole et al., 2019).

The Yilgarn Craton is subdivided into several terranes, including the Eastern Goldfields Superterrane (EGST), which formed between ca. 2720 and 2660 Ma (Cassidy et al., 2002; Osei et al., 2021) and the Youanmi, Narryer and Southwest terranes, which constitute the western extent of the Yilgarn Craton and comprising 3730–2610 Ma felsic and mafic intrusive rocks (Figure 3.1; Mole et al., 2019 and references therein). Compared to the EGST, the Youanmi Terrane is older, less isotopically evolved, and contains 2960–2730 Ma greenstone belts (Mole et al., 2019).

3.2.2. Albany–Fraser Orogen

Extending ~1200 km along the southeastern margin of the WAC, the AFO is a Paleo- to Mesoproterozoic arcuate belt that formed due to hyperextension and periodic compression of the Archean Yilgarn Craton (Figure 3.1) (Clark et al., 2000; Morrissey et al., 2017; Spaggiari et al., 2015). The AFO extends eastwards to the Madura Province, but the terrane boundary is obscured by Neoproterozoic to Cenozoic sedimentary rocks of the Bight and Eucla Basins (Figure 3.1) (Spaggiari et al., 2014a). The Madura Province contains Mesoproterozoic rocks with a more isotopically juvenile oceanic affinity (Kirkland et al., 2015a). The AFO contains variably deformed granulite- to amphibolite-facies gneisses and granites that are intruded by post-deformation granitoid plutons, all of which have a variable Archean source component (Kirkland et al., 2015a; Spaggiari et al., 2011).

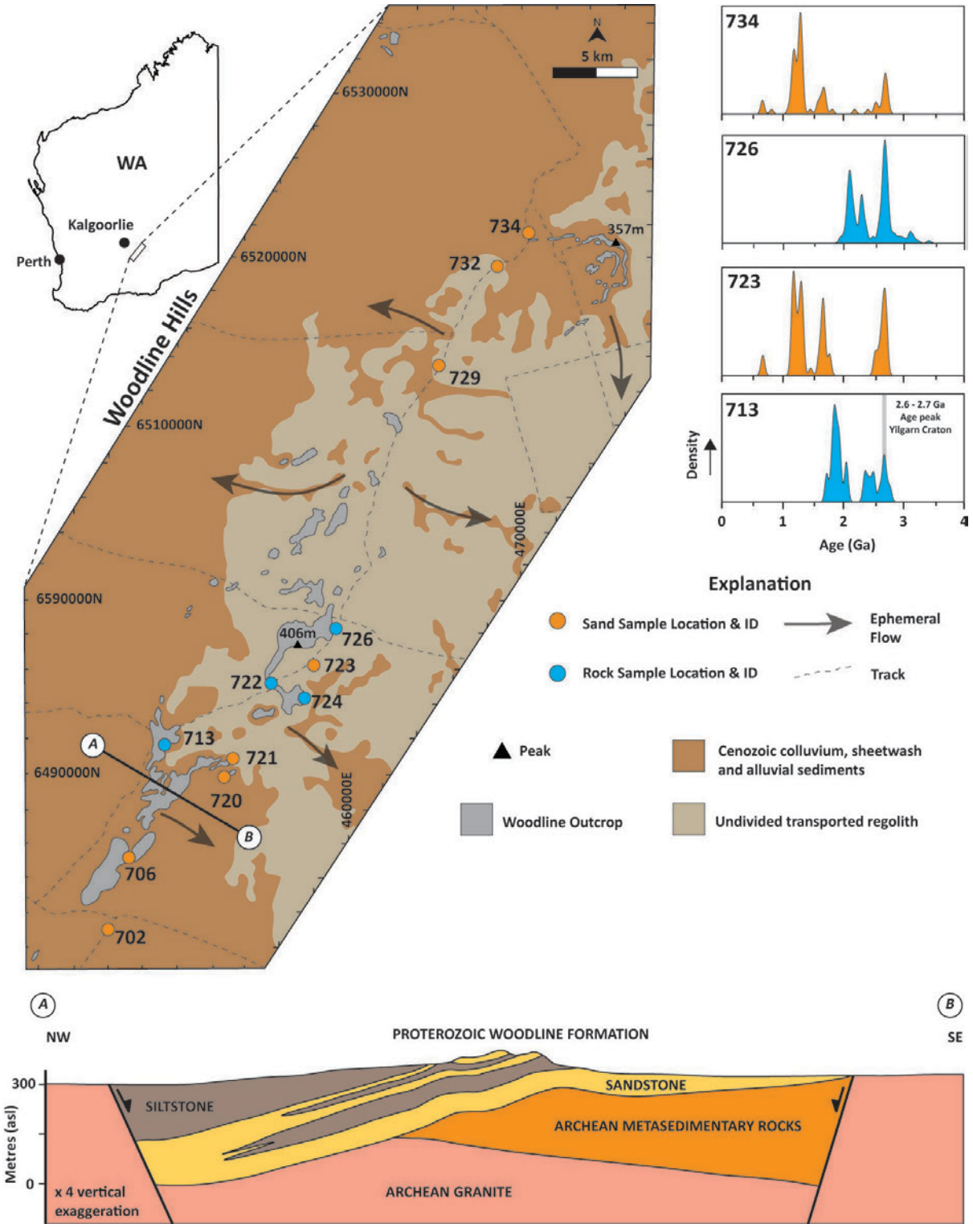

Figure 3.2. ***Left:*** *A simplified geological map and cross-section of the Woodline Formation show regolith, sample locations, and ephemeral flow directions. Map and cross-section modified after Hall et al. (2008). The coordinate system is from 1: 1,000,000 geological maps of Western Australia GSWA (2024).* ***Right:*** *Representative zircon kernel density estimates from typical sand and rock samples from the Woodline Hills.*

Two major tectonic divisions are recognised within the AFO: the Kepa Kurl Booya Province (KKBP) and the Northern Foreland (Kirkland et al., 2015a; Smithies et al., 2015; Spaggiari et al., 2009), and this distinction is based on the degree of Archean Yilgarn Craton crust versus juvenile Proterozoic juvenile crust addition (Kirkland et al., 2011; Spaggiari et al., 2014a). The Northern Foreland consists of Archean Yilgarn Craton granitoids that were metamorphosed to greenschist facies and granite deformed and metamorphosed at amphibolite-facies and intruded by Mesoproterozoic rocks during the Albany–Fraser Orogeny (Spaggiari et al., 2009; Spaggiari et al., 2014a). In contrast, the KKBP is dominated by Paleo- to Mesoproterozoic rocks with only rare, isolated remnants of Archean granite (Spaggiari et al., 2009). The KKBP is subdivided into three major fault-bound litho-tectonic zones: the Biranup, Fraser and Nornalup (Spaggiari et al., 2011; Spaggiari et al., 2014a).

The oldest documented Proterozoic lithology in the AFO is the ca. 2030–2010 Ma Moonyoora Suite, which is a series now concealed rift-related A-type granitoids that have been interpreted to mark the possible inception of rifting along the southeast margin of the Yilgarn Craton (Tucker et al., 2023). Orthogneisses with protolith ages of ca. 1815–1810 Ma from the Salmon Gums event in the Biranup Zone represent the oldest Proterozoic intrusive rocks presently exposed at the surface in the AFO (Spaggiari et al., 2014a).

AFO magmatism during the Mesoproterozoic primarily occurred in two stages (I and II). Both stages involved the reworking of Archean crust (Spaggiari et al., 2014a; Spaggiari et al., 2015). Various models are proposed to account for Stage I Mesoproterozoic magmatism (ca. 1345–1260 Ma). One model invokes delamination concomitant with orogenic collapse following oceanic arc accretion at ca. 1345 (Spaggiari et al., 2015). Alternatively, tectonic extension has been proposed to have occurred within a back-arc setting (Clark et al., 2014; Kirkland et al., 2011; Morrissey et al., 2017). Stage II tectonism (1215–1140 Ma) represents a period of intracratonic reactivation, high-temperature moderate-pressure metamorphism, and deformation, perhaps driven by lithospheric delamination (Liebmann et al., 2023; Smithies et al., 2015; Tucker et al., 2018).

3.2.3. Sedimentary Basins of the Albany–Fraser Orogen

Three supracrustal packages within the AFO, the Barren Basin (ca. 1815–1600 Ma), the Arid Basin (ca. 1400–1305 Ma) and the Ragged Basin (ca. 1280–1200 Ma), represent the remnants of three Proterozoic basins that formed along the southeast margin of the Yilgarn Craton (Spaggiari et al., 2014a). The Barren Basin comprises several lithological units

deposited within sub-basins: Stirling Range, Fly Dam and Lindsey Hill formations, Mount Barren Group, and the Woodline Formation (Figure 3.1). These units sit atop the Yilgarn Craton, Biranup Zone, Nornalup Zone, and the Northern Foreland (Spaggiari et al., 2014a). This spatial distribution suggests that the Barren Basin was once a laterally extensive and long-lived depocentre that flanked the southeast Yilgarn Craton for at least 1000 km (Spaggiari et al., 2014a). Detrital zircon ages and Hf isotope signatures suggest that the Barren Basin detritus was primarily sourced from the coeval Biranup Zone Paleoproterozoic magmas that were emplaced in a rift setting (Kirkland et al., 2011; Spaggiari et al., 2015). Sedimentation rates in AFO basins have been proposed to be closely linked to magmatic cycles, periodic uplift, and denudation, leading to detritus release into surrounding accommodation spaces (Spaggiari et al., 2015).

The remnants of the Barren Basin are structurally controlled, with the Woodline Formation preserved within a down-faulted graben (Hall et al., 2008) and the Stirling Range Formation situated within a Mesoproterozoic thrust sheet atop the Yilgarn Craton (Spaggiari et al., 2011). The Barren Basin sequences are characterised by mature quartz-rich sediments intercalated with silt and mudstones. Barren Basin deposition is (Spaggiari et al., 2014b) dominated by Neoarchean and Paleoproterozoic detrital zircons, implying infill derived predominantly from the erosion of the Yilgarn Craton granitoids (Spaggiari et al., 2014a).

The Gwynne Creek Gneiss and Malcolm Metamorphics, Fraser Range, and Snowys Dam Formation constitute the Arid Basin (Figure 3.1) (Spaggiari et al., 2014b). Following a hiatus in Barren Basin deposition at ca. 1600 Ma, a change in sediment source characterises the infill of the Arid Basin, which began forming at ca 1400 Ma (Kuper et al., 2024). Recent detailed detrital zircon geochronology on granulite facies rocks has refined the maximum depositional age for the Arid Basin to ca. 1400 Ma (Kuper et al., 2024), nearly coeval with the production of Loongana oceanic arc magmatism in the Madura Province (Spaggiari et al., 2018).

The Arid Basin is markedly different from the Barren Basin, consisting of highly variable, immature successions of intercalated sandstone, marls, calcareous rocks, and sub-parallel mafic and calc-silicate rocks (Spaggiari et al., 2014b). The provenance of the Arid Basin infill represents a shift in the tectonic setting, with the infill supply from the Yilgarn Craton becoming restricted. Notably, isotopically distinct exotic detritus from the Madura Province (including Loongana Arc) is recognised as a dominant component of the zircon load

in the basin, along with minor quantities of local Biranup and Nornalup detritus (Kuper et al., 2024; Spaggiari et al., 2014b).

3.2.4. Woodline Formation

The Woodline Formation is a minor sub-basin of the 1815–1600 Ma Barren Basin, which flanks the southeast margin of the Yilgarn Craton (Spaggiari et al., 2014a). The Woodline Formation is a late-Paleoproterozoic package of sedimentary rocks at least 250 m thick and 50 km long that forms a nonconformity with metasediments, metavolcanics, and granites of the underlying Yilgarn Craton (Figure 3.1) (Hall et al., 2008). The formation comprises mature quartzite and siltstone units interbedded with minor chert breccia and conglomerate (Figure 3.3A-F).

In contrast to the amphibolite-facies metamorphism in the surrounding Archean Yilgarn metasedimentary rocks, the Woodline Formation is limited to lower greenschist-facies (Hall et al., 2008). Gentle, upright open folds with a northeast orientation associated with minor thrust faults are observed throughout the formation and formed during compression during Stage I of the Albany-Fraser Orogeny (Hall et al., 2008). Later extension between Stage I and II resulted in the Woodline Formation becoming downfaulted within a northeast-trending graben, facilitating its preservation (Hall et al., 2008). A maximum depositional age for the Woodline Formation based on a single detrital zircon age is 1651 ± 26 Ma (Hall et al., 2008). More conservatively, a date of ca. 1696 Ma is defined based on the youngest detrital zircon age group (Spaggiari et al., 2014a). The onset of AFO Stage 1 deformation provides a minimum constraint on the timing of sedimentation to ca. 1345 Ma (Hall et al., 2008; Spaggiari et al., 2015).

3.2.5. Regolith Geology

Due to the geologically stable nature of the southeastern margin of the Yilgarn Craton since at least ca. 1000 Ma (Spaggiari et al., 2011) and a shifting climatic regime (Chandra et al., 2021), an extensive regolith cover up to 150 m thick, now blankets up to 95% of the AFO (Gonzalez-Alvarez et al., 2014). Deeply weathered profiles with thick regolith (>20 m) characterise the Kalgoorlie-Norseman region surrounding the Woodline Hills (Anand and Butt, 2010). Permian glaciation led to whole-scale erosion and transport of previously formed regolith within the area (Anand and Butt, 2010). The regolith above the Woodline Hills comprises colluvium, sheetwash, and ephemeral alluvial sediments, while the local area is dominated by undivided transported regolith and Eocene lacustrine deposits (GSWA, 2024).

3.3. Methods

3.3.1. Location and Sampling

Eight 1–2 kg samples of sand were collected from ephemeral streams, salt lake margins, alluvial wash-out plains, and dunes from the Woodline Hills area (Figures 3.2–3.3; Table 3.1). Four 3–5 kg rock samples were selected for analysis based on stratigraphic position from the base, middle, and upper portions of the exposed Woodline Formation (Figure 3.2; Table 3.1). This sampling strategy was adopted to constrain the ages of zircon-bearing rocks in the source area(s) throughout the depositional lifespan of the Woodline Formation (Table 3.1).

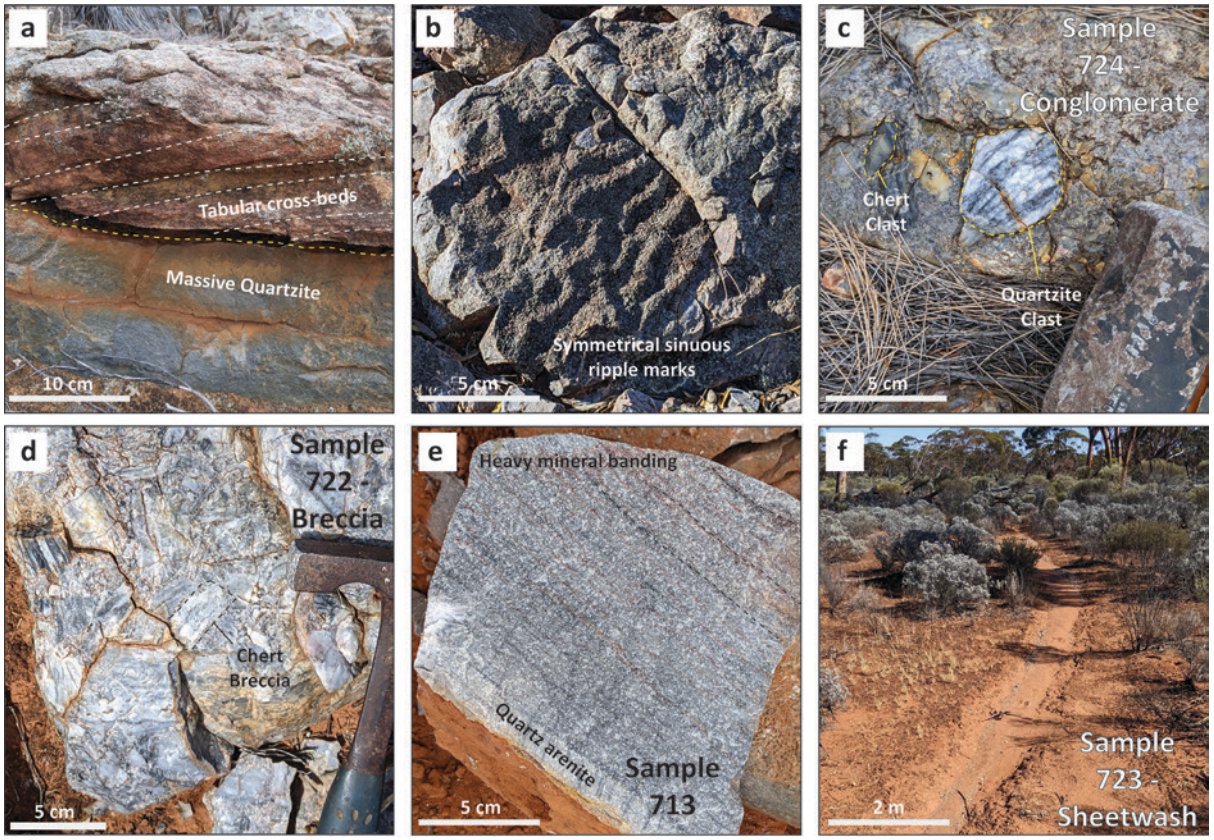

Figure 3.3. Annotated photographs of Woodline Formation outcrop samples and regolith from the Woodline Hills area.

SAND

SAMPLE ID	LATITUDE	LONGITUDE	UTM	ANALYSIS	LOCATION
734	-31.4420	122.6913	51J 470662 6521369	Zircon U–Pb, Lu–Hf	Ephemeral stream
732	-31.4615	122.6839	51J 469965 6519205	Zircon U–Pb, Lu–Hf	Salt lake margin
729	-31.5579	122.6089	51J 462880 6508496	Zircon U–Pb, Lu–Hf	Ephemeral stream
723	-31.6763	122.5440	51J 456781 6495347	Zircon U–Pb, Lu–Hf	Sheetwash
721	-31.7224	122.5093	51J 453515 6490223	Zircon U–Pb, Lu–Hf. Apatite U–Pb	Alluvial fan
720	-31.7289	122.5070	51J 453305 6489506	Apatite U–Pb	Alluvial fan
706	-31.7753	122.4397	51J 446948 6484330	Zircon U–Pb, Lu–Hf	Salt lake margin
702	-31.8156	122.4220	51J 445304 6479850	Zircon U–Pb, Lu–Hf	Dune on road

ROCK

SAMPLE ID	LATITUDE	LONGITUDE	UTM	ANALYSIS	LITHOLOGY
713	-31.7355	122.4584	51J 448702 6488754	Zircon U–Pb, Lu–Hf & Trace Elements, Apatite U–Pb	Basal quartzite
722	-31.6792	122.5338	51J 455814 6494958	Zircon U–Pb, Lu–Hf & Trace Elements, Apatite U–Pb	Breccia, mid sequence
724	-31.6841	122.5450	51J 456876 6494481	Zircon U–Pb, Lu–Hf & Trace Elements, Apatite U–Pb	Basal conglomerate
726	-31.6515	122.5646	51J 458729 6498101	Zircon U–Pb, Lu–Hf & Trace Elements	Quartzite, mid-upper sequence

Table 3.1. Summary table of sand and rock samples collected, and analysis undertaken from the Woodline Hills area.

3.3.2. Sample Processing

Mineral separation was undertaken to liberate apatite and zircon from eight sand samples at the John de Laeter Centre (JdLC), Curtin University. Sieved sand samples yielded approximately 300 g of the <425 μm fraction. The fine fraction subsequently underwent heavy mineral separation using a Jasper Canyon Research liquid shaking platform (Dumitru, 2016). A riffle splitter was then used to ensure all smaller subsequent fractions were representative. Heavy liquid separation was performed at 2.85 g/cm^3 using lithium hetero-poly-tungstate and was followed by Frantz isodynamic magnetic separation to yield the final concentrate.

Rocks were crushed and milled at the JdLC. Concentrates of apatite and zircon from each prepared rock sample were then prepared at Geotrack Mineral Separation Services, Melbourne, using the methodology described above. Apatite and zircon concentrate from sand and rock were bulk mounted onto 25 mm epoxy rounds and polished to a 1-μm finish. A TESCAN Integrated Mineral Analyser (TIMA) was used to compositionally map each mineral phase for laser ablation inductively coupled mass spectrometry (LA-ICP-MS) analysis. A TESCAN Clara field emission scanning electron microscope (FE-SEM) was used to aid spot placement during LA-ICP-MS analysis.

3.3.3. U–Pb and Lu–Hf Analysis of Zircon from Sand and Rock Samples

Three split-stream U–Pb and Lu–Hf sessions were undertaken by LA-ICP-MS setup at the GeoHistory Facility, JdLC. Zircon U–Pb data were collected using an Agilent 8900 ICP-MS, whereas Lu–Hf isotopes were measured simultaneously via a Nu Plasma II Multi collector ICP-MS. Ablations were created using a RESOlution LE193 nm ArF equipped with a Laurin Technic S155 cell. The carrier gas was high-purity Ar with a flow rate of 0.98 L min^{-1}. The spot size of 38 μm was combined with an on-sample fluence of ~ 2.8 J/cm^{-2} and a repetition rate of 10 Hz. Two cleaning pulses preceded each analysis, and signals from zircon and the background were analysed for 30 seconds. The sample cell was cleansed using ultrahigh purity He (350 mL min^{-1}) and N_2 (3.8 mL min^{-1}), which served as the carrier gas. Dwell times for U–Pb measurements included 0.1 s for ^{238}U and ^{232}Th, 0.2 s for ^{208}Pb, 0.7 s for ^{207}Pb, 0.4 s for ^{206}Pb and 0.3 s for ^{204}Pb and ^{202}Hg.

Session 1

Reference	Primary Reference	Reported Age (Ma)	2σ	Age Ma* (Weighted Mean 95% confidence)	2σ	MSWD	*p*	n
Plešovice	GJ1	337.13 (Sláma et al., 2008)	0.37	340	2	0.73	0.70	11
GJ1	Plešovice	601.95 (Jackson et at., 2004)	0.40	597	4	0.64	0.85	17
OG1	GJ1	3465.4 (Stern et al., 2009)	0.60	3468	7	0.73	0.77	17
Maniitsoq	GJ1	3008.7 (Marsh et al., 2019)	0.72	3012	7	1.4	0.12	18

Session 2

Reference	Primary Reference	Reported Age (Ma)	2σ	Age Ma* (Weighted Mean 95% confidence)	2σ	MSWD	*p*	n
Plešovice	GJ1	337.13 (Sláma et al., 2008)	0.37	339	2	0.81	0.61	10
GJ1	Plešovice	601.95 (Jackson et at., 2004)	0.40	602	2	0.49	0.96	18
OG1	GJ1	3465.4 (Stern et al., 2009)	0.60	3470	4	1.60	0.10	12
Maniitsoq	GJ1	3008.7 (Marsh et al., 2019)	0.72	3014	5	0.83	0.63	14

Session 3

Reference	Primary Reference	Reported Age (Ma)	2σ	Age Ma* (Weighted Mean 95% confidence)	2σ	MSWD	*p*	n
Plešovice	GJ1	337.13 (Sláma et al., 2008)	0.37	339	1	1.30	0.22	18
OG1	GJ1	3465.4 (Stern et al., 2009)	0.60	3462	4	0.71	0.22	11
GJ1	Plešovice	601.95 (Jackson et at., 2004)	0.40	600	2	0.71	0.74	15
Maniitsoq	GJ1	3008.7 (Marsh et al., 2019)	0.72	3006	4	0.37	0.99	18

Session 4

Reference	Primary Reference	Reported Age (Ma)	2σ	Age Ma* (Weighted Mean 95% confidence)	2σ	MSWD	*p*	n
Plešovice	GJ1	337.13 (Sláma et al., 2008)	0.37	339	1	0.73	0.75	16
OG1	GJ1	3465.4 (Stern et al., 2009)	0.60	3467	6	0.49	0.92	12
GJ1	Plešovice	601.95 (Jackson et at., 2004)	0.40	597	2	0.71	0.92	17
Maniitsoq	GJ1	3008.7 (Marsh et al., 2019)	0.72	3007	7	0.72	0.76	16

*Table 3.2. Summary table of U–Pb zircon secondary reference material. * Weighted Mean 95% confidence $^{207}Pb/^{206}Pb$ ages for zircons OG1 and Maniitsoq whereas $^{206}Pb/^{238}U$ ages are reported for all other reference material.*

GJ1 zircon 601.95 ± 0.40 Ma (Jackson et al., 2004) was the primary reference material for all zircon U–Pb analyses. Secondary reference zircons were analysed after every ~ 15 unknowns and included Plešovice = 337.13 ± 0.37 Ma, Sláma et al. (2008); OG1 = 3465.4 ± 0.6 Ma, Stern et al. (2009) and Maniitsoq = 3008.70 ± 0.72 Ma, Marsh et al. (2019). The calculated weighted mean U–Pb and Pb-Pb dates for secondary reference zircon were within 2σ uncertainty of published values (Table 3.2).

Subsequent data reduction was done using Iolite 4, including normalisation while accounting for instrumental drift and down-hole fractionation (Paton et al., 2011). We interpret concordant (≤ 10% discordant) single-spot concordia dates to represent the age of zircon-crystallising rocks from various detrital sources. We define discordance using the relative age difference (%) between $^{206}Pb/^{238}U$ and $^{207}Pb/^{206}Pb$ dates [($^{207}Pb/^{206}Pb$ age - $^{238}U/^{206}Pb$ age) / $^{207}Pb/^{206}Pb$ age x 100 %]. We use single-spot concordia ages given the range of detrital zircon dates (Phanerozoic – Archean), thus avoiding the need for an arbitrary swap between ratios used in age calculation.

Analyses of ^{172}Yb, ^{173}Yb, ^{175}Lu, $^{176}Hf + Yb + Lu$, ^{177}Hf, ^{178}Hf, ^{179}Hf and ^{180}Hf (with 1 second of on-peak integration time) were made simultaneously as U–Pb measurements. The primary reference material used for Lu–Hf zircon analysis was Mud Tank zircon, $^{176}Hf/^{177}Hf$ ratio = 0.282507 ± 0.00006; Woodhead and Hergt (2005). Lu–Hf isotope analyses of samples were interspersed with analysis of secondary reference zircon with reported $^{176}Hf/^{177}Hf$ ratios including GJ1 = 0.282000 ± 0.000025, (Morel et al., 2008); Plešovice = 0.282482 ± 0.000013 and FC1 = 0.282184 ± 0.000016, (Woodhead and Hergt, 2005); R33 = 0.282764 ± 0.000014, (Fisher et al., 2014); OG1 = 0.280633 ± 0.000034, (Kemp et al., 2017); Maniitsoq = 0.280862 ± 0.000021, (Marsh et al., 2019). The measured $^{176}Hf/^{177}Hf$ and $^{178}Hf/^{177}Hf$ ratios obtained for each secondary reference zircon were within two standard deviations of published values (Table 3.3). Corrections for isobaric interferences of ^{176}Yb and ^{176}Lu on the ^{176}Hf measurements were made using fixed ratios of $^{176}Yb/^{173}Yb = 0.7962$ and $^{176}Lu/^{175}Lu = 0.02655$ (Chu et al., 2002; Hartnady et al., 2019).

Data reduction for Lu–Hf isotopes was undertaken using Iolite v. 4.0 using the Nu Plasma DRS. The R package “detzrcr” (github.com/magnuskristoffersen/detzrcr) was used to calculate ƐHf values using the CHUR composition of Bouvier et al. (2008), the ^{176}Lu decay constant of Söderlund et al. (2004), and the depleted mantle values of Griffin et al. (2000).

Session 1

Reference	Primary Reference	Expected $^{176}Hf/^{177}Hf$	2SD	$^{176}Hf/^{177}Hf$ (Weighted Mean 95% confidence)	2σ	MSWD	$^{176}Hf/^{177}Hf$ (Arithmetic Mean)	2SD	*n*
Plešovice	Mudtank	0.282482 (Sláma et al., 2008)	0.000013	0.282500	0.000026	1.10	0.282500	0.000088	11
R33	Mudtank	0.282764 (Fisher et al., 2014)	0.000014	0.282766	0.000017	0.65	0.282762	0.000056	17
FC1	Mudtank	0.282184 (Woodhead & Hergt, 2005)	0.000016	0.282193	0.000024	0.88	0.282188	0.000066	10
GJ1	Mudtank	0.282000 (Morel et al., 2008)	0.000025	0.282012	0.000022	0.57	0.282011	0.000071	18
OG1	Mudtank	0.280633 (Kemp et al., 2017)	0.000034	0.280674	0.000020	1.60	0.280674	0.000101	18
Maniitsoq	Mudtank	0.280862 (Marsh et al., 2019)	0.000021	0.280867	0.000022	0.92	0.280864	0.000083	17

Session 2

Reference	Primary Reference	Expected $^{176}Hf/^{177}Hf$	2SD	$^{176}Hf/^{177}Hf$ (Weighted Mean 95% confidence)	2σ	MSWD	$^{176}Hf/^{177}Hf$ (Arithmetic Mean)	2SD	*n*
Plešovice	Mudtank	0.282482 (Sláma et al., 2008)	0.000013	0.282471	0.000020	1.10	0.282477	0.000062	11
R33	Mudtank	0.282764 (Fisher et al., 2014)	0.000014	0.282779	0.000015	0.88	0.282779	0.000051	15
GJ1	Mudtank	0.282000 (Morel et al., 2008)	0.000025	0.282028	0.000019	0.44	0.282030	0.000048	16
OG1	Mudtank	0.280633 (Kemp et al., 2017)	0.000034	0.280663	0.000017	1.30	0.280666	0.000054	14
FC1	Mudtank	0.282184 (Woodhead & Hergt, 2005)	0.000016	0.282197	0.000018	0.89	0.282195	0.000054	11
Maniitsoq	Mudtank	0.280862 (Marsh et al., 2019)	0.000021	0.280867	0.000015	1.50	0.280867	0.000074	17

Session 3

Reference	Primary Reference	Expected $^{176}Hf/^{177}Hf$	2SD	$^{176}Hf/^{177}Hf$ (Weighted Mean 95% confidence)	2σ	MSWD	$^{176}Hf/^{177}Hf$ (Arithmetic Mean)	2SD	*n*
Plešovice	Mudtank	0.282482 (Sláma et al., 2008)	0.000013	0.282486	0.000020	0.88	0.282489	0.000058	12
R33	Mudtank	0.282764 (Fisher et al., 2014)	0.000014	0.282763	0.000013	0.95	0.282808	0.000056	16
GJ1	Mudtank	0.282000 (Morel et al., 2008)	0.000025	0.282023	0.000019	0.66	0.282023	0.000065	18
OG1	Mudtank	0.280633 (Kemp et al., 2017)	0.000034	0.280624	0.000015	1.10	0.280691	0.000066	16
FC1	Mudtank	0.282184 (Woodhead & Hergt, 2005)	0.000016	0.282185	0.000018	0.78	0.282184	0.000050	10
Maniitsoq	Mudtank	0.280862 (Marsh et al., 2019)	0.000021	0.280883	0.000015	0.60	0.280882	0.000050	18

*Table 3.3. Summary table of Hf results for zircon secondary reference material. * Weighted Mean 95% confidence. ** Arithmetic Mean*

3.3.4. Trace Element Analysis of Zircon from Rock Samples

A single zircon trace element and U–Pb session was undertaken at the GeoHistory Facility, JdLC. Analyses were performed using an Agilent 8900 quadrupole mass-spectrometer with identical analytical conditions to those described above. U–Pb isotopic ratio calculations followed the data reduction procedure described above.

Grains previously analysed for U–Pb and Lu–Hf measurements, along with newly analysed zircon crystals, were analysed during this session. To constrain the enigmatic Paleoproterozoic detrital cargo, zircon, previously dated to 2300–2000 Ma, were preferentially targeted to characterise their trace element characteristics. Nineteen trace elements were analysed (Ti, Sr, Zr, Nb, La, Ce, Pr, Nd, Sm, Eu, Gd, Dy, Er, Yb, Lu, Hf, Pb, Th and, U), the dwell time for most elements was 0.02 s with Zr measured for 0.01 s.

The primary reference material used for trace element analysis was NIST 610 glass. ^{29}Si was used as the internal reference isotope, assuming a stoichiometric zircon composition of 14.76% Si. The secondary reference materials included NIST 612 glass (Jochum et al., 2005) and GJ1 zircon (Elhlou et al., 2006). The compositional values obtained from the secondary reference materials were typically within 5 – 10% of published values (Jochum et al., 2005). Data reduction was done using the Trace Elements DRS in Iolite v. 4.0 to calculate the trace element concentrations (Paton et al., 2011). Geochemical classification diagrams (Belousova et al., 2002; Grimes et al., 2015) were used to create time-constrained chemical groupings.

3.3.5. U–Pb Analysis of Apatite from Rock Samples

Apatite U–Pb analysis was undertaken at the GeoHistory Facility, JdLC. Analyses were done using the same instrumentation as for zircon U-Pb measurements. Instrumentation included a RESOlution LE193 ArF nm excimer laser ablation system connected to an Agilent 8900 ICPMS and a Laurin Technic S155 cell. Ablations were created using a ~38 µm spot size, a fluence of ~ 3.5 J/cm^{-2}, and a 5 Hz repetition rate. Following two cleaning pulses, each analysis included 30 s of background acquisition and 35 seconds of ablation. Ultra-high purity Ar was used as the plasma gas (flow rate 1 L min^{-1}), and following analyses, the sample cell was flushed using He (350 mL min^{-1}) and N_2 (3.8 mL min^{-1}). Dwell times in seconds are denoted in brackets for measured isotopes and include ^{204}Pb (0.1), ^{206}Pb (0.1), ^{207}Pb (0.1), ^{208}Pb (0.1), ^{232}Th (0.0125) and ^{238}U (0.0125).

The primary reference material used was the Madagascar (MAD2) apatite (475.25 ± 0.41 Ma) (Thompson et al., 2016). Secondary reference material included the Mt. McClure (MMC) apatite [523.51 ± 2.1 Ma; Schoene and Bowring (2006)], FC1 apatite [1099.1 ± 1.2 Ma; Schmitz et al. (2003)] and Durango apatite [31.4 ± 0.2 Ma; McDowell et al. (2005)]. Anchored regression (to reported $^{207}Pb/^{206}Pb_i$ values) through secondary reference material U–Pb data yielded lower intercept ages within 2σ uncertainty of accepted ages. Data reduction was undertaken in Iolite 4 using the VisualAge UcomPbine DRS (Paton et al., 2011), following the methodology of Chew et al. (2014).

3.4. Results

Here, we describe the salient isotopic and geochemical data trends from sand and rock samples of the Woodline Formation (Table 3.1; Figures 3.3–3.5). A description of results on a per-sample basis is provided in Appendix C.

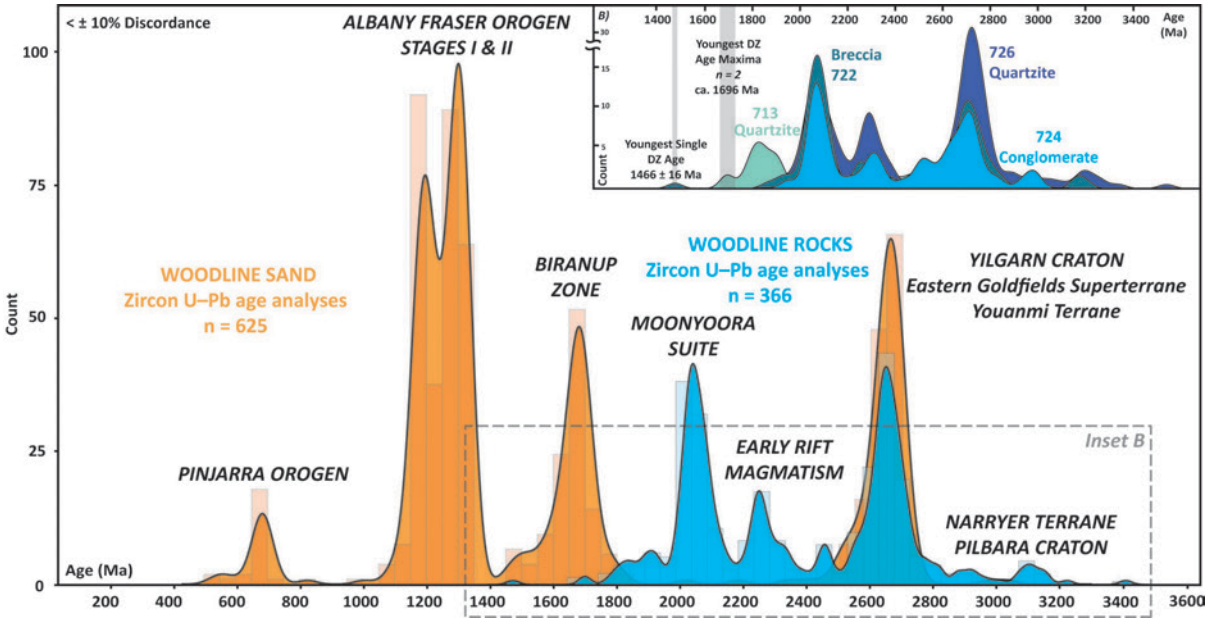

*Figure 3.4. Kernel density estimates of concordant zircon U-Pb ages from sand and rock. Age peaks are annotated with potential sources. Inset **B** shows a kernel density estimate of zircon ages from Woodline Formation rocks only.*

3.4.1. Zircon U–Pb and Lu–Hf

A total of 1042 coupled zircon U–Pb and Lu–Hf analyses were obtained from sand and rock samples across three analytical sessions, of which 835 were concordant (≤ 10% discordance per the relative age difference approach). Only concordant ages are plotted and considered in this work. Session 4 yielded 284 zircon U–Pb and trace element measurements. Ninety-three U–Pb ages (73 were concordant) and trace element analyses were obtained from grains previously dated from earlier sessions. One hundred ninety-one zircon U–Pb ages (of which 152 were concordant) and trace element data were collected from newly analysed grains.

3.4.2. Zircon U–Pb – Lu–Hf from Rock Samples

Concordant zircon U–Pb ages obtained from rock range from ca. 3436 to ca. 1466 Ma. Age peaks (Gehrels, 2011) defined by ≥ 5 or more concordant grains include components at ca. 2791 (*n=6*), 2659 (*n=53*), 2570 (*n=11*), 2346 (*n=10*), 2318 (*n=7*), 2256 (*n=7*), 2079 (*n=22*), 2039 (*n=34*), 1925 (*n=51*) and 1879 Ma (*n=8*) (Figure 3.4).

A single concordant zircon grain with a concordia U–Pb date of 1466 ± 16 Ma provides a maximum depositional age estimate for the Woodline Formation. More conservatively, the youngest detrital age group (≥2 grains from Sample 713) is at ca. 1697 Ma and overlaps with the 1696 Ma date reported by Spaggiari et al. (2014b). ƐHf in zircon grains from rock form a cluster at ca. 2700–2600 Ma (Figure 3.6). This Meso- to Paleoarchean ƐHf record is characterised by scattered supra-chondritic (+6) to sub-chondritic (-7) values.

Other ƐHf components from rock include ten analyses from sample 726 with sub-chondritic (-2 to -6) values at ca. 2250 Ma, along with a minor similar component in samples 722 and 724 (Table 3.1. Another population occurs at ca. 2000 Ma; this sub-chondritic component spans ƐHf -10 to -3 and is dominated by analyses from sample 722. A regression taken between rock zircon Hf analyses between Proterozoic ƐHf populations describes an evolution array equivalent to a $^{176}Lu/^{177}Hf$ ratio of 0.020.

ƐHf in zircon grains from rock form a cluster at ca. 2700–2600 Ma (Figure 3.6). This Meso- to Paleoarchean ƐHf record is characterised by scattered supra-chondritic (+6) to sub-chondritic (-7) values. Other ƐHf components from rock include ten analyses from sample 726 with sub-chondritic (-2 to -6) values at ca. 2250 Ma, along with a minor similar component in samples 722 and 724 (Table 3.1). Another population occurs at ca. 2000 Ma; this sub-chondritic component spans ƐHf -10 to -3 and is dominated by analyses from sample 722. Zircon Hf analyses between Proterozoic ƐHf populations imply an evolution array approximated by a $^{176}Lu/^{177}Hf$ of 0.020.

3.4.3. Zircon U–Pb–Lu–Hf from Sand Samples

Eight sand samples were selected for U–Pb and Lu–Hf analysis to provide an overview of the regolith atop the Woodline Formation (Figure 3.2; Table 3.1). Concordant zircon U–Pb dates obtained for sand span 3030–545 Ma. The detrital zircon age spectra include components at 658 (*n=6*), 676 (*n=10*), 1096 (*n=5*), 1189 (*n=79*), 1291 (*n=102*), 1490 (*n=6*), 1562 (*n=6*), 1592 (*n=10*), 1617 (*n=14*), 1678 (*n=53*), 1760 (*n=5*), 2510 (*n=7*), and 2669 Ma (*n=78*) (Figure 3.4).

ƐHf in zircon grains from sand samples form a cluster at ca. 2700–2600 Ma that overlaps with the ƐHf population from rock (Figure 3.6). This Meso- to Paleoarchean ƐHf for sand samples is also characterised by scattered supra-chondritic (+8) to sub-chondritic (-7) values. The dominance of the 2700 – 2600 age cluster is illustrated on the ƐHf versus age diagram (Figure 3.6). As shown in Figure 3.6 other ƐHf components from sand include ca.

1600, 1300, 1200, and 700 Ma populations. A diffuse cluster of broadly sub-CHUR analyses occur at ca. 1600 Ma, with ƐHf values between -12 and +4. The Mesoproterozoic zircon populations (ca. 1300 Ma and 1200 Ma) correspond to ƐHf values between -12 and +8. The zircon grains at 600 Ma yield ƐHf values between -2 and +4.

3.4.4. Zircon Trace Elements from Rock Samples

One hundred and forty-nine trace element analyses were collected from zircon grains with concordant U–Pb dates from ca. 3436 to 1697 Ma. A diverse range of trace element chemistry was obtained from the samples, consistent with the detrital origin of the zircons from rocks of the Woodline Formation. Most zircon grains exhibit positively sloping chondrite-normalised REE trends (Boynton, 1984) with cerium and europium anomalies (Figure 3.7). Some zircon show a flattening gradient of light REEs to heavy REEs [LREE/HREE, $(La/Sm)_{CN}$] (Figure 3.7), pointing towards the addition of non-stoichiometric elements into metamict zircon grains; these analyses typically yield discordant U–Pb dates. All analysed zircon grains from rock samples (Table 3.1) plot within the continental arc classification field based on their trace element compositions (Figure 3.7) (Grimes et al., 2015). As outlined, zircon from rock of the Woodline Formation with concordia dates between 2500–2100 Ma form a compositionally distinct population compared to other age populations (Figure 3.7).

3.4.5. Apatite U–Pb analysis from Rock Samples

Twenty-three apatite U–Pb analyses define two discrete isochron arrays on a Tera-Wasserburg concordia diagram (Figure 3.5), with the position of the analyses along those arrays reflecting the relative proportion of initial to radiogenic $^{207}Pb/^{206}Pb$ ratios (=F^{207}%). These isochrons are interpreted to reflect the mixing of radiogenic and common Pb components within apatite.

The older population comprises seven measurements from rocks of the Woodline Formation. These analyses range between an upper $^{207}Pb/^{206}Pb_i$ intercept of 0.978 ± 0.028 and a lower intercept yielding an apparent age of 2064 ± 22 Ma [MSWD = 2.2; $p(\chi^2) = 0.0047$]. We interpret this overdispersion about the lower intercept to reflect the variable passage of heterogenous detrital (grain size, presence of fast diffusion pathways) grains through the apatite U–Pb closure temperature of 375 – 600°C (Kirkland et al., 2018). F^{207} % defines the distance along the common-radiogenic mixing array and yields values between = 1.5% – 68.1%.

Sixteen apatite U–Pb analyses from sand define a younger mixing array with an upper $^{207}Pb/^{206}Pb_i$ intercept of 0.904 ± 0.013 and a lower intercept yielding an apparent age of 1284 ± 11 Ma [MSWD = 2.2; $p(\chi^2) = 0.054$, F^{207} % = 7.4% – 85.9%]. A correction for Pb_c based on a terrestrial Pb isotopic evolution model appropriate for the Yilgarn Craton (Zametzer et al., 2022) was used to calculate single-grain apatite U–Pb dates. The model common Pb value was iterated during calculation until the ^{207}Pb-corrected age converged (Figure 3.5) (Kirkland et al., 2018). The apparent ^{207}Pb-corrected age peaks (Gehrels, 2011) calculated via this approach for apatite from sand include 1291 Ma (*n* = 16) and rock 2090 Ma (*n* = *7*) overlap within uncertainty to the regression lower intercept ages (Figure 3.5).

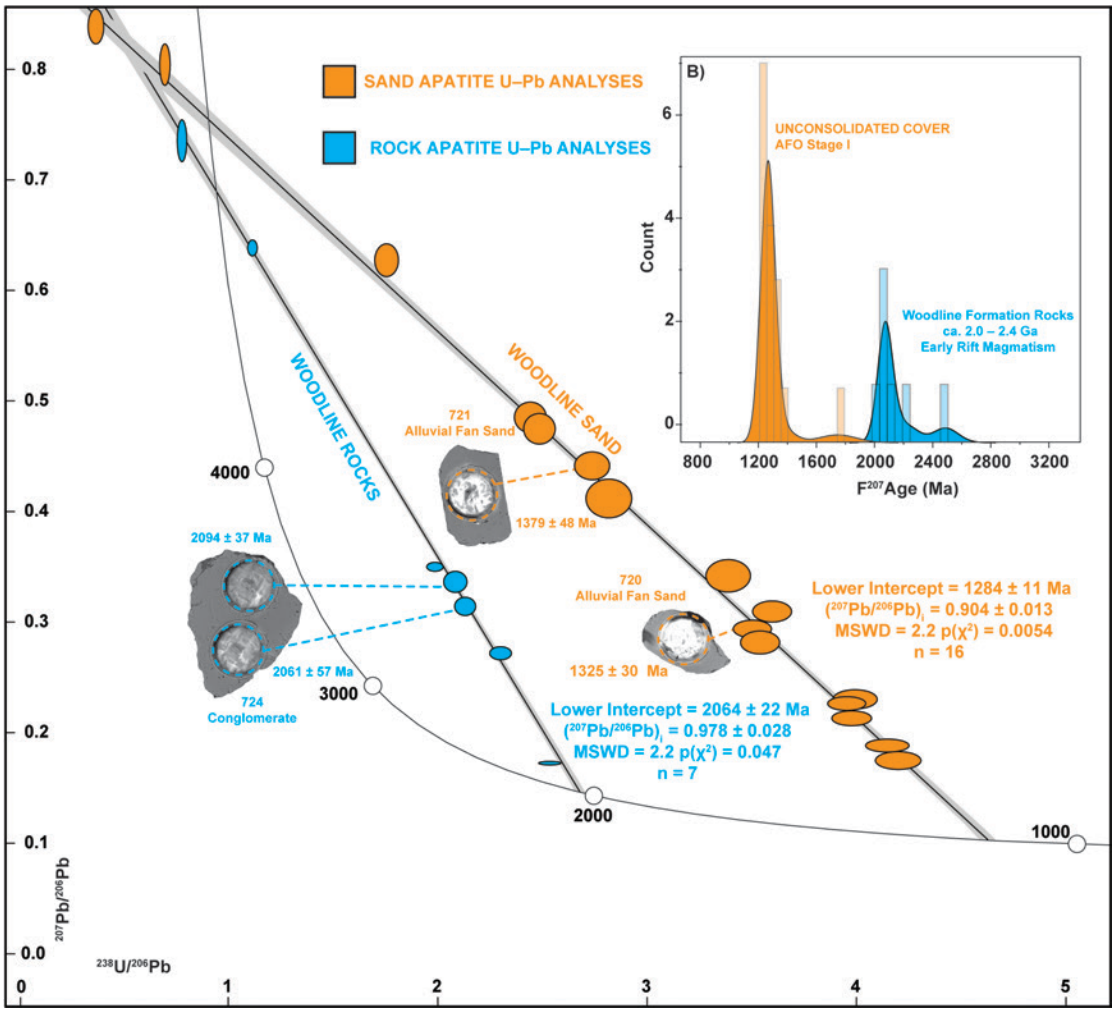

*Figure 3.5. Tera-Wasserburg plot of apatite from the Woodline Formation colour-coded to source, orange from unconsolidated cover and blue for apatite from rock. Inset **B** shows a kernel density estimate of ^{207}Pb corrected apatite ages, showing the bimodal age population of analyses.*

3.5. Discussion

3.5.1. Sand and Rock Record a Shared Archean Provenance

Prior to ca. 2400 Ma, zircon ages and ƐHf data obtained from sand and rocks of the Woodline Formation are broadly congruent, pointing towards a shared detrital source for both, in tandem with the recycling of basement rocks into overlying cover (Figure 3.4). A paleo-flow from the northwest to southeast is recorded in the siliciclastic rocks of the Woodline Formation (Hall et al., 2008), suggesting that infilling detritus was predominantly shed from the denuding Yilgarn Craton during the Proterozoic. Archean zircon grains comprise 32% of dates from sand and rock and yield age peaks at ca. 2662 and 2791 Ma, which can be age correlated with several late granitic suites in the Yilgarn Craton in the adjacent EGST and Youanmi Terranes (Cassidy et al., 2006; Champion and Cassidy, 2007; GSWA, 2024; Mole et al., 2019).

In sand and rock samples, other Archean age peaks, interpreted as reflecting magmatic sources, are identified at 2507 and 2573 Ma. Such 2600–2500 Ma zircon have a less obvious provenance, with no known coeval granitoid suites recognised in the Yilgarn Craton. Nonetheless, the 2520–2505 Ma Tropicana metamorphic event within the Northern Foreland of the AFO on the eastern Yilgarn Craton margin could provide a proximal source for these zircon grains. Furthermore, the Capricorn Orogen includes the 2550–1620 Ma Gascoyne Complex (Jahn et al., 2021; Johnson et al., 2011), which may have shed detrital zircon towards the southeastern margin of the WAC through multicycle pathways (Figure 3.1).

Although less voluminous than the younger ca. 2700–2600 Ma magmatic suites, granitic rocks with crystallisation ages ranging between 3000–2700 Ma are reported for the EGST and Youanmi Terranes (GSWA, 2024). Sources for the Paleoarchean (> 3200 Ma) zircon grains from this study could also include the Narryer Terrane (Kemp et al., 2010; Wang and Wilde, 2018) and less likely far-travelled detritus from the Pilbara Craton (GSWA, 2024; Hickman and Van Kranendonk, 2012), which would necessitate some cryptic multicycle pathway to the Woodline Formation (GSWA, 2024; Hall et al., 2008).

Published zircon Hf data from Yilgarn magmatic rocks span from +10 to -10 ƐHf (GSWA, 2024; Mole et al., 2019). Detrital zircon, in the 2700 – 2600 Ma range, from rocks of the Woodline Formation exhibit a bimodal ƐHf distribution, ranging also from supra-CHUR (+10 ƐHf) to sub-CHUR (-10 ƐHf) (Table 3.1; Figure 3.6). This bimodal Hf distribution is consistent with the compositional diversity exhibited by distinct Yilgarn Craton terranes. Generally, a greater proportion of more radiogenic and mafic magmas characterise the EGST,

whereas the Youanmi Terrane includes relatively more isotopically evolved crust (Champion and Cassidy, 2007; GSWA, 2024; Mole et al., 2019). In contrast to the rock record, the ƐHf values for sand zircon grains do not reveal this bimodality (Figure 3.6), suggesting that input from other WAC components has diluted, better mixed, or otherwise masked this bimodality.

3.5.2. Sand as a Record of West Australian Craton Magmatism and Sediment Flux

The zircon U–Pb ages obtained from sand samples in this study (Figure 3.4) indicate that various sources ultimately supplied detritus to form the Woodline Hills regolith. Dominant detrital sources, as interpreted from equivalent age-isotope signatures, include magmatic rocks that intruded during Stage I and II of the Albany–Fraser Orogeny, Proterozoic Biranup Zone magmatism and the Archean Yilgarn Craton granitic suites (Figure 3.4).

Compared to more distal sources, the immediate proximity of AFO sources such as the Recherche (1345–1260 Ma) and Esperance (1215–1140 Ma) (Spaggiari et al., 2014a) supersuites to the Woodline Formation account for their dominance as age components within sand. Minor detrital components are consistent with the age of zircon from granitic rocks in the 700–500 Ma Pinjarra Orogen, ~700 km away from the western flank of the WAC (Boger, 2011; Markwitz et al., 2017). Pinjarra-sourced detritus is widespread throughout unconsolidated material and Phanerozoic sedimentary rocks in the WAC (Clarke et al., 2023; Dröllner et al., 2022; Zutterkirch et al., 2021).

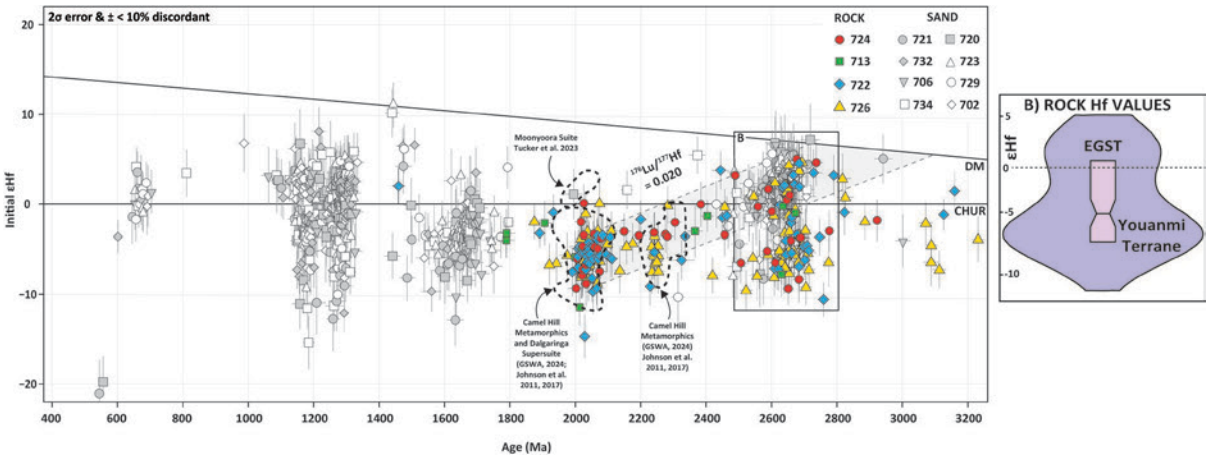

Figure 3.6. ***(A)*** *εHf versus age (Ma) plot for zircon from the Woodline Formation.* ***(B)*** *A box and violin plot of Yilgarn Craton-aged zircon (2800–2500 Ma) from the Woodline Formation rock samples. The plot shows a bimodal εHf value distribution with peaks at +1 and -7. Probable sources for more and less radiogenic zircon grains are highlighted. EGST = Eastern Goldfields Superterrane.*

Other Neoproterozoic sources include detrital zircon grains in the Canning Basin (Haines et al., 2013; Martin et al., 2019) and metamorphic zircon from the Musgrave Province in central Australia (Howard et al., 2015; Kirkland et al., 2013). Modern-day beach sands along the southern coast of Western Australia contain abundant Neoproterozoic to Palaeozoic zircon grains (Dröllner et al., 2022). Prolonged marine transport eastwards combined with continental-scale glacial-fluvial systems originating from the south during the late Palaeozoic (Morón et al., 2019) represent plausible mechanisms to relocate detritus laterally along the peripheries of the WAC and to the Woodline Hills (Figure 3.1).

Apatite U–Pb analyses from unconsolidated material in this study yielded a lower intercept date of 1284 ± 11 Ma (Figure 3.5), which overlaps with the age of Stage I of the AFO (ca. 1345–1260 Ma) (Clark et al., 2014; Clark et al., 2000; Spaggiari et al., 2015). Stage I involved coeval felsic and mafic magmatism (Recherche Supersuite), high-temperature and moderate-pressure metamorphism (Clark et al., 2000; Spaggiari et al., 2014a). The Woodline Formation is proximal to the Fraser Zone, which preserves Stage I zircon U–Pb ages but has a dearth of significant evidence for Stage II tectonism (Kirkland et al., 2016). Therefore, the 1284 ± 11 Ma detrital apatite U–Pb age obtained from the Woodline sand in this study are interpreted to be derived from granulite-facies metamorphic rocks and granitic rocks in the Fraser Zone and eastern Nornalup Zones (Clark et al., 2014; Kirkland et al., 2011).

Figure 3.4 shows that the U–Pb zircon and apatite detrital age spectra from the Woodline Hills basement rocks and the age spectra from the sand that overlays these rocks are disparate. Primarily, zircon and apatite grains aged 2400–1800 Ma are conspicuously absent from the cover sequence that spans 50 km, parallel to the Woodline Hills (Figure 3.3). This observation is also made north of the Woodline Hills (Figure 3.2), where sand samples overlying granite-greenstone successions in the EGST also lack Paleoproterozoic detrital age components. This discrepancy implies that the cover along the southeastern margin of the WAC is entirely transported from a region lacking exposed Paleoproterozoic detritus and that denudation of the Woodline Formation, which itself contains Paleoproterozoic detritus, is minimal.

The Woodline Hills are low-lying, highly vegetated hills in a semi-arid region with low erosion rates, limiting sediment release into the regolith (Gonzalez-Alvarez et al., 2014). However, our data are inconsistent with previous work in the nearby Symons Hill prospect, which concluded that localised areas of regolith along the AFO–WAC margin formed due to

recycling residual weathering profiles (Gonzalez-Alvarez et al., 2019). Such areas of localised reworking are assumed to represent paleo-topographic highs during marine inundations and associated regolith development in the Cenozoic (Gonzalez-Alvarez et al., 2019). *In-situ* weathering of exposed bedrock is the principal mechanism by which regolith forms within inland areas of the WAC, such as the Woodline Hills (Anand and Butt, 2010). However, the new results presented here demonstrate that the unconsolidated material in a broad northeast trending zone parallel (Figure 3.1 to the AFO–WAC margin did not form *in-situ* but instead represents the whole-scale replacement of cover along the southeastern margin of the WAC. The absence of Paleoproterozoic detritus in the east and southern WAC is, therefore, ubiquitous, from Quaternary sand dunes to weakly consolidated duricrust collected from the edges of salt lakes (Figure 3.2; Table 3.1).

Cover thickness in the southeast WAC increases towards the Cenozoic Eucla and Cretaceous to Paleogene Bight Basins (Figure 3.1) (Gartmair et al., 2022; Salama et al., 2016). Prolonged erosion during the humid and tropical Cretaceous in Australia (Anand and Butt, 2010) was followed by the replacement of cover via aeolian detritus derived from the Yilgarn Craton during the transition to the semi-arid climate of the Pliocene to present (Anand and Butt, 2010; Gonzalez-Alvarez et al., 2014). Detrital zircon and apatite from sand at the Yilgarn-AFO margin suggest that the cover sequence was transported from the northwest to the southeast. The Eucla and Bight Basins represent the ultimate sink for cover containing ca. 2 Ga grains. Although a minor component of the reported detrital zircon age spectra, Paleoproterozoic grains (2400–1800 Ma) occur within basins southeast of the Woodline Formation as recognised from drill core and surface outcrop samples (Gartmair et al., 2022; Reid et al., 2013).

3.5.3. West Australian Craton Paleoproterozoic Magmatism

From rocks of the Woodline Formation, Hall et al. (2008) reported detrital zircon age peaks at ca. 2245, 2034, and 1886 Ma. The oldest Proterozoic rocks identified in the AFO are the ca. 2030 Ma, an A-type rift-related granitoids termed the Moonyoora Suite, interpreted to mark the inception of rifting along the southeast margin of the Yilgarn Craton (Tucker et al., 2023). Although the Moonyoora Suite is a plausible source for ca. 2030–2010 Ma detritus in the Woodline Formation, other age maxima in the detrital zircon spectra are not readily accounted for by known magmatism in the WAC. Fifty-one zircon U–Pb analyses from Woodline Formation rocks define an age component at ca. 2039 Ma (Figure 3.4), which is coeval with the Moonyoora Suite. This ca. 2039 Ma age component is consistent with a ca.

2034 Ma detrital zircon age peak identified previously in the Woodline Formation by Hall et al. (2008).

Although coeval with the Moonyoora Suite, the ca. 2039 Ma population from the Woodline is isotopically distinct, forming a sub-chondritic cluster (ƐHf = -2 to -6) (Figure 3.6). In contrast, the Moonyoora Suite is characterised by a tightly clustered group of supra-chondritic analyses with ƐHf values between 0 – +5 (Figure 3.7) (Tucker et al., 2023). One possibility for this isotopic discrepancy is that ca. 2039 Ma detritus from the Woodline Formation represents a more isotopically evolved expression of Moonyoora Suite magmatism in the AFO. Northwest of the Woodline Formation, the Moonyoora Suite sits on a transport pathway that infilling Yilgarn Craton detritus may have been shed along. However, as Hall et al. (2008) noted, detrital zircon age components of the pre-1830 Ma Camel Hill Metamorphics of the Gascoyne Province, Capricorn Orogen are coeval with the ca. 2030 and 2245 Ma age peaks identified for the Woodline Formation (Figure 3.4). Our study shows that this similarity now extends to hafnium isotopic signatures, as the ƐHf values from zircon within the Camel Hill metamorphic also overlap the ƐHf values of ca. 2039 Ma and 2250 Ma zircon from the Woodline Formation (Figure 3.6).

Intriguingly, whilst the source of ca. 2000 Ma detrital zircon within the Camel Hill and metamorphics is well-constrained to a magmatic origin from the adjacent Dalgaringa Supersuite, the provenance of 2300–2100 Ma detrital zircon from the Gascoyne Province is less apparent (Johnson et al., 2017; Johnson et al., 2011). Much like the Woodline Formation, the source of 2300–2175 Ma zircon within the Camel Hill metamorphics is unclear as no rocks are dated to that age within the Gascoyne Province nor WAC (GSWA, 2024; Johnson et al., 2011). Thus, within metasedimentary rocks, on both margins of the Yilgarn Craton Paleoproterozoic zircon has a cryptic provenance (Figure 3.1).

Apatite U–Pb analyses from the Woodline Formation yield a lower intercept date of 2062 ± 22 Ma, within uncertainty of the zircon ca. 2039 Ma component. Compared to zircon, apatite is more labile and less likely to survive prolonged chemical weathering (Clarke et al., 2023; Gillespie et al., 2018; O'Sullivan et al., 2020). Apatite, therefore, points towards a proximal magmatic source for the ca. 2030 Ma component during the deposition of the Woodline Formation. Due to overlapping age and Hf-isotopic signatures, we interpret the Woodline Formation and Camel Hill Metamorphics, on adjoining sides of the Yilgarn Craton,

to contain 2300–2100 Ma detrital zircon sourced from the same magmatic source proximal to the AFO (Figure 3.1).

The Paleoproterozoic zircon (2300–2000 Ma) from Woodline Formation rocks exhibit distinct trace element chemistry groupings (Figure 3.7C, D, E). For instance, all zircons are classified within the continental arc field of Grimes et al. (2015). Such grouping helps demonstrate that Paleoproterozoic zircon is endemic to the Yilgarn rather than an exotic source with oceanic affinity, as expected from the adjacent Madura and Coompana Provinces (Kirkland et al., 2011; Kirkland et al., 2015b) (Figure 3.7). In addition, some 2300–2100 Ma age zircons show chemical signatures that correlate with a lower SiO_2, primitive source (Figure 3.7). Chondrite-normalised REE plots for the 2400 – 2000 Ma zircon show pronounced europium anomalies (Figure 3.7); such signatures are consistent with lower SiO_2 (Belousova et al., 2002). However, Eu behaviour within granitoid systems is complex and also sensitive to magmatic fO_2 conditions, depth of crystallisation and the associated pressure-temperature conditions, which influence plagioclase stability and the solubility of Eu in the melt. (Belousova et al., 2002). Nonetheless, shallower, water-poor magmas, A-type granites—characterised by high Fe/Mg and elevated HFSE (e.g., Nb, Y, and Zr)—tend to form under low fO_2 conditions (Wang et al., 2012). Although previous interpretations have linked Eu/Eu* anomalies to silica content and style of magmatism, the Eu anomaly alone does not unambiguously signify low SiO_2 or A-type magmatism.

Much like the Moonyoora Suite, which is a felsic A-type granitoid package (Tucker et al., 2023), ca. 2250 Ma zircons have signatures that point towards derivation from A-type granitoids (Figure 3.7) (Breiter et al., 2014). Taken together, distinct chemical signatures for 2500 – 2000 Ma zircons suggest derivation from lower Si, A-type granitoid sources consistent with extensional rift tectonics (Condie et al., 2023).

A crustal evolution curve with a $^{176}Lu/^{177}Hf$ ratio of 0.020 best describes the relationship between ƐHf populations for detrital zircon between 2500–2000 Ma (Figure 3.6). This elevated Lu/Hf ratio is consistent with the isotopic evolution of primitive lower SiO_2 crust (Mulder et al., 2021; Zeh et al., 2014). The input of more radiogenic, juvenile material at ca. 2250 and 2030 Ma into pre-existing Yilgarn Crust appears minimal as both populations are sub-chondritic, indicative of reworked crust. These zircon appear to fall on a crustal evolution curve with a Lu/Hf ratio of 0.020 extending through an older zircon population (2800–2500 Ma) in the same samples. The fitted evolution array points back to an isotopic reservoir

indistinguishable from the Yilgarn Craton (EGST) at 2500–2000 Ma. Therefore, these older zircon are age and isotope equivalents to zircon from Yilgarn Craton magmatic rocks. Thus, as with extensional magmatism in the Proterozoic Biranup Zone and later stages of the AFO (Kirkland et al., 2011; Morrissey et al., 2017), the autochthonous reworking of the Archean Yilgarn Craton characterised early 2100–2300 Ma magmatism recognised from detrital grains within the Woodline Formation.

The mafic, rift-related signatures for ca. 2245 Ma detritus from the Woodline Formation also complement ca. 2250 Ma detrital zircon, with ultramafic trace element characteristics obtained from an ephemeral stream draining the Gascoyne Province (Griffin et al., 2004). More direct evidence for mafic-ultramafic rift-magmatism at ca. 2250 Ma within the Yilgarn Craton is restricted to the Barren Basin and Camel Hill Metamorphics. However, as with the case for the Moonyoora Suite, we posit that the ultimate source for ca. 2250 Ma detritus, now disseminated across the Yilgarn Craton, likely remains obscured by Phanerozoic Basins of the Yilgarn Craton.

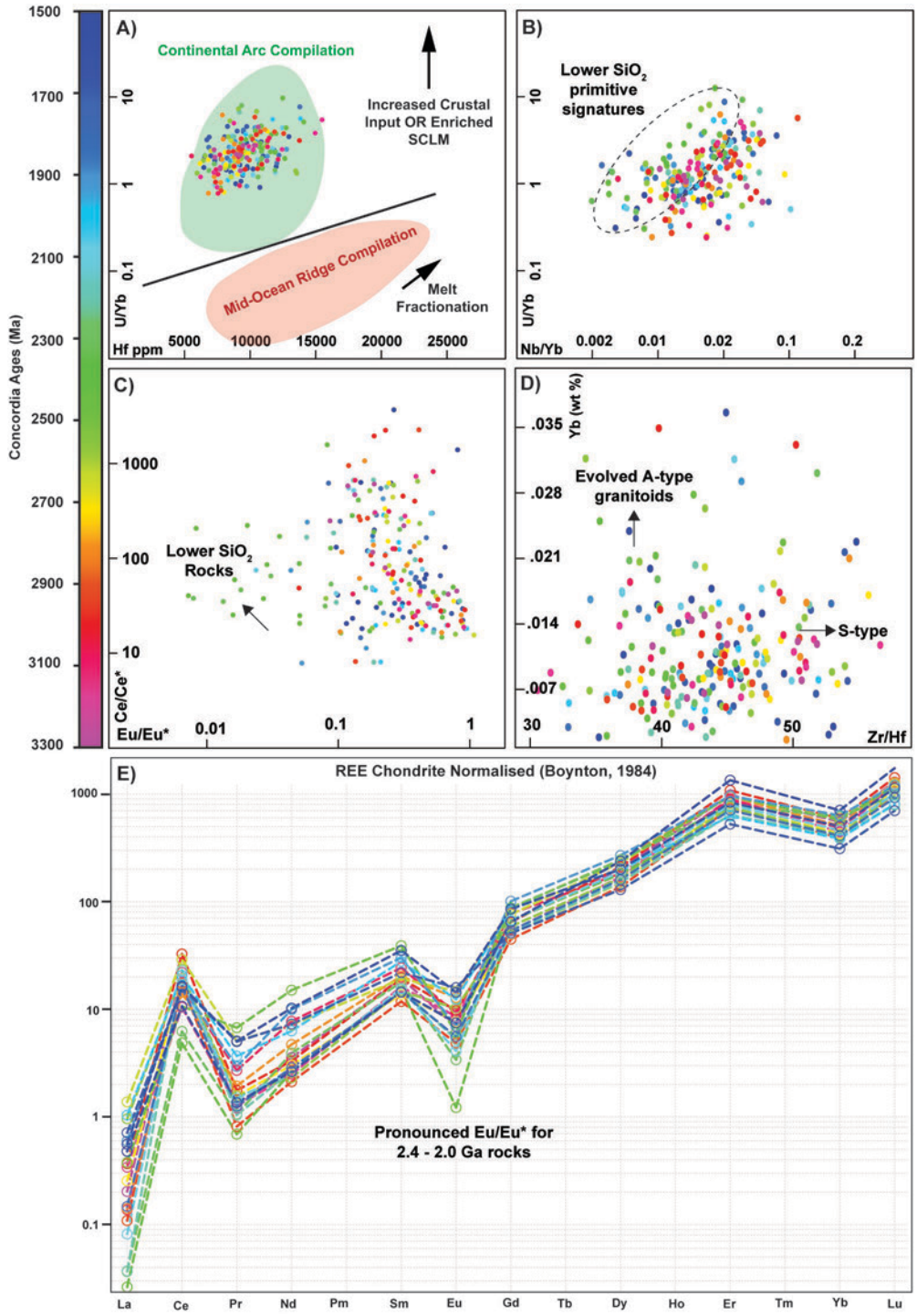

Figure 3.7. Chemical classification plots for concordant detrital zircon from rocks of the Woodline Formation, colour-coded by concordia age. ***A)*** *U/Yb vs Hf plot showing continental and mid-ocean ridge classification fields after Grimes et al. (2015).* ***B)*** *U/Yb vs Nb/Yb plot of zircon. The dashed field is a Mehalanobis distance ellipse (P=0.5) for 2.4——2.0 Ga zircon, highlighting consistent trace element grouping across different classification plots.* ***C)*** *Europium vs Cerium anomaly, showing the vector for mafic zircon classification after Belousova et al. (2002).* ***D)*** *Yb (wt %) versus Zr/Hf classification plot for granitoids adapted after Breiter et al. (2014). The arrows show the fractionation trend lines of typical granitoid types from Breiter et al. (2014).* ***E)*** *Chondrite-normalised (Boynton, 1984) zircon multi-element plot. Median values for colour-coded age groupings are shown and are consistent across plots.*

3.5.4. A Time-Constrained Supply of Paleoproterozoic Detritus?

The Barren Basin is today preserved as a series of sub-basins, such as the Woodline Formation (Figure 3.1), but it is interpreted to have once extended 1000 km along the southeastern margin of the WAC (Spaggiari et al., 2014b). Paleo-flow structures within the Woodline Formation show longshore drift towards the southwest (Hall et al., 2008); such a mechanism might have facilitated the distribution of Paleoproterozoic detritus throughout the Barren Basin (Figure 3.8).

There is a conspicuous absence of 2400–1900 Ma detrital zircon from metasedimentary units in the ca. 1600 Ma Arid Basin (Spaggiari et al., 2014b). Such a dearth of 2400–1900 Ma zircon from the Arid Basin points towards a discrete period in which Paleoproterozoic rocks were exposed and shedding detritus during the Proterozoic into basins. The lack of ca. 2 Ga detritus in Phanerozoic sedimentary rocks of the WAC (GSWA, 2024) suggests that this record of early Paleoproterozoic magmatism has not been accessed since the inception of the Arid Basin.

The extent and scale of sedimentary basins flanking the southeast WAC necessitate a crustal-scale mechanism to account for the distribution of Paleoproterozoic detritus in the Barren versus Arid Basin. The lithologies of the Barren and Arid Basins are markedly different; the former contains mature siliciclastic rocks, and the latter contains immature and heterogeneous infill (Spaggiari et al., 2014b). Both basins reflect a shift in the tectonic regime of the AFO from passive extension along a cratonic margin to convergence and oceanic-arc magmatism (Spaggiari et al., 2014b). Paleoproterozoic rifting to form the Biranup Zone and Barren Basin (ca. 1810-–1650 Ma) was likely associated with the development of a horst and graben rift architecture along the southeast margin of the WAC (Figure 3.8) (Kirkland et al., 2011; Spaggiari et al., 2014a). In this scenario, Paleoproterozoic detritus would have travelled unimpeded from the exposed Yilgarn Craton toward the Barren Basin. This sediment flux may have continued for up to ca. 300 Myr across the entire depositional lifespan of the Woodline Formation (Figure 3.8). Basement highs dictated the distribution of AFO basins (Spaggiari et al., 2014b; Spaggiari et al., 2015).

A shift to a compressional regime after ca. 1400 Ma resulted in Stage I of the Albany-Fraser Orogeny, which involved Recherche Supersuite magmas intruding into the reworked Yilgarn margin (Kirkland et al., 2011; Spaggiari et al., 2015) (Figure 3.8). We posit that reactivation of normal faults into reverse faults sufficiently modified the basin architecture

would have starved the Arid Basin of Yilgarn Craton detritus by creating a series of basement highs (Figure 3.8C). Such a process likely acted in tandem with the source of Paleoproterozoic becoming concealed or destroyed during compressional tectonics.

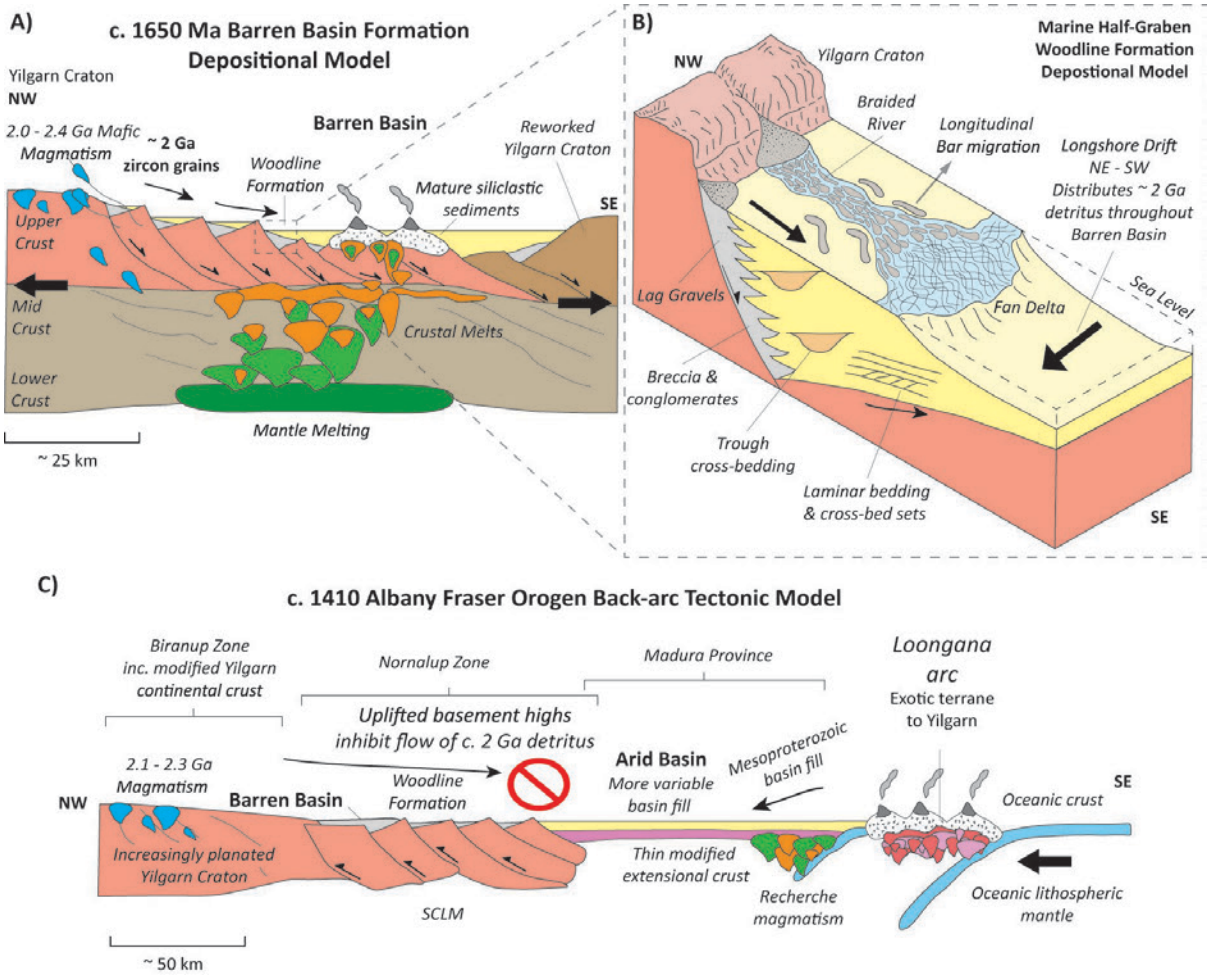

Figure 3.8. Tectonic evolution of the southeastern margin of the Yilgarn Craton throughout the Proterozoic, adapted after Spaggiari et al. (2015) and Morrissey et al. (2017). ***A)*** *Development of a horst and graben rift architecture during rifting. 2400 – 2000 Ma and Yilgarn detritus flowed from the then denuding craton towards the Barren Basin.* ***B)*** *A half-graben model of the Woodline Formation at ca. 1650 Ma.* ***C)*** *A back-arc tectonic model at ca. 1410 Ma whereby compression reactivated grabens, uplifted basement highs, and inhibited the flux of Yilgarn detritus to the Arid Basin.*

3.6. Conclusions

Here, U–Pb zircon-apatite geochronology, isotopic (Lu–Hf) signatures, and zircon trace element data offer insights into the earliest expressions of rifting along the southeast margin of the Yilgarn Craton during the Paleoproterozoic. Time-constrained detrital zircon geochemistry for 2500–2000 Ma grains show a continental crust affinity and derivation from lower SiO_2, unevolved A-type granitoid lithologies, which represent the earliest evidence for rifting along the southeastern margin of the Yilgarn Craton. The discovery of the Moonyoora Suite by Tucker et al. (2023) necessitated a revised inception of rifting along the southeast margin of the Yilgarn Craton by 200 Ma to ca. 2030 Ma; our data demonstrate that rifting had already commenced by at least ca. 2250 Ma, consistent with the geochemistry of the zircon implying an A-type granitoid source.

We present a model whereby an uplifted fault block inhibited the supply of Paleoproterozoic zircons to the Arid Basin (Figure 3.8). This process likely acted in tandem with early rift melts intruding out during subsequent Biranup magmatism. We also demonstrate the contrasting age-maxima of zircon and apatite obtained from unconsolidated material versus underlying geology within the Woodline Hills area along the southwest margin of the Yilgarn. This disparity offers a cautionary note to ongoing exploration efforts within this highly prospective corridor of the AFO – the regolith in this area does not represent underlying geology.

3.7. Acknowledgments

This research was funded by an Australian Research Council Discovery Project (DP200101881). Bradley McDonald and Noreen Evans are thanked for their technical expertise during LA-ICP-MS analysis. The authors thank the Geological Survey of Western Australia for their support during the fieldwork. RQdG publishes with the permission of the executive director of the GSWA. AC acknowledges helpful discussions with H. Olierook. We thank three anonymous referees for helpful comments that improved this contribution.

3.8. Data Availability

Isotopic (U–Pb, Lu–Hf) and trace element data for zircon and apatite (U–Pb) are available online as Supplementary data 2 – 4 via *DOI: 10.1016/j.precamres.2024.107602*.

3.9. References

Adams, M., 2012. Structural and geochronological evolution of the Malcolm Gneiss, Nornalup Zone, Albany-Fraser Orogen, Western Australia. Geological Survey of Western Australia.

Anand, R.R., Butt, C.R.M., 2010. A guide for mineral exploration through the regolith in the Yilgarn Craton, Western Australia. Australian Journal of Earth Sciences 57, 1015-1114.

Barham, M., Kirkland, C.L., Handoko, A.D., 2022. Understanding ancient tectonic settings through detrital zircon analysis. Earth and Planetary Science Letters 583, 117425.

Belousova, E., Griffin, W., O'Reilly, S.Y., Fisher, N., 2002. Igneous zircon: trace element composition as an indicator of source rock type. Contributions to Mineralogy and Petrology 143, 602-622.

Bhattacharya, G., Robinson, D.M., Wielicki, M.M., 2020. Detrital zircon provenance of the Indus Group, Ladakh, NW India: Implications for the timing of the India-Asia collision and other syn-orogenic processes. GSA Bulletin 133, 1007-1020.

Boger, S.D., 2011. Antarctica — Before and after Gondwana. Gondwana Research 19, 335-371.

Bouvier, A., Vervoort, J.D., Patchett, P.J., 2008. The Lu–Hf and Sm–Nd isotopic composition of CHUR: Constraints from unequilibrated chondrites and implications for the bulk composition of terrestrial planets. Earth and Planetary Science Letters 273, 48-57.

Boynton, W.V., 1984. Chapter 3 - Cosmochemistry of the Rare Earth Elements: Meteorite Studies, in: Henderson, P. (Ed.), Developments in Geochemistry. Elsevier, pp. 63-114.

Cassidy, K., Champion, D., Krapez, B., Barley, M., Brown, S.J.A., Blewett, R., Groenewald, B., Tyler, I., 2006. Cassidy, K.F., Champion, D.C., Krapez, B., Barley, M.E., Brown, S.J.A., Blewett, R.S., Groenewald, P.B. & Tyler, I.M., 2006, A revised geological framework for the Yilgarn Craton: Western Australia Geological Survey, Record 2006/8.

Breiter, K., Lamarão, C.N., Borges, R.M.K., Dall'Agnol, R., 2014. Chemical characteristics of zircon from A-type granites and comparison to zircon of S-type granites. Lithos 192-195, 208-225.

Cassidy, K.F., Champion, D.C., McNaughton, N., Fletcher, I., Whitaker, A.J., Bastrakova, I.V., Budd, A.R., 2002. Characterisation and Metallogenic Significance of Archaean Granitoids of the Yilgarn Craton, Western Australia: Results of Research Carried Out as MERlWA Project No. M281 at the Key Centre for Strategic Mineral Deposits, the

University of Western Australia and Australian Geological Survey Organisation. Minerals and Energy Research Institute of Western Australia.

Cawood, P.A., Hawkesworth, C.J., Dhuime, B., 2012. Detrital zircon record and tectonic setting. Geology 40, 875-878.

Cawood, P.A., Hawkesworth, C.J., Dhuime, B., 2013. The continental record and the generation of continental crust. GSA Bulletin 125, 14-32.

Champion, D., Cassidy, K., 2007. An overview of the Yilgarn craton and its crustal evolution, in Bierlein, F.P., and Knox-Robinson, C.M., eds., Proceedings of Geoconferences (WA) Inc., Kalgoorlie '07 Conference. Geoscience Australia Record 2007, 8-12.

Chandra, R., Cripps, S., Butterworth, N., Muller, R.D., 2021. Precipitation reconstruction from climate-sensitive lithologies using Bayesian machine learning. Environmental Modelling & Software 139, 105002.

Chew, D., O'Sullivan, G., Caracciolo, L., Mark, C., Tyrrell, S., 2020. Sourcing the sand: Accessory mineral fertility, analytical and other biases in detrital U-Pb provenance analysis. Earth-Science Reviews 202, 103093.

Chew, D.M., Petrus, J.A., Kamber, B.S., 2014. U–Pb LA–ICPMS dating using accessory mineral standards with variable common Pb. Chemical Geology 363, 185-199.

Choi, E., Fiorentini, M.L., Giuliani, A., Foley, S.F., Maas, R., Graham, S., 2021. Petrogenesis of Proterozoic alkaline ultramafic rocks in the Yilgarn Craton, Western Australia. Gondwana Research 93, 197-217.

Chu, N.C., Taylor, R.N., Chavagnac, V., Nesbitt, R.W., Boella, R.M., Milton, J.A., German, C.R., Bayon, G., Burton, K., 2002. Hf isotope ratio analysis using multi-collector inductively coupled plasma mass spectrometry: an evaluation of isobaric interference corrections. Journal of Analytical Atomic Spectrometry 17, 1567-1574.

Clark, C., Kirkland, C.L., Spaggiari, C.V., Oorschot, C., Wingate, M.T., Taylor, R.J., 2014. Proterozoic granulite formation driven by mafic magmatism: An example from the Fraser Range Metamorphics, Western Australia. Precambrian Research 240, 1-21.

Clark, D.J., Hensen, B.J., Kinny, P.D., 2000. Geochronological constraints for a two-stage history of the Albany–Fraser Orogen, Western Australia. Precambrian Research 102, 155-183.

Clarke, A.J.I., Kirkland, C.L., Glorie, S., Gillespie, J., Kinny, P.D., 2023. The unroofing of Archean crustal domes as recorded by detrital zircon and apatite. Precambrian Research 395, 107132.

Condie, K.C., Pisarevsky, S.A., Puetz, S.J., Roberts, N.M.W., Spencer, C.J., 2023. A-type granites in space and time: Relationship to the supercontinent cycle and mantle events. Earth and Planetary Science Letters 610, 118125.

Dawson, G.C., Krapež, B., Fletcher, I.R., McNaughton, N.J., Rasmussen, B., 2002. Did late Palaeoproterozoic assembly of proto-Australia involve collision between the Pilbara, Yilgarn and Gawler cratons? Geochronological evidence from the Mount Barren Group in the Albany–Fraser Orogen of Western Australia. Precambrian Research 118, 195-220.

Dhuime, B., Hawkesworth, C.J., Delavault, H., Cawood, P.A., 2017. Continental growth seen through the sedimentary record. Sedimentary Geology 357, 16-32.

Dröllner, M., Barham, M., Kirkland, C.L., 2023. Reorganisation of continent-scale sediment routing based on detrital zircon and rutile multi-proxy analysis. Basin Research 35, 363-386.

Dröllner, M., Kirkland, C.L., Barham, M., Evans, N.J., McDonald, B.J., 2022. A persistent Hadean–Eoarchean protocrust in the western Yilgarn Craton, Western Australia. Terra Nova n/a.

Dumitru, T.A., 2016. A New Zircon Concentrating Table Designed for Geochronologists, American Geophysical Union. AGU Fall Meeting Abstracts, San Francisco, pp. 23-2956.

Elhlou, S., Belousova, E., Griffin, W.L., Pearson, N.J., O'Reilly, S.Y., 2006. Trace element and isotopic composition of GJ-red zircon standard by laser ablation. Geochimica et Cosmochimica Acta 70, A158.

Fiorentini, M.L., O'Neill, C., Giuliani, A., Choi, E., Maas, R., Pirajno, F., Foley, S., 2020. Bushveld superplume drove Proterozoic magmatism and metallogenesis in Australia. Scientific Reports 10, 1-10.

Fisher, C.M., Vervoort, J.D., DuFrane, S.A., 2014. Accurate Hf isotope determinations of complex zircons using the "laser ablation split stream" method. Geochemistry, Geophysics, Geosystems 15, 121-139.

Gartmair, G., Barham, M., Kirkland, C.L., 2022. Detrital Zircon Perspectives on Heavy Mineral Sand Systems, Eucla Basin, Australia. Economic Geology 117, 383-399.

Gehrels, G., 2011. Detrital zircon U-Pb geochronology: Current methods and new opportunities. Tectonics of sedimentary basins: Recent advances, 45-62.

Gehrels, G., Kapp, P., DeCelles, P., Pullen, A., Blakey, R., Weislogel, A., Ding, L., Guynn, J., Martin, A., McQuarrie, N., Yin, A., 2011. Detrital zircon geochronology of pre-Tertiary strata in the Tibetan-Himalayan orogen. Tectonics 30.

Gillespie, J., Glorie, S., Khudoley, A., Collins, A.S., 2018. Detrital apatite U-Pb and trace element analysis as a provenance tool: Insights from the Yenisey Ridge (Siberia). Lithos 314-315, 140-155.

Gillespie, J., Kirkland, C.L., Kinny, P.D., Simpson, A., Glorie, S., Rankenburg, K., 2022. Lu–Hf, Sm–Nd, and U–Pb isotopic coupling and decoupling in apatite. Geochimica et Cosmochimica Acta 338, 121-135.

Glorie, S., Hand, M., Mulder, J., Simpson, A., Emo Robert, B., Kamber, B., Fernie, N., Nixon, A., Gilbert, S., 2024. Robust laser ablation Lu–Hf dating of apatite: an empirical evaluation. Geological Society, London, Special Publications 537, SP537-2022-2205.

Glorie, S., March, S., Nixon, A., Meeuws, F., O'Sullivan, G.J., Chew, D.M., Kirkland, C.L., Konopelko, D., De Grave, J., 2020. Apatite U–Pb dating and geochemistry of the Kyrgyz South Tian Shan (Central Asia): Establishing an apatite fingerprint for provenance studies. Geoscience Frontiers 11, 2003-2015.

Gonzalez-Alvarez, I., Anand, R.R., Hough, R., Salama, W., Laukamp, C., Sweetapple, M., Ley-Cooper, A., Sonntag, I., Lintern, M., Ibrahimi, T., Legras, M., Walshe, J., 2014. Greenfields geochemical exploration in a regolith dominated terrain: the Albany-Fraser Orogen/Yilgarn Craton margin YILGARN CRATON MARGIN.

Gonzalez-Alvarez, I., Salama, W., Ibrahimi, T., leGras, M., 2019. Insights on landscape geochemistry and mineral exploration in the Fraser Range, Albany-Fraser Orogen, Western Australia. ASEG Extended Abstracts 2019, 1-6.

Griffin, W., Pearson, N., Belousova, E., Jackson, S.v., Van Achterbergh, E., O'Reilly, S.Y., Shee, S., 2000. The Hf isotope composition of cratonic mantle: LAM-MC-ICPMS analysis of zircon megacrysts in kimberlites. Geochimica et cosmochimica acta 64, 133-147.

Griffin, W.L., Belousova, E.A., Shee, S.R., Pearson, N.J., O'Reilly, S.Y., 2004. Archean crustal evolution in the northern Yilgarn Craton: U–Pb and Hf-isotope evidence from detrital zircons. Precambrian Research 131, 231-282.

Grimes, C.B., Wooden, J.L., Cheadle, M.J., John, B.E., 2015. "Fingerprinting" tectono-magmatic provenance using trace elements in igneous zircon. Contributions to Mineralogy and Petrology 170, 46.

GSWA, 2024. Compilation of WAROX data : [Western Australia] / Government of Western Australia, Geological Survey of Western Australia, in: Peng, J., White, S.R. (Eds.). Geological Survey of Western Australia, East Perth, Western Australia.

Haines, P.W., Wingate, M., Kirkland, C.L., 2013. Detrital Zircon U–Pb Ages from the Paleozoic of the Canning and Officer Basins, Western Australia: Implications for Provenance and Interbasin Connections.

Hall, C.E., Jones, S.A., Bodorkos, S., 2008. Sedimentology, structure and SHRIMP zircon provenance of the Woodline Formation, Western Australia: Implications for the tectonic setting of the West Australian Craton during the Paleoproterozoic. Precambrian Research 162, 577-598.

Hartnady, M.I.H., Kirkland, C.L., Martin, L., Clark, C., Smithies, R.H., Spaggiari, C.V., 2019. Zircon oxygen and hafnium isotope decoupling during regional metamorphism: implications for the generation of low $\delta^{18}O$ magmas. Contributions to Mineralogy and Petrology 175, 9.

Hawkesworth, C., Cawood, P., Kemp, T., Storey, C., Dhuime, B., 2009. A Matter of Preservation. Science 323, 49-50.

Hickman, A.H., Van Kranendonk, M.J., 2012. Early Earth evolution: Evidence from the 3.5-1.8 Ga geological history of the Pilbara region of Western Australia. Episodes 35, 283-297.

Howard, H.M., Smithies, R.H., Kirkland, C.L., Kelsey, D.E., Aitken, A., Wingate, M.T.D., Quentin de Gromard, R., Spaggiari, C.V., Maier, W.D., 2015. The burning heart — The Proterozoic geology and geological evolution of the west Musgrave Region, central Australia. Gondwana Research 27, 64-94.

Jackson, S.E., Pearson, N.J., Griffin, W.L., Belousova, E.A., 2004. The application of laser ablation-inductively coupled plasma-mass spectrometry to in situ U–Pb zircon geochronology. Chemical Geology 211, 47-69.

Jahn, I., Clark, C., Reddy, S., Taylor, R.J.M., 2021. Zircon U–Pb Geochronology and Hf–O Isotope Characteristics of Granitoids from the Capricorn Orogen, Western Australia. Journal of Petrology 62.

Jochum, K.P., Nohl, U., Herwig, K., Lammel, E., Stoll, B., Hofmann, A.W., 2005. GeoReM: A New Geochemical Database for Reference Materials and Isotopic Standards. Geostandards and Geoanalytical Research 29, 333-338.

Johnson, S.P., Korhonen, F.J., Kirkland, C.L., Cliff, J.B., Belousova, E.A., Sheppard, S., 2017. An isotopic perspective on growth and differentiation of Proterozoic orogenic crust: From subduction magmatism to cratonization. Lithos 268-271, 76-86.

Johnson, S.P., Sheppard, S., Rasmussen, B., Wingate, M.T.D., Kirkland, C.L., Muhling, J.R., Fletcher, I.R., Belousova, E.A., 2011. Two collisions, two sutures: Punctuated pre-1950Ma assembly of the West Australian Craton during the Ophthalmian and Glenburgh Orogenies. Precambrian Research 189, 239-262.

Kemp, A., Wilde, S., Hawkesworth, C., Coath, C., Nemchin, A., Pidgeon, R., Vervoort, J., DuFrane, S., 2010. Hadean crustal evolution revisited: new constraints from Pb–Hf isotope systematics of the Jack Hills zircons. Earth and Planetary Science Letters 296, 45-56.

Kemp, A.I.S., Vervoort, J.D., Bjorkman, K.E., Iaccheri, L.M., 2017. Hafnium Isotope Characteristics of Palaeoarchaean Zircon OG1/OGC from the Owens Gully Diorite, Pilbara Craton, Western Australia. Geostandards and Geoanalytical Research 41, 659-673.

Kharkongor, M.B.K., Glorie, S., Mulder, J., Kirkland, C.L., Chew, D., Kohn, B., Simpson, A., 2023. Apatite laser ablation LuHf geochronology: A new tool to date mafic rocks. Chemical Geology 636, 121630.

Kinny, P.D., Clark, C., Kirkland, C.L., Hartnady, M., Gillespie, J., Johnson, T.E., McDonald, B., 2022. How old are the Jack Hills metasediments really?: The case for contamination of bedrock by zircon grains in transported regolith. Geology 50, 721-725.

Kirkland, C.L., Hartnady, M.I.H., Barham, M., Olierook, H.K.H., Steenfelt, A., Hollis, J.A., 2021. Widespread reworking of Hadean-to-Eoarchean continents during Earth's thermal peak. Nat Commun 12, 331.

Kirkland, C.L., Smithies, R.H., Spaggiari, C.V., 2015a. Foreign contemporaries – Unravelling disparate isotopic signatures from Mesoproterozoic Central and Western Australia. Precambrian Research 265, 218-231.

Kirkland, C.L., Smithies, R.H., Woodhouse, A.J., Howard, H.M., Wingate, M.T.D., Belousova, E.A., Cliff, J.B., Murphy, R.C., Spaggiari, C.V., 2013. Constraints and deception in the isotopic record; the crustal evolution of the west Musgrave Province, central Australia. Gondwana Research 23, 759-781.

Kirkland, C.L., Spaggiari, C.V., Johnson, T.E., Smithies, R.H., Danišík, M., Evans, N., Wingate, M.T.D., Clark, C., Spencer, C., Mikucki, E., McDonald, B.J., 2016. Grain

size matters: Implications for element and isotopic mobility in titanite. Precambrian Research 278, 283-302.

Kirkland, C.L., Spaggiari, C.V., Pawley, M.J., Wingate, M.T.D., Smithies, R.H., Howard, H.M., Tyler, I.M., Belousova, E.A., Poujol, M., 2011. On the edge: U–Pb, Lu–Hf, and Sm–Nd data suggests reworking of the Yilgarn craton margin during formation of the Albany-Fraser Orogen. Precambrian Research 187, 223-247.

Kirkland, C.L., Spaggiari, C.V., Smithies, R.H., Wingate, M.T.D., Belousova, E.A., Gréau, Y., Sweetapple, M.T., Watkins, R., Tessalina, S., Creaser, R., 2015b. The affinity of Archean crust on the Yilgarn—Albany–Fraser Orogen boundary: Implications for gold mineralisation in the Tropicana Zone. Precambrian Research 266, 260-281.

Kirkland, C.L., Yakymchuk, C., Szilas, K., Evans, N., Hollis, J., McDonald, B., Gardiner, N.J., 2018. Apatite: a U-Pb thermochronometer or geochronometer? Lithos 318-319, 143-157.

Kuper, K.M., Armstrong, R., Kirkland, C.L., Olierook, H.K.H., Clark, C., Evans, K., 2024. Implications of high-grade metamorphism on detrital zircon data sets: A case study from the Fraser Zone, Western Australia. Chemical Geology 647, 121918.

Liebmann, J., Ware, B., Hartnady, M.I.H., Kirkland, C.L., Timms, N.E., Evans, N.J., 2023. Albany K-Feldspar: A New Pb Isotope Reference Material. Geostandards and Geoanalytical Research 47, 637-655.

Markwitz, V., Kirkland, C.L., Evans, N.J., 2017. Early Cambrian metamorphic zircon in the northern Pinjarra Orogen: Implications for the structure of the West Australian Craton margin. Lithosphere 9, 3-13.

Marsh, J.H., Jørgensen, T.R.C., Petrus, J.A., Hamilton, M.A., Mole, D.R., 2019. U-Pb, trace element, and hafnium isotope composition of the Maniitsoq zircon: A potential new Archean zircon reference material, Goldschmidt, Barcalona.

Martin, J.R., Redfern, J., Horstwood, M.S.A., Mory, A.J., Williams, B.P.J., 2019. Detrital zircon age and provenance constraints on late Paleozoic ice-sheet growth and dynamics in Western and Central Australia. Australian Journal of Earth Sciences 66, 183-207.

McDowell, F., McIntosh, W., Farley, K., 2005. A precise ^{40}Ar–^{39}Ar reference age for the Durango apatite (U–Th)/He and fission-track dating standard. Chemical Geology 214, 249-263.

Mole, D.R., Kirkland, C.L., Fiorentini, M.L., Barnes, S.J., Cassidy, K.F., Isaac, C., Belousova, E.A., Hartnady, M., Thebaud, N., 2019. Time-space evolution of an Archean craton: A Hf-isotope window into continent formation. Earth-Science Reviews 196, 102831.

Morel, M.L.A., Nebel, O., Nebel-Jacobsen, Y., Miller, J., Vroon, P.Z., 2008. Hafnium isotope scharacterisation of the GJ-1 zircon reference material by solution and laser-ablation MC-ICPMS. Chemical Geology 255, 231-235.

Morón, S., Cawood, P.A., Haines, P.W., Gallagher, S.J., Zahirovic, S., Lewis, C.J., Moresi, L., 2019. Long-lived transcontinental sediment transport pathways of East Gondwana. Geology 47, 513-516.

Morrissey, L.J., Payne, J.L., Hand, M., Clark, C., Taylor, R., Kirkland, C.L., Kylander-Clark, A., 2017. Linking the Windmill Islands, east Antarctica and the Albany–Fraser Orogen: Insights from U–Pb zircon geochronology and Hf isotopes. Precambrian Research 293, 131-149.

Mulder, J.A., Nebel, O., Gardiner, N.J., Cawood, P.A., Wainwright, A.N., Ivanic, T.J., 2021. Crustal rejuvenation stabilised Earth's first cratons. Nat Commun 12, 3535.

O'Sullivan, G., Chew, D.M., Kenny, G., Henrichs, I., Mulligan, D., 2020. The trace element composition of apatite and its application to detrital provenance studies. Earth-Science Reviews 201.

Osei, K.P., Kirkland, C.L., Mole, D.R., 2021. Nd and Hf isoscapes of the Yilgarn Craton, Western Australia and implications for its mineral systems. Gondwana Research 92, 253-265.

Paton, C., Hellstrom, J.C., Paul, B., Woodhead, J.D., Hergt, J.M., 2011. Iolite: Freeware for the visualisation and processing of mass spectrometric data. Journal of Analytical Atomic Spectrometry 26, 2508-2518.

Rasmussen, B., Bengtson, S., Fletcher, I.R., McNaughton, N.J., 2002. Discoidal Impressions and Trace-Like Fossils More Than 1200 Million Years Old. Science 296, 1112-1115.

Reid, A., Keeling, J., Boyd, D., Belousova, E., Hou, B., 2013. Source of zircon in world-class heavy mineral placer deposits of the Cenozoic Eucla Basin, southern Australia from LA-ICPMS U–Pb geochronology. Sedimentary Geology 286-287, 1-19.

Salama, W., González-Álvarez, I., Anand, R.R., 2016. Significance of weathering and regolith/landscape evolution for mineral exploration in the NE Albany-Fraser Orogen, Western Australia. Ore Geology Reviews 73, 500-521.

Schmitz, M.D., Bowring, S.A., Ireland, T.R., 2003. Evaluation of Duluth Complex anorthositic series (AS3) zircon as a U-Pb geochronological standard: new high-precision isotope dilution thermal sionisation mass spectrometry results. Geochimica et Cosmochimica Acta 67, 3665-3672.

Schoene, B., Bowring, S., 2006. U-Pb systematics of the McClure Mountain syenite: Thermochronological constraints on the age of the $^{40}Ar/^{39}Ar$ standard MMhb. Contributions to Mineralogy and Petrology 151, 615-630.

Sláma, J., Košler, J., Condon, D.J., Crowley, J.L., Gerdes, A., Hanchar, J.M., Horstwood, M.S.A., Morris, G.A., Nasdala, L., Norberg, N., Schaltegger, U., Schoene, B., Tubrett, M.N., Whitehouse, M.J., 2008. Plešovice zircon — A new natural reference material for U–Pb and Hf isotopic microanalysis. Chemical Geology 249, 1-35.

Smithies, R.H., Spaggiari, C., Kirkland, C., 2015. Building the crust of the Albany-Fraser Orogen: Constraints from granite geochemistry.

Söderlund, U., Patchett, P.J., Vervoort, J.D., Isachsen, C.E., 2004. The 176Lu decay constant determined by Lu–Hf and U–Pb isotope systematics of Precambrian mafic intrusions. Earth and Planetary Science Letters 219, 311-324.

Spaggiari, C., Bodorkos, S., Barquero-Molina, M., Tyler, I., Wingate, M., 2009. Interpreted bedrock geology of the south Yilgarn and central Albany-Fraser orogen, Western Australia. Geological Survey of Western Australia, Record 10, 84.

Spaggiari, C., Kirkland, C., Pawley, M., Smithies, R., Wingate, M., Doyle, M., Blenkinsop, T., Clark, C., Oorschot, C., Fox, L., 2011. The geology of the east Albany-Fraser Orogen—a field guide. Geological Survey of Western Australia Record 2011, 92.

Spaggiari, C., Kirkland, C., Smithies, R., Occhipinti, S., Wingate, M., 2014a. Geological framework of the Albany-Fraser Orogen, pp. 12-27.

Spaggiari, C., Kirkland, C., Smithies, R.H., Wingate, M.T.D., 2014b. Tectonic links between Proterozoic sedimentary cycles, basin formation and magmatism in the Albany-Fraser Orogen, Western Australia.

Spaggiari, C.V., Kirkland, C.L., Smithies, R.H., Wingate, M.T.D., Belousova, E.A., 2015. Transformation of an Archean craton margin during Proterozoic basin formation and magmatism: The Albany–Fraser Orogen, Western Australia. Precambrian Research 266, 440-466.

Spaggiari, C.V., Smithies, R.H., Kirkland, C.L., Wingate, M.T.D., England, R.N., Lu, Y.-J., 2018. Buried but preserved: The Proterozoic Arubiddy Ophiolite, Madura Province, Western Australia. Precambrian Research 317, 137-158.

Spencer, C.J., Murphy, J.B., Kirkland, C.L., Liu, Y., Mitchell, R.N., 2018. A Palaeoproterozoic tectono-magmatic lull as a potential trigger for the supercontinent cycle. Nature Geoscience 11, 97-101.

Stern, R.A., Bodorkos, S., Kamo, S.L., Hickman, A.H., Corfu, F., 2009. Measurement of SIMS Instrumental Mass Fractionation of Pb Isotopes During Zircon Dating. Geostandards and Geoanalytical Research 33, 145-168.

Strachan, R.A., Olierook, H.K.H., Kirkland, C.L., 2021. Evidence from the U–Pb–Hf signatures of detrital zircons for a Baltican provenance for basal Old Red Sandstone successions, northern Scottish Caledonides. Journal of the Geological Society 178.

Thompson, J., Meffre, S., Maas, R., Kamenetsky, V., Kamenetsky, M., Goemann, K., Ehrig, K., Danyushevsky, L., 2016. Matrix effects in Pb/U measurements during LA-ICP-MS analysis of the mineral apatite. Journal of Analytical Atomic Spectrometry 31, 1206-1215.

Tucker, N.M., Hand, M., Kelsey, D.E., Taylor, R., Clark, C., Payne, J.L., 2018. A tripartite approach to unearthing the duration of high temperature conditions versus peak metamorphism: An example from the Bunger Hills, East Antarctica. Precambrian Research 314, 194-220.

Tucker, N.M., Payne, J.L., Kemp, A.I., Kirkland, C.L., Smyth, A., Tunmer, W., Harvey, S., Stinear, M., Machuca, A., Rangel Suarez, S., De Waele, B., 2023. A newly discovered 2030–2010 Ma magmatic suite records the dawn of Proterozoic extension on the southern margin of the Yilgarn Craton. Precambrian Research 397, 107192.

Waddell, P.-J.A., Timms, N.E., Spaggiari, C.V., Kirkland, C.L., Wingate, M.T.D., 2015. Analysis of the Ragged Basin, Western Australia: Insights into syn-orogenic basin evolution within the Albany–Fraser Orogen. Precambrian Research 261, 166-187.

Wang, Q., Wilde, S.A., 2018. New constraints on the Hadean to Proterozoic history of the Jack Hills belt, Western Australia. Gondwana Research 55, 74-91.

Wang, Q., Zhu, D.-C., Zhao, Z.-D., Guan, Q., Zhang, X.-Q., Sui, Q.-L., Hu, Z.-C., Mo, X.-X., 2012. Magmatic zircons from I-, S- and A-type granitoids in Tibet: Trace element characteristics and their application to detrital zircon provenance study. Journal of Asian Earth Sciences 53, 59-66.

Woodhead, J.D., Hergt, J.M., 2005. A Preliminary Appraisal of Seven Natural Zircon Reference Materials for In Situ Hf Isotope Determination. Geostandards and Geoanalytical Research 29, 183-195.

Zametzer, A., Kirkland, C.L., Hartnady, M.I.H., Barham, M., Champion, D.C., Bodorkos, S., Smithies, R.H., Johnson, S.P., 2022. Applications of Pb isotopes in granite K-feldspar and Pb evolution in the Yilgarn Craton. Geochimica et Cosmochimica Acta 320, 279-303.

Zeh, A., Stern, R.A., Gerdes, A., 2014. The oldest zircons of Africa—Their U–Pb–Hf–O isotope and trace element systematics, and implications for Hadean to Archean crust–mantle evolution. Precambrian Research 241, 203-230.

Zutterkirch, I.C., Kirkland, C.L., Barham, M., Elders, C., 2021. Thin-section detrital zircon geochronology mitigates bias in provenance investigations. Journal of the Geological Society 179.

3.10. Appendix C

3.10.1. Sample 702

This sample was collected from a sand dune on a NE-SW dirt road through the Woodline Hills. The regolith geology, with a maximum age of 541 Ma, is lithic–rich colluvium derived from the underlying Woodline Formation (GSWA, 2023). 98 zircon U–Pb/Lu–Hf isotopic analyses were undertaken on this sample, and 78 were concordant (± 10% of concordance). Concordant U–Pb analyses ranged from 693 to 2731 Ma. Age maxima were defined at 1183, 1302, 1682, 2585 and 2644 Ma by 10, 15, 4, 5 and 14 grains, respectively.

3.10.2. Sample 706

This sample was collected from a lacustrine deposit margin, forming a prominent dune on the eastern edge of an ephemeral lake. The regolith geology, with a maximum age of 541 Ma, is lithic–rich colluvium derived from the underlying Woodline Formation (GSWA, 2023). 88 zircon U–Pb/Lu–Hf isotopic analyses were undertaken on this sample, and 75 were concordant (± 10% of concordance). Concordant U–Pb analyses ranged from 656 to 3031 Ma. Age maxima were defined at 1156, 1198, 1282, 1335, 1689, 2564, and 2644 Ma by 3, 11, 6, 3, 12, 3, and 21 grains respectively.

3.10.3. Sample 720

Sample 720 was collected from a dune forming the northeastern margin of an ephemeral lake. The regolith geology is a residual lacustrine unit formed during the Cenozoic with a maximum age of 514 Ma. The bedrock geology is the Woodline Formation (GSWA, 2023).

99 zircon U–Pb/Lu–Hf isotopic analyses were undertaken, and 81 were concordant (± 10% of concordance). Concordant U–Pb zircon analyses ranged from 557 to 2744 Ma. Age maxima were defined at 1172, 1244, 1292, 1687, 2640, and 2679 Ma by 10, 8, 21, 13, 5 and 8 grains, respectively. Thirteen apatite U–Pb analyses were performed, which yield Pb^{207} corrected ages between 1269 – 1601 Ma and F^{207} % between 7.4 – 85.9%.

3.10.4. Sample 721

This sample was collected from a clay–and silt-rich alluvial fan, which drains into the ephemeral lake where sample 720 was collected. The regolith is residual and formed during the Cenozoic, with a maximum age of 541 Ma (GSWA, 2023).

97 zircon U–Pb/Lu–Hf analyses were obtained, of which 90 were concordant (± 10% of concordance). Concordant U–Pb analyses give ages that range from 546 to 2970 Ma. Age populations were defined at 1184, 1211, 1290, 1498, 1651, 2600 and 2667 Ma by 4, 3, 19, 3, 13, 6 and 12 grains, respectively. Three apatite U–Pb analyses were obtained, which yielded ^{207}Pb corrected ages between 1261 – 1379 Ma and F^{207} % between 19.7 – 42.3%.

3.10.5. Sample 723

Sample 723 was collected along an unnamed northeast–southwest track from ephemeral river sand. The regolith geology is a relict unit of yellow sand with pisolitic laterite. Localised areas of ferruginised silcrete and clay lenses cap the poorly consolidated sands. The unit has a maximum age of 541 Ma and was formed during the Cenozoic (GSWA, 2023). This sample was collected atop the eastern contact of the 2600 – 3010 Ma Yilgarn Granites and the Woodline Formation (GSWA, 2023; Hall et al., 2008).

94 zircon U–Pb/Lu–Hf analyses were obtained, of which 79 were concordant (± 10% of concordance). Concordant U–Pb analyses give ages that range from 656 to 2699 Ma. Concordant grains defined age maxima at 1158, 1186, 1215, 1254, 1282, 1306, 1591, 1659, 1761, 2506, 2571, 2631, 2674 Ma by 8, 7, 3, 3, 5, 7, 3, 9, 3, 3, 3, 8, 9 grains respectively

3.10.6. Sample 729

Sample 729 was collected on an unnamed northwards track. The collected sand formed a 2 m wide ephemeral stream, whilst the regolith geology is residual yellow sand containing minor pisolitic laterite. The local area was dominated by ferruginised silcrete, intercalated clay, and silt layers. The bedrock geology is the northwestern margin of the Woodline Formation (GSWA, 2023; Hall et al., 2008).

95 zircon U–Pb/Lu–Hf analyses were obtained, and 76 were concordant (± 10% of concordance). The ages of concordant zircon grains ranged from 512 to 2692 Ma. Concordant grains defined age maxima at 678, 1194, 1260, 1290, 1549, 1683, 2629, and 2673 Ma by 6, 13, 3, 16, 3, 4, 6, 8 grains respectively.

3.10.7. Sample 732

Sample 732 was collected from the margin of a playa lake, 20 m northwest of an unnamed track. The regolith geology is lacustrine units consisting of mixed dunes with

localised evaporite lenses and ephemeral alluvial deposits. The maximum age of the regolith is 541 Ma, and it was predominantly formed during the Cenozoic (GSWA, 2023).

The bedrock geology is an isolated northern outcrop of the Woodline Formation; however, the surrounding geology varies. 500 m to the west are greenstone successions of the Eastern Goldfields Superterrane, composed of mafic to ultramafic volcanics formed between 2650 to 2960 Ma. 500 m to the north are intercalated packages of supracrustal siliciclastics, shale and chert of the Eastern Goldfields Superterrane. 500 m to the northwest is an east–west trending Widgiemooltha Dolerite dyke, dated 2420 – 2400 Ma (GSWA, 2023).

99 zircon U–Pb/Lu–Hf were obtained, and 69 were concordant (± 10% of concordance). Concordant U–Pb zircon ages ranged from 603 to 2698 Ma. Concordant grains defined age maxima at 1192, 1224, 1273, 1316, and 2692 Ma by 17, 5, 4, 18 and 3 grains, respectively.

3.10.8. Sample 734

This sample was collected 50 m east of a northbound track following an ephemeral stream. The regolith geology is a lacustrine unit comprising localised evaporite deposits and dunes. The maximum age of the regolith is 541 Ma, and is a residual unit formed during the Cenozoic. The underlying geology is the contact between the greenstone and supracrustal successions of the Eastern Goldfields Superterrane, dated 2650 – 2960 Ma and the Woodline Formation. 86 zircon U–Pb analyses were obtained, of which 77 were concordant (± 10% of concordance). Concordant ages obtained from zircon ranged from 660 – 2732 Ma. Zircon within this sample defined age maxima at 1154, 1187, 1221, 1282, 1307, 1668, and 2674 Ma by 5, 10, 3, 15, 12, 4 and 6 grains, respectively.

3.10.9. Sample 713

Sample 713 was collected atop the southern exposure of the Woodline Hills along a west–to–east transect. The sample is a basal quartzite from the lowermost 20 m sandstone of the exposed Woodline Formation and is a grey, weakly metamorphosed, medium-grained (0.0625 – 2 mm) quartz arenite. The sandstone lacks lithic and feldspar fragments, consistent with the mature and homogenous character of the Woodline Formation.

52 zircon U–Pb/Lu–Hf analyses were obtained in Session 2, of which 11 were concordant (± 10% of concordance). Concordant zircon analyses ranged from 1798 to 2686 Ma, while three concordant zircon grains defined a single age peak at 2024 Ma.

In Session 4, 10 U–Pb repeat analyses were obtained on grains previously analysed during Session 2. 33 U–Pb analyses were obtained on new zircon, of which 20 were concordant. Thus, Sample 713 yielded 31 concordant ages, spanning 1697 – 2743 Ma.

3.10.10. Sample 722

Sample 722 was collected from a rock outcrop on the edge of an ephemeral stream 50 m north of an unnamed northwest-southeast track.

Sample 722 is a clast–supported monomict chert breccia that formed layers (5 – 10 m thick) interbedded within massive sandstone. Angular to subangular clasts of chert and quartzite are extremely poorly sorted within a quartzite matrix and chert fragments. This breccia represents a mid-stratigraphic portion of the Woodline Formation, collected 70 – 80 m above the basal nonconformity.

During Session 2, 76 zircon U–Pb analyses were obtained, of which 70 were concordant (± 10% of concordance). Concordant zircon grains ranged from 1900 – 3175 Ma. Concordant zircon grains defined age maxima at 2015, 2115, 2465, 2656, 2681, and 2763 Ma by 18, 5, 3, 7, 9, 3 grains respectively.

During Session 4, 45 repeat analyses were obtained on zircon analysed during Session 2. 21 new concordant ages were obtained. Thus, Sample 713 yielded 91 concordant ages, which spanned 1466 – 3175 Ma. Two apatite U–Pb analyses were obtained, yielding Pb^{207} corrected ages between 2080 – 2424 Ma and F^{207} % between 18.6 – 68%.

3.10.11. Sample 724

This sample was collected from a vertical outcrop on the side of an ephemeral stream atop the Woodline Hills at an elevation of 354 m. As a result of the anticlinal folding of the Woodline Formation, this sample represents a basal conglomerate collected from the lowermost 40 m of the Woodline Formation. Sample 724 was collected from a 5 – 10 m layer of conglomerate interbedded with massive quartzite. Poorly sorted and rounded cobbles of chert and quartzite between 40 – 80 mm form a clast–supported conglomerate.

In Session 2, 69 zircon U–Pb analyses were obtained, and 42 were concordant (± 10% of concordance). Concordant zircon analyses ranged from 2012 to 2936 Ma, and age maxima were defined at 2035, 2072, 2607, 2667, and 2691 Ma by 10, 5, 4, 6, and 6 grains, respectively.

Five apatite U–Pb analyses were obtained, which yielded Pb^{207} corrected ages between 2039 – 2199 Ma and F^{207} % between 1.5 – 57%. 17 repeat analyses were undertaken in Session 4 and 15 new concordant ages were obtained. Thus 57 concordant ages were obtained from Sample 724, which spanned 1978 – 3120.

3.10.12. Sample 726

Sample 726 is a quartzite collected from the mid to upper portion of the Woodline Formation stratigraphy (100 m above the basal contact). The sample is a grey, undeformed and weakly metamorphosed, coarse–grained (0.1 – 2 mm) quartz arenite.

In Session 3, 89 zircon U–Pb analyses were undertaken, and 87 were concordant (± 10% of concordance). Concordant ages ranged from 1884 – 3247 Ma, and age maxima at 2041, 2084, 2255, 2558, 2659, 2698, and 3100 were defined by 12, 5, 11, 3, 16, 10, and 3 grains, respectively.

In Session 4 21 repeat analyses were obtained from grains analysed during Session 3. 96 new concordant zircon ages were obtained. Thus, 183 concordant ages were obtained from Sample 726, which spanned 1884 – 3436 Ma.

Chapter 4. A detective duo of apatite and zircon geochronology for East Avalonia, Johnston Complex, Wales

This chapter is published as:

Clarke, A. J. I., Kirkland, C. L., and Glorie, S., 2023, A detective duo of apatite and zircon geochronology for East Avalonia, Johnston Complex, Wales: Journal of the Geological Society, v. 180, no. 3.

Doi: 10.1144/jgs2022-178

Minor post-publication changes and clarifications have been made.

The Johnston Complex represents a rare inlier of the Neoproterozoic basement of southern Britain and offers a window into the tectonomagmatic regime of East Avalonia during the assembly of Gondwana. This work presents *in-situ* zircon (U–Pb, Lu–Hf), apatite (U–Pb), and trace element chemistry for both minerals from the Complex. Zircon and apatite yield a coeval crystallisation age of 570 ± 3 Ma, and a minor antecrystic zircon core component is identified at 615 ± 11 Ma. Zircon Lu–Hf data imply a broadly chondritic source, comparable to Nd data from East Avalonia, and T_{DM}^2 model ages of ca. 1.5 Ga indicate source extraction during the Mesoproterozoic. Zircon trace element chemistry is consistent with an ensialic calc-alkaline continental arc setting and demonstrates that magmatism was ongoing prior to terrane dispersal at 570 Ma. Apatite trace element chemistry implies a sedimentary component within the melt consistent with voluminous S-type granite production during the formation of Gondwana. The similarity of ƐHf and geochemistry between both zircon age populations suggest derivation from a uniform source that did not undergo significant modification between 615 – 570 Ma. Time-constrained apatite-zircon chemistry addresses complexities in dating S-type granitoids (zircon inheritance) and permits inferences on post-magmatic thermal histories.

4.1. Introduction

The assembly of Gondwana over 800 – 550 Ma (Meert and Van Der Voo, 1997) coincides with a crucial time in the evolution of Earth systems. Neoproterozoic lithologies provide evidence for the emergence of complex multicellular life (Shen et al., 2008), global glaciation (Shields-Zhou et al., 2016), and an important period of continental crust production in the Pan-African orogeny (Rino et al., 2008). Key to understanding these interrelated processes are paleotectonic reconstructions, which give constraints on the timing, duration, and style of magmatism. The construction of Gondwana was a protracted and complex process whereby microcontinents, such as Avalonia, were amalgamated onto and incorporated within the emerging landmass (Cawood et al., 2021). The Neoproterozoic of southern Britain represents a prolonged (ca. 200 Ma) period of discontinuous magmatism, which necessitates accurate age-constrained isotopic and geochemical signatures to reconstruct the tectonic setting of Peri-Gondwanan terranes in this area (Compston et al., 2002; Pharaoh and Carney, 2000; Schofield et al., 2016).

Drill-core and geophysical data indicate that England and Wales (south of the Iapetus suture) are underlain by a mosaic of Avalonian terranes, which from west to east include the Cymru, Wrekin, Charnwood and Fenland terranes (McIlroy and Horak, 2006; Pharaoh and Carney, 2000; Schofield et al., 2016). However, complications arise from the sparsely distributed, fault-uplifted tectonic inliers (Figure 4.1) and the varying degrees of deformation and metamorphism sustained by Precambrian basement lithologies during the Caledonian, Variscan, and Alpine orogenies (Pharaoh and Carney, 2000). The Johnston Complex, the Arfon and Sarn Groups of North Wales, and the Pebidian Supergroup of North Pembrokeshire have been assigned to the Cymru Terrane (Pharaoh and Carney, 2000; Schofield et al., 2016) (Figure 4.1). However, other workers have questioned the reliability of such broad terrane associations based on limited basement outcrops and the internal complexities of individual inliers (Compston et al., 2002; Schofield et al., 2016). The Johnston Complex typifies this issue; based on published zircon U-Pb ages and its calc-alkaline geochemistry, it has been alternatively classified into the Wrekin Terrane (McIlroy and Horak, 2006) or Cymru Terrane (Figure 4.1) (Compston et al., 2002; Pharaoh and Carney, 2000; Schofield et al., 2016).

East Avalonian terranes are interpreted to represent remnants of a single late-Neoproterozoic subduction margin (Pharaoh et al., 1987). As such, constraining tectonomagmatic processes during this formative period in the evolution of Earth systems relies on accurate terrane designations, which, in turn, underpin paleo-continental reconstructions,

essential to constraining the relationships between different planetary geochemical reservoirs during important intervals in Earth's history (Figure 4.1) (Nance et al., 2008; Strachan et al., 2007).

As there is a general paucity of recent isotopic studies, previous terrane classification work has relied on sparse isotopic and geochemical data (Figure 4.1) (Pharaoh and Carney, 2000; Schofield et al., 2016). The Johnston Complex of southwest Wales is a case in point, with research into the Johnston Complex being limited to Cantrill et al. (1916), Thorpe (1972), and the isotopic analyses of Patchett and Jocelyn (1979) and Schofield et al. (2016). Despite representing some of the oldest rocks in southern Britain, with a reported zircon U-Pb age of 643 +5/-28 Ma (Patchett and Jocelyn, 1979), little other isotopic data is available for the Complex, aside from a whole-rock Nd analysis undertaken by Schofield et al. (2016). Hence, the context of the Johnston Complex within the broader Peri-Gondwanan magmatic realm is

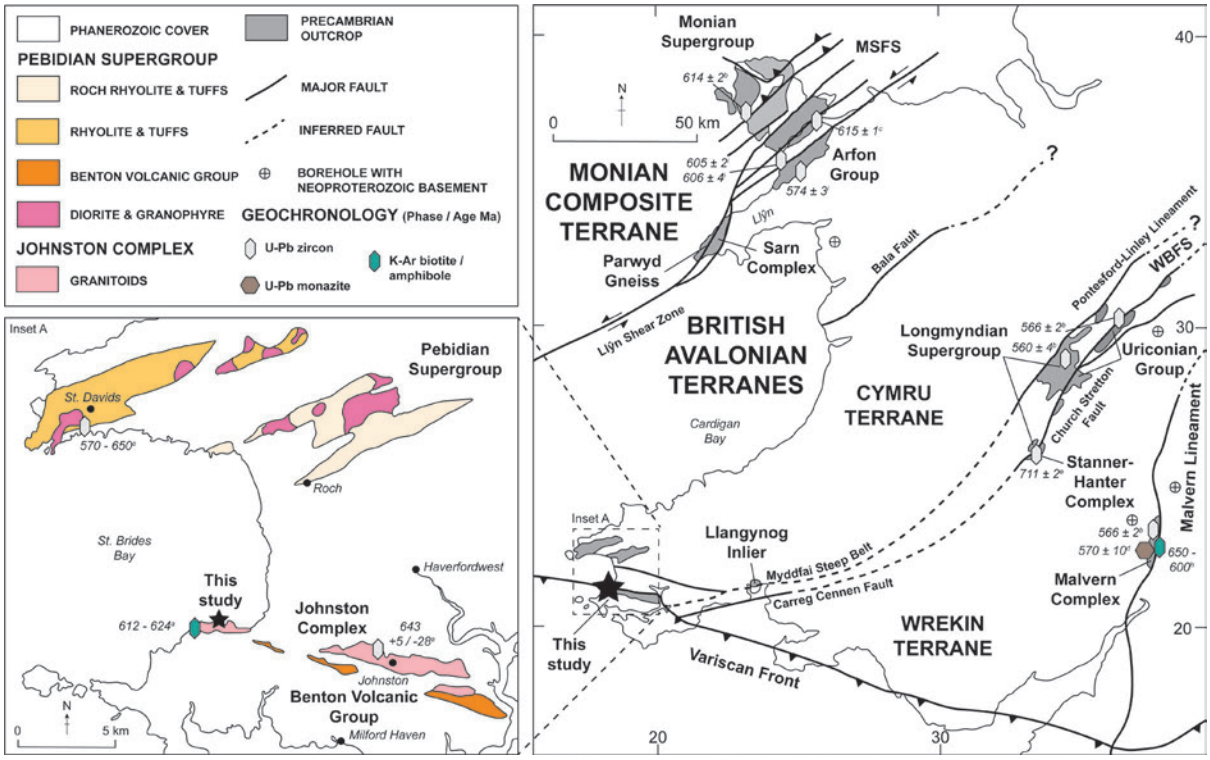

*Figure 4.1. The distribution of Precambrian outcrops in southern Britain. Previous ages obtained include (a) Patchett and Jocelyn (1979) and (b) Unpublished K-Ar ages for muscovite and hornblende discussed by Patchett and Jocelyn (1979). The schematic tectonic map of southern Britain is adapted after Pharaoh and Carney (2000). Inset **A** is a map of Precambrian geology in Pembrokeshire is modified after Bloxam and Dirk (1988). The coordinate system used is the British National Grid. Abbreviations include WBFS = Welsh Borderland Fault System and MSFS = Menai Strait Fault System. Data sources are listed in superscript letters and include a) Patchett and Jocelyn (1979), b) Tucker and Pharaoh (1991), c) Horak et al. (1996), d) Thorpe et al. (1984), e) Schofield et al. (2010), f) Noble et al. (1993), g) Beckinsale et al. (1984), h) Strachan et al. (1996), i) (Compston et al., 2002).*

yet to be fully determined. Several details remain unresolved, including the degree of heterogeneity within the Complex (single pluton vs composite magmatic body), the character of its source rocks, the relationship of the Complex to surrounding inliers, and its ultimate terrane classification.

This work presents *in-situ* zircon (U–Pb, Lu–Hf), apatite (U–Pb) and trace element data for both minerals from the Johnston Complex. Our results demonstrate that the Complex is a composite magmatic body composed of discrete quartz diorite plutons along its c. 20 km length. Our data show that calc-alkaline magmatism persisted in an ensialic setting in East Avalonia to ca. 570 Ma, prior to oblique convergence and terrane dispersal. We demonstrate that the source melt of the Johnston Complex was derived from a uniform and broadly chondritic source from 615 – 570 Ma, consistent with evolved ℇNd values from East Avalonia. The chemical data presented here reinforce the classification of the Complex within the Cymru Terrane of East Avalonia and show an S-type component within the melt. We demonstrate that a combined apatite and zircon geochronology approach constrains inherited vs primary zircon within S-type granitoids and clarifies the post-magmatic history of an igneous body.

4.2. Geological Background

4.2.1. Regional Geology

The Menai Strait Fault separates the Precambrian geology of southern Britain into the Avalonian and Monian tectonic blocks (Figure 4.1) (Schofield et al., 2016; Strachan et al., 2007; Woodcock et al., 2012). Several terranes within these blocks (e.g., Cymru, Charnwood, Fenland and Wrekin) comprise the Avalon Composite Terrane, which is primarily concealed by Phanerozoic rocks (Pharaoh and Carney, 2000; Schofield et al., 2016). Major fault zones, such as the Malvern Fault System and the Welsh Borderland Fault System, represent the broad structural controls on the distribution of Neoproterozoic inliers in southern Britain (Figure 4.1) (Pharaoh and Carney, 2000; Woodcock et al., 2012). The ultimate relationship between the Avalonian and Monian terranes remains unresolved. However, both share a history of calc-alkaline magmatism, accretionary prism and basement gneiss amalgamation during the late Neoproterozoic (Schofield et al., 2016; Woodcock et al., 2012). Isotopic and structural data point towards a shared genesis for both units (Horak et al., 1996), and taken together, they are termed the Avalon Superterrane.

4.2.2. Geology of the Johnston Complex

The Precambrian rocks of southwest Wales crop out in two areas north and south of St. Brides Bay (Figure 4.1). To the south is the Johnston Complex, an east-west trending intrusive suite of felsic plutons comprising diorites, tonalites, and granodiorites (Thorpe, 1972). These rocks are cross-cut by metre-scale dolerite dykes emplaced during the Variscan orogeny (Patchett and Jocelyn, 1979; Thorpe, 1972; Thorpe, 1979).

The Johnston Complex is exposed in two outcrops: a coastal section on the southern end of St. Brides Bay and an inland area within the Bolton Hill Quarry near the eponymous town of Johnston (Figure 4.1). The Johnston Complex is thrust atop Palaeozoic sedimentary rocks and is entrained within the hanging wall of the Johnston-Benton thrust zone (Woodcock et al., 2012). The coastal outcrop of the Johnston Complex is comprised of quartz diorite, which is dominated by plagioclase (oligoclase to andesine), quartz, partially altered primary mafic minerals (hornblende and biotite) now occurring as chlorite, sericite and illite, and minor iron-titanium oxides (Figure 4.2).

There is some lithological variability between the inland portion and coastal outcrops. The inland lithologies have an increased abundance of hornblende and biotite, but alkali feldspar is mainly absent (Thorpe, 1972; Thorpe, 1979). In contrast, the coastal outcrops have a more homogenous quartz diorite composition and contain orthoclase at < 2% modal abundance (Thorpe, 1972).

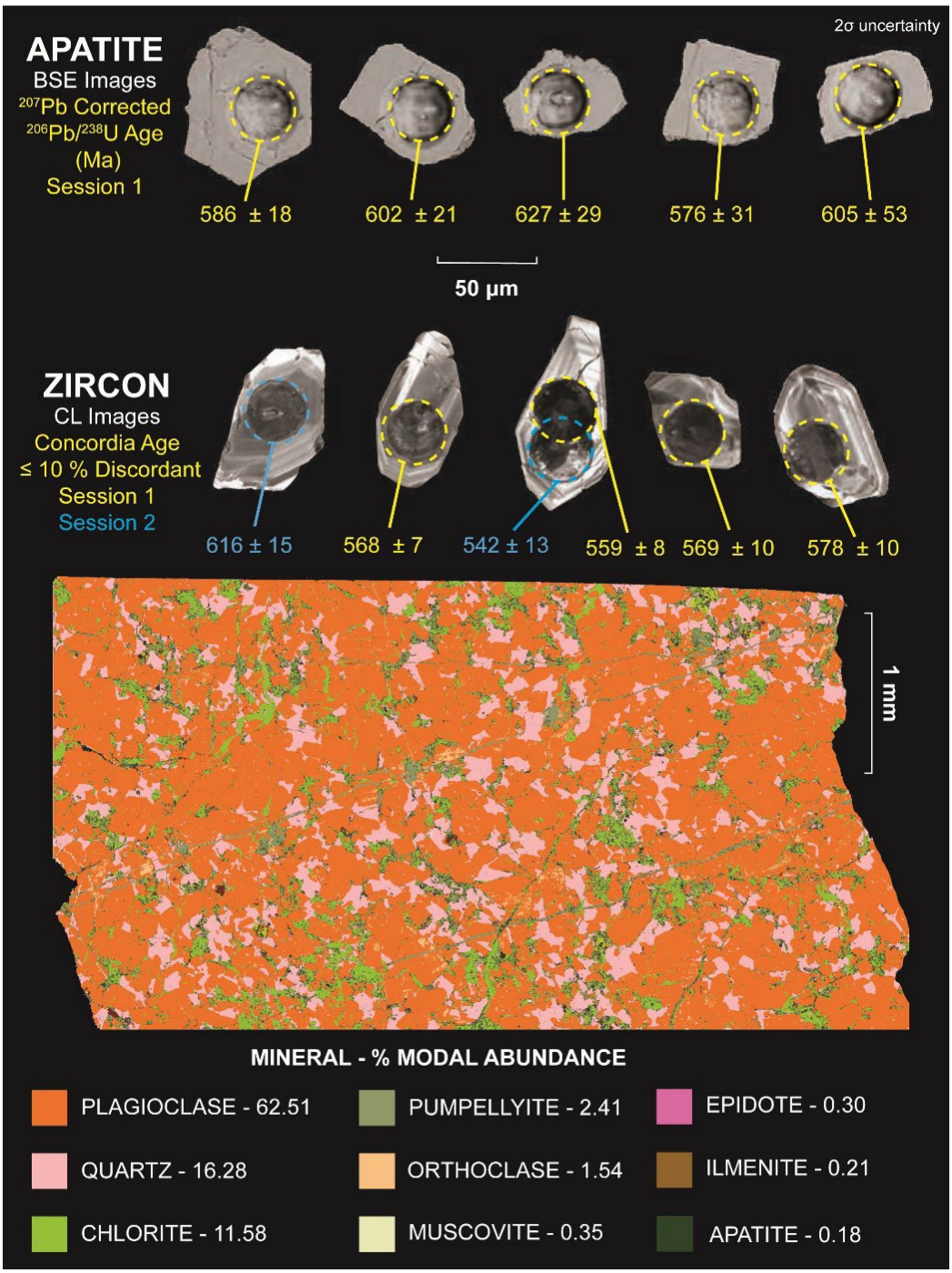

Figure 4.2. ***Top Row:*** *Backscatter electron images of representative apatite, with a 38 µm spot and* F^{207} *corrected age shown.* ***Bottom Row:*** *Cathodoluminescence Images of zircon, with concordia ages and the 38 µm spot obtained from separate sessions shown.* ***Bottom Figure:*** *A Tescan Integrated Mineral Analyser phase map of minerals with a mass % above 0.10 for the quartz diorite of the Johnston Complex.*

4.3. Methods

4.3.1. Mineral Separation

A sample of quartz dolerite from the Johnston Complex was collected from south of St. Brides Bay (51°46'21.6"N 5°08'57.1"W). Zircon and apatite grains were separated following standard procedures at the John de Laeter Centre (JdLC), Curtin University. The sample was crushed using a ring mill and sieved to yield the ≤ 425 μm fraction. This fraction underwent heavy mineral separation via a Jasper Canyon Research water shaking table (Dumitru, 2016). Lithium heteropolytungstate heavy liquid separation at 2.85 g/cm^3 and Frantz isodynamic separation followed to produce a final fraction which was mounted in entirety onto a 25 mm epoxy resin round.

A polished 4 x 2 cm block was also prepared and analysed via a Tescan Integrated Mineral Analyser (TIMA) to provide insights into texture and mineralogy. The round mount and block were polished using a 1 μm diamond suspension fluid and imaged using reflected and transmitted light. TIMA analysis was used to identify mineral phases on the mount and block, and a Clara FE-SEM was then used to provide high-resolution images of internal grain morphology – aiding spot placement during LA-ICP-MS analysis.

4.3.2. Isotopic Analysis

4.3.3. Zircon U-Pb and Lu-Hf

A split-stream zircon U-Pb and Lu-Hf analysis session was undertaken at the GeoHistory Facility at the JdLC, Curtin University. A RESOlution LE193 nm ArF and a Lauren Technic S155 cell were used to ablate zircon with an Agilent 8900 ICPMS to collect U-Pb data, whilst Lu-Hf isotopes were collected simultaneously via a Nu Plasma II MC-ICPMS. The relatively small grain size of zircon (typically < 70 μm in length) and internal complexities necessitated a comparatively small spot size of ~38 μm diameter.

The matrix-matched primary reference material used for zircon U-Pb data reduction was GJ1 (Jackson et al., 2004). Plešovice, 337.13 ± 0.37 Ma; (Sláma et al., 2008) and 91500, 1063.78 ± 0.65 Ma; (Wiedenbeck et al., 1995) secondary reference materials were used to monitor the accuracy of the $^{238}U/^{206}Pb$ ratio measurement. To check the accuracy of $^{207}Pb/^{206}Pb$ ages, OG1, 3465.4 ± 0.6 Ma (Stern et al., 2009) was reduced against Maniitsoq, 3008.70 ± 0.72 Ma; (Marsh et al., 2019). All weighted mean ages for secondary reference materials were within 2σ uncertainty of accepted values.

Mud Tank zircon (Woodhead et al., 2004) was the primary reference material for zircon Lu-Hf analyses. Several secondary reference zircon including GJ1, 0.282000 ± 0.000025; (Morel et al., 2008), 91500, 0.282306 ± 0.00004; (Woodhead and Hergt, 2005; Woodhead et al., 2004) and R33, 0.282764 ± 0.000014; (Fisher et al., 2014a) were measured to confirm accuracy. All reference materials gave $^{176}Hf/^{177}Hf$ ratios within 2σ uncertainty of the accepted values, whilst the stable $^{178}Hf/^{177}Hf$ ratio was also within 2σ uncertainty of the expected ratio (Fisher et al., 2014b; Sláma et al., 2008).

4.3.4. Apatite U-Pb

Two apatite U-Pb isotopic analysis sessions were completed at the GeoHistory Facility, JdLC, using a RESOlution 193 nm ArF with a Lauren Technic S155 cell and an Agilent 8900 ICPMS. Given the small-grain size (< 50 µm) of apatite from the Johnston Complex, a 38 µm spot size was ablated using a 5 Hz repetition rate and a fluence of ~ 2 J/cm^{-2}. Madagascar (MAD-2) (Thompson et al., 2016) and Mt. McClure (MMC) (Schoene and Bowring, 2006) apatite were used as the primary reference material for sessions 1 and 2, respectively. Secondary reference material analysed included the MMC apatite (523.51 ± 1.47 Ma), Duluth Complex (FC) apatite (U-Pb zircon age of 1099.1 ± 0.2 Ma (Schmitz et al., 2003) and the Durango apatite (31.44 ± 0.18 Ma) (McDowell et al., 2005). Ages obtained via unanchored regressions through the secondary reference apatite were within 2σ uncertainty of accepted ages.

4.3.5. Apatite and Zircon Trace Elements

A single session of zircon and apatite trace elements was performed at the GeoHistory Facility at the JdLC. *In-situ* trace element measurements were made on some grains not previously analysed during earlier U–Pb sessions using an Agilent 8900 ICPMS. The size of zircon and apatite grains necessitated a 38 µm spot size at a fluence of 2.5 J/cm^{-2} and a 5 Hz laser pulse rate.

NIST 610 was used as the primary reference material for zircon analyses to calculate elemental abundance and correct for instrumental drift. The internal reference isotope used was ^{29}Si, assuming a stoichiometric zircon composition of 14.76 wt% silicon. Secondary reference materials included the 91500 zircon, using the reported values of Sano et al. (2002) and the NIST 612 (Jochum et al., 2005). For both reference materials, measured abundances were within 5–10% of reported values.

NIST 610 was the primary reference material for apatite trace element analyses. ^{29}Si was used as the internal reference isotope, assuming an appetite Si content of 0.41 wt% (Azadbakht et al., 2018). Secondary reference materials included the Durango apatite and NIST 612 glass; measured abundances were generally within 10% of reported values (Jochum et al., 2005; McDowell et al., 2005).

4.4. Results

4.4.1 Petrography

Automated mineralogy undertaken via TIMA is consistent with previous petrographic accounts of Cantrill et al. (1916) and Thorpe (1972). The Johnston Complex sample is a mesocratic medium-grained (1–5 mm) quartz diorite to tonalite principally composed of plagioclase feldspar (oligoclase to andesine) and quartz (Figure 4.2). Primary mafic minerals (hornblende and biotite) are variably altered to hydrous secondary phases, including chlorite, sericite, and illite. Accessory minerals within this rock include apatite, zircon, muscovite, and iron-titanium oxides, including rutile and hematite (Figure 4.2). Orthoclase occurs at low modal abundances (<2%) within antiperthite textures. Veinlets of pumpellyite crosscut the sample (Figure 4.2), consistent with the low-grade metamorphism experienced by the Complex and other Neoproterozoic inliers in southwest Wales (Patchett and Jocelyn, 1979; Thorpe, 1972). There is a general lack of significant metamorphic and deformational overprint on the sample, with only limited strained quartz, consistent with the rock fabric being dominantly magmatic.

4.4.2. Zircon Morphology

Zircon grains from the Johnston Complex are colourless to light brown, tabular, euhedral to subhedral and are mainly intact crystals. Pristine grains have aspect ratios of ≥ 3:1. The grain size is variable but does not typically exceed 200 μm in length. Sharp, oscillatory zoning, with well-defined core-rim relationships (based on cathodoluminescence response), is apparent in the zircon population. Small anhedral ≤10 μm apatite inclusions are found within some zircon crystals.

Zircon grains are predominantly situated on the margins of quartz or are contained within plagioclase and quartz (Figure 4.3A-B). Zircon is also associated with altered hydrous phases such as chlorite (Figure 4.3A). A petrographic relationship between zircon and mafic minerals has been observed in many granitoids and attributed to enhanced local Zr saturation (Bacon, 1989; Elburg, 1996) or greater zircon growth potential in localised volatile-rich melt

pockets (Erdmann et al., 2013; Miller et al., 2007). Zircon is absent in the late pumpellyite veinlets (Figure 4.3A).

4.4.3. Zircon U-Pb, Lu-Hf and Trace Elements

Over two analytical sessions, 124 U–Pb isotopic analyses were performed on zircon grains, from which 29 were less than 10% discordant. In Tera-Wasserburg plots, some zircon analyses scatter towards lower $^{238}U/^{206}Pb$ ratios at constant $^{207}Pb/^{206}Pb$, interpreted to reflect recent radiogenic-Pb loss (Figure 4.4). The concordant analyses define two coherent groups of ages (Population 1 & 2). Group 1 yields a concordia age of 569 ± 2 Ma, n = 27, MSWD = 1.9, $p(\chi^2) = 0.079$, which is interpreted as the magmatic crystallisation age for the quartz diorite, consistent with the oscillatory zoned zircon textures for this component (Figure 4.2).

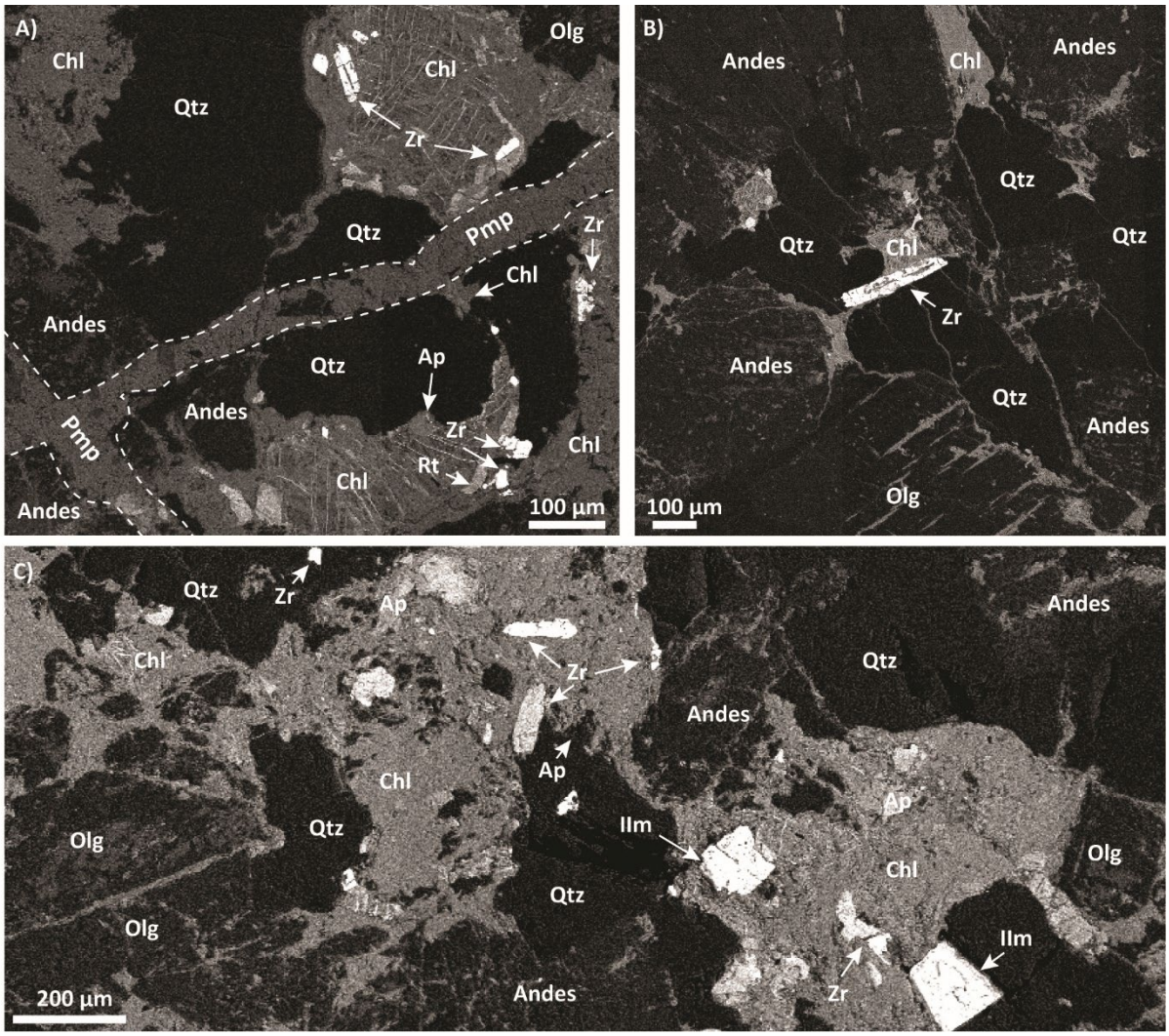

Figure 4.3. Compilation of representative backscatter electron images showing zircon and apatite mineral associations. Abbreviations: Andes = Andesine, Ap = Apatite, Chl = Chlorite, Ilm = Ilmenite, Olg = Oligoclase, Pmp = Pumpellytite, Qtz = Quartz, Rt = Rutile and Zr = Zircon.

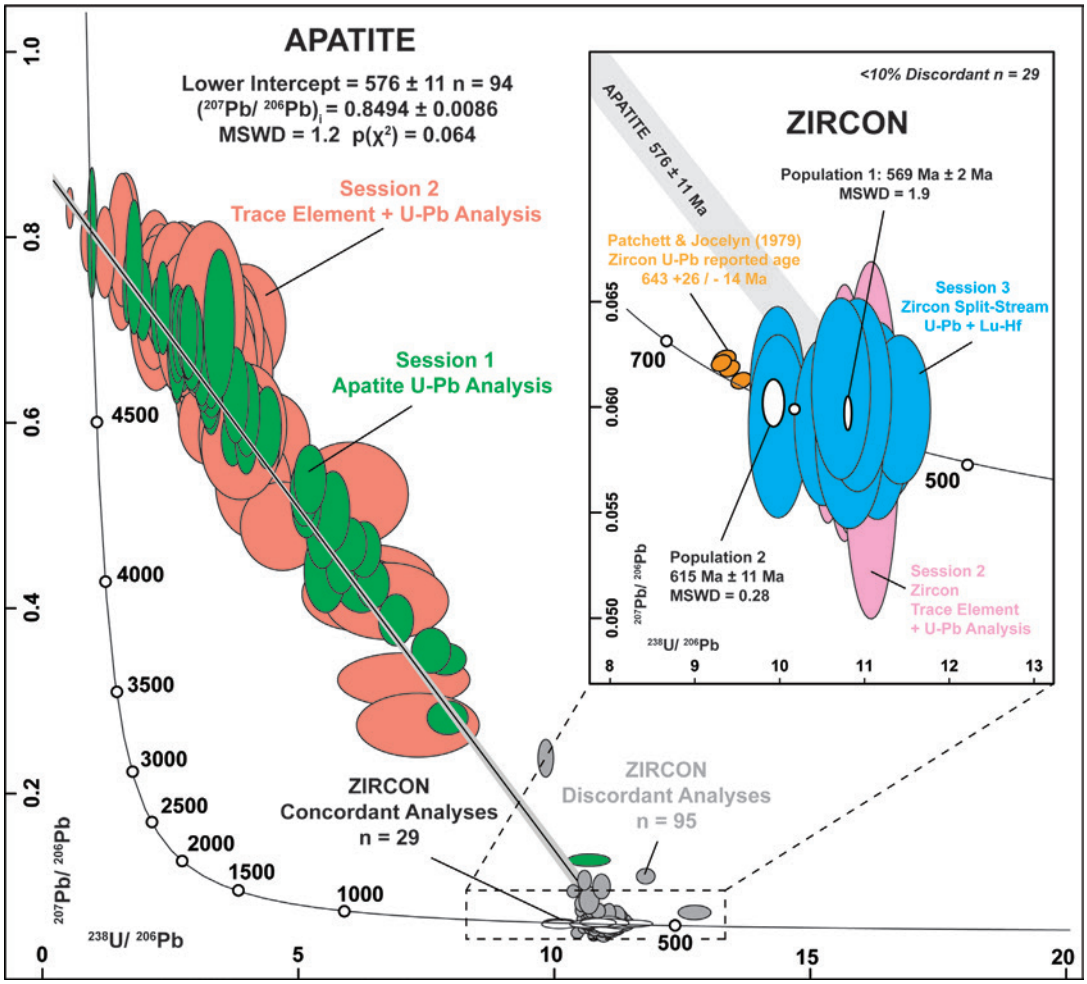

Figure 4.4. Tera-Wasserburg plot for zircon and apatite of the Johnston Complex. Note the different precisions of U-Pb analyses across each session, a function of LA-ICP-MS counting time during U-Pb, and trace elements compared to split-stream U-Pb and Lu-Hf. The inset shows the lower intercept of the apatite U-Pb regression, a magnified view of zircon U-Pb analyses, and the earlier TIMS results of Patchett and Jocelyn (1979).

Two zircon core analyses define Population 2 and is statistically distinct from Population 1, yielding an older concordia age of 615 ± 11 Ma, MSWD = 0.28, $p(\chi^2) = 0.89$. Population 2 is interpreted to represent older cores and was exclusively collected from larger zircon grains, which permitted individual cores to be analysed (Figure 4.2). Given the low number of analyses, these grains could represent either rare inherited zircons assimilated from the wall rock or an antecrystic component from an earlier magmatic episode within the same longer-lived system igneous system. The similarity of zircon REE and Lu-Hf chemistry between Populations 1 and 2 supports the latter interpretation.

Zircon REE chondrite-normalised (Boynton, 1984) plots show positively sloping gradients with cerium enrichment and europium depletion (Figure 4.5). The mean cerium anomaly (Ce/Ce*) for zircon from the Johnston Complex is +1.48, whilst the Eu anomaly $(Eu/Eu^*)_{CN}$ is strongly negative at 0.28. Some analyses show flattening of the light REE slope

(LREE/MREE, $(La/Sm)_{CN}$), consistent with a gain of non-stoichiometric elements into metamict zircon. These analyses typically yield discordant U-Pb isotopic results (Figure 4.4).

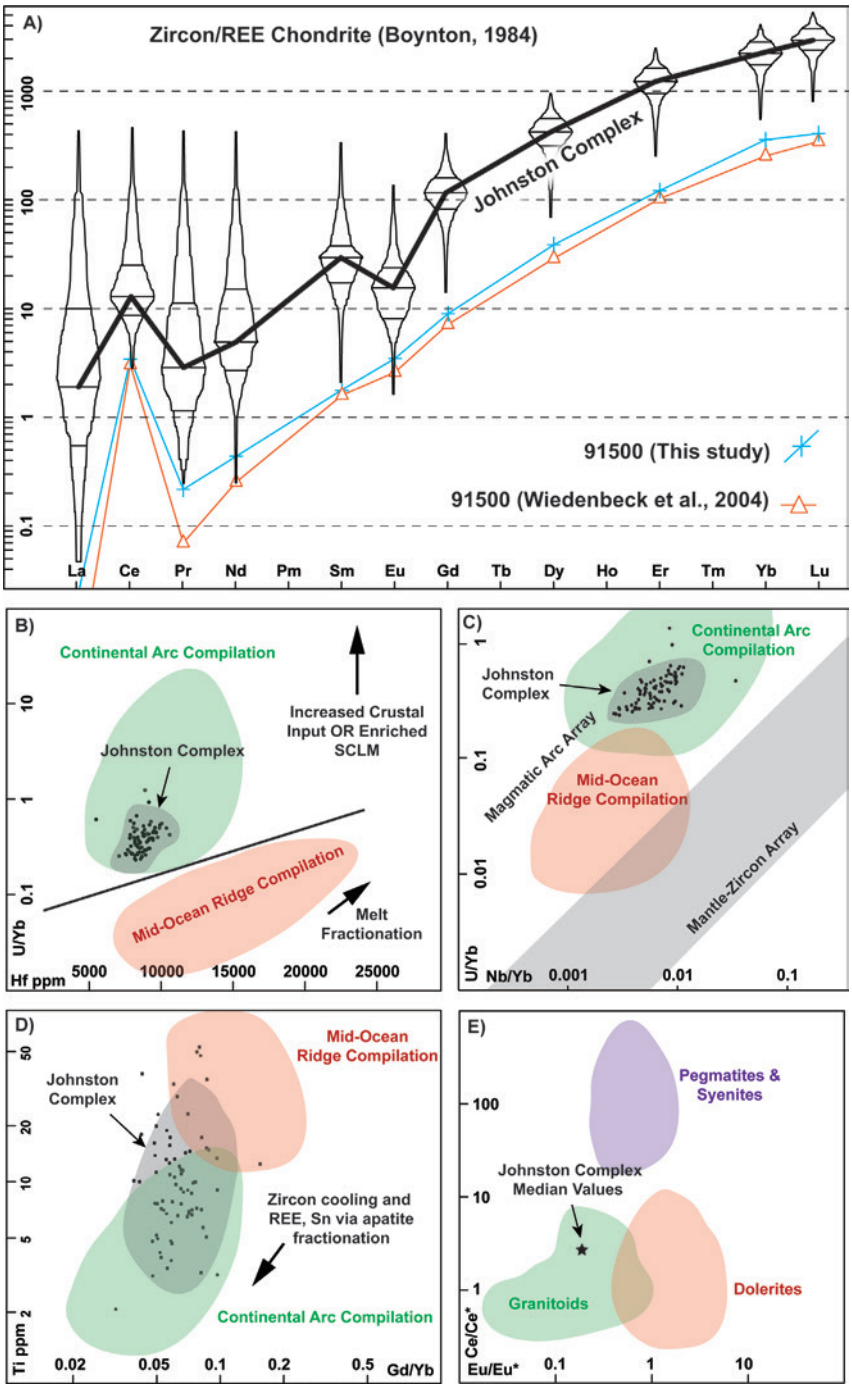

Figure 4.5. Zircon geochemistry discrimination diagrams. ***A)*** *REE Chondrite normalised zircon multi-element plot (Boynton, 1984).* ***B-D)*** *Bivariate plots of zircon geochemistry with compositional reference fields after Grimes et al. (2015).* ***E)*** *Eu/Eu* vs Ce/Ce* anomalies. Compositional reference fields adapted from Belousova et al. (2002b).*

A total of 44 zircon Lu-Hf analyses were obtained (Figure 4.6). Analyses of concordant zircon yield ƐHf of -4.0 to 2.9 for Population 1 with a weighted mean of -0.41 ± 1.38 (MSWD = 0.68). Population 2 ƐHf values range from -4.0 to -1.2 (Figure 4.6). Both populations yield similar model ages with a mean Lu-Hf T_{DM}^2 of 1521 Ma.

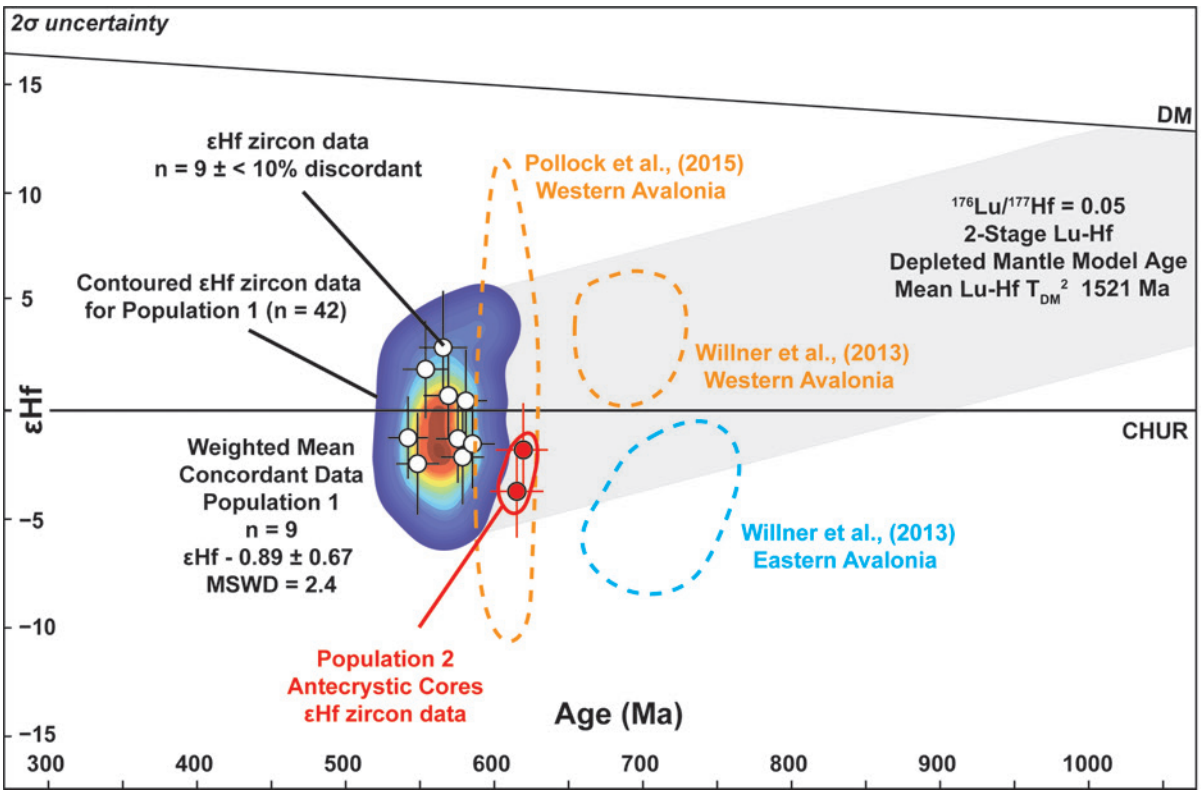

Figure 4.6. ƐHf plot for zircon of the Johnston Complex and other Avalonian Terranes. Data contoured using a kernel bandwidth of 10 for the X-axis and 1.25 intervals for the Y-axis. ƐHf data compiled from Pollock et al. (2015) and Willner et al. (2013).

4.4.4. Apatite Morphology

Apatite from the Johnston Complex typically occurs as small (~ 50 μm) (Figure 4.3C) subhedral, equant grains; however, the largest euhedral apatite is over 120 μm in length. Most grains are intact, with hexagonal basal sections. Apatite grains are largely colourless to light brown and internally homogenous without inclusions. Apatite is primarily associated with hydrous minerals (i.e., chlorite), and some grains occur within quartz, oligoclase and andesine (Figure 4.3).

4.4.5. Apatite U–Pb

A total of 94 apatite U–Pb analyses define a discordant array on the Tera Wasserburg concordia diagram spanning between a $^{207}Pb/^{206}Pb$ value of 0.85 ± 0.0086 at the upper intercept to an apparent age of 576 ± 11 Ma at the radiogenic lower intercept, MSWD = 1.2: $p(\chi^2)$ = 0.064. The F^{207}% of apatite analyses range from 12 – 99%, with a mean value of 69% (Figure 4.4). F^{207}% defines the distance along a mixing line between the non-radiogenic (common Pb) and radiogenic Pb component, where a higher % implies a greater common Pb component (Kirkland et al., 2017).

4.4.6. Apatite Trace Elements

The uranium concentration of the apatite ranges from 1.3 to 151.6 ppm, and the mean concentration is 9.2 ppm. Thorium concentrations range from 2.9 to 203.5 ppm, with a mean value of 25.8 ppm. REE chondrite-normalised plots (Boynton, 1984) show a characteristic negative slope from light to heavy REE, with a median $(La/Sm)_{CN}$ value of 2.6. The apatite's europium anomaly (Eu/Eu*) is comparable to that in zircon at 0.35 (Figure 4.7).

4.5. Results

4.5.1. The Johnston Complex: A Composite Magmatic Body

The ages yielded by population 1 zircon and apatite analyses are identical within uncertainty and yield a combined weighted mean age of 570 ± 3 Ma (MSWD = 1.5) (Figure 4.4), interpreted as the crystallisation age of the quartz diorite component of the Johnston Complex. This ca. 570 Ma age contrasts with the only previously reported U-Pb age for the Johnston Complex of 643 +5/-28 Ma (Patchett and Jocelyn, 1979) (Figure 4.1). Previous workers, including Patchett and Jocelyn (1979) and Thorpe (1979), concluded that the entire Johnston Complex (aside from the dolerite dykes) was emplaced at ca. 643 Ma. Assuming that the multigrain zircon fractions reported by Patchett and Jocelyn (1979) reflect a magmatic

event, the apparent ca. 643 Ma U-Pb age implies an earlier stage of magmatism for an inland component of the Johnson Complex. This interpretation is consistent with the observation that different multigrain size fractions of the Patchett and Jocelyn (1979) data set define a single lower intercept with no excess dispersion (Figure 4.4). Here, we also report an older ≥ 615 Ma antecrystic zircon core component (Population 2) within the coastal outcrop of the Complex (Figure 4.4).

In this work, we analysed a sample collected 9 km to the west of the study site of Patchett and Jocelyn (1979). Geophysical data and field observations show that both outcrops of the Complex are bound within the Johnston-Benton thrust zone and share a quartz diorite composition (Thorpe, 1979; Woodcock et al., 2012). Therefore, our isotopic data indicate that the Complex represents discrete magmatic units with ages spanning over 40 Ma (Figure 4.4). Hence, previous accounts that the Complex represented a single magmatic episode at ca. 650 Ma (Pharaoh and Carney, 2000; Valley et al., 2014; Woodcock et al., 2012) now appear inconsistent with the younger Cryogenian history of plutonism recorded within the apatite and zircon of the western Johnston Complex.

Neoproterozoic igneous activity in southern Britain has been summarised via a three-stage model (Pharaoh and Carney, 2000; Woodcock et al., 2012). Based on the new geochronology reported herein, the Johnston Complex retains information from each stage (Figure 4.8). An early ca. 700 – 640 Ma period of magmatism is recorded throughout the basement of southern Britain and is characterised by pluton emplacement at mid-crustal depths within the Wrekin Terrane, e.g. Stanner-Hanter, Malverns (Figure 4.1) (Pharaoh and Carney, 2000). The inland ca. 643 Ma pluton of the Johnston Complex (Patchett and Jocelyn, 1979) thus brackets the end of this earliest stage of magmatism.

Calc–alkaline arc plutons (Sarn Complex, Arfon Group) and volcanic sequences (Pebidian Supergroup) dominated a later period of magmatism from ca. 620 – 585 Ma during the so-called Main Magmatic Event within the British Avalonian Terranes (Pharaoh and Carney, 2000). The ca. 615 Ma zircon core age and ca. 570 Ma zircon and apatite U-Pb age (Figure 4.4) constrain the age of the western portion of the Johnston Complex to a hitherto unidentified younger expression of the Main Magmatic Event. The ca. 615 Ma zircon core age is coeval with a 614 ± 2 Ma age reported for the Arfon Group (Figure 4.8) (Tucker and Pharaoh, 1991), pointing towards an interval of calc-alkaline plutonism in the Cymru Terrane at this time (Schofield et al., 2016). Furthermore, zircon U-Pb data from the Fenland Terrane also

record magmatism at 615 ± 6 Ma (Noble et al., 1993). Based on the shared ca. 615 Ma age and ƐNd signatures, Schofield et al. (2016) posited that the Fenland Terrane, Arfon and Sarn Complex were the disrupted remains of a single basement unit. The context of the Johnston Complex to this purported basement block remains enigmatic as we report only two ca. 615 Ma grain cores; nonetheless, it is noteworthy that magmatism of this age has not been documented from the Cymru, Wrekin, and Charnwood Terranes (Schofield et al., 2016).

Despite their close geographical proximity (Figure 4.1), the relationship between the Pebidian Group and Johnston Complex remains unresolved, and this has led to these two inliers having variable terrane classifications, see McIlroy and Horak (2006) cf. Pharaoh and Carney (2000). A minimum age of ca. 587 +25/-14 Ma is reported for the Pebidian Group from the cross-cutting St. David's granophyre (Patchett and Jocelyn, 1979). The ca. 570 Ma age obtained from zircon and apatite in this study, combined with the strongly calc-alkaline affinities of both inliers, point towards a genetic relationship between the Pebidian Supergroup and Johnston Complex, thereby supporting the position of the Complex within the Cymru Terrane. If so, the coastal pluton of the Johnston Complex would be constrained to the final stage of magmatism, defined by the transition from a magmatic-dominated regime to one of sedimentation and oblique terrane dispersal (Pharaoh and Carney, 2000; Woodcock et al., 2012).

McIlroy and Horak (2006) posited that the Welsh Borderland Fault System (WBFS, Figure 4.1) represented a terrane boundary between the Wrekin and Cymru Terrane. The combined ca. 570 Ma apatite and zircon magmatic crystallisation age and their continental-arc geochemical signatures support the association of the Johnston Complex to the Cymru Terrane. Northern constituents of the Cymru Terrane (e.g., Arfon Group and Sarn Complex) share a geochemical affinity to the Pebidian Supergroup and Johnston Complex. To the east, the undated Coomb Volcanic Formation differs significantly, possessing intra-continental bimodal geochemical signatures (Figure 4.1) (Bevins et al., 1995). Other components of the Wrekin Terrane, such as the Longmyndian and Uriconian Groups, also share a pronounced intra-plate geochemistry, suggesting a decreasing influence of subduction-related magmatism towards the east (McIlroy and Horak, 2006). We therefore suggest that the eastern margin of the Johnston Complex, the inferred extension of the Carreg Cennen Fault, is a terrane boundary separating the Cymru and Wrekin Terranes (Figure 4.1).

The relationship between the Benton Volcanic Group and the Johnston Complex is uncertain (Figure 4.1). Nonetheless, the entrainment of both inliers within the Johnston-Benton

thrust zone and their shared calc-alkaline chemistry (Bevins et al., 1995; Thorpe, 1972) implies a common magmatic source for both units. The rhyolitic lavas and tuffs of the Benton Group are posited to represent more evolved expressions of eruptives in the Pebidian Supergroup to the north (Baker, 1982; Bevins et al., 1995). Given the potential linkage between the Pebidian and Johnston Complex, the Benton Group warrants further analysis to determine its broader terrane affinity and relationship to the Johnston Complex. The Johnston Complex now provides constraints on the evolution of the Cymru Terrane itself, representing some of the oldest ca. 640 Ma (Patchett and Jocelyn, 1979) and youngest ca. 615 – 570 Ma magmatism in the area.

4.5.2. Zircon Geochemistry: Continental Magmatic Arc Affinities

Previous accounts of the geochemistry of the Cymru Terrane (Bevins et al., 1995; Pharaoh et al., 1987; Thorpe, 1972) have reported calc-alkaline geochemical signatures consistent with subduction-related continental arc magmatism. New zircon and apatite data reinforce these earlier interpretations and provide insights into the geochemistry of late-Main Stage magmatism in the Cymru Terrane. The chondrite normalised (Boynton, 1984) REE plots for zircon of the Johnston Complex show positive sloping trends with Ce and Sm enrichment and Pr and Eu depletion (Figure 4.5). Oxidised Ce^{4+} is more compatible with zircon than more reduced cations of Ce (Belousova et al., 2002b). Accordingly, the positive cerium anomaly (+1.48, Figure 4.5) is a broad reflection of the oxidised nature of the source magma for the Complex (Belousova et al., 2002b). Subduction-derived melts are typically oxidised, with the zircon Ce enrichment of the Johnston Complex analogous to the modern Indonesian subduction system (Bénard et al., 2018; Woodcock et al., 2012).

Zircon crystals derived from fractionated granitoid melts generally show a negative Eu anomaly, representing Eu^{2+} sequestration during oligoclase and andesine crystallisation. The zircon Eu anomaly reported here (0.28) is consistent with an evolved source melt and the high abundance of plagioclase within the quartz diorite of the Complex (Figure 4.2).

Geochemical data suggest that evolved calc-alkaline plutonism persisted in the Cymru Terrane to at least ca. 570 Ma, and the emplacement of the Johnston Complex was, therefore, contemporaneous with the terrane dispersal and oblique convergence associated with the final stage of Neoproterozoic magmatism in southern Britain (Pharaoh and Carney, 2000). The geochemical profiles of the Johnston Complex and the Pebidian Supergroup represent an archive of the evolving tectonic setting of the Cymru Terrane from a time of mid-crustal plutonism at ca. 640 – 615 Ma (Johnston Complex) to intercalated volcanism and sedimentation within the Welsh Basin during the Palaeozoic (Pebidian Supergroup). Late-Neoproterozoic < 580 Ma components of the Wrekin Terrane, such as the Uriconian and Warren House Groups, have geochemical affinities that shifted towards more intra-plate bi-modal components. Such geochemical trends point towards later arc-rifting, i.e. suggesting a more distal location from the subducting front for these units (Bevins et al., 1995; Pharaoh and Carney, 2000). Our geochemical data (Figure 4.5) are consistent with the Johnston Complex retaining a uniform evolved calc-alkaline magmatic signature from ca. 640 to 570 Ma, suggesting a lack of source magma modification before terrane dispersal after ca. 570 Ma.

4.5.3. Apatite Geochemistry: Gondwanan S-type Granite Production

Unlike zircon from the Johnston Complex, apatites do not show a pronounced Ce anomaly (Ce/Ce* = 0.02) (Figure 4.7). Such a trend is typical in evolved felsic melts, where Ce is sequestered into fractionating plagioclase (London, 1992). Although Ce sequestration can occur into epidote-group minerals (Glorie et al., 2019), this process appears minimal in the Johnston Complex, given the absence of primary epidote-group minerals or allanite (Figure 4.2).

Sha and Chappell (1999) demonstrated that apatites in S-type and I-type granites show a chondrite-normalised depletion in Th and LREEs and, thus, a shallower slope, which flattens with increasing atomic mass in REE plots (Figure 4.7). Conversely, I-type granites can typically show a distinct enrichment in LREE and HREEs, compared to U and MREEs – a trend not evident in apatite from the Johnston Complex. Instead, the apatite has a negatively sloping REE trend, with a moderate negative Eu anomaly of 0.35 and a mean $(Ce/Yb)_{cn}$ of 7.3, typical of apatite grains derived from evolved granitoids (Figure 4.7) (Belousova et al., 2002a; Chu et al., 2009; Sha and Chappell, 1999). Accordingly, the Johnston Complex apatite falls within the range of S-type granites compiled by O'Sullivan et al. (2020) (Figure 4.7). The mineralogy of the Johnston Complex is also consistent with an S-type source, including apatite being relatively abundant (~0.20% modal abundance) and an absence of diagnostic minerals for I-type granites such as allanite and magnetite (Chappell and White, 2001). The predominant association of zircon within altered mafic minerals (chlorite and hornblende) in the Complex (Figure 4.3) is also consistent with an S-type classification (Clemens et al., 2016).

Continental arc granitoids, such as the Johnston Complex (Figure 4.8), typically form by melting pre-existing crust with potential input from juvenile material (Hawkesworth et al., 2010). I-type felsic melts can transition to a more peraluminous composition following assimilation with material derived from subduction, such as greywackes and shales (Chappell and White, 2001). Extensive continental collision and orogenesis, associated with the assembly of Gondwana, were posited to have led to the uplift and production of giant turbidite fans (Zhu et al., 2020). Erosion of the uplifted hinterland supported prolonged delivery of supracrustal detritus via subduction-related erosion followed by transfer to the upper plate. Our data suggest the Johnston Complex, an S-type granite from a peri-Gondwanan terrane, is a consequence of this process.

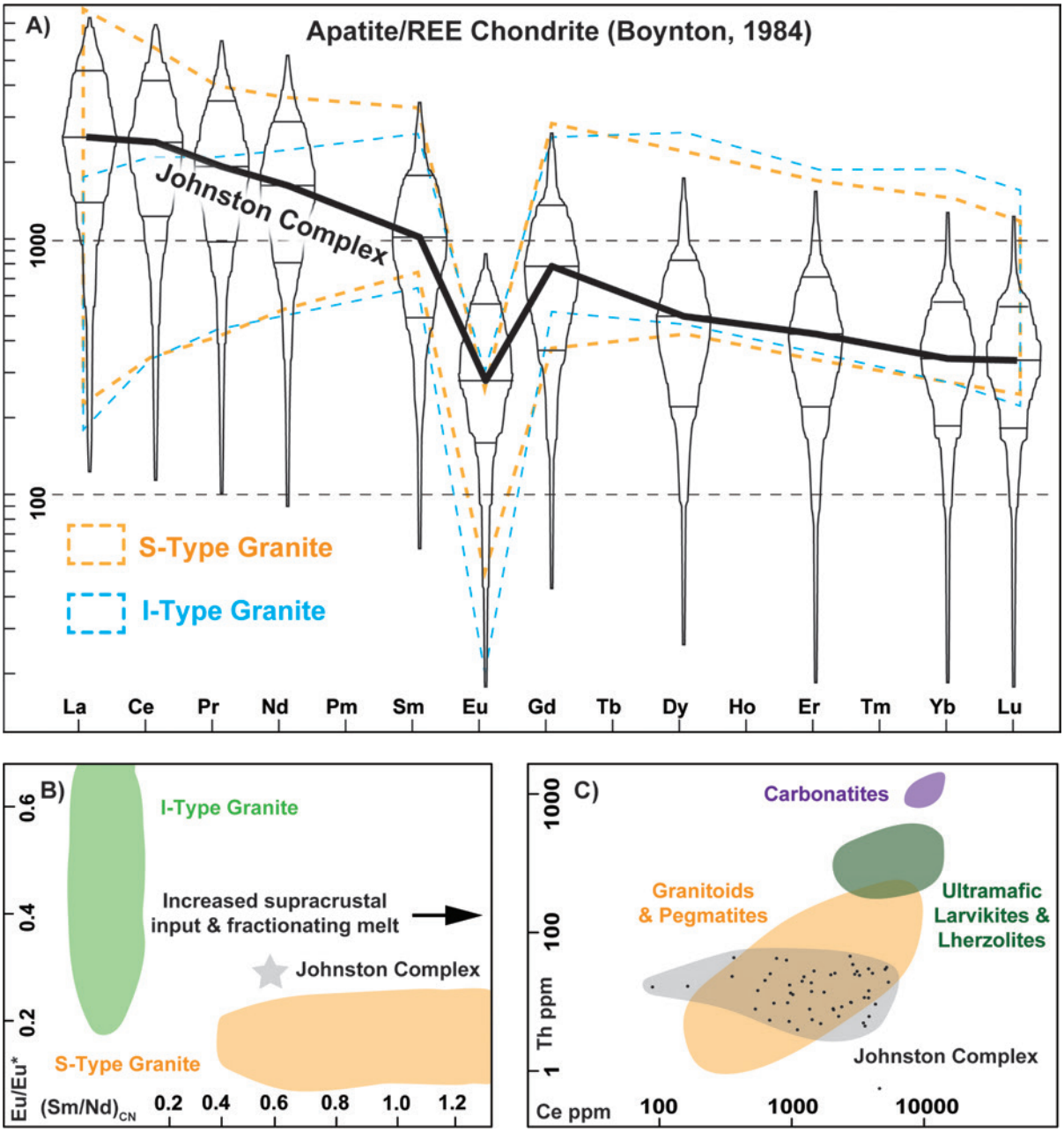

Figure 4.7. Apatite geochemistry discrimination diagrams. ***A)*** *REE chondrite normalised apatite multi-element plot (Boynton, 1984). Compositional data for granitoids from O'Sullivan et al. (2020).* ***B)*** *Bivariate plot of the mean europium anomaly* $(Eu/Eu^*)_c$ *vs chondrite normalised* Sm/Nd_c. *Contoured compositional fields after Sha and Chappell (1999).* ***C)*** *Bivariate plot of apatite Th vs Ce abundance. Compositional reference fields adapted after Belousova et al. (2002a).*

4.5.4. Coupled Apatite-Zircon Analyses in S-type Granitoids

Obtaining primary magmatic crystallisation ages can be challenging for S-type granites due to the common presence of inherited zircons, with difficulties in definitively identifying neoblastic growth in such rocks (Collins et al., 2021; Kelsey et al., 2022). Differentiating primary vs inherited zircon has important implications for accurate terrane classification, where zircon U-Pb crystallisation ages are often the key discrimination or association parameter between disparate inliers (Pharaoh and Carney, 2000; Schofield et al., 2016).

Given solubility considerations, apatite is much less likely to be an inherited phase in felsic melts than zircon (Wolf and London, 1994). Where both zircon and apatite yield similar crystallisation ages, and the host rock shows little evidence of recrystallisation, this provides a compelling case for coeval magmatic growth. Coeval ages for both minerals also imply rapid cooling (i.e. shallow, epizonal emplacement) through the radiogenic Pb closure temperature of both minerals (zircon ≥ 900°C and apatite ≥ 350°C) (Figure 4.4) (Chew and Spikings, 2021).

Apatite and zircon ages at ca. 570 Ma for the Johnston Complex imply that calc-alkaline magmatism was ongoing during the final stages of Eastern Avalonian arc magmatism in the Cymru Terrane (Woodcock et al., 2012). Across the inliers of southern Britain, an absence of calc-alkaline magmatism post ca. 570 Ma has been attributed to the increasingly oblique convergence of East Avalonia with Laurentia and the detachment of coherent geology into tectonic slivers and subsequent terrane dispersal (Figure 4.9) (Horak et al., 1996; Woodcock et al., 2012). The rapid cooling of the Johnston Complex at ca. 570 Ma and its low metamorphic grade is consistent with structurally controlled emplacement into the shallow crust. Increasing rates of oblique convergence and transpression along strike-slip faults have been proposed to reduce the geothermal gradient of mid to upper-crustal sections (Alvarado et al., 2016; Collett et al., 2019). Hence, the 570 Ma age of the Johnston Complex is consistent with Eastern Avalonian terrane dispersal along the subduction front (Woodcock et al., 2012). During this process, strike-slip faults would have provided conduits for melt emplacement and crystallization of the Johnston Complex at shallow, epizonal depths (Murphy et al., 2022).

In addition, these new data imply that the Johnston Complex has undergone minimal thermal disturbance following magmatic crystallisation at ca. 570 Ma. The U-Pb closure temperature of apatite is highly dependent on microstructures, grain size and cooling rates. Consequently, reported closure temperatures range between 350 – 600°C (Chew and Spikings, 2015; Kirkland et al., 2018). Nonetheless, apatite U-Pb ages typically represent metamorphic

perturbances at mid to upper-crust conditions or protracted cooling through the closure temperature range (Chew and Spikings, 2015; Gillespie et al., 2022; Kirkland et al., 2018). The similarity between apatite and zircon U-Pb ages implies that the Johnston Complex cannot have resided at temperatures ≥ 350°C for a protracted period. Rather, the isotopic data imply rapid cooling through both minerals' U-Pb closure temperatures. Rapid cooling at a relatively shallow depth of emplacement is consistent with the coeval crystallisation of apatite and zircon within this constituent body of the Johnston Complex (Figure 4.1).

K–Ar hornblende data from another coastal outcrop of the Complex has yielded ca. 612 – 624 Ma ages, and biotite from the Dutch Gin series, a so-called metre-scale band of localised deformation at the western margin of the Complex, yields a K-Ar date of ca. 612 Ma (Thorpe, 1979). The relatively lower closure temperature of the K-Ar system in both minerals (300 – 600°C) (Harrison, 1982) further suggests that the Complex experienced minimal post-magmatic thermal perturbations. The Johnston Complex is now bound within a Variscan thrust zone and was also emplaced prior to the Caledonian orogeny, yet neither tectonic event caused extensive metamorphism of the Complex (Patchett and Jocelyn, 1979; Thorpe, 1972). Indeed, across the Neoproterozoic rocks of southwest Wales, metamorphism is limited to prehnite-pumpellyite facies (Figure 4.1) (Thorpe, 1972).

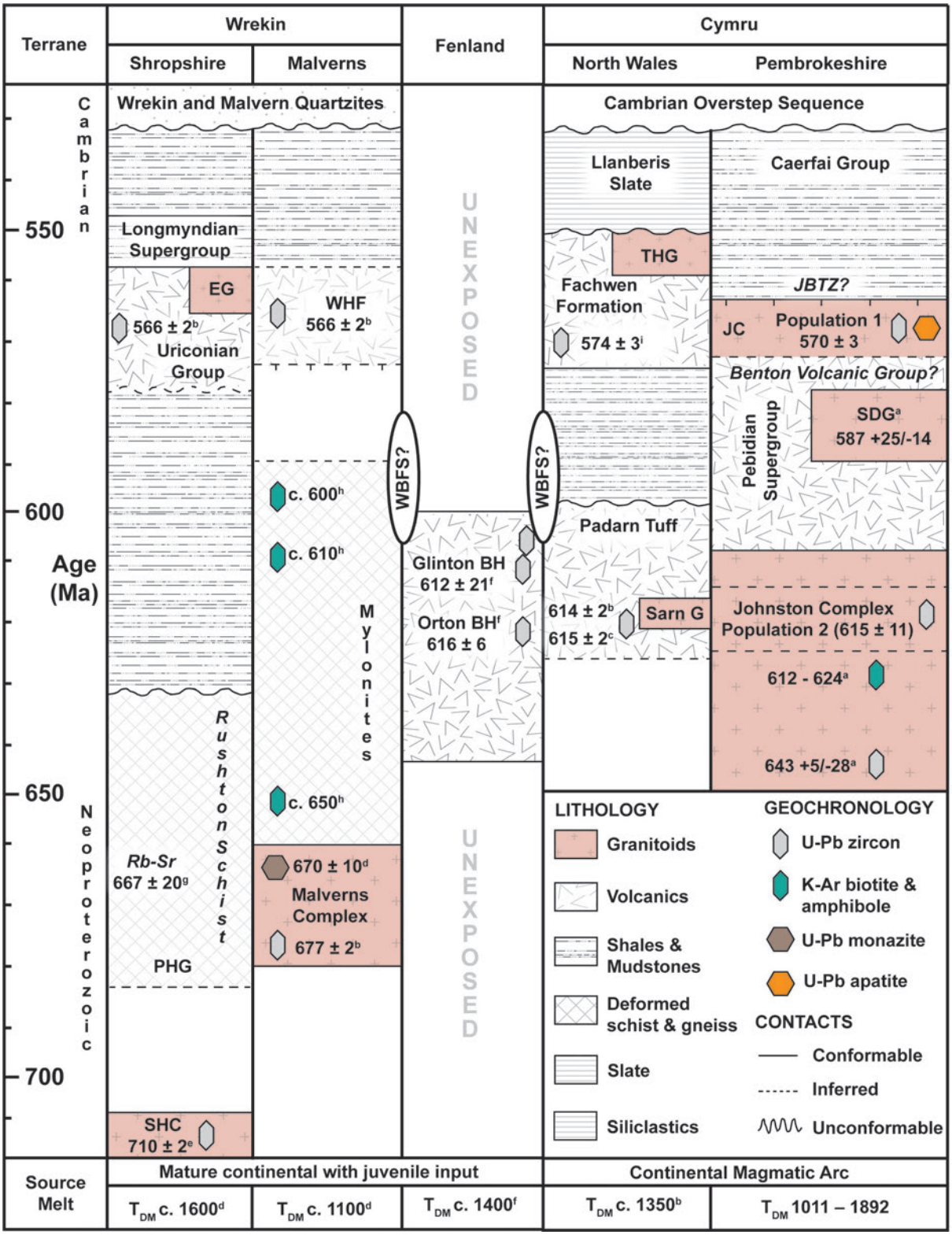

Figure 4.8. A stratigraphic terrane correlation chart of select areas adapted after Pharaoh and Carney (2000). Abbreviations include WBFS = Welsh Borderland Fault System, SHC = Stanner-Hanter Complex, THG = Twt Hill Group, SDG = St. David's Granophyre, BH = Bore-hole data, EG = Ercall Granophyre, JBTZ = Johnston Benton Thrust Zone. Data sources are listed in superscript letters and include a) Patchett and Jocelyn (1979), b) Tucker and Pharaoh (1991), c) Horak et al. (1996), d) Thorpe et al. (1984), e) Schofield et al. (2010), f) Noble et al. (1993), g) Beckinsale et al. (1984), h) Strachan et al. (1996), i) Compston et al. (2002).

4.5.5 Zircon Lu-Hf: A Mesoproterozoic Source Melt?

Zircon ƐHf data for ca. 570 Ma crystals (Population 1) forms a broadly sub-chondritic cluster, with a mean ƐHf of -0.41 ± 1.38. The older ca. 615 Ma (Population 2) cores have ƐHf values that are not significantly different (Figure 4.5), suggesting that both magmatic episodes were derived from compositionally similar sources (at least in terms of Lu/Hf ratio) that did not undergo significant evolution or modification during the ca. 615 – 570 Ma interval.

A Lu/Hf ratio of 0.05 was chosen to reflect a felsic source for the parental melt of the Johnston Complex, consistent with other S-type Proterozoic granitoids from the database compiled by Bea et al. (2018). Two-stage depleted mantle Lu-Hf model ages (T_{DM}^2) imply late Mesoproterozoic 1011 – 1892 Ma crust-extraction dates, with a mean T_{DM}^2 of 1521 Ma. Model ages, especially in the case of S-type granitoids, may only provide a minimum age for the oldest component within a mixed magma. Nonetheless, the zircon Hf isotopic signature, with a source crustal residence time of at least 800 – 500 Ma, is similar to other Avalonian granitoids (Figure 4.6) (Henderson et al., 2016; Pollock et al., 2015; Schofield et al., 2016).

A whole rock ƐNd value of -1.8 with a T_{DM}^2 of 1437 Ma was reported for the Johnston Complex from the inland outcrop (Schofield et al., 2016). Along with the Lu-Hf T_{DM}^2 for zircon reported here, these data imply variable degrees of crustal contamination. Complementary ƐHf data from Western Avalonia granitoids yield analogous late Mesoproterozoic T_{DM}^2 ages, implying a similar source for most Avalonian micro-continental blocks during the late Neoproterozoic (Figure 4.6) (Henderson et al., 2016; Pollock et al., 2015; Willner et al., 2013).

Although localised areas of considerably older Proterozoic ≥ 1.6 Ga crust in West Avalonia have been inferred by ƐHf data (Henderson et al., 2016; Pollock et al., 2015; Willner et al., 2013), there is no evidence of similarly ancient crust based on the sparse Lu-Hf dataset for the Cymru Terrane. Nonetheless, the presence of older, mid-Proterozoic crustal components within the Cymru Terrane is implied by Sm–Nd model ages of ca. >1.35 Ga for the Parwyd Gneisses and Sarn Granites (Figure 4.1) (McIlroy and Horak, 2006). Other areas show more definitive evidence of older underlying crust. For example, the Malverns Complex (Figure 4.1) has yielded inherited zircon age maxima of ca. 1.6 Ga and whole-rock Sm-Nd model ages of ca. 1.4 – 1.6 Ga (McIlroy and Horak, 2006; Murphy et al., 2000). Such older crustal components provide an important distinction between the Cymru and Wrekin Terranes, in which the latter appears to incorporate an older crustal component.

Zircon data from other East Avalonian lithologies also show similar ƐHf patterns to the Johnston Complex. For example, zircon grains from the Stavelot-Venn Massif of East Avalonia imply felsic melt generation from a chondritic source of similar age and composition to the Johnston Complex (Figure 4.6) (Willner et al., 2013). Hence, ƐHf data from the Johnston Complex, when considered with data from other terranes, support the interpretation that Avalonian terranes formed from a relatively uniform Neoproterozoic continental arc system with a broadly chondritic melt source (Figure 4.6) (Pollock et al. (2015) variably contaminated with older Meso to Paleoproterozoic crust (e.g. Wrekin Terrane) (Thorpe et al., 1984). This contamination could represent localised input into the subduction system of allochthonous structurally emplaced older crust during the Proterozoic (Pollock et al., 2015).

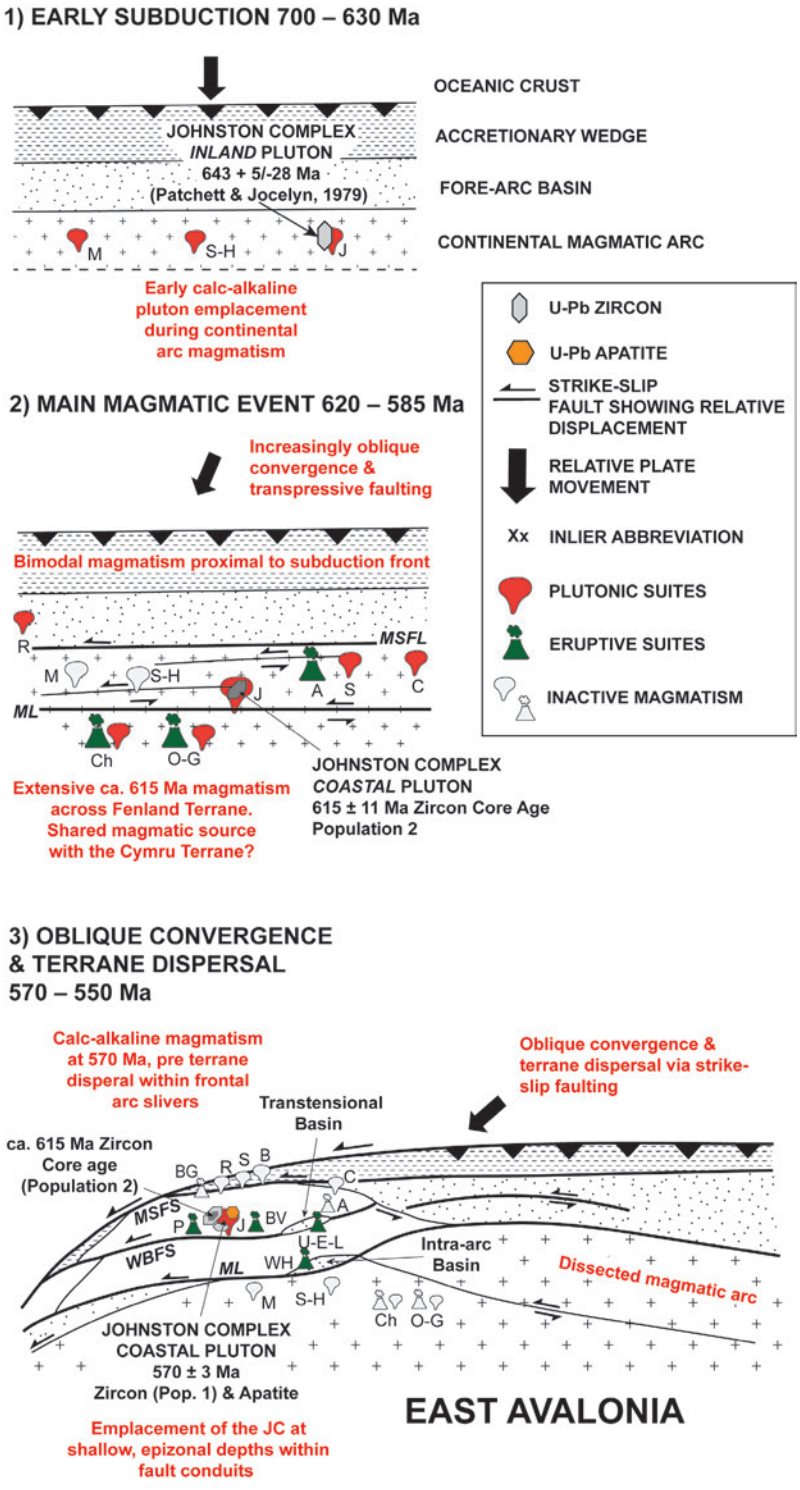

Figure 4.9. Schematic model showing the late-Neoproterozoic evolution of the Johnston Complex within the East Avalonian tectonic regime. Model adapted after Horak et al. (1996) and Pharaoh and Carney (2000). Abbreviations include: WBFS = Welsh Borderland Fault System, MSFS = Menai Strait Fault System, ML = Malverns Lineament, A= Arfon Group, B= Anglesey Blueschists, BG = Bwlch Gwyn Tuff, BV = Benton Volcanic Group, C = Coedana Complex, Ch = Charnian Supergroup, J = Johnston Complex, P = Pebidian Supergroup, O-G = Orton and Glinton Bore holes, R = Rosslare Complex, S = Sarn Complex, S-H = Stanner-Hanter Complex, U-E-L = Uriconian Volcanics, Ercall Granophyre, Longmyndian Supergroup, WH = Warren House Volcanics.

4.6. Conclusions

Time-constrained (U–Pb) isotopic (Lu–Hf) and trace element data from the Johnston Complex, Wales, help constrain magmatism in East Avalonia during the late Neoproterozoic. We report ages for a coastal pluton of the Complex from coeval apatite and zircon at 570 ± 3 Ma. Combined with a previously reported age of ca. 643 Ma for an inland component, we demonstrate that the Complex is a composite suite of quartz diorite plutons along its ca. 20 km length (Figure 4.9). Our data necessitate that calc-alkaline igneous activity was ongoing to ca. 570 Ma in East Avalonia.

Apatite and zircon geochemistry provide complementary insights into late Neoproterozoic magmatism in southern Britain. Zircon trace elements demonstrate an oxidised calc-alkaline source magma typical of the Complex's ensialic subduction belt setting. A sedimentary component within the melt is revealed through apatite trace element profiles, consistent with voluminous S-type granitoid production during the assembly of Gondwana. ƐHf values imply a broadly chondritic source melt for both zircon populations with a mean T_{DM}^2 of 1.5 Ga.

Classification of the Precambrian terranes of southern Britain has primarily been facilitated through correlating geochemical signatures, structural relationships, and Nd (model) ages. Generally, sparse U-Pb magmatic crystallisation dates have underpinned associations of otherwise disparate lithologies into unified terranes. Given this approach, the presented work offers a cautionary note. On the km scale, the Johnston Complex varies in age by over ca. 40 Ma (Figure 4.9). Although individual zircon grains trace a multi-stage history with components at ca. 615 and 570 Ma, the combined zircon-apatite approach gives confidence in magmatic age assignment and facilitates terrane association in partially obscured basement areas.

Thus, when the closure temperature of Pb in apatite has not been exceeded, applying combined zircon and apatite geochronology may remove some ambiguity related to zircon inheritance when dating rocks.

4.7. Acknowledgments

This research was funded by an Australian Research Council Discovery Project (DP200101881). The authors thank Bradley McDonald and Noreen Evans for assistance with LA-ICP-MS data collection. Instruments in the John deLaeter Centre, Curtin University, were funded via AuScope, the Australian Education Investment Fund, the National Collaborative Research Infrastructure Strategy, and the Australian Government. We thank Brendan Murphy and Damian Nance for reviews that improved this work and Yildirim Dilek for facilitating a constructive review process.

4.8. Data Availability

Isotopic data and trace element data for zircon (U–Pb, Lu–Hf) and apatite (U–Pb & trace element) are available online as Supplementary Information 1 – 2 via *DOI: 10.1144/jgs2022-178 and 10.6084/m9.figshare. c.6484464.v2*.

4.9. References

Alvarado, A., Audin, L., Nocquet, J. M., Jaillard, E., Mothes, P., Jarrín, P., Segovia, M., Rolandone, F., and Cisneros, D., 2016, Partitioning of oblique convergence in the Northern Andes subduction zone: Migration history and the present-day boundary of the North Andean Sliver in Ecuador: Tectonics, v. 35, no. 5, p. 1048-1065.

Azadbakht, Z., Lentz, D., and McFarlane, C., 2018, Apatite Chemical Compositions from Acadian-Related Granitoids of New Brunswick, Canada: Implications for Petrogenesis and Metallogenesis: Minerals, v. 8, no. 12.

Bacon, C. R., 1989, Crystallization of accessory phases in magmas by local saturation adjacent to phenocrysts: Geochimica et Cosmochimica Acta, v. 53, no. 5, p. 1055-1066.

Baker, J. W., 1982, The Precambrian of south-west Dyfed, south-west Wales, *in* Bassett, M. G., ed., Geological excursions in Dyfed, south-west Wales: Cardiff, National Museum of Wales, p. 15-25.

Bea, F., Montero, P., Molina, J. F., Scarrow, J. H., Cambeses, A., and Moreno, J. A., 2018, Lu-Hf ratios of crustal rocks and their bearing on zircon Hf isotope model ages: The effects of accessories: Chemical Geology, v. 484, p. 179-190.

Beckinsale, R. D., Evans, J. A., Thorpe, R. S., Gibbons, W., and Harmon, R. S., 1984, Rb-Sr whole-rock isochron ages, $\delta^{18}O$ values and geochemical data for the Sarn Igneous Complex and the Parwyd gneisses of the Mona Complex of Llŷn, N Wales: Journal of the Geological Society, v. 141, no. 4, p. 701-709.

Belousova, E., Griffin, W., O'Reilly, S. Y., and Fisher, N., 2002a, Apatite as an indicator mineral for mineral exploration: Trace-element compositions and their relationship to host rock type: Journal of Geochemical Exploration, v. 76, p. 45-69.

Belousova, E., Griffin, W., O'Reilly, S. Y., and Fisher, N., 2002b, Igneous zircon: trace element composition as an indicator of source rock type: Contributions to Mineralogy and Petrology, v. 143, no. 5, p. 602-622.

Bénard, A., Klimm, K., Woodland, A. B., Arculus, R. J., Wilke, M., Botcharnikov, R. E., Shimizu, N., Nebel, O., Rivard, C., and Ionov, D. A., 2018, Oxidising agents in sub-arc mantle melts link slab devolatilisation and arc magmas: Nature Communications, v. 9, no. 1, p. 3500.

Bevins, R., Pharaoh, T., Cope, J., and Brewer, T., 1995, Geochemical character of Neoproterozoic volcanic rocks in southwest Wales: Geological Magazine, v. 132, p. 339-349.

Bloxam, T. W., and Dirk, M. H. J., 1988, The petrology and geochemistry of the St. David's Granophyre and the Cwm Bach Rhyolite, Pembrokeshire, Dyfed: Mineralogical Magazine, v. 52, no. 368, p. 563-575.

Boynton, W. V., 1984, Chapter 3 - Cosmochemistry of the Rare Earth Elements: Meteorite Studies, *in* Henderson, P., ed., Developments in Geochemistry, Volume 2, Elsevier, p. 63-114.

Cantrill, T. C., Dixon, E. E. L., Thomas, H. W., and Jones, O. T., 1916, The geology of the south Wales Coalfield, Part XII, The country around Milford: His Majesty's Stationery Office.

Cawood, P. A., Martin, E. L., Murphy, J. B., and Pisarevsky, S. A., 2021, Gondwana's interlinked peripheral orogens: Earth and Planetary Science Letters, v. 568.

Chappell, B. W., and White, A. J. R., 2001, Two contrasting granite types: 25 years later: Australian Journal of Earth Sciences, v. 48, no. 4, p. 489-499.

Chew, D. M., and Spikings, R. A., 2015, Geochronology and Thermochronology Using Apatite: Time and Temperature, Lower Crust to Surface: Elements, v. 11, no. 3, p. 189-194.

Chew, D. M., and Spikings, R. A., 2021, Apatite U-Pb Thermochronology: A Review: Minerals, v. 11, no. 10.

Chu, M. F., Wang, K. L., Griffin, W., Chung, S. L., O'Reilly, S. Y., Pearson, D. G., and Iizuka, Y., 2009, Apatite Composition: Tracing Petrogenetic Processes in Transhimalayan Granitoids: Journal of Petrology, v. 50, no. 10, p. 1829-1855.

Clemens, J. D., Buick, I. S., and Kisters, A. F. M., 2016, The Donkerhuk batholith, Namibia: A giant S-type granite emplaced in the mid crust, in a fore-arc setting: Journal of the Geological Society, v. 174, no. 1, p. 157-169.

Collett, C. M., Duvall, A. R., Flowers, R. M., Tucker, G. E., and Upton, P., 2019, The Timing and Style of Oblique Deformation Within New Zealand's Kaikōura Ranges and Marlborough Fault System Based on Low-Temperature Thermochronology: Tectonics, v. 38, no. 4, p. 1250-1272.

Collins, W. J., Murphy, J. B., Blereau, E., and Huang, H. Q., 2021, Water availability controls crustal melting temperatures: Lithos, v. 402-403, p. 106351.

Compston, W., Wright, A. E., and Toghill, P., 2002, Dating the Late Precambrian volcanicity of England and Wales: Journal of the Geological Society, v. 159, no. 3, p. 323-339.

Dumitru, T. A., 2016, A New Zircon Concentrating Table Designed for Geochronologists, American Geophysical Union, Volume 2016: San Francisco, AGU Fall Meeting Abstracts, p. 23-2956.

Elburg, M. A., 1996, U-Pb ages and morphologies of zircon in micrograniteoid enclaves and peraluminous host granite: evidence for magma mingling: Contributions to Mineralogy and Petrology, v. 123, no. 2, p. 177-189.

Erdmann, S., Wodicka, N., Jackson, S., and Corrigan, D., 2013, Zircon textures and composition: Refractory recorders of magmatic volatile evolution?: Contributions to Mineralogy and Petrology, v. 165.

Fisher, C. M., Vervoort, J. D., and DuFrane, S. A., 2014a, Accurate Hf isotope determinations of complex zircons using the "laser ablation split stream" method: Geochemistry, Geophysics, Geosystems, v. 15, no. 1, p. 121-139.

Fisher, C. M., Vervoort, J. D., and Hanchar, J. M., 2014b, Guidelines for reporting zircon Hf isotopic data by LA-MC-ICPMS and potential pitfalls in the interpretation of these data: Chemical Geology, v. 363, p. 125-133.

Gillespie, J., Kirkland, C. L., Kinny, P. D., Simpson, A., Glorie, S., and Rankenburg, K., 2022, Lu–Hf, Sm–Nd, and U–Pb isotopic coupling and decoupling in apatite: Geochimica et Cosmochimica Acta, v. 338, p. 121-135.

Glorie, S., Jepson, G., Konopelko, D., Mirkamalov, R., Meeuws, F., Gilbert, S., Gillespie, J., Collins, A. S., Xiao, W., Dewaele, S., and De Grave, J., 2019, Thermochronological and geochemical footprints of post-orogenic fluid alteration recorded in apatite: Implications for mineralisation in the Uzbek Tian Shan: Gondwana Research, v. 71, p. 1-15.

Grimes, C. B., Wooden, J. L., Cheadle, M. J., and John, B. E., 2015, "Fingerprinting" tectono-magmatic provenance using trace elements in igneous zircon: Contributions to Mineralogy and Petrology, v. 170, no. 5, p. 46.

Harrison, T. M., 1982, Diffusion of ^{40}Ar in hornblende: Contributions to Mineralogy and Petrology, v. 78, no. 3, p. 324-331.

Hawkesworth, C. J., Dhuime, B., Pietranik, A. B., Cawood, P. A., Kemp, A. I. S., and Storey, C. D., 2010, The generation and evolution of the continental crust: Journal of the Geological Society, v. 167, no. 2, p. 229-248.

Henderson, B. J., Collins, W. J., Murphy, J. B., Gutierrez-Alonso, G., and Hand, M., 2016, Gondwanan basement terranes of the Variscan–Appalachian orogen: Baltican, Saharan

and West African hafnium isotopic fingerprints in Avalonia, Iberia and the Armorican Terranes: Tectonophysics, v. 681, p. 278-304.

Horak, J., Doig, R., Evans, J., and Gibbons, W. D., 1996, Avalonian magmatism and terrane linkage: New isotopic data from the Precambrian of North Wales: Journal of the Geological Society, v. 153, p. 91-99.

Jackson, S. E., Pearson, N. J., Griffin, W. L., and Belousova, E. A., 2004, The application of laser ablation-inductively coupled plasma-mass spectrometry to in situ U–Pb zircon geochronology: Chemical Geology, v. 211, no. 1, p. 47-69.

Jochum, K. P., Nohl, U., Herwig, K., Lammel, E., Stoll, B., and Hofmann, A. W., 2005, GeoReM: A New Geochemical Database for Reference Materials and Isotopic Standards: Geostandards and Geoanalytical Research, v. 29, no. 3, p. 333-338.

Kelsey, D. E., Wingate, M., Spaggiari, C. V., Smithies, R. H., Fielding, I. O. H., Lu, Y., Porter, J. K., and Finch, E. G., 2022, Crystalline basement beneath the eastern Canning Basin at the Top Up Rise prospect, Perth, Geological Survey of Western Australia, Accelerated Geoscience Program (AGP), 16 p.:

Kirkland, C. L., Hollis, J., Danišík, M., Petersen, J., Evans, N. J., and McDonald, B. J., 2017, Apatite and titanite from the Karrat Group, Greenland; implications for charting the thermal evolution of crust from the U-Pb geochronology of common Pb-bearing phases: Precambrian Research, v. 300, p. 107-120.

Kirkland, C. L., Yakymchuk, C., Szilas, K., Evans, N., Hollis, J., McDonald, B., and Gardiner, N. J., 2018, Apatite: a U-Pb thermochronometer or geochronometer?: Lithos, v. 318-319, p. 143-157.

London, D., 1992, Phosphorus in S-type magmas: The P_2O_5 content of feldspars from peraluminous granites, pegmatites, and rhyolites: American Mineralogist, v. 77, no. 1-2, p. 126-145.

McDowell, F., McIntosh, W., and Farley, K., 2005, A precise ^{40}Ar–^{39}Ar reference age for the Durango apatite (U–Th)/He and fission-track dating standard: Chemical Geology, v. 214, no. 3-4, p. 249-263.

McIlroy, D., and Horak, J., 2006, The Neoproterozoic of England and Wales, *in* Brenchly, P. J., and Rawson, P. F., eds., The Geology of England and Wales: London, Geological Society of London, p. 9-24.

Meert, G. J., and Van Der Voo, R., 1997, The assembly of Gondwana 800-550 Ma: Journal of Geodynamics, v. 23, no. 3, p. 223-235.

Miller, J. S., Matzel, J. E. P., Miller, C. F., Burgess, S. D., and Miller, R. B., 2007, Zircon growth and recycling during the assembly of large, composite arc plutons: Journal of Volcanology and Geothermal Research, v. 167, no. 1, p. 282-299.

Morel, M. L. A., Nebel, O., Nebel-Jacobsen, Y., Miller, J., and Vroon, P. Z., 2008, Hafnium isotope characterization of the GJ-1 zircon reference material by solution and laser-ablation MC-ICPMS: Chemical Geology, v. 255, p. 231-235.

Murphy, J. B., Collins, W. J., and Archibald, D. B., 2022, Logan Medallist 7. Appinite Complexes, Granitoid Batholiths and Crustal Growth: A Conceptual Model: Geoscience Canada, v. 49, no. 3-4, p. 237-249.

Murphy, J. B., Strachan, R. A., Nance, R. D., Parker, K. D., and Fowler, M. B., 2000, Proto-Avalonia: A 1.2–1.0 Ga tectonothermal event and constraints for the evolution of Rodinia: Geology, v. 28, no. 12, p. 1071-1074.

Nance, R. D., Murphy, J. B., Strachan, R. A., Keppie, J. D., Gutiérrez-Alonso, G., J., F.-S., Quesada, C., Linnemann, U., D'Lemos, R. S., and Pisarevsky, A. S., 2008, Neoproterozoic-Early Palaeozoic tectonostratigraphy and palaeogeography of the peri-Gondwanan terranes: Amazonian v. West African connections: Geological Society London Special Publications, v. 297, p. 345–383.

Noble, S. R., Tucker, R. D., and Pharaoh, T. C., 1993, Lower Palaeozoic and Precambrian igneous rocks from eastern England, and their bearing on late Ordovician closure of the Tornquist Sea: constraints from U-Pb and Nd isotopes: Geological Magazine, v. 130, no. 6, p. 835-846.

O'Sullivan, G., Chew, D. M., Kenny, G., Henrichs, I., and Mulligan, D., 2020, The trace element composition of apatite and its application to detrital provenance studies: Earth-Science Reviews, v. 201.

Patchett, P. J., and Jocelyn, J., 1979, U–Pb zircon ages for late Precambrian igneous rocks in South Wales: Journal of the Geological Society, v. 136, no. 1, p. 13-19.

Pharaoh, T. C., and Carney, J. N., 2000, Introduction to the Precambrian Rocks of England and Wales, *in* Carney, J. N., ed., Geological Conservation Review Series, Volume 138: Peterborough, Joint Nature Conservation Committee, p. 127-136.

Pharaoh, T. C., Webb, P. C., Thorpe, R. S., and Beckinsale, R. D., 1987, Geochemical Evidence for the Tectonic Setting of Late Proterozoic Volcanic Suites in Central England: Geological Society, London, Special Publications, v. 33, no. 1, p. 541-552.

Pollock, J., Sylvester, P., and Barr, S. M., 2015, Lu–Hf zircon and Sm–Nd whole-rock isotope constraints on the extent of juvenile arc crust in Avalonia: examples from

Newfoundland and Nova Scotia, Canada: Canadian Journal of Earth Sciences, v. 52, p. 161-181.

Rino, S., Kon, Y., Sato, W., Maruyama, S., Santosh, M., and Zhao, D., 2008, The Grenvillian and Pan-African orogens: World's largest orogenies through geologic time, and their implications on the origin of superplume: Gondwana Research, v. 14, no. 1, p. 51-72.

Sano, Y., Terada, K., and Fukuoka, T., 2002, High mass resolution ion microprobe analysis of rare earth elements in silicate glass, apatite and zircon: lack of matrix dependency: Chemical Geology, v. 184, no. 3, p. 217-230.

Schmitz, M. D., Bowring, S. A., and Ireland, T. R., 2003, Evaluation of Duluth Complex anorthositic series (AS3) zircon as a U-Pb geochronological standard: new high-precision isotope dilution thermal ionization mass spectrometry results: Geochimica et Cosmochimica Acta, v. 67, no. 19, p. 3665-3672.

Schoene, B., and Bowring, S., 2006, U-Pb systematics of the McClure Mountain syenite: Thermochronological constraints on the age of the $^{40}Ar/^{39}Ar$ standard MMhb: Contributions to Mineralogy and Petrology, v. 151, p. 615-630.

Schofield, D., Millar, I. L., Wilby, P., and Evans, J., 2010, A new, high precision U–Pb date from the oldest known rocks in southern Britain: Geological Magazine, v. 147.

Schofield, D., Potter, J., Barr, S. M., Horák, J. M., Millar, I. L., and Longstaffe, F. J., 2016, Reappraising the Neoproterozoic ‘East Avalonian’ terranes of southern Great Britain: Gondwana Research, v. 35, p. 257-271.

Sha, L. K., and Chappell, B. W., 1999, Apatite chemical composition, determined by electron microprobe and laser-ablation inductively coupled plasma mass spectrometry, as a probe into granite petrogenesis: Geochimica et Cosmochimica Acta, v. 63, no. 22, p. 3861-3881.

Shen, B., Dong, L., Xiao, S., and Kowalewski, M., 2008, The Avalon Explosion: Evolution of Ediacara Morphospace: Science, v. 319, no. 5859, p. 81-84.

Shields-Zhou, G. A., Porter, S., and Halverson, G. P., 2016, A new rock-based definition for the Cryogenian Period (circa 720 - 635 Ma): Episodes, v. 39, no. 1, p. 3-8.

Sláma, J., Košler, J., Condon, D. J., Crowley, J. L., Gerdes, A., Hanchar, J. M., Horstwood, M. S. A., Morris, G. A., Nasdala, L., Norberg, N., Schaltegger, U., Schoene, B., Tubrett, M. N., and Whitehouse, M. J., 2008, Plešovice zircon — A new natural reference material for U–Pb and Hf isotopic microanalysis: Chemical Geology, v. 249, no. 1, p. 1-35.

Stern, R. A., Bodorkos, S., Kamo, S. L., Hickman, A. H., and Corfu, F., 2009, Measurement of SIMS Instrumental Mass Fractionation of Pb Isotopes During Zircon Dating: Geostandards and Geoanalytical Research, v. 33, no. 2, p. 145-168.

Strachan, R. A., Collins, A., Buchan, C., Nance, R. D., Murphy, J. B., and D'Lemos, R. S., 2007, Terrane analysis along a Neoproterozoic active margin of Gondwana: Insights from U-Pb zircon geochronology: Journal of the Geological Society, v. 164, p. 57-60.

Strachan, R. A., Nance, R. D., Dallmeyer, R., D'Lemos, R. S., Murphy, J. B., and Watt, G. R., 1996, Late Precambrian tectonothermal evolution of the Malverns Complex: Journal of the Geological Society, v. 153, p. 589-600.

Thompson, J., Meffre, S., Maas, R., Kamenetsky, V., Kamenetsky, M., Goemann, K., Ehrig, K., and Danyushevsky, L., 2016, Matrix effects in Pb/U measurements during LA-ICP-MS analysis of the mineral apatite: Journal of Analytical Atomic Spectrometry, v. 31, no. 6, p. 1206-1215.

Thorpe, R. S., 1972, Possible subduction origin for two Pre-Cambrian calc-alkaline plutonic complexes from southern Britain: Geological Society of America Bulletin, v. 83, p. 36-63.

Thorpe, R. S., 1979, Late Precambrian igneous activity in Southern Britain: Geological Society, London, Special Publications, v. 8, no. 1, p. 579-584.

Thorpe, R. S., Beckinsale, R. D., Patchett, P. J., Piper, J. D. A., Davies, G. R., and Evans, J. A., 1984, Crustal growth and late Precambrian-early Palaeozoic plate tectonic evolution of England and Wales: Journal of the Geological Society, v. 141, no. 3, p. 521-536.

Tucker, R. D., and Pharaoh, T. C., 1991, U-Pb zircon ages for Late Precambrian igneous rocks in southern Britain: Journal of the Geological Society, v. 148, no. 3, p. 435-443.

Valley, J. W., Cavosie, A. J., Ushikubo, T., Reinhard, D. A., Lawrence, D. F., Larson, D. J., Clifton, P. H., Kelly, T. F., Wilde, S. A., Moser, D. E., and Spicuzza, M. J., 2014, Hadean age for a post-magma-ocean zircon confirmed by atom-probe tomography: Nature Geoscience, v. 7, no. 3, p. 219-223.

Wiedenbeck, M., Allé, P., Corfu, F., Griffin, W. L., Meier, M., Oberli, F., Quadt, A. V., Roddick, J. C., and Spiegel, W., 1995, Three natural zircon standards for U-Th-Pb, Lu-Hf, trace element and REE analyses: Geostandards Newsletter, v. 19, no. 1, p. 1-23.

Willner, A. P., Barr, S. M., Gerdes, A., Massonne, H. J., and White, C. E., 2013, Origin and evolution of Avalonia: evidence from U-Pb and Lu-Hf isotopes in zircon from the Mira terrane, Canada, and the Stavelot-Venn Massif, Belgium: Journal of the Geological Society, v. 170, p. 769-784.

Wolf, M. B., and London, D., 1994, Apatite dissolution into peraluminous haplogranitic melts: An experimental study of solubilities and mechanisms: Geochimica et Cosmochimica Acta, v. 58, no. 19, p. 4127-4145.

Woodcock, N., Holdsworth, R. E., and Strachan, R. A., 2012, The Grampian Orogeny: Mid-Ordovician Arc–Continent Collision along the Laurentian Margin of Iapetus, *in* Woodcock, N., and Strachan, R. A., eds., Geological History of Britain and Ireland: Chichester, Wiley-Blackwell, p. 91 - 109.

Woodhead, J. D., and Hergt, J. M., 2005, A Preliminary Appraisal of Seven Natural Zircon Reference Materials for In Situ Hf Isotope Determination: Geostandards and Geoanalytical Research, v. 29, no. 2, p. 183-195.

Woodhead, J. D., Hergt, J. M., Shelley, M., Eggins, S., and Kemp, R., 2004, Zircon Hf-isotope analysis with an excimer laser, depth profiling, ablation of complex geometries, and concomitant age estimation: Chemical Geology, v. 209, no. 1-2, p. 121-135.

Zhu, Z., Campbell, I. H., Allen, C. M., and Burnham, A. D., 2020, S-type granites: Their origin and distribution through time as determined from detrital zircons: Earth and Planetary Science Letters, v. 536, p. 116140.

Chapter 5. U–Pb zircon-rutile dating of the Llangynog Inlier, Wales: constraints on an Ediacaran shallow marine fossil assemblage from East Avalonia

This chapter is published as:

Clarke, A.J.I., Kirkland, C.L., Menon, L.R., Condon, D.J., Cope, J.C.W., Bevins, R.E., Glorie, S., 2024. U–Pb zircon–rutile dating of the Llangynog Inlier, Wales: constraints on an Ediacaran shallow-marine fossil assemblage from East Avalonia. Journal of the Geological Society 181, jgs2023-2081.

Doi.org/10.1144/jgs2023-081

Minor post-publication changes and clarifications have been made.

The Llangynog Inlier of south Wales contains an assemblage of Ediacaran macrofossils from a shallow-marine environment, including discoidal morphs of *Aspidella* and rare examples of *Hiemalora*, *Palaeopascichnus* and *Yelovichnus*. These are taxa found in other sites in the Avalonian microcontinent (e.g., Charnwood Forest and eastern Newfoundland) and in the younger White Sea Ediacaran assemblages. As the Charnwood fossils reflect a deep-water environment, and no macrofossils have been found in the Ediacaran rocks of the Long Mynd, the fossils of the Llangynog Inlier represent a unique glimpse of shallow marine life in southern Britain (East Avalonia). However, the lack of absolute age constraints has hampered direct comparison with other assemblages. Here, we report *in-situ* zircon and rutile U–Pb dates from a rhyolitic ash-flow layer of the Coed Cochion Volcaniclastic Member, Llangynog Inlier, which constrains the age of the fossiliferous strata. A weighted mean single grain zircon ID-TIMS U–Pb age of 564.09 ± 0.70 Ma is interpreted as the rhyolite's crystallisation age. This age is consistent with *in-situ* LA-ICPMS zircon and rutile U–Pb dating. The Llangynog age temporally correlates these fossils to dated horizons within East Avalonia at the Beacon Hill Formation, Charnwood (565.22 ± 0.89 Ma), and the Stretton Shale Formation, Long Mynd (566.6 ± 2.9 Ma). Correlations to West Avalonia include the time-equivalent Fermeuse Formation, St John’s Group, eastern Newfoundland (564.13 ± 0.65 Ma). The data presented here establish the biota of the Llangynog Inlier as a lateral equivalent to the similarly shallow marine, tidally influenced ecosystem of the upper Fermeuse Formation. Intra-terrane depositional environmental variability also affects what is preserved in Avalonian fossil sites. Further, time-constrained geochemical data reinforce the Llangynog Inlier's classification within the Wrekin Terrane.

5.1. Introduction

The Ediacaran period represents a pivotal time in the evolution of life as it contains the earliest unequivocal fossil evidence for large-scale multicellular organisms, including the first animals. Ediacaran biota demonstrates examples of heterotrophy, locomotion, sexual reproduction, and organisation into complex ecosystems (Dunn et al., 2018; Eden et al., 2022; Liu et al., 2014; Mitchell and Butterfield, 2018; Mitchell et al., 2015).

Ediacaran biota are known from over forty sites worldwide and strata from ca. 580 – 539 Ma (Matthews et al., 2020; Nelson et al., 2022). These occurrences are generally grouped into three temporally successive fossil assemblages: the Avalon assemblage, with major fossil sites in Britain and Newfoundland; the White Sea assemblage of Russia and the Flinders Hills, Australia; and the youngest, the Nama assemblage of Namibia (Waggoner, 2003). Comparison of the taxa preserved in these assemblages may indicate evolutionary developments in the diversity and complexity of organisms (Droser and Gehling, 2015), but they may also primarily reflect different environments (Gehling and Droser, 2013; Grazhdankin, 2004). Each grouping records the response of the Ediacaran biota to the fluctuating environmental conditions of the late Neoproterozoic (Droser et al., 2017; Fedonkin et al., 2007), which included profound shifts in climate (global glaciation to greenhouse climate) and ocean oxidation state, and continental arrangement (Droser et al., 2017; Planavsky et al., 2015).

The oldest ca. 580 – 560 Ma Avalon assemblage is characterised by relatively low taxonomic diversity but large disparity and reflects rapid radiation to fill a morphospace, which was not further enlarged by the later assemblages (Shen et al., 2008). The Avalon assemblage includes rangeomorphs such as *Charnia masoni* and the spindle-shaped *Fractofusus misrai* (Gehling and Narbonne, 2007) and arboreomorphs such as *Charniodiscus concentricus* (Ford, 1958; Pérez-Pinedo et al., 2022), as well as various *incertae sedis,* including *Gigarimaneta samsoni* (Taylor et al., 2021). Indeed, *Haootia quadriformis,* discovered in the Bonavista Peninsula, Newfoundland, represents, at ca. 560 Ma, the earliest identified fossil that is recognizably eumetazoan - a cnidarian displaying muscle fibres (Liu et al., 2014).

The slightly younger White Sea assemblages exhibit a marked increase in diversity and include organisms showing greater architectural complexity and mobility, representing a move towards more recognisable crown members of Phanerozoic fauna (Droser et al., 2017; Seilacher et al., 2005). The youngest Nama assemblage shows a decline in diversity, which

may have resulted from an environmentally driven extinction of much of the Ediacaran biota or ecological restructuring (Eden et al., 2022; Evans et al., 2022).

Geochronological constraints have revealed that the Ediacaran biota emerged and proliferated within the final ca. 30 Ma of the Neoproterozoic (Droser et al., 2017; Wood et al., 2019). Some of the best-preserved archives of this early period of possible animal evolution are found in the Neoproterozoic rocks of Newfoundland (West Avalonia) and southern Britain (East Avalonia) (Dunn et al., 2018). Together, these sequences are fragments of the microcontinent Avalonia. During the Neoproterozoic, this peri-Gondwanan landmass sat at latitudes between 40° and 60° (Murphy and Nance, 1989).

In the case of eastern Newfoundland, the post ca. 580 Ma Drook and ca. 565 Ma Mistaken Point Formations of the Conception Group and the post ca. 564 Ma Fermeuse Formation, St John's Group (Matthews et al., 2020) offer important snapshots into the style

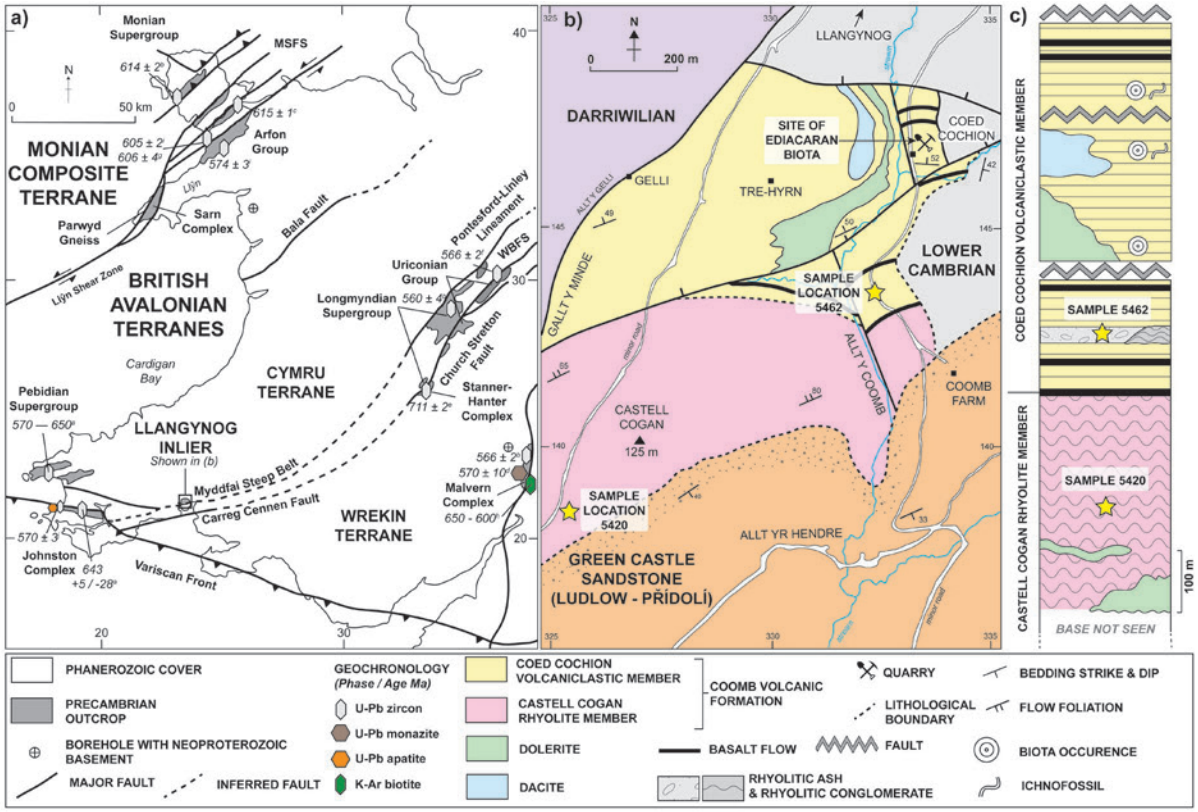

Figure 5.1. ***A)*** *Outcrops of Neoproterozoic southern Britain adapted after Pharaoh and Carney (2000) and Schofield et al. (2016). Data sources are listed in superscript letters and include a) Patchett and Jocelyn (1979), b) Tucker and Pharaoh (1991), c) Horak et al. (1996), d) Thorpe et al. (1984), e) Schofield et al. (2010), f) Noble et al. (1993), g) Beckinsale et al. (1984), h) Strachan et al. (1996), i) Compston et al. (2002), j) Clarke et al. (2023). Abbreviations include WBFS = Welsh Borderland Fault System and MSFS = Menai Strait Fault System.* ***B)*** *Neoproterozoic rocks of the Llangynog Inlier, adapted after Cope and Bevins (1993).* ***C)*** *A schematic stratigraphic log of the Neoproterozoic rocks of the Llangynog Inlier, modified after Cope and Bevins (1993). The coordinate system used is the British National Grid.*

and mode of early Ediacaran life in deep marine (Drook and Mistaken Point Formations) and shallow marine (upper Fermeuse Formation) settings, following the end of the Gaskiers glaciation at ca. 580 Ma (Liu et al., 2015; McIlroy et al., 2021). This ~ 1500 m thick package of fossiliferous strata is comparatively well-constrained with absolute age determinations from interbedded volcanic (zircon-bearing) horizons within the deep marine to shallow, deltaic succession (Matthews et al., 2020; Pu et al., 2016). In Newfoundland, radiometric age determinations have facilitated the correlation of fossiliferous horizons, allowed palaeo-sedimentation rates to be quantified, and helped constrain the stratigraphic range of taxa (Matthews et al., 2020).

In contrast to Newfoundland, the late Neoproterozoic basement of southern Britain crops out in a series of fault-bound, small, tectonically complex, and often poorly exposed inliers concealed by Phanerozoic sediments (Figure 5.1A) (Pharaoh and Carney, 2000; Schofield et al., 2016). Two East Avalonian terranes are known to house Ediacaran fossil sites: the Wrekin (Llangynog Inlier, and microbial mats in the Long Mynd) and Charnwood Terrane (Charnwood Forest) (McIlroy and Horak, 2006) (Figure 5.1A).

U–Pb age constraints indicate that the Long Mynd and Charnwood successions are broadly coeval (Compston et al., 2002; McIlroy et al., 1998; McIlroy and Horak, 2006; Noble et al., 2015) at ca. 570 – 555 Ma. However, there can be strong environmental controls on the composition of assemblages (Liu et al., 2015) and the presence or absence of macrobiota. Consequently, constraining evolutionary paths and understanding relationships between fossiliferous horizons within disparate inliers is difficult, highlighting the need for radiometric age determinations (Matthews et al., 2020).

Correlating the fossil-bearing sites in southern Britain draws upon a sparse dataset of radiometric ages (Pharaoh and Carney, 2000; Schofield et al., 2016), with the Llangynog Inlier of Carmarthenshire in south Wales being a case in point (Figure 5.1B). Despite Avalon-assemblage biota being first described from Llangynog in the late 1970s (Cope, 1977, 1983), the inlier is yet to receive a published absolute age constraint. Furthermore, intriguing connections have been drawn between the fossils of the Llangynog Inlier and those of the upper Fermeuse Formation in Newfoundland (Gehling et al., 2000; Liu and McIlroy, 2015), pointing towards a cosmopolitan assemblage of biota within Avalonian waters during the late-Neoproterozoic. However, as Liu and McIlroy (2015) highlighted, comparisons to other fossil assemblages must remain speculative until an absolute age for the Llangynog Inlier is

established. The presence of intimately associated (zircon and rutile bearing) volcanic and fossiliferous horizons in the Llangynog Inlier (Figure 5.1C) provides an opportunity to constrain the age of the biota precisely.

This study presents zircon and rutile LA-ICP-MS and zircon ID-TIMS U–Pb isotopic data for rhyolitic tuff obtained from the Coed Cochion Volcaniclastic Member, Llangynog Inlier, south Wales (Figure 5.2). We report an age of 564.09 ± 0.70 Ma for the fossils of the Llangynog Inlier. These data represent a temporal constraint on the Avalon assemblage of Ediacaran organisms in southern Britain and support comparisons to the biota of the upper Fermeuse Formation of eastern Newfoundland, Canada. In addition, the placement of the Llangynog Inlier within the Wrekin Terrane becomes unequivocal (Figure 5.1A).

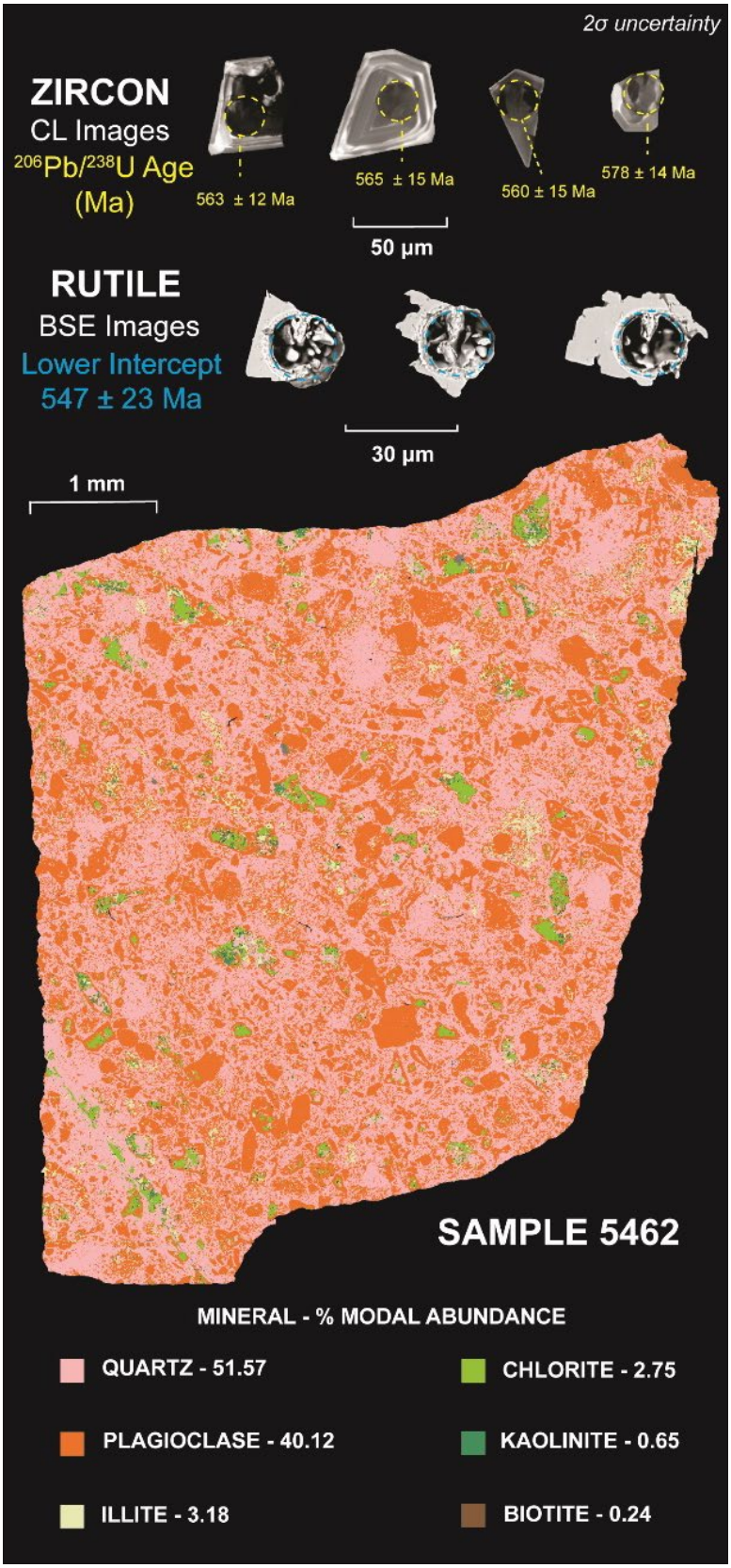

Figure 5.2. ***Top Row****: Representative cathodoluminescence images of zircon grains ablated and the* $^{206}Pb/^{238}U$ *age obtained from sample 5462.* ***Bottom Row:*** *Backscatter electron images of rutile.* ***Bottom Figure:*** *An automated mineralogy map of the Coed Cochion rhyolite (sample 5462) minerals with a modal abundance > 0.1 %.*

5.2. Geological Background

5.2.1. Llangynog Inlier

The Neoproterozoic basement of southern Britain crops out in a series of tectonically uplifted inliers primarily entrained within major fault zones (Figure 5.1A). The Llangynog Inlier is an outcrop of Neoproterozoic to Early Palaeozoic rocks upthrown to the north of the Llandyfaelog-Carreg Cennen Fault, a southwestern extension of the Welsh Borderland Fault System (Figure 5.1A) (Cope and Bevins, 1993; Cope and Rushton, 1992). Flanking the inlier to the south is an unconformable basal contact with the Green Castle Sandstone Formation, forming the base of the Old Red Sandstone across Carmarthenshire and here of Late Silurian age (Cope, 2018). Other boundaries are poorly exposed unconformable or fault-bound contacts with early Palaeozoic rocks (Figure 5.1B) (Cope and Bevins, 1993). Splays of the Church Stretton Fault dissect the antiformal structure of the inlier into a series of fault-spliced outcrops (Cope and Rushton, 1992).

5.2.2. Coomb Volcanic Formation

At the centre of this faulted structure is the Neoproterozoic Coomb Volcanic Formation (CVF) (Figure 5.1B) (Cope and Bevins, 1993). The CVF is a ≥1100 m thick package of interbedded volcanic and volcaniclastic sequences, including tuff beds, minor hyaloclastite and basaltic breccia horizons (Cope and Bevins, 1993). Successions of bimodal basaltic to rhyolitic lavas, intruded by dolerite and dacite sills, occur throughout the CVF and show closer petrological and geochemical affinities to the Uriconian Group (Wrekin Terrane) than to the nearby Pebidian Volcanic Group of the Cymru Terrane (Figure 5.1A) (Bevins et al., 1995).

Two subdivisions comprise the CVF: the lower Castell Cogan Rhyolite (CCR) and the upper Coed Cochion Volcaniclastic Members (CCV) (Figure 5.1C). The CCR, of which 400 m is exposed above a concealed base, is dominated by extensively silicified and variably flow-banded extrusive rhyolites (Cope and Bevins, 1993). The CCV comprises volcaniclastic successions, intercalated basaltic lavas, and one rhyolite lava and conglomerate association (Figure 5.1C). The top 475 m of volcaniclastic siltstones contain sedimentary structures (cross-bedding, flaser bedding) indicative of deposition in a shallow-marine, tidally influenced environment with locally reworked ash and volcanic material (Cope and Bevins, 1993).

5.2.3. Ediacaran Biota

In this upper portion of volcaniclastic siltstones of the CCV, a fossil assemblage of Ediacaran age is found, occurring as variably preserved hyporeliefs within a silty mudstone (Figure 5.3). Virtually all the fossils come from a series of mudstone laminae within a 2-m thickness of rock at the Coed Cochion Quarry (Figure 5.1B). A single fossil was found at the base of the CCV on the west side of the river valley, and a few specimens came from just below the dolerite on the west side of the valley, NW of Coed Cochion; the latter locality's stratigraphical relationship to the Coed Cochion horizon is unclear (Figure 5.1B). The limitation of fossils to the mudstone laminae led Cope and Bevins (1993) to suggest that particular conditions, such as preservation via blanketing ash falls, were necessary to preserve the soft-bodied biota. Interspersed with the mudstone laminae are thin (0.5 – 1.0 m) rhyolitic ash-flow horizons (Figure 5.2), which were sampled in this study (Sample 5462) to obtain U–Pb isotopic data (Figure 5.1C).

The fossil assemblage of the CCV is dominated by *Aspidella terranovica* Billings 1872 [*Aspidella sensu stricto*; Figure 5.3A; Billings (1872); Gehling et al. (2000); Cope (2000)]. This distinctive small discoidal form, with a central ridge or furrow and faint radial lines, first described from the Fermeuse Formation in St John's, Newfoundland, and dominating the upper part of that formation (Gehling et al., 2000), has rarely been found elsewhere, and has not been described from the deep marine assemblages of the Conception Group, Newfoundland, or the Charnian Supergroup of southern Britain. This form has demonstrated evidence of horizontal and vertical locomotion and may have been a simple polyp of Cnidarian affinity (Menon et al., 2013); therefore, its presence in the Llangynog biota is particularly interesting.

Less abundant are flat, annulate *Spriggia*-type and more convex *Ediacaria*-type discs, synonymised as taphomorphs of *Aspidella* by Gehling et al. (2000), here termed *Aspidella sensu lato*), and assumed to be frond holdfasts (Figure 5.3B, C, G) (Cope, 1977, 1983). Associated with *Aspidella s.l.* are rare examples of the rayed disc *Hiemalora* (Fedonkin, 1982), also recognised as a frond holdfast (Burzynski et al., 2017; Hofmann et al., 2008; Wang et al., 2020) (Figure 5.3D). No fronds are preserved associated with *Aspidella s.l.* or *Hiemalora*, unlike many examples with attached fronds in deep marine assemblages of Newfoundland and Charnwood (although no fronds are observed attached to *Hiemalora* in the Charnwood assemblage).

Also found in the Llangynog biota, as in the Fermeuse and White Sea assemblages, are serially chambered palaeopascichnids, both *Palaeopascichnus* and *Yelovichnus*-type forms [Fedonkin (1982); Palij (1976); Figure 5.3E, F]. The nature of palaeopascichnids has been widely debated, but they are now established as body fossils, likely of protistan affinity (Hawco et al., 2021). Simple horizontal trace fossils, such as meandering feeding trails, are also found in the CCV [Figure 5.3H; Cope and Bevins (1993)]. The Llangynog fossils have been deposited in Amgueddfa Cymru-Museum Wales under the registered number NMW.79.16G.

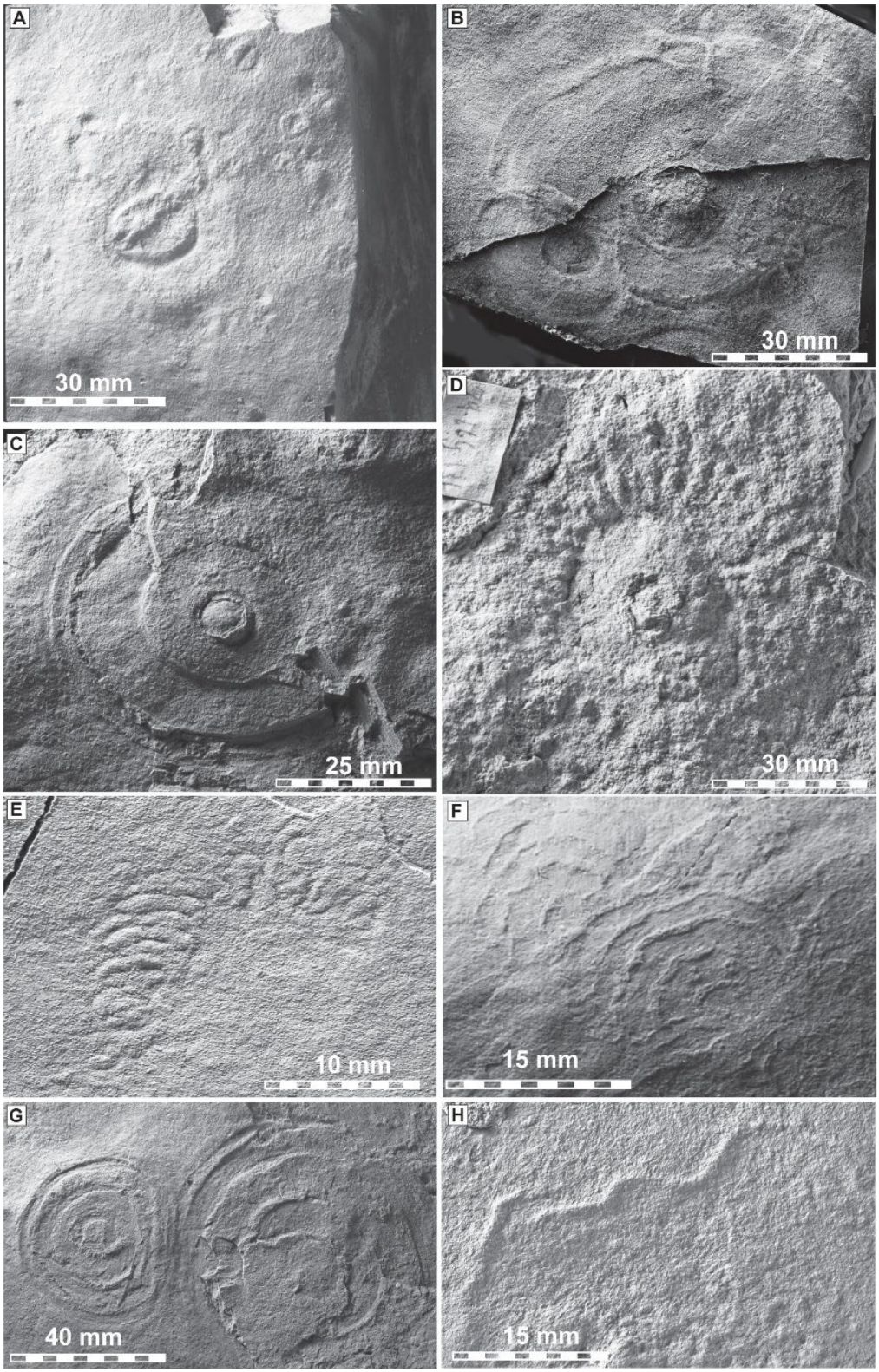

Figure 5.3. Photographs of the Ediacaran biota from the Llangynog Inlier. Note the variable scale of each image. ***A)*** *Group of Aspidella s.s.* ***B)*** *Pair of Ediacaria-type morphs of Aspidella s.l., showing growth interference.* ***C)*** *Ediacaria-type morph of Aspidella s.l.* ***D)*** *Hiemalora.* ***E)*** *Palaeopascichnus sp.* ***F)*** *Yelovichnus sp.* ***G)*** *A pair of Spriggia-type morphs of Aspidella.* ***H)*** *Sinusoidal trace fossil. The Llangynog fossils have been deposited in Amgueddfa Cymru-Museum Wales under the registered number NMW.79.16G.*

5.3. Methods

5.3.1. Petrography

This work analysed two 30 μm thick thin sections. Sample 5462 was collected at 51°48'13.4"N 4°25'11.5"W, ~ 300 m southwest of a small excavation containing Ediacaran fossils (Figure 5.1B). Sample 5420 was collected from an outcrop of the Castell Cogan Rhyolite at 51°47′55″N,004°25′48″W, ~ 25 m west of a north-south minor road (Figure 5.1B).

Sample 5462 is a fine-grained (≤ 1 mm) unwelded, shardic rhyolitic tuff containing quartz and plagioclase (oligoclase to andesine) in approximately equal abundance (Figure 5.2). Primary mafic phases, including biotite and hornblende, are now altered mainly to hydrous secondary phases, including illite, chlorite, and kaolinite. Accessory minerals (< 0.20 % modal abundance) include zircon and rutile (Figure 5.2).

Sample 5420 is a fine-grained (1-5 mm) rhyolite sparsely porphyritic in alkali feldspar (up to 2 mm long). Primary mafic phases are unaltered and include biotite and hornblende. Accessory phases are limited to zircon (Cope and Bevins, 1993).

For sample 5462, a Tescan Integrated Mineral Analyser (TIMA), a petrographic light microscope and a Clara-FE-SEM were used to identify phases, characterise textures (including internal mineral features), and guide spot placement for *in-situ* LA-ICP-MS analysis. Given their likely primary igneous (volcanic) genesis, rutile and zircon were selected as the most abundant phases for isotopic analysis and age determination using LA-ICP-MS.

Within sample 5462, zircon grains are distributed throughout the sample and occur as pristine, colourless, euhedral crystals up to 60 μm in length with aspect ratios of ≥ 2:1 (Figure 5.2). Cathodoluminescence response shows sharp, oscillatory zoning with well-defined crystal margins parallel to these internal surfaces. Such zircon characteristics reflect minimal physical abrasion during transport, consistent with ash-flow zircon. Rutile is disseminated throughout the rhyolite and occurs as subhedral to anhedral grains that lack pronounced zoning. Typically, rutile does not exceed ~ 40 μm in length (Figure 5.2).

5.3.2. Zircon and Rutile U–Pb LA-ICP-MS

One zircon U–Pb analysis session on sample 5462 was performed at the GeoHistory Facility in the John De Laeter Centre (JdLC), Curtin University, Australia. Internal complexities (as interpreted from cathodoluminescence response) within relatively small zircon grains dictated a comparatively small spot size of ~ 30 μm diameter (Figure 5.2).

Ablations for both rutile and zircon analyses were created using a RESOlution LE193 ArF with a Lauren Technic S155 Cell, and isotopic data were collected using an Agilent 8900 ICPMS. Data reduction for both minerals was undertaken in Iolite 4 using the U–Pb geochronology data reduction scheme. Age determinations and regression calculations were performed in IsoplotR (Vermeesch, 2018).

For zircon U–Pb data reduction, 91500 zircon (Wiedenbeck et al., 1995) was used as the primary, matrix-matched reference material for U–Pb and Pb–Pb ratios. Secondary reference zircons, including Plešovice, 337.13 ± 0.37 Ma (Sláma et al., 2008) and GJ-1, 601.95 ± 0.40 Ma (Jackson et al., 2004), were used to verify the accuracy of $^{238}U/^{206}Pb$ isotopic ratio measurements. To monitor the accuracy of $^{207}Pb/^{206}Pb$ ratio measurements, OGC zircon (Stern et al., 2009) was reduced against Maniitsoq zircon, 3008.70 ± 0.72 Ma (Marsh et al., 2019). All secondary reference material gave weighted mean ages within 2σ uncertainty of reported values.

A single rutile U–Pb analysis session was conducted at the JdLC. A ~ 24 µm spot size was necessitated by the small grain size (< 30 µm), anhedral, and disseminated nature of rutile crystals throughout the rhyolite. Measured U–Pb and Pb–Pb isotopic ratios were reduced against reference rutile R10 (Luvizotto et al., 2009). R19 rutile, with an accepted age of 489.5 ± 0.90 Ma (Zack et al., 2011), was used as secondary reference material and gave a weighted mean $^{206}Pb/^{238}U$ age of 491 ± 10 Ma [MSWD = 0.87; $p(x^2) = 0.57$)].

5.3.3. Zircon U–Pb ID-TIMS

Separated zircon grains were annealed, leached, and chemically abraded after the method of Mattinson (2005), and then isotope ratios were measured on a Thermo-Electron Triton thermal ionisation mass spectrometer (TIMS) at the NERC Isotope Geoscience Laboratories at the British Geological Survey in Keyworth, U.K. Data were analysed using the methods described by Condon et al. (2015) and McLean et al. (2015). Reported uncertainty for TIMS analyses includes internal and external error components, including decay constant and tracer uncertainty. Uncertainty was propagated using the algorithms of Schmitz and Schoene (2007).

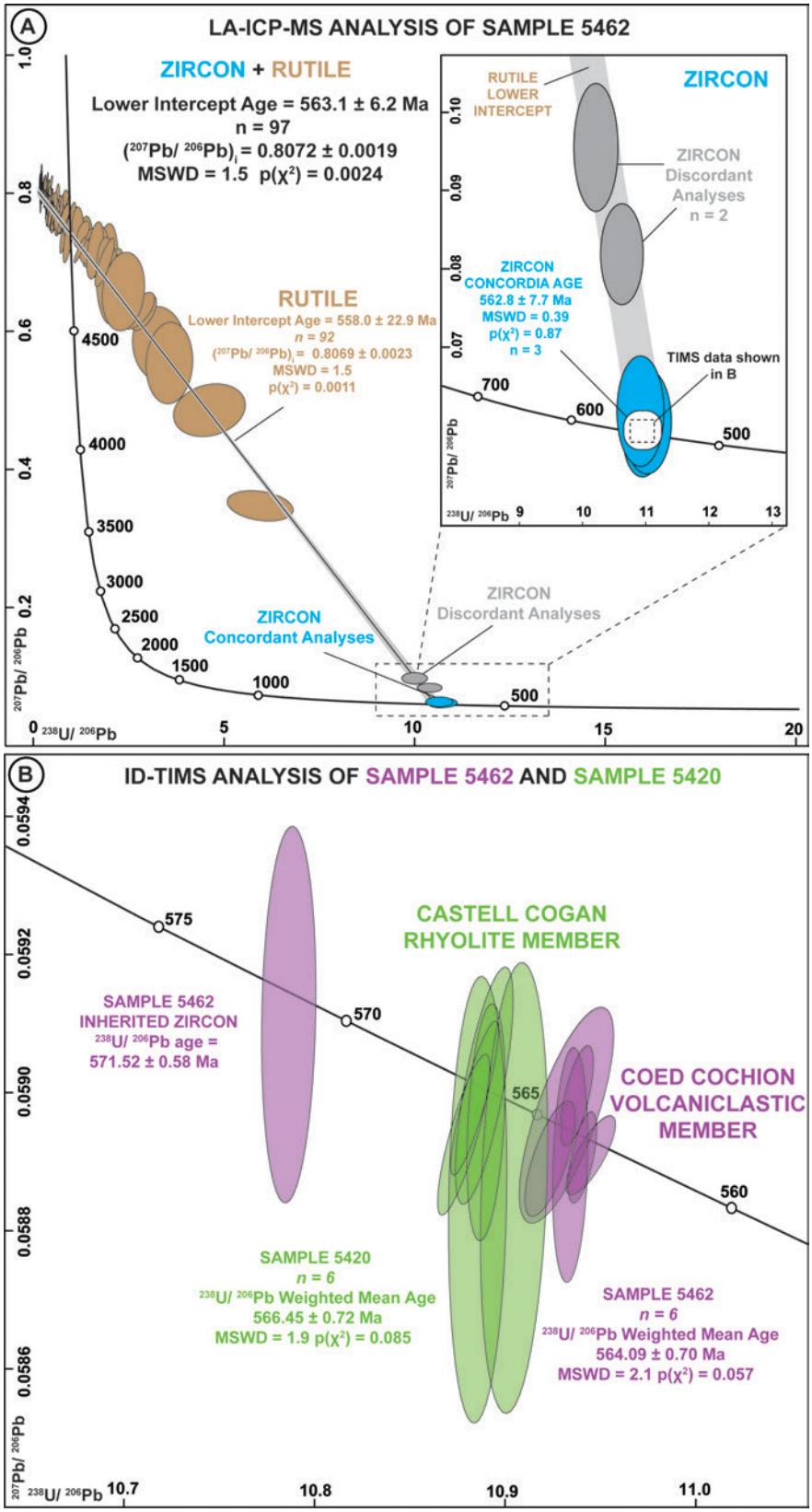

Figure 5.4. ***A)*** *Tera-Wasserburg plot of LA-ICP-MS U–Pb rutile and zircon analyses from sample 5462. The inset shows a magnified view of the rutile U–Pb lower intercept and zircon analyses. Grey uncertainty ellipses are zircon U–Pb analyses with > 15 % discordance.* ***B)*** *ID-TIMS U–Pb analyses of zircon from samples 5462 and 5420.*

5.4. Results & Discussion

5.4.1. A Zircon ID-TIMS Age for the Llangynog Inlier

Two samples (5420 and 5462) of zircon crystals were recovered from rhyolite specimens within the CVF to constrain the age of the Llangynog Inlier (Figure 5.1C). Six zircon U–Pb analyses were obtained on single grains from sample 5420 and together yielded a weighted mean $^{238}U/^{206}Pb$ age of 566.53 ± 0.72 Ma [MSWD = 1.9, p(χ^2) = 0.085] (Figure 5.4), interpreted as the crystallisation age of the CCR (Figure 5.1).

Seven zircon U–Pb analyses were obtained from individual grains from sample 5462. Six analyses yield a weighted mean $^{238}U/^{206}Pb$ age of 564.09 ± 0.70 Ma [MSWD = 2.1, p(χ^2) = 0.057], interpreted as the magmatic crystallisation age of the CCV. A single zircon analysis (*z8*) from sample 5462 yielded a distinctly older $^{238}U/^{206}Pb$ age of 571.52 ± 0.58 Ma, interpreted to reflect an inherited zircon component entrained within the primary magma (Figure 5.4B).

Sample 5420 was collected at the mid-point of the ~400 m of exposed CCR stratigraphy, providing a maximum age for the eruption of the overlying part of the CCV (Figure 5.1C). Sample 5462 was retrieved from above the CCR and is, therefore, a minimum age for the CCV (Figure 5.1). Therefore, the preferred age of the CCV and a definitive maximum age of the fossiliferous beds at Llangynog Inlier is 564.09 ± 0.70 Ma based on sample 5462 (Figure 5.1C; Figure 5.2).

The analysed sample 5462 is a tuffaceous, shardic ash-flow rhyolite which, following eruption, underwent immediate sub-aerial, atmospheric cooling and deposition into a shallow marine setting (Figure 5.1C) (Appendix D) (Cope and Bevins, 1993). Ash layers atop the macrofossils at Llangynog seemingly represent a crucial factor for their preservation (Cope and Bevins, 1993). There can often be uncertainty surrounding the mechanism by which dated (zircon-bearing) horizons are associated with fossiliferous horizons (e.g. primary water lain tuffs vs. turbidite delivered) (Matthews et al., 2020). However, we interpret the rhyolite horizon dated to be a primary ash-flow deposit, which exhibits local, cm-scale reworking. Indeed, the intimate relationship between the biota and volcanism demonstrates that the obtained U–Pb age for the volcanic eruption (Figure 5.4) can be considered essentially contemporaneous with the Ediacaran ecosystem. A detailed interpretation of sedimentary structures within the Coed Cochion Volcaniclastic Member is provided in Appendix D.

5.4.2. Rutile-zircon LA-ICP-MS Age Constraints for the Llangynog Inlier

From sample 5462 of the CCV, five zircon U–Pb analyses were obtained on five grains. Three of these are concordant (≤ 15% discordance, defined using the relative age difference approach) and yield a concordia age of 562.8 ± 7.7 Ma [MSWD = 0.39, $p(\chi^2) = 0.87$], within uncertainty of the TIMS analyses (Figure 5.4).

Rutile yields a two-component mixing line between a common and radiogenic component, with a lower intercept of age 558.0 ± 22.9 Ma (MSWD = 1.5; n = 92), interpreted to date the time since the Pb closure temperature was reached in this mineral. The upper intercept yields a Pb_i of 0.8069 ± 0.0023 (Figure 5.4A). The Stacey and Kramers (1975) Pb evolution model predicts a Pb_i of 0.874 at c. 560 Ma; thus, the measured initial Pb ratio implies derivation from a comparatively unradiogenic source for the CCV. Geochemical data from the CCV shows little enrichment in trace elements compared to mid-ocean-ridge basalts (Bevins et al., 1995), consistent with derivation from unenriched, reworked crust within an ensialic setting for the CCV, much like other peri-Gondwanan terranes (Krmíčková et al., 2020; Schofield et al., 2016).

The coeval age for zircon and rutile implies rapid cooling through the radiogenic Pb-closure temperature of both minerals, including rutile, ≥ 600°C (Cherniak, 2000; Zack and Kooijman, 2017) and zircon, ≥ 900°C (Chew and Spikings, 2021), consistent with the combined LA-ICP-MS age reflecting the time of crystallisation. The combined lower intercept age of 563.1 ± 6.2 Ma (MSWD = 1.5) for zircon and rutile provides an age of the volcanic horizon compatible with the ID-TIMS result (Figure 5.4B). Moreover, the discordant zircon component lies along the same regression line as the rutile common-radiogenic mixing array, implying a shared initial Pb source (Figure 5.4A). Given the low common Pb content in the TIMS zircon analyses, no meaningful age difference results from using different terrestrial common Pb models.

Much like other Neoproterozoic inliers of South Wales, the metamorphic grade of the Llangynog Inlier is limited to prehnite-pumpellyite facies metamorphism (Cope and Bevins, 1993; Patchett and Jocelyn, 1979). This low regional metamorphic grade was likely another key aspect that facilitated the preservation of the biota in the Llangynog Inlier. The coeval rutile-zircon U–Pb ages further demonstrate the minimal thermal overprinting of the CCV, in that the strata cannot have resided above the ~ 600°C Pb closure temperature of rutile for an extended period (Cherniak, 2000; Zack and Kooijman, 2017). In the case of prolonged heating,

rutile U–Pb systematics could be expected to exhibit radiogenic Pb-loss and excess dispersion (and, therefore, elevated regression MSWD) on the Tera-Wasserburg plot (Figure 5.4A). Additionally, the similarity of the zircon and rutile ages provides greater confidence in a primary genesis of both minerals in the volcanic system rather than inheritance into this system, as rutile preservation potential is distinct from zircon (Borisov and Aranovich, 2020; Xiong et al., 2009). For example, compared to zircon, monazite, and apatite, rutile is more soluble during metasomatic reactions during prograde metamorphism (Ayers et al., 1997).

5.4.3. Terrane Classification

The context of the Llangynog Inlier within the terrane classification scheme for Neoproterozoic rocks of southern Britain is yet to be fully resolved (Figure 5.1A) (Schofield et al., 2016). Previous workers have alternatively classed the Llangynog Inlier within the Cymru Terrane (Schofield et al., 2016) or the Wrekin Terrane (Bevins et al., 1995; Pharaoh and Carney, 2000). Often, disparate inliers are grouped into coherent terranes, representing discrete tectonic blocks in a single peri-Gondwanan subduction zone (Pharaoh and Carney, 2000). Importantly, terrane classifications represent robust working models used for paleogeographic reconstructions and constraining Neoproterozoic magmatism in southern Britain (Nance et al., 2008; Strachan et al., 2007).

Bevins et al. (1995) documented the intra-continental chemical signatures of the CVF, which were consistent with constituents of the Wrekin Terrane, including the Uriconian Group and Longmyndian Supergroup (Figure 5.1A). Across the terrane-dividing Welsh Borderland Fault System to the west, components of the Cymru Terrane typically show calc-alkaline, subduction-related geochemical patterns and younger U–Pb ages (Figure 5.1A) (Bevins et al., 1995; Clarke et al., 2023; Schofield et al., 2016).

Although proximal to significant outcrops of the Cymru Terrane (e.g. Pebidian Supergroup, Johnston Complex), the Llangynog Inlier postdates the so-called Main Magmatic Event between ca. 620 – 570 Ma (Clarke et al., 2023; Pharaoh and Carney, 2000; Schofield et al., 2016) that is well represented in the Cymru Terrane. The Wrekin Terrane (Warren House Formation, Uriconian Group) preserves a history of later volcanism and sedimentation following terrane dispersal in East Avalonia from ca. 570 – 550 Ma (Woodcock et al., 2012). The now time-constrained geochemical data of Bevins et al. (1995) reinforces the classification of the Llangynog Inlier within the Wrekin Terrane.

5.4.4. Comparisons with Other Fossil Assemblages in East Avalonia

The zircon age reported here for the CCV of the Llangynog Inlier gives a temporal constraint for one of the last undated Neoproterozoic inliers in southern Britain (Figure 5.1A). Two East Avalonian terranes host Ediacaran macrofossil sites: the Wrekin (Llangynog Inlier) and Charnwood Terrane (Charnwood Forest) (Figure 5.1A).

The Long Mynd in the Wrekin Terrane preserves microbial mats and related features (Callow et al., 2011; Peat, 1984). In detail, Longmyndian strata record a shallow-marine to fluvial succession of siliciclastic sediments (McIlroy et al., 2005). Two minor lapilli tuff layers within the Stretton Group of the Longmyndian Supergroup are dated to 566.6 ± 2.9 and 555.9 ± 3.5 Ma (Compston et al., 2002). The older constraint is derived from the Stretton Shale Formation, which can be considered coeval with the Llangynog age obtained in this study (Figure 5.5). The overlying Burway and Synalds Formations also display a range of microbially induced sedimentary structures (MISS), including "Arumberia" (McIlroy and Walter, 1997) and small discoidal markings previously thought to be Ediacaran macrofossils (Longmyndian “Intrites”, “Medusinites”, and “Beltanelliformis”) (McIlroy et al., 2005), but now understood to be microstromatolites and other features resulting from the response of microbial-mat-covered surfaces to small-scale fluid escape (Menon et al., 2017; Menon et al., 2015). No examples of *Aspidella* or frondose taxa have been observed in the Longmyndian Supergroup (McIlroy et al., 2005) (Figure 5.5).

Although most closely temporally correlated to the Stretton Shale Formation (566.6 ± 2.9 Ma) (McIlroy et al., 2005), the CCV represents a shallow-marine, tidally influenced environment (Cope and Bevins, 1993). By contrast, the Stretton Shale Formation is interpreted as a deep-marine succession of distal turbidite and basin floor facies (McIlroy et al. 2005). Therefore, a more appropriate depositional environment correlation to the CCV might be expected in the overlying Burway, Synalds and Lightspout Formations, the top of the latter dated at 555.9 ± 3.5 Ma (Compston et al., 2002). These transitional formations represent a shift from the deep-marine setting of the Stretton Shale Formation to a shallow, near-shore, deltaic environment and an alluvial floodplain in the overlying Portway Formation [Figure 5.5; Pauley (1990, 1991)]. The apparent absence of Ediacaran macrobiota in the Burway and Synalds Formations suggests some other, as yet unidentified, environmental constraint.

The 564.09 ± 0.70 Ma age presented here indicates that the Llangynog Inlier is contemporary with the Charnwood Forest fossil assemblage (Compston et al., 2002; Noble et

al., 2015) at ca. 570 – 555 Ma (Figure 5.5). The ~ 3200 m thick Charnian Supergroup is comparatively well-constrained with zircon U–Pb ages for tuff horizons throughout the succession (Noble et al., 2015; Schofield et al., 2016) (Figure 5.5). In contrast to the fossil sites of the Wrekin Terrane, the Charnwood Succession was predominantly deposited by gravity flow processes (turbidites) in a deep-marine setting (Pharaoh and Carney, 2000).

A variety of Ediacaran organisms have been described from Charnwood. These include frondose forms such as *Charnia* and *Charniodiscus*, the bushy *Bradgatia*, and *Hiemalora*, found in Charnwood without an attached frond (Boynton and Ford, 1995; Ford, 1958; Kenchington et al., 2018; Wilby et al., 2011). A proposed crown-group cnidarian has also been described from the richly fossiliferous Bradgate Formation (Dunn et al., 2022). Enigmatic ivesheadiomorphs in the oldest Ives Head Formation are now understood to be likely effaced frondose organisms (Liu et al., 2011) (Figure 5.5). Approximately intermediate in stratigraphic position to both is the ~ 1500 m thick Beacon Hill Formation, the middle portion of which is dated to 565.22 ± 0.89 Ma (Noble et al., 2015). Much like the CCV, the Beacon Hill Formation yields discoidal fossils of *Aspidella s.l.* (Figure 5.5) and shares some lithological similarities, including water-lain successions of siltstones, mudstones, and tuffs containing devitrified glass shards (Cope and Bevins, 1993). However, compared to the CCV, the Beacon Hill Formation represents a deeper marine environment with distal turbidite lithologies (Noble et al., 2015). It also preserves ivesheadiomorphs, which are not found in the Llangynog biota. The differences in Ediacaran macrobiota preserved in the Llangynog Inlier and Charnwood, and their apparent absence in Longmyndian outcrops of the same age, may be attributed to inter- and intra-terrane environmental variations, variable sedimentary facies, and differing depositional environments (Figure 5.5) (Liu et al., 2015).

5.4.5. Links to the Ediacaran Assemblages of Newfoundland

Here, zircon–rutile U–Pb isotopic data give insights into the temporal context of the Llangynog Inlier and permit comparisons to other Ediacaran fossil sites, providing quantitative evidence of a correlation between the Ediacaran biota of south Wales and Newfoundland (Figure 5.5). Taxonomic links between the fossil assemblages of southern Britain and Newfoundland have long been recognised, and based on shared taxa, workers have posited that both assemblages are contemporaneous (Gehling et al., 2000; Liu and McIlroy, 2015; Liu et al., 2015). Indeed, up to 60% of the taxa at Charnwood are shared with those at Mistaken Point, though some differences are notable, such as the absence of prostrate rangeomorphs like *Fractofusus* in the Charnwood assemblage (Wilby et al., 2011). The Ediacaran biota of the Avalonian microcontinent was evidently widespread in deep marine environments. However, the context of the Llangynog Inlier to this broader ecosystem has remained elusive.

As demonstrated by Matthews et al. (2020) and Noble et al. (2015) at the Mistaken Point Ecological Reserve and Charnwood Forest, respectively, and more generally by Yang et al. (2021) for Ediacaran assemblages, geochronological studies are a powerful tool for tracking evolutionary patterns and fluctuating environmental conditions.

Recent work in eastern Newfoundland has yielded a maximum age for the Fermeuse Formation of 564.13 ± 0.65 Ma from a basal tuff layer (Matthews et al., 2020). The fossil-rich Shingle Head horizon (Clapham et al., 2003) lies below this tuff layer, at the top of the Trepassey Formation. Another age coeval with the CCV, at 564.71 ± 0.88 Ma, was obtained from the LC-1 fossil horizon in the Trepassey Formation (Figure 5.5) (Matthews et al., 2020). As noted above, the fossil assemblage of the upper Fermeuse Formation shares several taxa with the Llangynog Inlier, including *Aspidella s.s.* and various morphs of *Aspidella s.l.*, *Hiemalora*, and *Palaeopascichnus*. Moreover, as Liu and McIlroy (2015) noted, the large discoidal body fossil assemblages on the often crowded horizons of the CCV are strikingly similar to that of the upper Fermeuse Formation (Figure 5.5), while both also share simple horizontal trace fossils (Liu and McIlroy, 2015). No definitive evidence for preserved fronds has been found in either of these assemblages [although Gehling et al. (2000) propose a possible example].

The upper Fermeuse Formation records a similar depositional environment to the CCV in that interbedded mudstones and crossbedded channel sandstones are interpreted to represent shallow-marine delta front to upper slope environment facies (Gehling et al., 2000; Liu and

McIlroy, 2015; Wood et al., 2003). This environment contrasts with the underlying deep-marine and turbidite-influenced Trepassey and Mistaken Point Formations, which contain abundant frondose taxa (Figure 5.5) (Matthews et al., 2020; Wood et al., 2003), and the similarly deep-marine depositional environment of the Charnian Supergroup (Pharaoh and Carney, 2000), with its diverse frondose fossils.

The key interpretation is that the upper Fermeuse Formation and CCV can be considered contemporaneous shallow-marine Ediacaran ecosystems with a closely similar composition captured in similar depositional environments. Both sites have preserved discoidal forms - notably the rarely seen *Aspidella s.s.* as well as *Aspidella s.l.*, which are presumably holdfasts without their fronds - but also palaeopascichnids and surface traces not observed in the deep-marine assemblages of Avalonia (Figure 5.5).

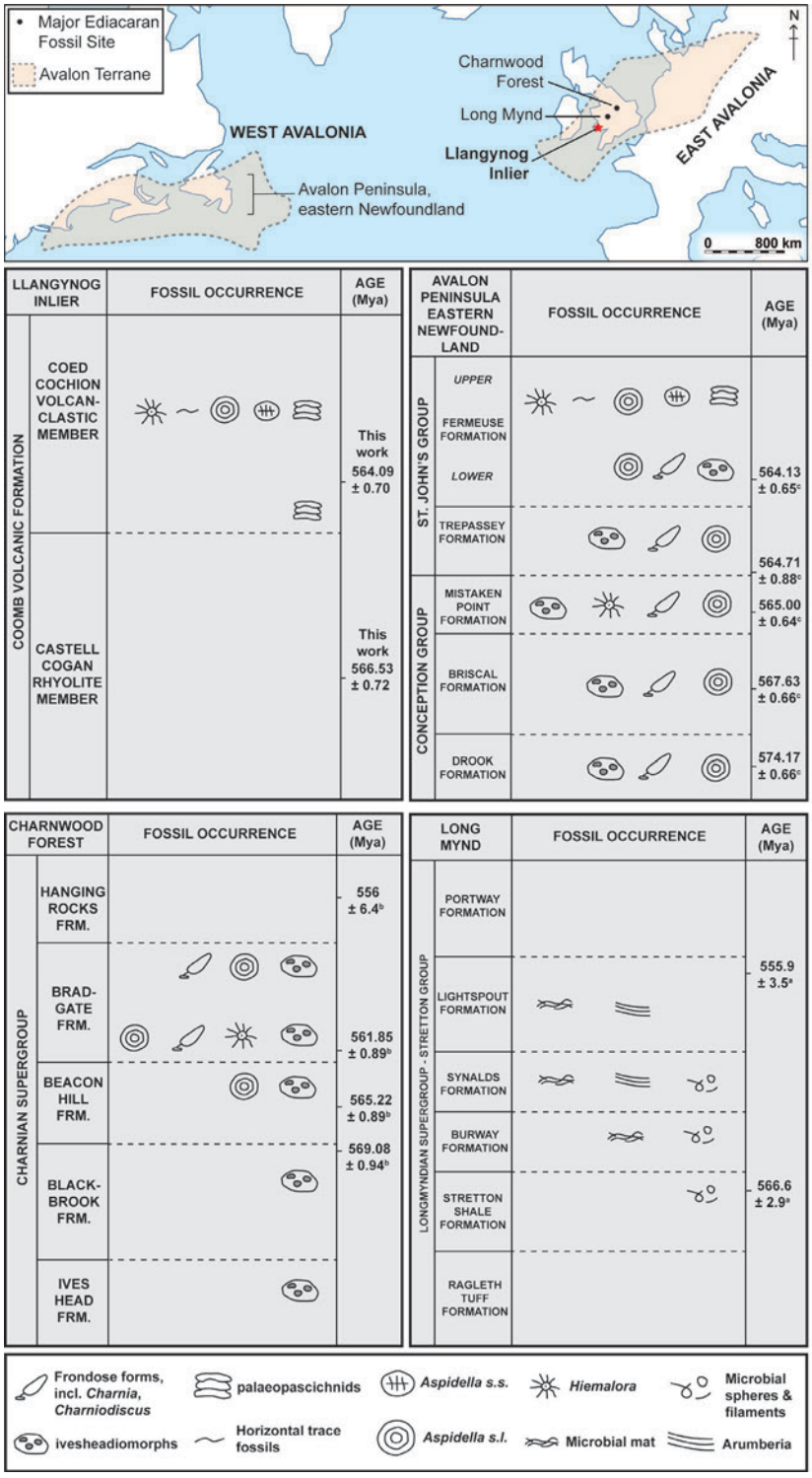

Figure 5.5. Biostratigraphic charts for major fossil sites within the Avalonian microcontinent. Superscript letters denote the source of age data, including ***a)*** *Compston et al. (2002),* ***b)*** *Noble et al. (2015), and* ***c)*** *Matthews et al. (2020). All TIMS age uncertainty show internal and external error components, including decay constant and tracer uncertainty. LA-ICP-MS age uncertainties are reported to one decimal place. Fossil occurrences for the Llangynog Inlier are sourced from Cope (1977, 1983). Occurrence data for Newfoundland was obtained from Matthews et al. (2020) and references therein. For the Charnwood Forest assemblage, fossil occurrences were compiled after Wilby et al. (2011) and Kenchington et al. (2018). Long Mynd fossil occurrences were sourced from Callow et al. (2011); Menon et al. (2015); Peat (1984), and Menon et al. (2017).*

5.5. Conclusions

This work presents new chronostratigraphy constraints for the Llangynog Inlier, south Wales and compares the Ediacaran biota to other fossiliferous sites throughout the Avalonian microcontinent. We report an age of 564.09 ± 0.70 Ma for the CCV, which gives a maximum age for the fossils of the Llangynog Inlier. Furthermore, zircon and rutile U–Pb data from the CCV yield a mid-Ediacaran age at 563.1 ± 6.2 Ma, consistent with the ID-TIMS. Coeval rutile and zircon constrain the rocks' thermal history, providing strong confidence that both minerals are igneous (volcanically) derived and share a common isotopic reservoir based on initial Pb ratios.

The 564.09 ± 0.70 Ma age for the Llangynog Inlier is coeval with the Beacon Hill Formation, Charnwood (565.22 ± 0.89 Ma); the Stretton Shale Formation, Long Mynd (566.6 ± 2.9 Ma) in southern Britain; and the Mistaken Point Formation (565.00 ± 0.64 Ma, E surface) and the Fermeuse Formation (564.13 ± 0.65 Ma) of eastern Newfoundland.

As the shallowing-upwards Long Mynd succession does not yield any Ediacaran macrobiota, despite well-preserved microfossils and MISS, the fossil assemblage of the Llangynog Inlier provides an important, indeed so far unique, glimpse of Ediacaran life in the shallow marine setting in East Avalonia. Furthermore, the Llangynog biota is remarkably similar to that preserved in the upper Fermeuse Formation of West Avalonia, including the presence of the rarely seen small, invaginated *Aspidella terranovica* (Billings, 1872). Thus, establishing the age of the Llangynog Inlier enables a comparison of Ediacaran life in two similar shallow-marine environments across Avalonia, showing the cosmopolitan distribution of organisms in shallow marine and deep marine Avalonian waters. Beyond Avalonia, these assemblages also share taxa such as palaeopascichnids and *Hiemalora* with shallow marine White Sea assemblages across the East European Platform, such as those of the Khatyspyt Formation of Arctic Siberia (Kolesnikov et al., 2018; Vodanjuk, 1989).

The striking variations between assemblages in these roughly coeval formations of East and West Avalonia, with only microfossils observed in the Longmyndian Supergroup, while diverse frondose forms are found in Mistaken Point and Bradgate Formations and discs but no fronds in the CCV and upper Fermeuse Formation (Figure 5.5), suggest a strong environmental control on distribution of these organisms, as well as differences in preservational mode and surfaces captured at different stages of colonisation.

This work demonstrates that the precision of age determinations obtained from comparatively few *in-situ* zircon U–Pb ablations can be improved by incorporating rutile analyses (with higher common Pb contents) from the same rock. The 2σ uncertainty on the zircon concordia age of 562.8 ± 7.7 Ma (n = 3) is improved by 25 % to 563.1 ± 6.2 Ma (n = 97) when a regression through both rutile and zircon U–Pb analyses is calculated. Zircon inheritance in volcanic rocks can complicate U–Pb interpretations; however, more robust age determinations can be obtained by incorporating additional minerals, such as rutile, with varying melt solubilities. Integrating igneous rutile with zircon U–Pb analyses can facilitate more precise crystallisation age interpretations in otherwise zircon-poor lithologies. The regression fit supports a distinctly unradiogenic common Pb composition within the primary magma and demonstrates rapid cooling over the ca. 900 to 600°C interval. Furthermore, the tandem zircon-rutile approach can also help constrain an igneous rock's post-magmatic history, with no prolonged thermal heating ≥ 600°C (rutile U–Pb closure temperature) inferred for the Coed Cochion Volcaniclastic Member. Lastly, the now time-constrained geochemical data of Bevins et al. (1995) reinforces the classification of the Llangynog Inlier with the Wrekin Terrane of East Avalonia.

The U–Pb zircon and rutile age reported here (564.09 ± 0.70 Ma) represents an advance in clarifying the age of Ediacaran biota in southern Britain and allows for more detailed taxonomic comparisons of the biota at Llangynog with West Avalonian fossil assemblages in Newfoundland, and other Ediacaran assemblages such as the slightly younger, shallow-marine White Sea assemblages.

5.6. Acknowledgements

This work was funded by an Australian Research Council Discovery Project (DP20010881). We thank Bradley McDonald and Noreen Evans for their assistance during LA-ICP-MS analysis. AC thanks R. Rohrer and C. Joseph for helpful discussions that improved data presentation. R.D. Hillier is thanked for commenting on sedimentary structures in Appendix D. This research was undertaken on samples 5462 and 5420 received on loan from Amgueddfa Cymru-Museum Wales. We thank Ashleigh Hood for her editorial handling. Duncan McIlroy and two anonymous reviewers are thanked for comments that improved this work.

5.7. Data Availability

Isotopic data for zircon and rutile (U–Pb, Lu–Hf) and a description of sedimentary structures from the Llangynog Inlier are available as Supplementary Information 1 – 2 via *DOI: 10.1144/jgs2023-081 and 10.6084/m9.figshare. c.6965642.v1*.

5.8. References

Ayers, J. C., Watson, E. B., Tarney, J., Pickering, K. T., Knipe, R. J., and Dewey, J. F., 1997, Solubility of apatite, monazite, zircon, and rutile in supercritical aqueous fluids with implications for subduction zone geochemistry: Philosophical Transactions of the Royal Society of London. Series A: Physical and Engineering Sciences, v. 335, no. 1638, p. 365-375.

Beckinsale, R. D., Evans, J. A., Thorpe, R. S., Gibbons, W., and Harmon, R. S., 1984, Rb-Sr whole-rock isochron ages, $\delta^{18}O$ values and geochemical data for the Sarn Igneous Complex and the Parwyd gneisses of the Mona Complex of Llŷn, N Wales: Journal of the Geological Society, v. 141, no. 4, p. 701-709.

Bevins, R., Pharaoh, T., Cope, J., and Brewer, T., 1995, Geochemical character of Neoproterozoic volcanic rocks in southwest Wales: Geological Magazine, v. 132, p. 339-349.

Billings, E., 1872, On some fossils from the primordial rocks of Newfoundland: The Canadian Naturalist, v. 6, p. 465-479.

Borisov, A., and Aranovich, L., 2020, Rutile solubility and TiO_2 activity in silicate melts: An experimental study: Chemical Geology, v. 556, p. 119817.

Boynton, H. E., and Ford, T. D., 1995, Ediacaran fossils from the Precambrian (Charnian Supergroup) of Charnwood Forest, Leicestershire, England: Mercian Geologist, v. 13, p. 165-182.

Burzynski, G., Narbonne, G. M., Alexander Dececchi, T., and Dalrymple, R. W., 2017, The ins and outs of Ediacaran discs: Precambrian Research, v. 300, p. 246-260.

Callow, R. H. T., McIlroy, D., and Brasier, M. D., 2011, John Salter and the Ediacara Fauna of the Longmyndian Supergroup: Ichnos, v. 18, no. 3, p. 176-187.

Cherniak, D. J., 2000, Pb diffusion in rutile: Contributions to Mineralogy and Petrology, v. 139, no. 2, p. 198-207.

Chew, D. M., and Spikings, R. A., 2021, Apatite U-Pb Thermochronology: A Review: Minerals, v. 11, p. 1095.

Clapham, M., Narbonne, G., and Gehling, J., 2003, Paleoecology of the oldest known animal communities: Ediacaran assemblages at Mistaken Point, Newfoundland: Paleobiology, v. 29, p. 527-544.

Clarke, A. J. I., Kirkland, C. L., and Glorie, S., 2023, A detective duo of apatite and zircon geochronology for East Avalonia, Johnston Complex, Wales: Journal of the Geological Society, v. 180.

Compston, W., Wright, A. E., and Toghill, P., 2002, Dating the Late Precambrian volcanicity of England and Wales: Journal of the Geological Society, v. 159, no. 3, p. 323-339.

Condon, D. J., Schoene, B., McLean, N. M., Bowring, S. A., and Parrish, R. R., 2015, Metrology and traceability of U–Pb isotope dilution geochronology (EARTHTIME Tracer Calibration Part I): Geochimica et Cosmochimica Acta, v. 164, p. 464-480.

Cope, J. C. W., 1977, An Ediacara-type fauna from South Wales: Nature, v. 268, no. 5621, p. 624-624.

-, 1983, Precambrian faunas from the Carmarthen district: Nature in Wales, v. 1, p. 11-16.

-, 2000, The Precambrian palaeontology of Coed Cochion, *in* Carney, J. N., ed., Precambrian Rocks of England and Wales, Volume 20: Peterborough, Joint Nature Conservation Committee, p. 196-198.

-, 2018, The Green Castle Sandstone Formation: A new name for the Cwmffrwd Formation (Old Red Sandstone) preoccupied by an Ordovician Member: Proceedings of the Geologists Association, v. 129, no. 1.

Cope, J. C. W., and Bevins, R. E., 1993, The stratigraphy and setting of the Precambrian rocks of the Llangynog Inlier, Dyfed, South Wales: Geological Magazine, v. 130, no. 1, p. 101-111.

Cope, J. C. W., and Rushton, A. W. A., 1992, Cambrian and early Tremadoc rocks of the Llangynog Inlier, Dyfed, South Wales: Geological Magazine, v. 129, no. 5, p. 543-552.

Droser, M. L., and Gehling, J. G., 2015, The advent of animals: The view from the Ediacaran: Proceedings of the National Academy of Sciences, v. 112, no. 16, p. 4865-4870.

Droser, M. L., Tarhan, L. G., and Gehling, J. G., 2017, The Rise of Animals in a Changing Environment: Global Ecological Innovation in the Late Ediacaran: Annual Review of Earth and Planetary Sciences, v. 45, no. 1, p. 593-617.

Dunn, F. S., Kenchington, C. G., Parry, L. A., Clark, J. W., Kendall, R. S., and Wilby, P. R., 2022, A crown-group cnidarian from the Ediacaran of Charnwood Forest, UK: Nature Ecology & Evolution, v. 6, no. 8, p. 1095-1104.

Dunn, F. S., Liu, A. G., and Donoghue, P. C. J., 2018, Ediacaran developmental biology: Biological Reviews, v. 93, no. 2, p. 914-932.

Eden, R., Manica, A., and Mitchell, E. G., 2022, Metacommunity analyses show an increase in ecological specialisation throughout the Ediacaran period: PLOS Biology, v. 20, no. 5, p. e3001289.

Evans, S. D., Tu, C., Rizzo, A., Surprenant, R. L., Boan, P. C., McCandless, H., Marshall, N., Xiao, S., and Droser, M. L., 2022, Environmental drivers of the first major animal

extinction across the Ediacaran White Sea-Nama transition: Proceedings of the National Academy of Sciences, v. 119, no. 46, p. e2207475119.

Fedonkin, M. A., 1982, A new generic name for some Precambrian coelenterates: Paleontological Journal, v. 16, no. 2, p. 127.

Fedonkin, M. A., Gehling, J. G., Grey, K., Narbonne, G. M., and Vickers-Rich, P., 2007, The rise of animals: evolution and diversification of the kingdom Animalia, JHU Press.

Ford, T. D., 1958, Pre-Cambrian Fossils from the Charnwood Forest: Proceedings of the Yorkshire Geological Society, v. 31, no. 3, p. 211-217.

Gehling, J. G., and Droser, M. L., 2013, How well do fossil assemblages of the Ediacara Biota tell time?: Geology, v. 41, no. 4, p. 447-450.

Gehling, J. G., and Narbonne, G. M., 2007, Spindle-shaped Ediacara fossils from the Mistaken Point assemblage, Avalon Zone, Newfoundland: Canadian Journal of Earth Sciences, v. 44, no. 3, p. 367-387.

Gehling, J. G., Narbonne, G. M., and Anderson, M. M., 2000, The first named Ediacaran body fossil, *Aspidella Terranovica*: Palaeontology, v. 43, no. 3, p. 427-456.

Grazhdankin, D., 2004, Patterns of Distribution in the Ediacaran Biotas: Facies versus Biogeography and Evolution: Paleobiology, v. 30, no. 2, p. 203-221.

Hawco, J. B., Kenchington, C. G., and McIlroy, D., 2021, A quantitative and statistical discrimination of morphotaxa within the Ediacaran genus *Palaeopascichnus*: Papers in Palaeontology, v. 7, no. 2, p. 657-673.

Hofmann, H. J., O'Brien, S. J., and King, A. F., 2008, Ediacaran biota on Bonavista Peninsula, Newfoundland, Canada: Journal of Paleontology, v. 82, no. 1, p. 1-36.

Horak, J., Doig, R., Evans, J., and Gibbons, W. D., 1996, Avalonian magmatism and terrane linkage: New isotopic data from the Precambrian of North Wales: Journal of the Geological Society, v. 153, p. 91-99.

Jackson, S. E., Pearson, N. J., Griffin, W. L., and Belousova, E. A., 2004, The application of laser ablation-inductively coupled plasma-mass spectrometry to in situ U–Pb zircon geochronology: Chemical Geology, v. 211, no. 1, p. 47-69.

Kenchington, C. G., Harris, S. J., Vixseboxse, P. B., Pickup, C., and Wilby, P. R., 2018, The Ediacaran fossils of Charnwood Forest: Shining new light on a major biological revolution: Proceedings of the Geologists' Association, v. 129, no. 3, p. 264-277.

Kolesnikov, A., Rogov, V., Bykova, N., Danelian, T., Clausen, S., Maslov, A., and Grazhdankin, D., 2018, The oldest skeletal macroscopic organism *Palaeopascichnus linearis*: Precambrian Research, v. 316, p. 24–37.

Krmíčková, S., Krmíček, L., Romer, R. L., and Ulrych, J., 2020, Lead isotope evolution of the Central European upper mantle: Constraints from the Bohemian Massif: Geoscience Frontiers, v. 11, no. 3, p. 925-942.

Liu, A., and McIlroy, D., 2015, Horizontal surface traces from the Fermeuse Formation, Ferryland (Newfoundland, Canada), and their place within the Late Ediacaran ichnological revolution: Geological Association of Canada - Special Paper, v. 9, p. 141-156.

Liu, A. G., Kenchington, C. G., and Mitchell, E. G., 2015, Remarkable insights into the paleoecology of the Avalonian Ediacaran macrobiota: Gondwana Research, v. 27, no. 4, p. 1355-1380.

Liu, A. G., Matthews, J. J., Menon, L. R., McIlroy, D., and Brasier, M. D., 2014, *Haootia quadriformis* n. gen., n. sp., interpreted as a muscular cnidarian impression from the Late Ediacaran period (approx. 560 Ma): Proceedings of the Royal Society B: Biological Sciences, v. 281, no. 1793, p. 20141202.

Liu, A. G., McIlroy, D., Antcliffe, J. B., and Brasier, M. D., 2011, Effaced preservation in the Ediacara biota and its implications for the early macrofossil record: Palaeontology, v. 54, no. 3, p. 607-630.

Luvizotto, G., Zack, T., Meyer, H. P., Ludwig, T., Triebold, S., Kronz, A., Münker, C., Stockli, D., Prowatke, S., Klemme, S., Jacob, D., and Eynatten, H., 2009, Rutile crystals as potential trace element and isotope mineral standards for microanalysis: Chemical Geology, v. 261, p. 346-369.

Marsh, J. H., Jørgensen, T. R. C., Petrus, J. A., Hamilton, M. A., and Mole, D. R., 2019, U-Pb, trace element, and hafnium isotope composition of the Maniitsoq zircon: A potential new Archean zircon reference material, Goldschmidt: Barcalona.

Matthews, J. J., Liu, A. G., Yang, C., McIlroy, D., Levell, B., and Condon, D. J., 2020, A Chronostratigraphic Framework for the Rise of the Ediacaran Macrobiota: New Constraints from Mistaken Point Ecological Reserve, Newfoundland: GSA Bulletin, v. 133, no. 3-4, p. 612-624.

Mattinson, J. M., 2005, Zircon U–Pb chemical abrasion (“CA-TIMS”) method: Combined annealing and multi-step partial dissolution analysis for improved precision and accuracy of zircon ages: Chemical Geology, v. 220, no. 1, p. 47-66.

McIlroy, D., Brasier, A. T., and Moseley, J. B., 1998, The Proterozoic–Cambrian transition within the ‘Charnian Supergroup’ of central England and the antiquity of the Ediacara fauna: Journal of the Geological Society, v. 155, no. 2, p. 401-411.

McIlroy, D., Crimes, T. P., and Pauley, J. C., 2005, Fossils and matgrounds from the Neoproterozoic Longmyndian Supergroup, Shropshire, UK: Geological Magazine, v. 142, p. 441 - 455.

McIlroy, D., Dufour, S. C., Taylor, R., and Nicholls, R., 2021, The role of symbiosis in the first colonization of the seafloor by macrobiota: Insights from the oldest Ediacaran biota (Newfoundland, Canada): Biosystems, v. 205, p. 104413.

McIlroy, D., and Horak, J., 2006, The Neoproterozoic of England and Wales, *in* Brenchly, P. J., and Rawson, P. F., eds., The Geology of England and Wales: London, Geological Society of London, p. 9-24.

McIlroy, D., and Walter, M. R., 1997, A reconsideration of the biogenicity of *Arumberia banksi* Glaessner & Walter: Alcheringa: An Australasian Journal of Palaeontology, v. 21, no. 1, p. 79-80.

McLean, N. M., Condon, D. J., Schoene, B., and Bowring, S. A., 2015, Evaluating uncertainties in the calibration of isotopic reference materials and multi-element isotopic tracers (EARTHTIME Tracer Calibration Part II): Geochimica et Cosmochimica Acta, v. 164, p. 481-501.

Menon, L. R., McIlroy, D., and Brasier, M. D., 2013, Evidence for Cnidaria-like behavior in ca. 560 Ma Ediacaran *Aspidella*: Geology, v. 41, no. 8, p. 895-898.

-, 2017, 'Intrites' from the Ediacaran Longmyndian Supergroup, UK: a new form of microbially-induced sedimentary structure (MISS), *in* Brasier, A. T., McIlroy, D., and McLoughlin, N., eds., Earth System Evolution and Early Life: A Celebration of the Work of Martin Brasier, Volume 448, Geological Society of London Special Publications, p. 271-283.

Menon, L. R., McIlroy, D., Liu, A. G., and Brasier, M. D., 2015, The dynamic influence of microbial mats on sediments: fluid escape and pseudofossil formation in the Ediacaran Longmyndian Supergroup, UK: Journal of the Geological Society, v. 173, no. 1, p. 177-185.

Mitchell, E. G., and Butterfield, N. J., 2018, Spatial analyses of Ediacaran communities at Mistaken Point: Paleobiology, v. 44, no. 1, p. 40-57.

Mitchell, E. G., Kenchington, C. G., Liu, A. G., Matthews, J. J., and Butterfield, N. J., 2015, Reconstructing the reproductive mode of an Ediacaran macro-organism: Nature, v. 524, no. 7565, p. 343-346.

Murphy, J. B., and Nance, R. D., 1989, Model for the evolution of the Avalonian-Cadomian belt: Geology, v. 17, no. 8, p. 735-738.

Nance, R. D., Murphy, J. B., Strachan, R. A., Keppie, J. D., Gutiérrez-Alonso, G., J., F.-S., Quesada, C., Linnemann, U., D'Lemos, R. S., and Pisarevsky, A. S., 2008, Neoproterozoic-Early Palaeozoic tectonostratigraphy and palaeogeography of the peri-Gondwanan terranes: Amazonian v. West African connections: Geological Society London Special Publications, v. 297, p. 345–383.

Nelson, L. L., Ramezani, J., Almond, J. E., Darroch, S. A. F., Taylor, W. L., Brenner, D. C., Furey, R. P., Turner, M., and Smith, E. F., 2022, Pushing the boundary: A calibrated Ediacaran-Cambrian stratigraphic record from the Nama Group in northwestern Republic of South Africa: Earth and Planetary Science Letters, v. 580, p. 117396.

Noble, S. R., Condon, D. J., Carney, J. N., Wilby, P. R., Pharaoh, T. C., and Ford, T. D., 2015, U-Pb geochronology and global context of the Charnian Supergroup, UK: Constraints on the age of key Ediacaran fossil assemblages: GSA Bulletin, v. 127, no. 1-2, p. 250-265.

Noble, S. R., Tucker, R. D., and Pharaoh, T. C., 1993, Lower Palaeozoic and Precambrian igneous rocks from eastern England, and their bearing on late Ordovician closure of the Tornquist Sea: constraints from U-Pb and Nd isotopes: Geological Magazine, v. 130, no. 6, p. 835-846.

Palij, V., 1976, Remains of soft-bodied animals and trace fossils from the Upper Precambrian and Lower Cambrian of Podolia, *in* Ryabenko, V., ed., Paleontologiya i stratigraphiya verkhnego dokembriya I nizhnego kembriya yugo-zapada Vostochno-Europeiskoi platformy: Kiev, Naulova Dumka, p. 63-76.

Patchett, P. J., and Jocelyn, J., 1979, U–Pb zircon ages for late Precambrian igneous rocks in South Wales: Journal of the Geological Society, v. 136, no. 1, p. 13-19.

Pauley, J., 1990, Sedimentology, structural evolution and tectonic setting of the late Precambrian Longmyndian Supergroup of the Welsh Borderland, UK: Geological Society, London, Special Publications, v. 51, no. 1, p. 341-351.

-, 1991, A revision of the stratigraphy of the Longmyndian Supergroup, Welsh borderland, and of its relationship to the Uriconian volcanic complex: Geological Journal, v. 26, p. 167-183.

Peat, C. J., 1984, Precambrian microfossils from the Longmyndian of Shropshire: Proceedings of the Geologists' Association, v. 95, no. 1, p. 17-22.

Pérez-Pinedo, D., McKean, C., Taylor, R., Nicholls, R., and McIlroy, D., 2022, *Charniodiscus* and *Arborea* Are Separate Genera Within the Arboreomorpha: Using the Holotype of

C. concentricus to Resolve a Taphonomic/Taxonomic Tangle: Frontiers in Earth Science, v. 9.

Pharaoh, T. C., and Carney, J. N., 2000, Introduction to the Precambrian Rocks of England and Wales, *in* Carney, J. N., ed., Geological Conservation Review Series, Volume 138: Peterborough, Joint Nature Conservation Committee, p. 127-136.

Planavsky, N. J., Tarhan, L. G., Bellefroid, E. J., Evans, D. A. D., Reinhard, C. T., Love, G. D., and Lyons, T. W., 2015, Late Proterozoic Transitions in Climate, Oxygen, and Tectonics, and the Rise of Complex Life: The Paleontological Society Papers, v. 21, p. 47-82.

Pu, J., Bowring, S., Ramezani, J., Myrow, P., Raub, T., Landing, E., Mills, A., Hodgin, E., and Macdonald, F., 2016, Dodging snowballs: Geochronology of the Gaskiers glaciation and the first appearance of the Ediacaran biota: Geology, v. 44, p. 955-958.

Schmitz, M. D., and Schoene, B., 2007, Derivation of isotope ratios, errors, and error correlations for U-Pb geochronology using ^{205}Pb-^{235}U-(^{233}U)-spiked isotope dilution thermal ionization mass spectrometric data: Geochemistry, Geophysics, Geosystems, v. 8, no. 8.

Schofield, D., Millar, I. L., Wilby, P., and Evans, J., 2010, A new, high precision U–Pb date from the oldest known rocks in southern Britain: Geological Magazine, v. 147.

Schofield, D., Potter, J., Barr, S. M., Horák, J. M., Millar, I. L., and Longstaffe, F. J., 2016, Reappraising the Neoproterozoic 'East Avalonian' terranes of southern Great Britain: Gondwana Research, v. 35, p. 257-271.

Seilacher, A., Buatois, L. A., and Mángano, M. G., 2005, Trace fossils in the Ediacaran–Cambrian transition: behavioral diversification, ecological turnover and environmental shift: Palaeogeography, Palaeoclimatology, Palaeoecology, v. 227, no. 4, p. 323-356.

Shen, B., Dong, L., Xiao, S., and Kowalewski, M., 2008, The Avalon Explosion: Evolution of Ediacara Morphospace: Science, v. 319, no. 5859, p. 81-84.

Sláma, J., Košler, J., Condon, D. J., Crowley, J. L., Gerdes, A., Hanchar, J. M., Horstwood, M. S. A., Morris, G. A., Nasdala, L., Norberg, N., Schaltegger, U., Schoene, B., Tubrett, M. N., and Whitehouse, M. J., 2008, Plešovice zircon — A new natural reference material for U–Pb and Hf isotopic microanalysis: Chemical Geology, v. 249, no. 1, p. 1-35.

Stacey, J. S., and Kramers, J. D., 1975, Approximation of terrestrial lead isotope evolution by a two-stage model: Earth and Planetary Science Letters, v. 26, no. 2, p. 207-221.

Stern, R. A., Bodorkos, S., Kamo, S. L., Hickman, A. H., and Corfu, F., 2009, Measurement of SIMS Instrumental Mass Fractionation of Pb Isotopes During Zircon Dating: Geostandards and Geoanalytical Research, v. 33, no. 2, p. 145-168.

Strachan, R. A., Collins, A., Buchan, C., Nance, R. D., Murphy, J. B., and D'Lemos, R. S., 2007, Terrane analysis along a Neoproterozoic active margin of Gondwana: Insights from U-Pb zircon geochronology: Journal of the Geological Society, v. 164, p. 57-60.

Strachan, R. A., Nance, R. D., Dallmeyer, R., D'Lemos, R. S., Murphy, J. B., and Watt, G. R., 1996, Late Precambrian tectonothermal evolution of the Malverns Complex: Journal of the Geological Society, v. 153, p. 589-600.

Taylor, R., Matthews, J., Nicholls, R., and McIlroy, D., 2021, A re-assessment of the taxonomy, palaeobiology and taphonomy of the rangeomorph organism *Hapsidophyllas flexibilis* from the Ediacaran of Newfoundland, Canada: PalZ, v. 95, p. 187-207.

Thorpe, R. S., Beckinsale, R. D., Patchett, P. J., Piper, J. D. A., Davies, G. R., and Evans, J. A., 1984, Crustal growth and late Precambrian-early Palaeozoic plate tectonic evolution of England and Wales: Journal of the Geological Society, v. 141, no. 3, p. 521-536.

Tucker, R. D., and Pharaoh, T. C., 1991, U-Pb zircon ages for Late Precambrian igneous rocks in southern Britain: Journal of the Geological Society, v. 148, no. 3, p. 435-443.

Vermeesch, P., 2018, IsoplotR: A free and open toolbox for geochronology: Geoscience Frontiers, v. 9, no. 5, p. 1479-1493.

Vodanjuk, S. A., 1989, Remains of non-skeletal metazoans from Khatyspyt Formation of Olehyok Uplift: Late Precambrian and early Paleozoic of Siberia. Trudy Inst. Geol. Geofiz., Sibirsk. Otd. SSSR Akad. Nauk, Novosibirsk, p. 61-74.

Waggoner, B., 2003, The Ediacaran Biotas in Space and Time: Integrative and Comparative Biology, v. 43, no. 1, p. 104-113.

Wang, X., Pang, K., Chen, Z., Wan, B., Xiao, S., Zhou, C., and Yuan, X., 2020, The Ediacaran frondose fossil *Arborea* from the Shibantan limestone of South China: Journal of Paleontology, v. 94, no. 6, p. 1034-1050.

Wiedenbeck, M., Allé, P., Corfu, F., Griffin, W. L., Meier, M., Oberli, F., Quadt, A. V., Roddick, J. C., and Spiegel, W., 1995, Three natural zircon standards for U-Th-Pb, Lu-Hf, trace element and REE analyses: Geostandards Newsletter, v. 19, no. 1, p. 1-23.

Wilby, P., Carney, J., and Howe, M., 2011, A rich Ediacaran assemblage from eastern Avalonia: Evidence of early widespread diversity in the deep ocean: Geology, v. 39, p. 655-658.

Wood, D. A., Dalrymple, R. W., Narbonne, G. M., Gehling, J. G., and Clapham, M. E., 2003, Paleoenvironmental analysis of the late Neoproterozoic Mistaken Point and Trepassey

formations, southeastern Newfoundland: Canadian Journal of Earth Sciences, v. 40, no. 10, p. 1375-1391.

Wood, R., Liu, A. G., Bowyer, F., Wilby, P. R., Dunn, F. S., Kenchington, C. G., Cuthill, J. F. H., Mitchell, E. G., and Penny, A., 2019, Integrated records of environmental change and evolution challenge the Cambrian Explosion: Nature Ecology & Evolution, v. 3, no. 4, p. 528-538.

Woodcock, N., Holdsworth, R. E., and Strachan, R. A., 2012, Late Neoproterozoic to Cambrian Accretionary History of Eastern Avalonia and Armorica on the Active Margin of Gondwana, *in* Woodcock, N., and Strachan, R. A., eds., Geological History of Britain and Ireland: Chichester, Wiley-Blackwell, p. 133-149.

Xiong, X., Keppler, H., Audétat, A., Gudfinnsson, G., Sun, W., Song, M., Xiao, W., and Yuan, L., 2009, Experimental constraints on rutile saturation during partial melting of metabasalt at the amphibolite to eclogite transition, with applications to TTG genesis: American Mineralogist, v. 94, no. 8-9, p. 1175-1186.

Yang, C., Rooney, A. D., Condon, D. J., Li, X.-H., Grazhdankin, D. V., Bowyer, F. T., Hu, C., Macdonald, F. A., and Zhu, M., 2021, The tempo of Ediacaran evolution: Science Advances, v. 7, no. 45, p. eabi9643.

Zack, T., and Kooijman, E., 2017, Petrology and Geochronology of Rutile: Reviews in Mineralogy and Geochemistry, v. 83, no. 1, p. 443-467.

Zack, T., Stockli, D., Luvizotto, G., Barth, M., Belousova, E., Wolfe, M., and Hinton, R., 2011, In situ U–Pb rutile dating by LA-ICP-MS: ^{208}Pb correction and prospects for geological applications: Contributions to Mineralogy and Petrology, v. 162, p. 515-530.

5.9. Appendix D

5.9.1. Llangynog Inlier Sedimentary Structures

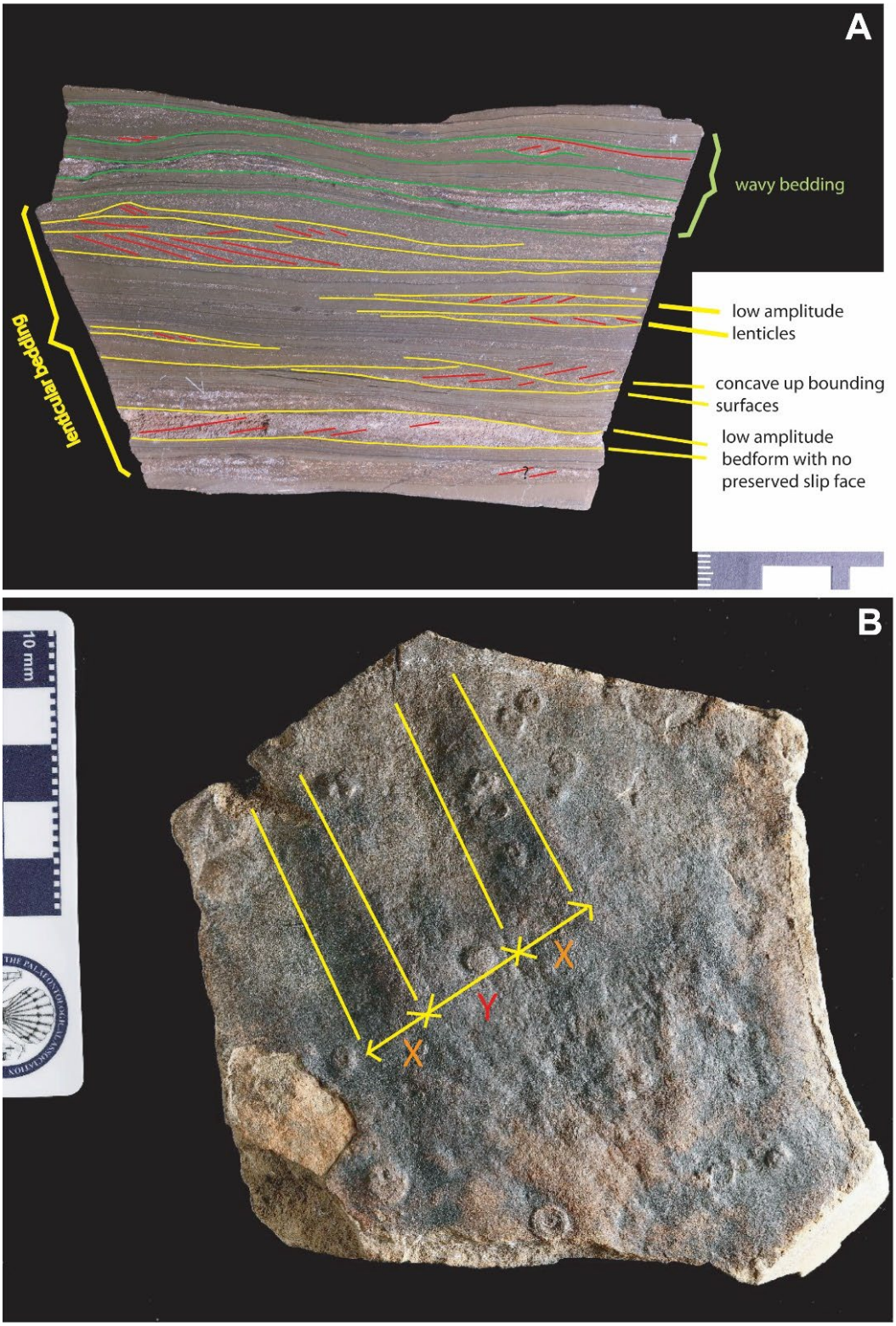

A) Cross-sectional view of a typical rock specimen that shows a range of small-scale bedforms in a strongly heterolithic bed set. Some main bedform bounding surfaces are indicated in yellow and green, and the foreset laminae in red. The preserved bedforms are all low amplitude, with only one apparent well-defined crest. Basal bounding surfaces are curvilinear to wavy, with some concave upward geometry highlighted. There are no obvious oscillatory ripples. The style of stratification displayed is typical of combined flow bedforms (oscillation/wave and current) with small scale, low amplitude bedforms and "washed-out" morphologies rather than strongly defined ripple crests. The lamina-sets are lenticular in the basal part and wavy in the upper part. Foreset lamination shows herringbone structures. The mudstone laminae and the mud/silt within sandstone lenticels may have inhibited the creation of strongly defined/crested ripples. This sample is deposited under NMW 76.16G.R.1.

B) Bedding plane view showing discoid fossils' frequency and straight crested low amplitude bedforms. The difference in measured distance between X and Y indicates bedform asymmetry, indicating a probable unidirectional current component to genesis. NMW 76.16G.R.2.

Panels A and B have been selected to show some observed depositional features. The heterolithic lenticular/wavy bedding with a combined flow genesis indicates probable shallow water. The fossils (in comparison with other localities worldwide) would suggest a marine environment, but a lacustrine setting cannot be ruled out. The frequency of mudstone laminae could reflect flocculation in a coastal setting with a freshwater input. It seems possible that there are instances of muddy drapes on some foreset laminae. Such structures are present on modern tidal flats, within tidal channels, and subaqueous reaches of flats/channels. They present similarities to examples from the Wenlock Series Gray Sandstone Formation of Pembrokeshire (SW Wales) that is interpreted as the product of prodelta and tidal channel deposits.

Chapter 6. A Scottish Provenance for the Altar Stone of Stonehenge

This chapter is published as:

Clarke, A. J. I., Kirkland, C. L., Bevins, R. E., Pearce, N. J. G., Glorie, S., and Ixer, R. A., 2024, A Scottish provenance for the Altar Stone of Stonehenge: Nature, v. 632, no. 8025, p. 570-575.

Doi.org/10.1038/s41586-024-07652-1

Minor post-publication changes and clarifications have been made.

Understanding the provenance of megaliths used in the Neolithic stone circle at Stonehenge, southern England, gives insight into the culture and connectivity of prehistoric Britain. The source of the Altar Stone, the central recumbent sandstone megalith, has been unknown, with recent work discounting an Anglo-Welsh Basin origin (Bevins et al., 2023b; Bevins et al., 2020). Here, we present the age and chemistry of detrital zircon, apatite, and rutile grains from within fragments of the Altar Stone. The detrital zircon load largely comprises Mesoproterozoic and Archaean sources, whereas rutile and apatite are dominated by a mid-Ordovician source. The ages of these grains indicate derivation from an ultimate Laurentian crystalline source region that was overprinted by Grampian (ca. 460 Ma) magmatism. Detrital age comparisons to sedimentary packages throughout Britain and Ireland reveal a remarkable similarity to the Old Red Sandstone of the Orcadian Basin in northeast Scotland. Such a provenance implies that the Altar Stone, a six-tonne-shaped block, was sourced at least 750 km from its current location. The difficulty of long-distance overland transport of such massive cargo from Scotland, navigating topographic barriers, suggests marine shipping. Such routing demonstrates a high level of societal organisation with intra-Britain transport during the Neolithic.

6.1. Introduction

Stonehenge, the Neolithic standing stone circle located on the Salisbury Plain in Wiltshire, England, offers valuable insight into prehistoric Britain. Construction at Stonehenge began as early as 3000 BC, with subsequent modifications during the following two millennia (Pearson et al., 2022; Pitts, 2022). The megaliths of Stonehenge are divided into two major categories: sarsen stones and bluestones (Figure 6.1a). The larger sarsens comprise duricrust silcrete predominantly sourced from the West Woods, Marlborough, ~25 km north of Stonehenge (Nash et al., 2021; Nash et al., 2020). Bluestone — the generic term for rocks considered exotic to the local area, includes volcanic tuff, rhyolite, dolerite, and sandstone lithologies (Figure 6.1a) (Pitts, 2022). Some lithologies are linked with Neolithic quarrying sites in the Mynydd Preseli area of west Wales (Pearson et al., 2015a; Pearson et al., 2019). An unnamed Lower Palaeozoic sandstone, associated with the west Wales area based on acritarch fossils (Ixer et al., 2017), is present only as widely disseminated debitage at Stonehenge and possibly as buried stumps (Stones 40g and 42c).

The central megalith of Stonehenge, the Altar Stone (Stone 80), is the largest of the bluestones, measuring 4.9 x 1 x 0.5 m, and is a six-tonne recumbent stone (Figure 6.1b) composed of pale-green micaceous sandstone with distinctive mineralogy (containing baryte, calcite, and clay minerals, whilst K-feldspar is notably absent) (Bevins et al., 2023b; Bevins et al., 2020; Ixer and Turner, 2006) (Figure 6.2).

Previous petrographic work on the Altar Stone has implied an association to the Old Red Sandstone (ORS) (Ixer et al., 2020; Ixer and Turner, 2006; Thomas, 1923). The ORS is a late Silurian to Devonian sedimentary rock assemblage that crops out widely throughout Great Britain and Ireland (Appendix E 6.13.1). ORS lithologies are dominated by terrestrial siliciclastic sedimentary rocks deposited in continental fluvial, lacustrine, and aeolian environments (Kendall, 2017). Each ORS basin reflects local subsidence and sediment infill and thus contains proximal crystalline signatures (Kendall, 2017; Woodcock et al., 2012).

Constraining the Altar Stone's provenance could give insights into the connectivity of Neolithic people who left no written record (Pearson et al., 2015b). When the Altar Stone arrived at Stonehenge is uncertain; however, it may have been placed within the central trilithon horseshoe during the second construction phase at ca. 2620 – 2480 BC (Pearson et al., 2022). Whether the Altar Stone once stood upright as a ~ 4 m high megalith is unclear (Pearson et al.,

2015b); nevertheless, the current arrangement has Stones 55b and 156 from the collapsed Great Trilithon resting atop the prone and broken Altar Stone (Figure 6.1b).

An early proposed source for the Altar Stone from Mill Bay, Pembrokeshire (Cosheston Subgroup of the Anglo-Welsh ORS Basin), close to the Mynydd Preseli source of the doleritic and rhyolitic bluestones, strongly influenced the notion of a sea transport route via the Bristol Channel (Thomas, 1923). However, inconsistencies in petrography and detrital zircon ages between the Altar Stone and the Cosheston Subgroup have ruled this source out (Bevins et al., 2020; Ixer et al., 2020). Nonetheless, a source from elsewhere in the ORS of the Anglo-Welsh Basin was still considered likely, with an inferred collection and overland transport of the Altar Stone en route to Stonehenge from the Mynydd Preseli (Bevins et al., 2020). However, a source from the Senni Formation is inconsistent with geochemical and petrographic data, which shows that the Anglo-Welsh Basin is highly unlikely to be the source (Bevins et al., 2023b). Thus, the ultimate provenance of the Altar Stone had remained an open question.

Studies of detrital mineral grains are widely deployed to address questions throughout the Earth sciences and have utility in archaeological investigations (Kelloway et al., 2014; Shewan et al., 2021). Sedimentary rocks commonly contain a detrital component derived from a crystalline igneous basement, which may reflect a simple or complex history of erosion, transport, and deposition cycles. This detrital cargo can fingerprint a sedimentary rock and its hinterland. More detailed insights become evident when a multi-mineral strategy is implemented, which benefits from the varying degrees of robustness to sedimentary transportation in the different minerals (Barham et al., 2016; Fairey et al., 2018; Gillespie et al., 2018).

Here, we present *in-situ* U–Pb, Lu–Hf, and trace element isotopic data for zircon, apatite, and rutile from two fragments of the Altar Stone collected at Stonehenge: MS3 and 2010K.240 (Bevins et al., 2022; Bevins et al., 2023c). In addition, we present comparative apatite U–Pb dates for the Orcadian Basin from Caithness and Orkney. We employ statistical tools (Figure 6.3) to compare the obtained detrital mineral ages and chemistry to crystalline terranes and Old Red Sandstone successions across Great Britain, Ireland, and Europe (Figure 6.4; Appendix E 6.13.1).

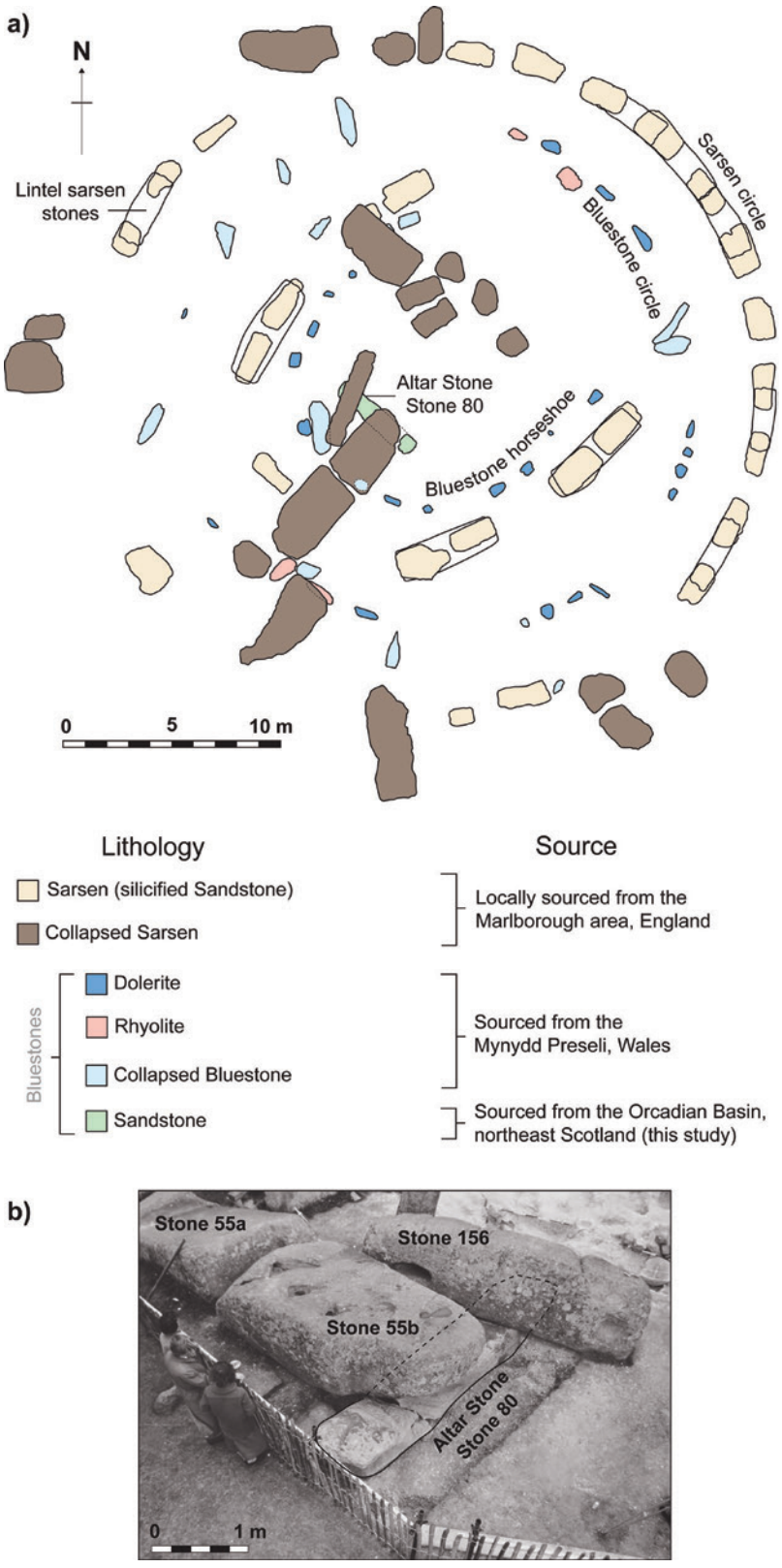

Figure 6.1. The layout of Stonehenge and the appearance of the Altar Stone. ***a)*** *Plan view of Stonehenge showing exposed constituent megaliths and their provenance. The plan of Stonehenge was adapted from Nash, et al. 2021 under a CC BY 4.0 license. Changes in scale and colour were made, and annotations were added.* ***b)*** *An annotated photograph shows the Altar Stone during a 1958 excavation. The Altar Stone photograph is from the Historic England archive. Reuse not permitted*

6.2. Laurentian Basement Signatures

The crystalline basement terranes of Great Britain and Ireland, from north to south, are Laurentia, Ganderia, Megumia, and East Avalonia (Figure 6.4a; Appendix E 6.13.1). Cadomia-Armorica is south of the Rheic Suture and encompasses basement rocks in western Europe, including northern France and Spain. East Avalonia, Megumia, and Ganderia are partly separated by the Menai Strait Fault System (Figure 6.4a). Each terrane has discrete age components, which have imparted palaeogeographic information into overlying sedimentary basins (Kendall, 2017; Morton et al., 2021; Woodcock et al., 2012). Laurentia was a palaeocontinent that collided with Baltica and Avalonia (a peri-Gondwanan microcontinent) during the early Palaeozoic Caledonian Orogeny to form Laurussia (Cawood et al., 2007; Woodcock et al., 2012). West Avalonia is a terrane that includes parts of eastern Canada and comprises Avalonia's western margin (Appendix E 6.13.1).

Statistical comparisons, using a Kolmogorov-Smirnov (KS) test, between zircon ages from the Laurentian crystalline basement and the Altar Stone indicate that, at a 95% confidence level, no distinction in provenance is evident between Altar Stone detrital zircon U–Pb ages and those from the Laurentian basement. That is, we cannot reject the null hypothesis that both samples are from the same underlying age distribution (KS test: $P>0.05$) (Figure 6.3a).

Detrital zircon age components, defined by concordant analyses from ≥ 4 grains in the Altar Stone, include maxima at 1047, 1091, 1577, 1663, and 1790 Ma (Appendix E 6.13.2), corresponding to known tectonomagmatic events and sources within Laurentia and Baltica, including the Grenville (1095 – 980 Ma), Labrador (1690 – 1590 Ma), Gothian (1660 – 1520 Ma), and Svecokarellian (1920 – 1770 Ma) orogenies (Strachan et al., 2021).

Laurentian terranes are crystalline lithologies north of the Iapetus Suture Zone (which marks the collision zone between Laurentia and Avalonia) and include the Southern Uplands, Midland Valley, Grampian, Northern Highlands, and Hebridean Terranes (Figure 6.4a). Together, these terranes preserve a Proterozoic to Archaean record of zircon production (Cawood et al., 2007), distinct from the southern Gondwanan-derived terranes of Britain (Figure 6.4a; Appendix E 6.13.3) (Fairey et al., 2018; Stevens and Baykal, 2021).

Age data from Altar Stone rutile grains also point towards an ultimate Laurentian source with several discrete age components (Appendix E 6.13.4). Group 2 rutile U–Pb analyses from the Altar Stone include Proterozoic ages from 1724 – 591 Ma, with three grains constituting an age peak at 1607 Ma, overlapping with Laurentian magmatism, including the Labrador and

Pinwarian (1690 – 1380 Ma) orogenies (Cawood et al., 2007). Southern terranes in Britain are not characterised by a large Laurentian (Mesoproterozoic) crystalline age component (Figure 6.4b; Appendix E 6.13.3) (Strachan et al., 2021). Instead, terranes south of the Iapetus Suture are defined by Neoproterozoic to early Palaeozoic with minor ca. 2 Ga age components (Figure 6.3b; Figure 6.4b).

Altar Stone apatite U–Pb analyses define two distinct age groupings. Group 2 apatite U–Pb analyses define a lower intercept age of 1018 ± 24 Ma (n = 9) (Appendix E 6.13.5), which overlaps, within uncertainty, to a zircon age component at 1047 Ma, consistent with a Grenville source (Strachan et al., 2021). Apatite Lu–Hf dates at 1496 and 1151 Ma also imply distinct Laurentian sources (Figure 6.4b; Appendix E 6.13.6) (Strachan et al., 2021). Ultimately, the presence of Grenvillian apatite in the Altar Stone suggests direct derivation from the Laurentian basement, given the lability of apatite during prolonged chemical weathering (Fairey et al., 2018; O'Sullivan et al., 2020).

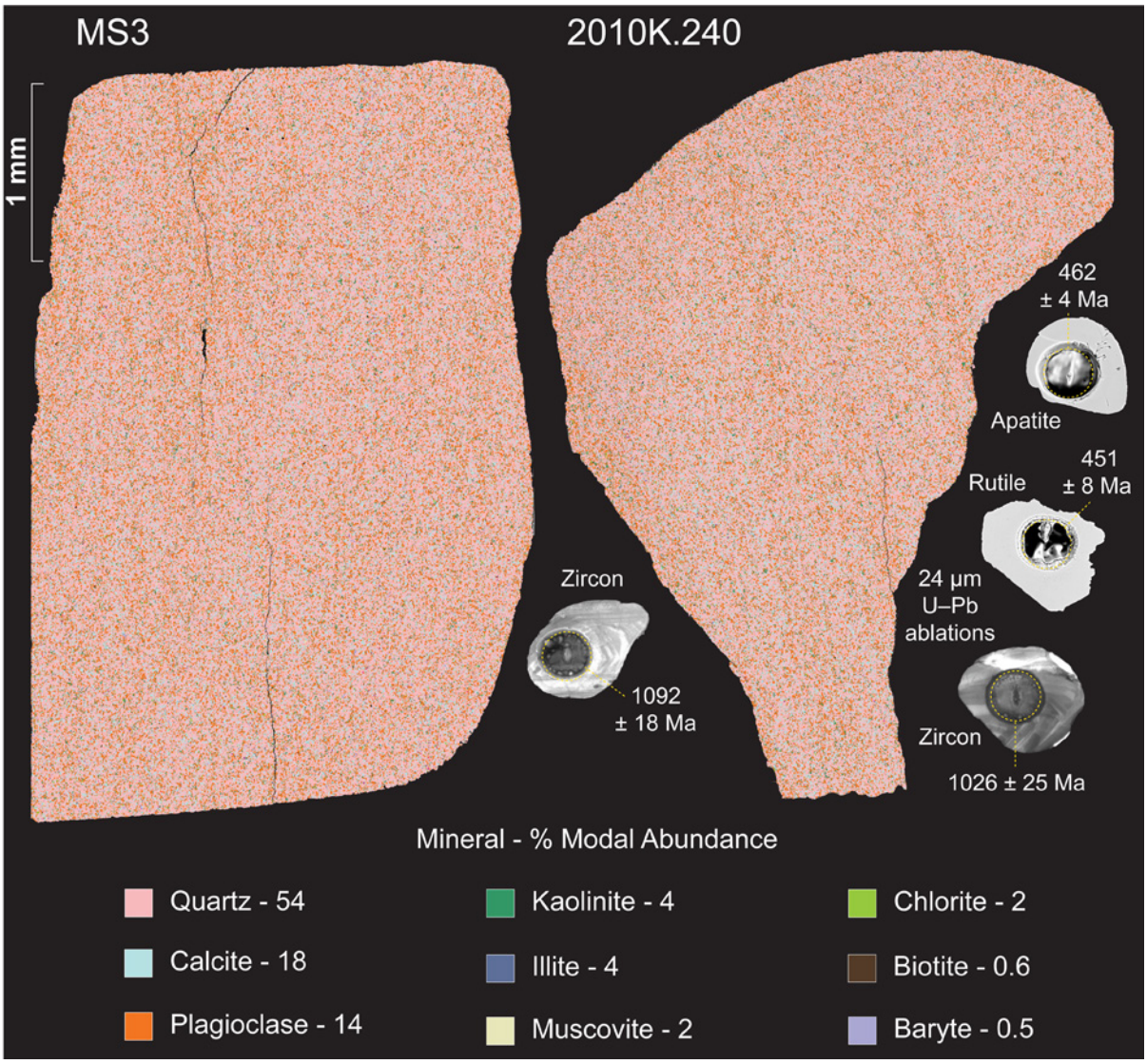

Figure 6.2. False colour automated mineralogy maps from thin-sections of the Altar Stone. Minerals with a modal abundance > 0.5 % are shown with compositional values averaged across both thin-sections. LA-ICP-MS U–Pb ablation pits are shown with age (in millions of years) with uncertainty at the two-sigma level.

6.3. Grampian Terrane Detrital Grains

Apatite and rutile U–Pb analyses from the Altar Stone are dominated by regressions from common Pb that yield lower intercepts of 462 ± 4 Ma (n = 108) and 451 ± 8 Ma (n = 83), respectively. A single concordant zircon analysis also yields an early Palaeozoic age of 498 ± 17 Ma. Hence, with uncertainty from both lower intercepts, Group 1 apatite and rutile analyses demonstrate a mid-Ordovician (443 – 466 Ma) age component in the Altar Stone. These mid-Ordovician ages are confirmed by *in-situ* apatite Lu–Hf analyses, which define a lower intercept of 470 ± 29 Ma (n = 16) (Appendix E 6.13.6).

Throughout the Altar Stone are sub-planar 100 – 200 µm bands of concentrated heavy resistive minerals. These resistive minerals are interpreted to be magmatic in origin, given internal textures (oscillatory zonation), lack of mineral overgrowths (in all dated minerals) (Figure 6.2) and the igneous apatite trace element signatures (Appendix E 6.13.7) (O'Sullivan et al., 2020). Moreover, there is a general absence of detrital metamorphic zircon grains, further supporting a magmatic origin for these grains.

The most appropriate source region for such mid-Ordovician grains within Laurentian basement is the Grampian Terrane of northeast Scotland (Figure 6.4a). Situated between the Great Glen Fault to the north and the Highland Boundary Fault to the south, the terrane comprises Neoproterozoic to Lower Palaeozoic metasediments termed the Dalradian Supergroup (Oliver et al., 2008), which are intruded by a compositionally diverse suite of early Palaeozoic granitoids and gabbros (Figure 6.4a). The 466 – 443 Ma age component from Group 1 apatite and rutile U–Pb analyses overlaps with the terminal stages of Grampian magmatism and subsequent granite pluton emplacement north of the Highland Boundary Fault (Figure 6.4a) (Oliver et al., 2008).

Geochemical classification plots for the Altar Stone apatite imply a compositionally diverse source, much like the lithological diversity within the Grampian Terrane (Oliver et al., 2008), with 61% of apatite classified as coming from felsic sources, 35% mafic, and 4% alkaline (Appendix E 6.13.7). Specifically, igneous rocks within the Grampian Terrane are largely granitoids, thus accounting for the predominance of felsic-classified apatite grains (Fleischer and Altschuler, 1986). We posit that the dominant supply of 466 – 443 Ma detritus came from the numerous similarly aged granitoids formed on the Laurentian margin (Oliver et al., 2008), which are present in both the Northern Highlands and the Grampian Terranes (Oliver et al., 2008) (Figure 6.4a). The alkaline to calc-alkaline suites in these terranes are

volumetrically small, consistent with the scarcity of alkaline apatite grains within the Altar Stone (Appendix E 6.13.7). Indeed, the 447 ± 3 Ma Glen Dessary syenite is the only age-appropriate felsic-alkaline pluton in the Northern Highlands Terrane (Goodenough et al., 2011).

The Stacey and Kramers (1975) model of terrestrial Pb-isotopic evolution predicts a $^{207}Pb/^{206}Pb_i$ of 0.8601 for 465 Ma continental crust. Mid-Ordovician regressions through Group 1 apatite and rutile U–Pb analyses yield upper intercepts for $^{207}Pb/^{206}Pb_i$ of 0.8603 ± 0.0033 and 0.8564 ± 0.0014, respectively. The similarity between apatite and rutile $^{207}Pb/^{206}Pb_i$ implies they were sourced from the same Mid-Ordovician magmatic fluids. Ultimately, the calculated $^{207}Pb/^{206}Pb_i$ value is consistent with the older (Laurentian) crust north of the Iapetus Suture in Britain (Evans et al., 2022) (Figure 6.4a).

6.4. Orcadian Basin Old Red Sandstone

The detrital zircon age spectra confirm petrographic associations between the Altar Stone and the ORS. Furthermore, the Altar Stone cannot be a New Red Sandstone (NRS) lithology of Permo-Triassic age. The NRS, deposited from ca. 280 – 240 Mya, unconformably overlies the ORS (Woodcock et al., 2012). NRS, such as that within the Wessex Basin (Appendix E 6.13.1), has characteristic detrital zircon age components, including Carboniferous to Permian zircon grains, which are not present in the Altar Stone (Appendix E 6.13.3) (Bevins et al., 2020; Morton et al., 2013; Morton et al., 2016; Morton et al., 2021; Stevens and Baykal, 2021).

An ORS classification for the Altar Stone provides the basis for further provenance interpretation (Appendix E 6.13.1), given that the ORS crops out in distinct areas of Great Britain and Ireland, including the Anglo-Welsh border and south Wales, the Midland Valley, and northeast Scotland, reflecting former Palaeozoic depocentres (Figure 6.4a) (Woodcock et al., 2012).

Previously reported detrital zircon ages and petrography show that ORS outcrops of the Anglo-Welsh Basin in the Cosheston Subgroup (Bevins et al., 2020) and Senni Formation (Bevins et al., 2023b) are unlikely to be the sources of the Altar Stone (Figure 6.4a). ORS within the Anglo-Welsh Basin is characterised by mid-Palaeozoic zircon age maxima and minor Proterozoic components (Figure 6.4a). Ultimately, the detrital zircon age spectra of the Altar Stone are statistically distinct from the Anglo-Welsh Basin (Figure 6.3a). In addition, the ORS outcrops of southwest England (i.e. south of the Variscan front), including north Devon and Cornwall (Cornubian Basin) (Figure 6.4a), show characteristic facies, including marine

sedimentary structures and fossils along with a metamorphic fabric (Kendall, 2017; Stevens and Baykal, 2021), inconsistent with the unmetamorphosed, terrestrial facies of the Altar Stone (Bevins et al., 2020; Ixer et al., 2020).

Another ORS succession with published age data for comparison is the Dingle Peninsula Basin, southwest Ireland. However, the presence of late Silurian (430 – 420 Ma) and Devonian (400 – 350 Ma) apatite, zircon, and muscovite from the Dingle Peninsula ORS discount a source for the Altar Stone from southern Ireland (Fairey et al., 2018). The conspicuous absence of < 450 Ma apatite grains in the Altar Stone precludes the input of Late Caledonian magmatic grains to the source sediment of the Altar Stone and demonstrates that the ORS of the Altar Stone was deposited prior to or distally from areas of Late Caledonian magmatism, unlike the ORS of the Dingle Peninsula (Fairey et al., 2018). Notably, no distinction in provenance between the Anglo-Welsh Basin and the Dingle Peninsula ORS is evident (KS test: $P>0.05$), suggesting that ORS basins south of the Iapetus Suture are relatively more homogenous in terms of their detrital zircon age components (Figure 6.4a).

In Scotland, ORS predominantly crops out in the Midland Valley and Orcadian Basins (Figure 6.4a). The Midland Valley Basin is bound between the Highland Boundary Fault and the Iapetus Suture and is located within the Midland Valley and Southern Uplands Terranes. Throughout Midland Valley ORS stratigraphy, detrital zircon age spectra broadly show a bimodal age distribution between Lower Palaeozoic and Mesoproterozoic components (McKellar et al., 2019; Phillips et al., 2009) (Appendix E 6.13.3). Indeed, throughout 9 km of ORS stratigraphy in the Midland Valley Basin and across the Sothern Uplands Fault, no major changes in provenance are recognised (McKellar et al., 2019) (Figure 6.4a). Devonian zircon, including grains as young as 402 ± 5 Ma (McKellar et al., 2019) from the northern ORS in the Midland Valley Basin, further differentiates this basin from the Altar Stone (Figure 6.3a; Appendix E 6.13.3). The scarcity of Archaean to late Palaeoproterozoic zircon grains within the Midland Valley ORS shows that the Laurentian basement was not a dominant detrital source for those rocks (Phillips et al., 2009). Instead, ORS of the Midland Valley is primarily defined by ca. 475 Ma zircon interpreted to represent the detrital remnants of Ordovician volcanism within the Midland Valley Terrane, with only minor and periodic input from Caledonian plutonism (Phillips et al., 2009).

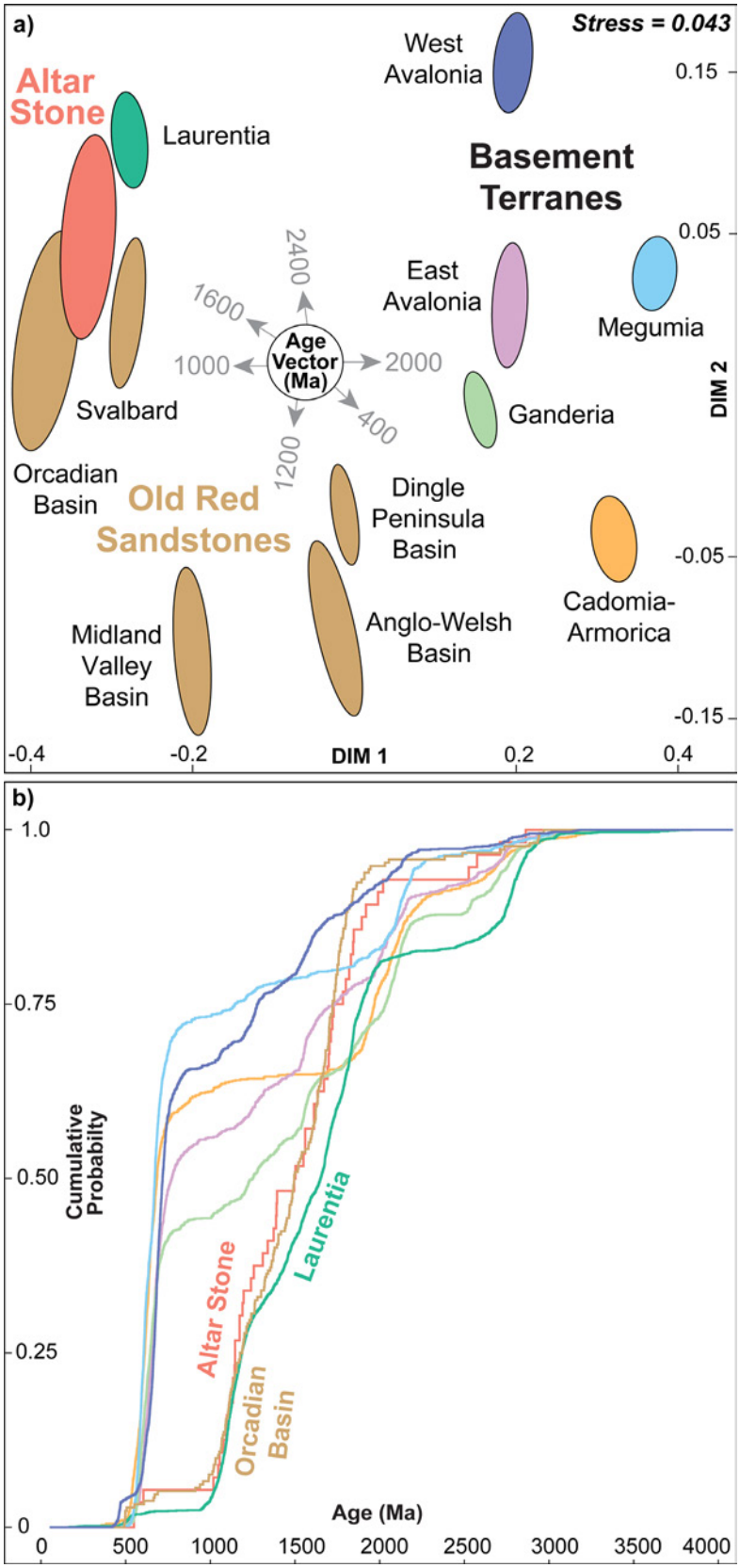

Figure 6.3. Comparisons of detrital zircon U–Pb ages from the Altar Stone and crystalline terranes of Britain, Ireland, and Europe. ***a)*** *Multidimensional scaling plot of concordant zircon U–Pb ages from the Altar Stone and comparative age datasets, with ellipses at the 95% confidence level (Nordsvan et al., 2020).* ***b)*** *Cumulative probability plot of zircon U–Pb ages from crystalline terranes, the Orcadian Basin, and the Altar Stone.*

The Orcadian Basin of northeast Scotland, within the Grampian and Northern Highlands terranes, contains a thick package of mostly Mid-Devonian ORS, ~4 km thick in Caithness and up to ~8 km thick in Shetland (Figure 6.4a) (Woodcock et al., 2012). The detrital zircon age spectra from Orcadian Basin ORS provides the closest match to the Altar Stone detrital ages (Strachan et al., 2021) (Figure 6.3; Appendix E 6.13.8). A KS test on age spectra from the Altar Stone and the Orcadian Basin fails to reject the null hypothesis that they are derived from the same underlying distribution (KS test: $P > 0.05$) (Figure 6.3a). To the north, ORS on the Svalbard archipelago formed on Laurentian and Baltican basement rocks (Beranek et al., 2020). Similar KS test results, where each detrital zircon dataset are statistically indistinguishable, are obtained for ORS from Svalbard, the Orcadian Basin, and the Altar Stone.

Apatite U–Pb age components from Orcadian Basin samples from Spittal, Caithness (AQ1) and Cruaday, Orkney (CQ1) (Figure 6.4a) match those from the Altar Stone. Group 2 apatite from the Altar Stone at 1018 ± 24 Ma is coeval with a Grenvillian age from Spittal at 1013 ± 35 Ma. Early Palaeozoic apatite components at 473 ± 25 Ma and 466 ± 6 Ma, from Caithness and Orkney, respectively (Appendix E 6.13.5), are also identical, within uncertainty, to Altar Stone Group 1 (462 ± 4 Ma) apatite U–Pb analyses and a Lu–Hf component at 470 ± 28 Ma supporting a provenance from the Orcadian Basin for the Altar Stone (Appendix E 6.13.6).

During the Palaeozoic, the Orcadian Basin was situated between Laurentia and Baltica on the Laurussian palaeocontinent (Woodcock et al., 2012). Correlations between detrital zircon age components imply that both Laurentia and Baltica supplied sediment into the Orcadian Basin (McKellar et al., 2019; Strachan et al., 2021). Detrital grains >900 Ma within the Altar Stone are consistent with sediment recycling from intermediary Neoproterozoic supracrustal successions (e.g. Dalradian Supergroup) within the Grampian Terrane but also from the Särv and Sparagmite successions of Baltica (McKellar et al., 2019; Strachan et al., 2021). At ca. 470 Ma, the Grampian Terrane began to denude (Oliver et al., 2008). Subsequently, first-cycle detritus, such as that represented by Group 1 apatite and rutile, was shed towards the Orcadian Basin from the southeast (Strachan et al., 2021). Thus, the resistive mineral cargo in the Altar Stone represents a complex mix of first and multi-cycle grains from multiple sources. Regardless of total input from Baltica versus Laurentia into the Orcadian Basin, crystalline terranes north of the Iapetus Suture (Figure 6.4a) have distinct age components that match the Altar Stone in contrast to Gondwanan-derived terranes to the south.

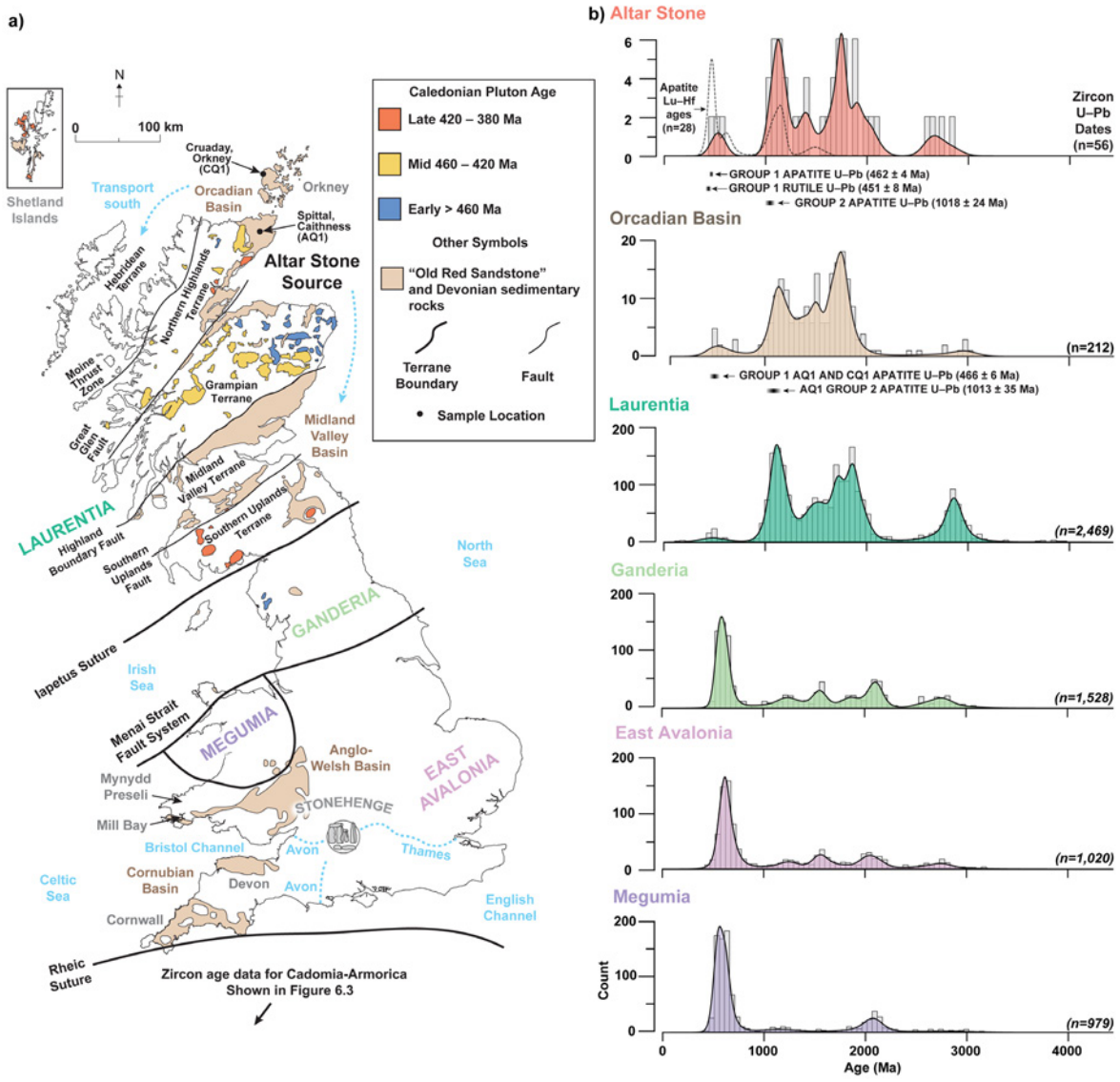

Figure 6.4. The zircon age spectra of geological terranes and Old Red Sandstone basins of Britain compared to the Altar Stone. ***a)*** *Schematic map of Britain showing outcrops of Old Red Sandstone and other Devonian sedimentary rocks, basement terranes, and major faults. Potential Caledonian source plutons are colour-coded based on age (Oliver et al., 2008).* ***b)*** *Kernel density estimate diagrams displaying zircon U–Pb age (red histogram) and apatite Lu–Hf age (dashed line) spectra from the Altar Stone, the Orcadian Basin (Strachan et al., 2021), and plausible crystalline source terranes.*

6.5. The Altar Stone and Neolithic Britain

Isotopic data for detrital zircon and rutile (U–Pb) and apatite (U–Pb, Lu–Hf, and trace elements) indicate that the Altar Stone of Stonehenge has a provenance from the ORS in the Orcadian Basin of northeast Scotland (Figure 6.4a). Given this detrital mineral provenance, the Altar Stone cannot have been sourced from southern Britain (i.e., south of the Iapetus Suture) (Figure 6.4a), including the Anglo-Welsh Basin (Bevins et al., 2023b; Bevins et al., 2020).

Some postulate a glacial transport mechanism for the Mynydd Preseli (Figure 6.4a) bluestones to Salisbury Plain (John, 2018, 2024). However, such transport for the Altar Stone is difficult to reconcile with ice-sheet reconstructions that show a northwards movement of glaciers (and erratics) from the Grampian Mountains towards the Orcadian Basin during the Last Glacial Maximum and, indeed, previous Pleistocene glaciations (Clark et al., 2022; Gibbard and Clark, 2011). Moreover, there is little evidence of extensive glacial deposition in central southern Britain (Clark et al., 2022), nor are Scottish glacial erratics found at Stonehenge (Bevins et al., 2023a). Sr and Pb isotopic signatures from animal and human remains from henges on Salisbury Plain demonstrate the mobility of Neolithic people within Britain (Evans et al., 2006; Evans et al., 2022; Snoeck et al., 2018; Viner et al., 2010). Furthermore, shared architectural elements and rock art motifs between Neolithic monuments in Orkney, northern Britain, and Ireland point towards the long-distance movement of people and construction materials (Bradley, 2023, 2024).

Hence, we posit that the Altar Stone was anthropogenically transported to Stonehenge from northeast Scotland, consistent with evidence of Neolithic inhabitation in this region (Bayliss et al., 2017; Fairweather and Ralston, 1993). Whereas the igneous bluestones were brought ~ 225 km from the Mynydd Preseli to Stonehenge (Parker Pearson et al., 2020) (Figure 6.4a), a Scottish provenance for the Altar Stone demands a transport distance of at least 750 km (Figure 6.4a). Nonetheless, even with assistance from beasts of burden (Pigière and Smyth, 2023), rivers and topographical barriers, including the Grampians, Southern Uplands, and the Pennines, along with the heavily forested landscape of prehistoric Britain (Godwin, 1975), would have posed formidable obstacles for overland megalith transportation.

At ca. 5000 BP, Neolithic people introduced the common vole (*Microtus arvalis*) from continental Europe to Orkney, consistent with the long-distance marine transport of cattle and goods (Martínková et al., 2013). A Neolithic marine trade network of quarried stone tools is found throughout Britain, Ireland, and continental Europe (Bradley and Edmonds, 2005). For

example, a saddle quern, a large stone grinding tool, was discovered in Dorset and determined to have a provenance in central Normandy (Peacock et al., 2010), implying the shipping of stone cargo over open water during the Neolithic. Furthermore, the river transport of shaped sandstone blocks in Britain is known from at least ca. 1500 BC (Hanson Log Boat) (Pinder et al., 2017). In Britain and Ireland, sea levels approached present-day heights from ca. 4000 BC (Harff et al., 2017), and although coastlines have shifted, the geography of Britain and Ireland would have permitted sea routes southward from the Orcadian Basin towards southern England (Figure 6.4a). A Scottish provenance for the Altar Stone implies Neolithic transport spanning the length of Great Britain.

6.6. Methods

6.6.1. Overview

This work analysed two 30 µm polished thin sections of the Altar Stone (MS3 and 2010K.240) and two sections of Old Red Sandstone from northeast Scotland (Table 6.1). CQ1 is from Cruaday, Orkney (59°04'34.2" N, 3°18'54.6" W), and AQ1 is from near Spittal, Caithness (58°28'13.8" N, 3°27'33.6" W). Conventional optical microscopy (transmitted and reflected light) and automated mineralogy via a TESCAN Integrated Mineral Analyser gave insights into texture and mineralogy and guided spot placement during LA-ICP-MS analysis. A Clara-FE-SEM was used for textural characterisation of individual minerals (zircon, apatite, rutile) through high-resolution µm-scale imaging under both back-scatter electron and cathodoluminescence. The Altar Stone is fine-grained and well-sorted sandstone with a mean grain size diameter of ≤ 300 µm. Quartz grains are sub-rounded and monocrystalline. Feldspars are variably altered to fine-grained white mica. MS3 and 2010K.240 have a weakly developed planar fabric and non-planar heavy mineral laminae approximately 100 – 200 µm thick. Resistive heavy mineral bands are dominated by zircon, rutile, and apatite, with grains typically 10 – 40 µm wide. The rock is mainly cemented by carbonate, with localised areas of barite and quartz cement. A detailed account of Altar Stone petrography is provided in Bevins et al. (2020) and Ixer et al. (2019).

Altar Stone Samples

Sample	Automated Mineralogy	Zircon U–Pb	Rutile U–Pb	Apatite U–Pb	Apatite Lu–Hf	Apatite Trace Elements
MS3	**X**	**X**	**X**	**X**		**X**
2010K.240	**X**	**X**			**X**	

Orcadian Basin Samples

Sample	Automated Mineralogy	Zircon U–Pb	Rutile U–Pb	Apatite U–Pb	Apatite Lu–Hf	Apatite Trace Elements
Spittal, Caithness (AQ1)	**X**			**X**		
Cruaday, Orkney (CQ1)	**X**			**X**		

Table 6.1. A summary of analyses performed on each Altar Stone and Orcadian Basin sample. X denotes the analysis undertaken.

6.7. Zircon Analysis

6.7.1. Zircon U–Pb Methods

Two zircon U–Pb analysis sessions were completed at the GeoHistory facility in the John De Laeter Centre (JdLC), Curtin University, Australia. Ablations within zircon grains used an excimer laser RESOlution LE193 nm ArF with a Laurin Technic S155 cell. Isotopic data was collected with an Agilent 8900 triple quadrupole mass spectrometer, with high-purity Ar as the plasma carrier gas (flow rate 1 L min). An on-sample energy of ~2.3 – 2.7 J cm^{-2} with a 5 – 7 Hz repetition rate was used to ablate minerals for 30 – 40 seconds (with 25 – 60 seconds of background capture). Two cleaning pulses preceded analyses, and ultra-high purity He (320 mL min^{-1}) and N_2 (1.2 mL min^{-1}) were used to flush the sample cell. A block of reference mineral was analysed following 15 – 20 unknowns.

The small, highly rounded target grains of the Altar Stone (usually < 30 µm in width) necessitated using a ~24 µm spot size diameter for all ablations. Isotopic data was reduced using Iolite 4 (Paton et al., 2011) with the U-Pb Geochronology data reduction scheme, followed by additional calculation and plotting via Isoplot R (Vermeesch, 2018). The primary matrix-matched reference zircon used to correct instrumental drift and mass fractionation was GJ-1, 601.95 ± 0.40 Ma (Jackson et al., 2004). Secondary reference zircon included Plešovice, 337.13 ± 0.37 Ma (Sláma et al., 2008), 91500, 1063.78 ± 0.65 Ma (Wiedenbeck et al., 1995), OG1 3465.4 ± 0.6 Ma (Stern et al., 2009) and Maniitsoq 3008.7 ± 0.6 Ma (Marsh et al., 2019). Weighted mean U–Pb ages for secondary reference materials were within 2σ uncertainty of reported values (Table 6.2).

Session 1 (MS3)

Reference	Primary Reference	Weighted Mean Age (Ma)*	± 2σ	MSWD*	*P**	*n*
91500		**1059**	**10**	**0.72**	**0.69**	**10**
Published age	GJ1	1063.78	0.65	*Wiedenbeck et al., 1995*		
Plešovice		**336**	**3**	**0.69**	**0.78**	**15**
Published age	GJ1	337.13	0.37	*Slama et al., 2008*		
OG1		**3468**	**4**	**0.73**	**0.75**	**16**
Published age	GJ1	3465.40	0.60	*Stern et al., 2009*		
Maniitsoq		**3014**	**6**	**0.65**	**0.85**	**17**
Published age	GJ1	3008.70	0.60	*Marsh et al., 2019*		

Session 2 (2010K.240)

Reference	Primary Reference	Weighted Mean Age (Ma)*	± 2σ	MSWD*	*P**	*n*
91500		**1060**	**3**	**1.20**	**0.23**	**24**
Published age	GJ1	1063.78	0.65	*Wiedenbeck et al., 1995*		
Plešovice		**338**	**1**	**1.20**	**0.27**	**18**
Published age	GJ1	337.13	0.37	*Slama et al., 2008*		
OG1		**3466**	**7**	**0.78**	**0.79**	**29**
Published age	GJ1	3465.40	0.60	*Stern et al., 2009*		

*Table 6.2. A summary of ages obtained for zircon U–Pb secondary reference material. *Where MSWD and P are the mean square of the weighted deviation value and the associated MSWD age homogeneity test chi-squared P-value, both metrics are one-sided measurements.*

6.7.2. Zircon U–Pb Results

Across two LA-ICP-MS sessions, 83 U–Pb measurements were obtained on as many zircon grains; 41 were concordant (≤ 10 % discordant), where discordance is defined using the concordia log distance (%) approach (Vermeesch, 2021). We report single-spot (grain) concordia ages, which have numerous benefits over conventional U–Pb/Pb–Pb ages, including providing an objective measure of discordance that is directly coupled to age and avoids the arbitrary switch between $^{206}Pb/^{238}U$ and $^{207}Pb/^{206}Pb$. Furthermore, given the spread in ages (Early Palaeozoic to Archean), concordia ages provide optimum use of both U–Pb/Pb–Pb ratios, offering greater precision over $^{206}Pb/^{238}U$ or $^{207}Pb/^{206}Pb$ ages alone.

Given that no direct sampling of the Altar Stone is permitted, we are limited in the amount of material available for destructive analysis, such as LA-ICP-MS. We collate our zircon age data with the U–Pb analyses (Bevins et al., 2020) of FN593 (another fragment of the Altar Stone), filtered using the same concordia log distance (%) discordance filter (Vermeesch, 2021). The total concordant analyses used in this work is thus 56 over three thin sections, each showing no discernible provenance differences. Zircon concordia ages span from 498 to 2812 Ma. Age maxima (peak) were calculated after Gehrels (2011), and peak ages defined by ≥4 grains include 1047, 1091, 1577, 1663 and 1790 Ma.

For 56 concordant ages from 56 grains at > 95% certainty, the largest unmissed fraction is calculated at 9% of the entire uniform detrital population (Vermeesch, 2004). In any case, the most prevalent and hence provenance significant components will be sampled for any number of analyses (Vermeesch, 2004). We analysed all zircon grains within the spatial limit of the technique in the thin sections (Dröllner et al., 2021). We used *in-situ* thin-section analysis to mitigate contamination and sampling biases in detrital studies (Zutterkirch et al., 2021). Adding apatite (U–Pb and Lu–Hf) and rutile (U–Pb) analyses bolsters our confidence in provenance interpretations as these minerals will respond dissimilarly during transport.

6.7.3. Comparative Zircon Datasets

Zircon U–Pb compilations of the basement terranes of Britain and Ireland were sourced from Fairey et al. (2018) and Stevens and Baykal (2021). Old Red Sandstone detrital zircon datasets used for comparison include isotopic data from the Dingle Peninsula Basin (Fairey et al., 2018), Anglo-Welsh Basin (Morton et al., 2015), Midland Valley Basin (Phillips et al., 2009), Svalbard Old Red Sandstone (Beranek et al., 2020), and Orcadian Basin (Strachan et al., 2021). New Red Sandstone zircon U–Pb ages were sourced from the Wessex Basin (Morton et al., 2016). Comparative datasets were filtered for discordance as per our definition above (Fairey et al., 2018; Stevens and Baykal, 2021). Kernel density estimates for age populations were created within IsoplotR (Vermeesch, 2018) using a kernel and histogram bandwidth of 50 Ma. A two-sample Kolmogorov-Smirnov (KS) statistical test was implemented to compare the compiled zircon age datasets with the Altar Stone (Table 6.3). This two-sided test compares the maximum probability difference between two cumulative density age functions, evaluating the null hypothesis that both age spectra are drawn from the same distribution based on a critical value dependent on the number of analyses and a chosen confidence level.

The number of zircon ages within the comparative datasets used varies from the Altar Stone (n = 56) to Laurentia (n = 2469). Therefore, to address the degree of dependence on sample n, we also implemented a Monte-Carlo resampling (1000 times) procedure for the KS test, including the uncertainty on each age determination to recalculate P-values and standard deviations (Table 6.4), based on the resampled distribution of each sample. The results from KS tests, using Monte Carlo resampling (and multidimensional analysis), taking uncertainty due to sample n into account, also support the interpretation that at >95% certainty, no distinction in provenance can be made between the Altar Stone zircon age dataset (n = 56) and those from the Orcadian Basin (n = 212), Svalbard Old Red Sandstone (n = 619) and the Laurentian basement (Table 6.4). Multidimensional scaling plots (MDS) for zircon datasets were created using the MATLAB script of Nordsvan, et al. 2020 (Nordsvan et al., 2020). Here, we adopted a bootstrap resampling (>1000 times) with Procrustes rotation of KS values, which outputs uncertainty ellipses at a 95% confidence level (Figure 6.3a). In MDS plots, stress is a goodness of fit indicator between dissimilarities in the datasets and distances on the MDS plot. Stress values below 0.15 are desirable (Nordsvan et al., 2020). For the MDS plot in Figure 6.3a, the value is 0.043, which indicates an “excellent” fit (Nordsvan et al., 2020).

Table 6.3. KS Test Results. Highlighted green values are P>0.05 and blue values are the associated D-values for P>0.05).

Svalbard	Midland Valley	Dingle Peninsula Basin	Anglo-Welsh Basin	Orcadian Basin	Armorica-Cadomia	West Avalonia	Megumia	Ganderia	Laurentia	East Avalonia	Altar Stone	
0.36	0.00	0.00	0.00	0.72	0.00	0.00	0.00	0.00	0.10	0.00		**Altar Stone**
0.00	0.00	0.00	0.00	0.00	0.00	0.00	0.00	0.00	0.00		0.51	**East Avalonia**
0.00	0.00	0.00	0.00	0.00	0.00	0.00	0.00	0.00		0.53	0.16	**Laurentia**
0.00	0.00	0.00	0.00	0.00	0.00	0.00	0.00		0.42	0.12	0.40	**Ganderia**
0.00	0.00	0.00	0.00	0.00	0.00	0.00		0.29	0.71	0.21	0.68	**Megumia**
0.00	0.00	0.00	0.00	0.00	0.00		0.23	0.24	0.63	0.15	0.61	**West Avalonia**
0.00	0.00	0.00	0.00	0.00		0.22	0.15	0.18	0.60	0.18	0.57	**Armorica-Cadomia**
0.06	0.00	0.00	0.00		0.57	0.61	0.68	0.39	0.23	0.50	0.10	**Orcadian Basin**
0.00	0.00	0.33		0.44	0.26	0.25	0.30	0.29	0.47	0.28	0.45	**Anglo-Welsh Basin**
0.00	0.00		0.10	0.42	0.25	0.21	0.28	0.27	0.45	0.21	0.43	**Dingle Peninsula Basin**
0.00		0.25	0.26	0.37	0.39	0.43	0.50	0.25	0.41	0.33	0.32	**Midland Valley**
	0.34	0.37	0.35	0.11	0.52	0.55	0.63	0.34	0.21	0.45	0.13	**Svalbard**

	Altar Stone	East Avalonia	Laurentia	Ganderia	Megumia	West Avalonia	Armorica-Cadomia	Orcadian Basin	Anglo-Welsh Basin	Dingle Peninsula Basin	Midland Valley	Svalbard
Altar Stone		0.00	0.05	0.00	0.00	0.00	0.00	0.16	0.00	0.00	0.00	0.10
East Avalonia	0.00		0.00	0.00	0.00	0.00	0.00	0.00	0.00	0.00	0.00	0.00
Laurentia	0.11	0.00		0.00	0.00	0.00	0.00	0.00	0.00	0.00	0.00	0.00
Ganderia	0.00	0.00	0.00		0.00	0.00	0.00	0.00	0.00	0.00	0.00	0.00
Megumia	0.00	0.00	0.00	0.00		0.00	0.00	0.00	0.00	0.00	0.00	0.00
West Avalonia	0.00	0.00	0.00	0.00	0.00		0.00	0.00	0.00	0.00	0.00	0.00
Armorica-Cadomia	0.00	0.00	0.00	0.00	0.00	0.00		0.00	0.00	0.00	0.00	0.00
Orcadian Basin	0.67	0.00	0.00	0.00	0.00	0.00	0.00		0.00	0.00	0.00	0.03
Anglo-Welsh Basin	0.00	0.00	0.00	0.00	0.00	0.00	0.00	0.00		0.19	0.00	0.00
Dingle Peninsula Basin	0.00	0.00	0.00	0.00	0.00	0.00	0.00	0.00	0.38		0.00	0.00
Midland Valley	0.00	0.00	0.00	0.00	0.00	0.00	0.00	0.00	0.00	0.00		0.00
Svalbard	0.33	0.00	0.00	0.00	0.00	0.00	0.00	0.06	0.00	0.00	0.00	

Table 6.4. KS Test Results, with Monte-Carlo resampling. This KS test is two-sided (i.e. this test checks for any difference in distribution). Highlighted green values are P>0.05, and blue values are two standard deviation values for those P>0.05).

6.8. Rutile Analysis

6.8.1. Rutile U–Pb Methods

One rutile U–Pb analysis session was completed at the GeoHistory facility in the John De Laeter Centre (JdLC), Curtin University, Australia. Rutile grains were ablated (24 µm) using a Resonetics RESOlution M-50A-LR sampling system, using a Compex 102 excimer laser, and measured using an Agilent 8900 triple quadrupole mass analyser. The analytical parameters included an on-sample energy of 2.7 J cm^{-2}, a repetition rate of 7 Hz for a total analysis time of 45 seconds, and 60 seconds of background data capture. The sample chamber was purged with ultrahigh purity He at a flow rate of 0.68 L min^{-1} and N_2 at 2.8 mL min^{-1}.

U–Pb data for rutile analyses was reduced against the R-10 rutile primary reference material (1091 ± 4 Ma) (Luvizotto et al., 2009). The secondary reference material used to monitor the accuracy of U–Pb ratios was R-19 rutile. The mean weighted $^{238}U/^{206}Pb$ age obtained for R-19 was 491 ± 10 [MSWD = 0.87, $p(\chi^2)$ = 0.57] within uncertainty of the accepted age of 489.5 ± 0.9 Ma (Zack et al., 2011). Rutile grains with negligible Th concentrations can be corrected for common Pb using a ^{208}Pb-correction (Zack et al., 2011). Previously used thresholds for Th content have included Th/U <0.1 (Dröllner et al., 2023) or a Th concentration >5% U (Liebmann et al., 2023). However, Th/U ratios for rutile from MS3 are typically > 1; thus, a ^{208}Pb-correction is not applicable. Instead, we use a ^{207}-based common Pb correction (Stacey and Kramers, 1975) to account for the presence of common Pb. Rutile isotopic data was reduced within Iolite 4 (Paton et al., 2011) using the U-Pb Geochronology reduction scheme and IsoplotR (Vermeesch, 2018).

6.8.2. Rutile U–Pb Results

Ninety-two rutile U–Pb analyses were obtained in a U–Pb single session, which defined two coherent age groupings on a Tera-Wasserburg plot. Group 1 constitutes 83 U–Pb rutile analyses, forming a well-defined mixing array on a Tera-Wasserburg plot between common and radiogenic Pb components. This array yields an upper intercept of $^{207}Pb/^{206}Pb_i = 0.8563 \pm 0.0014$. The lower intercept implies an age of 451 ± 8 Ma. The scatter about the line (MSWD = 2.7) is interpreted to reflect the variable passage of rutile of diverse grain sizes through the radiogenic-Pb closure temperature at ~ 600°C during and after magmatic crystallisation (Zack and Kooijman, 2017).

Group 2 comprises 9 grains, with ^{207}Pb corrected $^{238}U/^{206}Pb$ ages ranging from 591 – 1724 Ma. Three grains from Group 2 define an age peak at 1607 Ma (Gehrels, 2011). Given the spread in U–Pb ages, we interpret these Proterozoic grains to represent detrital rutile derived from various sources.

6.9. Apatite Analysis

6.9.1. Apatite U–Pb Methods

Two apatite U–Pb LA-ICP-MS analysis sessions were conducted at the GeoHistory facility in the John De Laeter Centre (JdLC), Curtin University, Australia. For both sessions, ablations were created using a RESOlution 193 nm excimer laser ablation system connected to an Agilent 8900 ICP–MS with a RESOlution LE193 nm ArF and a Laurin Technic S155 cell ICP–MS. Other analytical details include a fluence of 2 J/cm^2 and a 5 Hz repetition rate.

For the Altar Stone section (MS3) and the Orcadian Basin samples (Table 6.1), 24 and 20 µm spot sizes were used, respectively. The matrix-matched primary reference material used for apatite U–Pb analyses was the Madagascar apatite (MAD-1) (Thompson et al., 2016). A range of secondary reference apatite was analysed, including FC-1 (Duluth Complex) with an age of 1099.1 ± 0.6 Ma (Schmitz et al., 2003), Mount McClure 526 ± 2.1 Ma (Schoene and Bowring, 2006; Thomson et al., 2012), Otter Lake 913 ± 7 Ma (Barfod et al., 2005) and Durango 31.44 ± 0.18 Ma (McDowell et al., 2005). Anchored regressions (through reported $^{207}Pb/^{206}Pb_i$ values) for secondary reference material yielded lower intercept ages within 2σ uncertainty of reported values (Table 6.5).

6.9.2. Altar Stone Apatite U–Pb Results

This first session of apatite U–Pb of MS3 from the Altar Stone yielded 117 analyses. On a Tera-Wasserburg plot, these analyses form two discordant mixing arrays between common and radiogenic Pb components with distinct lower intercepts.

The array from Group 2 apatite, comprised of 9 analyses, yields a lower intercept equivalent to an age of 1018 ± 24 Ma (MSWD = 1.4) with an upper intercept $^{207}Pb/^{206}Pb_i$ = 0.8910 ± 0.0251. The f^{207}% of apatite analyses in Group 2 ranges from 16.66 – 88.8%, with a mean of 55.76%. Group 1 apatite is defined by 108 analyses yielding a lower intercept of 462 ± 4 Ma (MSWD = 2.4) with an upper intercept $^{207}Pb/^{206}Pb_i$ = 0.8603 ± 0.0033. The f^{207}% of apatite analyses in Group 1 range from 10.14 – 99.91%, with a mean of 78.65%. The slight over-dispersion of the apatite regression line may reflect some variation in Pb closure temperature in these crystals (Kirkland et al., 2018).

6.9.3. Orcadian Basin Apatite U–Pb Results

The second apatite U–Pb session yielded 138 analyses from samples CQ1 and AQ1. These data form three discordant mixing arrays between radiogenic and common Pb components on a Tera-Wasserburg plot. An unanchored regression through Group 1 apatite (*n = 14*) from the Cruaday sample (CQ1) yields a lower intercept of 473 ± 25 Ma (MSWD = 1.8) with an upper intercept of $^{207}Pb/^{206}Pb_i$ = 0.8497 ± 0.0128. The f^{207}% spans 38 – 99%, with a mean value of 85%.

Group 1 from the Spittal sample (AQ1), comprised of 109 analyses, yields a lower intercept equal to 466 ± 6 Ma (MSWD = 1.2). The upper $^{207}Pb/^{206}Pb_i$ is equal to 0.8745 ± 0.0038. f^{207}% values for this group range from 6 – 99%, with a mean value of 83%. A regression through Group 2 analyses (*n = 17*) from the Spittal sample yields a lower intercept of 1013 ± 35 Ma (MSWD = 1) and an upper intercept $^{207}Pb/^{206}Pb_i$ of 0.9038 ± 0.0101. f^{207}% values span 25 – 99%, with a mean of 76%. Combined U–Pb analyses from Groups 1 from CQ1 and AQ1 (*n = 123*) yield a lower intercept equivalent to 466 ± 6 Ma (MSWD = 1.4) and an upper intercept $^{207}Pb/^{206}Pb_i$ of 0.8726 ± 0.0036, which is presented beneath the Orcadian Basin kernel density estimate in Figure 6.4b.

Session 1 (MS3)

Reference	Primary Reference	Age (Ma)	± 2σ	MSWD*	P*	n
Otter Lake	**MAD-1**	**926**	**7**	**1.7**	**0.06**	**15**
Published age		913	7	*Barfod et al., 2005*		
FC-1	**MAD-1**	**1109**	**16**	**1.5**	**0.08**	**17**
Published age		1099.1	0.6	*Schmitz et al., 2003*		
Mount McClure	**MAD-1**	**526**	**8**	**1.5**	**0.10**	**17**
Published age		523.5	1.5	*Schoene at al., 2006; Thompson et al., 2012*		

Session 2 (Orcadian Basin Samples CQ1 and AQ1)

Reference	Primary Reference	Age (Ma)	± 2σ	MSWD*	P*	n
Durango	**MAD-1**	**28**	**3**	**0.55**	**0.90**	**15**
Published age		31.44	0.18	*McDowell et al., 2005*		
FC-1	**MAD-1**	**1088**	**12**	**1.4**	**0.13**	**17**
Published age		1099.1	0.6	*Schmitz et al., 2003*		
Mount McClure	**MAD-1**	**527**	**5**	**0.6**	**0.86**	**16**
Published age		523.5	1.5	*Schoene et al., 2006; Thompson et al., 2012*		

*Table 6.5. A summary of ages obtained for apatite U–Pb secondary reference material. *Where MSWD and P are the mean square of the weighted deviation value and the associated MSWD age homogeneity test chi-squared P-value. Both metrics are one-sided.*

6.9.4 Apatite Lu–Hf Methods

Apatite grains were dated in thin-section by the *in-situ* Lu–Hf method at the University of Adelaide, using a RESOlution-LR 193 nm excimer laser ablation system, coupled to an Agilent 8900 ICP-MS/MS (Glorie et al., 2024; Simpson et al., 2021). A gas mixture of NH_3 in He was used in the mass spectrometer reaction cell to promote high-order Hf reaction products, while equivalent Lu and Yb reaction products were negligible. The mass-shifted (+82 amu) reaction products of $^{176+82}$Hf and $^{178+82}$Hf reached the highest sensitivity of the measurable range and were analysed free from isobaric interferences. ^{177}Hf was calculated from ^{178}Hf, assuming natural abundances. ^{175}Lu was measured on mass as a proxy for ^{176}Lu (Simpson et al., 2021). Laser ablation was conducted with a laser beam of 43 µm at 7.5 Hz repetition rate and a fluency of approximately 3.5 J/cm^2. The analysed isotopes (with dwell times in milliseconds between brackets) are ^{27}Al (2), ^{43}Ca (2), ^{57}Fe (2), ^{88}Sr (2), $^{89+85}$Y (2), $^{90+83}$Zr (2), $^{140+15}$Ce (2), ^{146}Nd (2), ^{147}Sm (2), ^{172}Yb (5), ^{175}Lu (10), $^{175+82}$Lu (50), $^{176+82}$Hf (200), $^{178+82}$Hf (150). Isotopes with short dwell times (<10 ms) were measured to confirm apatite chemistry and to monitor for inclusions. $^{175+82}$Lu was monitored for interferences on $^{176+82}$Hf.

Relevant isotope ratios were calculated in LADR (Norris and Danyushevsky, 2018) using NIST 610 as the primary reference material (Nebel et al., 2009). Subsequently, reference apatite OD-306 (1597 ± 7 Ma (Thompson et al., 2016)) was used to correct the Lu-Hf isotope ratios for matrix-induced fractionation [crf. Glorie et al. (2023): Kharkongor et al. (2023)]. Reference apatites Bamble-1 (1597 ± 5 Ma), HR-1 (344 ± 2 Ma) and Wallaroo (1574 ± 6 Ma) were monitored for accuracy verification (Glorie et al., 2022; Glorie et al., 2023; Simpson et al., 2021). Measured Lu–Hf dates of 1098 ± 7 Ma, 346.0 ± 3.7 Ma and 1575 ± 12 Ma, respectively, are in agreement with published values. All reference materials have negligible initial Hf, and weighted mean Lu–Hf dates were calculated in IsoplotR (Vermeesch, 2018) directly from the (matrix-corrected) ^{176}Hf/^{176}Lu ratios.

For the Altar Stone apatites, which have variable ^{177}Hf/^{176}Hf compositions, single-grain Lu–Hf dates were calculated by anchoring isochrons to an initial ^{177}Hf/^{176}Hf composition of 3.55 ± 0.05 [cf. (Glorie et al., 2022)], which spans the entire range of initial ^{177}Hf/^{176}Hf ratios of the terrestrial reservoir [e.g. Spencer et al. (2020)]. The reported uncertainties for the single-grain Lu–Hf dates are presented as 95% confidence intervals, and dates are displayed on a Kernel Density Estimate plot.

6.9.5. Apatite Lu–Hf Results

Forty-five apatite Lu–Hf analyses were obtained from 2010K.240. Those with radiogenic Lu ingrowth or lacking common Hf gave Lu–Hf ages, defining four coherent isochrons and age groups.

Group 1, defined by 16 grains, yields a Lu–Hf isochron with a lower intercept of 470 ± 28 Ma [MSWD = 0.16, $p(\chi^2) = 1$]. A second isochron through five analyses (Group 2) constitutes a lower intercept equivalent to 604 ± 38 Ma [MSWD = 0.14, $p(\chi^2) = 0.94$]. Twelve apatite Lu–Hf analyses define Group 3 with a lower intercept of 1123 ± 42 Ma [MSWD = 0.75, $p(\chi^2) = 0.68$]. Three grains constitute the oldest grouping, Group 4 at 1526 ± 186 Ma [MSWD = 0.014, $p(\chi^2) = 0.91$].

6.9.6. Apatite Trace Elements Methods

A separate session of apatite trace element analysis was undertaken. Instrumentation and analytical set-up were identical to that described in 4.1. NIST 610 glass was the primary reference material for apatite trace element analyses. ^{43}Ca was used as the internal reference isotope, assuming an apatite Ca concentration of 40 wt.%. Secondary reference materials included NIST 612 and the BHVO-2g glasses (Jochum et al., 2005). Elemental abundances for secondary reference material were generally within 5 – 10% of accepted values. Apatite trace element data was examined using the Geochemical Data Toolkit (Janousek et al., 2006).

6.9.7. Apatite Trace Elements Results

One hundred and thirty-six apatite trace element analyses were obtained from as many grains. Geochemical classification schemes for apatite were used after Fleischer and Altschuler 1986, and three compositional groupings (felsic, mafic-intermediate, and alkaline) were defined. Felsic-classified apatite grains (n=83 or 61% of analyses) are defined by La/Nd of < 0.6 and (La+Ce+Pr)/ΣREE of < 0.5. The median values of felsic grains show a flat to slightly negative gradient on the chondrite-normalised REE (Rare Earth Element) plot from light to heavy REEs (Boynton, 1984). Felsic apatite's median europium anomaly (Eu/Eu*) is 0.59, a moderately negative signature.

Mafic-intermediate apatite (n=48, 35% of grains) are defined by (La+Ce+Pr)/ΣREE of 0.5 – 0.7 and a La/Nd of 0.5 – 1.5 (Fleischer and Altschuler, 1986). In addition, apatite grains of this group typically exhibit a chondrite normalised Ce/Yb of > 5 and ΣREEs up to 1.25 wt %. Apatite grains classified as mafic-intermediate show a negative gradient on a chondrite

normalised REE plot from light to heavy REEs. The apatite grains of this group generally show the most enrichment in REEs compared to chondrite (Boynton, 1984). The median europium (Eu/Eu*) of mafic-intermediate apatite is 0.62, a moderately negative anomaly. Lastly, alkaline apatite grains (n=5, 4% of analyses) are characterised by La/Nd > 1.5 and a (La+Ce+Pr)/ΣREE >0.8 (Fleischer and Altschuler, 1986). The median europium anomaly of this group is 0.45. This grouping also shows elevated chondrite normalised Ce/Yb of > 10 and > 0.5 wt % for the ΣREEs.

6.10. Data Availability Statement

The authors declare that the isotopic and chemical data supporting the findings of this study are available within the paper via *DOI:10.1038/s41586-024-07652*-1.

6.11. Acknowledgments

Funding was provided by an Australian Research Council Discovery Project (DP200101881). Sample material was loaned from the Salisbury Museum and Amgueddfa Cymru – Museum Wales and sampled with permission. We thank A. Green for assistance in accessing the Salisbury Museum material. B. McDonald, N. Evans, K. Rankenburg, and S. Gilbert are thanked for their help during isotopic analysis. P. Sampaio is thanked for assistance with statistical analysis. Instruments in the John deLaeter Centre, Curtin University, were funded via AuScope, the Australian Education Investment Fund, the National Collaborative Research Infrastructure Strategy, and the Australian Government. R. Bevins acknowledges a Leverhulme Trust Emeritus Fellowship.

6.12. References

Barfod, G. H., Krogstad, E. J., Frei, R., and Albarède, F., 2005, Lu-Hf and PbSL geochronology of apatites from Proterozoic terranes: A first look at Lu-Hf isotopic closure in metamorphic apatite: Geochimica et Cosmochimica Acta, v. 69, no. 7, p. 1847-1859.

Barham, M., Kirkland, C. L., Reynolds, S., O'Leary, M. J., Evans, N. J., Allen, H., Haines, P. W., Hocking, R. M., McDonald, B. J., Belousova, E., and Goodall, J., 2016, The answers are blowin' in the wind: Ultra-distal ashfall zircons, indicators of Cretaceous super-eruptions in eastern Gondwana: Geology, v. 44, no. 8, p. 643-646.

Bayliss, A., Marshall, P., Richards, C., and Whittle, A., 2017, Islands of history: the Late Neolithic timescape of Orkney: Antiquity, v. 91, no. 359, p. 1171-1188.

Beranek, L. P., Gee, D. G., and Fisher, C. M., 2020, Detrital zircon U-Pb-Hf isotope signatures of Old Red Sandstone strata constrain the Silurian to Devonian paleogeography, tectonics, and crustal evolution of the Svalbard Caledonides: GSA Bulletin, v. 132, no. 9-10, p. 1987-2003.

Bevins, R., Ixer, R., Pearce, N., Scourse, J., and Daw, T., 2023a, Lithological description and provenancing of a collection of bluestones from excavations at Stonehenge by William Hawley in 1924 with implications for the human versus ice transport debate of the monument's bluestone megaliths: Geoarchaeology, v. 38, p. 771-785.

Bevins, R. E., Pearce, N. J. G., Ixer, R. A., Hillier, S., Pirrie, D., and Turner, P., 2022, Linking derived debitage to the Stonehenge Altar Stone using portable X-ray fluorescence analysis: Mineralogical Magazine, v. 86, no. 4, p. 688-700.

Bevins, R. E., Pearce, N. J. G., Ixer, R. A., Pirrie, D., Andò, S., Hillier, S., Turner, P., and Power, M., 2023b, The Stonehenge Altar Stone was probably not sourced from the Old Red Sandstone of the Anglo-Welsh Basin: Time to broaden our geographic and stratigraphic horizons?: Journal of Archaeological Science: Reports, v. 51, p. 104215.

Bevins, R. E., Pearce, N. J. G., Pirrie, D., Ixer, R. A., Hillier, S., Turner, P., and Power, M., 2023c, Assessing the authenticity of a sample taken from the Altar Stone at Stonehenge in 1844 using portable XRF and automated SEM-EDS: Journal of Archaeological Science: Reports, v. 49, p. 103973.

Bevins, R. E., Pirrie, D., Ixer, R. A., O'Brien, H., Pearson, M. P., Power, M. R., and Shail, R. K., 2020, Constraining the provenance of the Stonehenge 'Altar Stone': Evidence from automated mineralogy and U–Pb zircon age dating: Journal of Archaeological Science, v. 120, p. 105188.

Boynton, W. V., 1984, Chapter 3 - Cosmochemistry of the Rare Earth Elements: Meteorite Studies, *in* Henderson, P., ed., Developments in Geochemistry, Volume 2, Elsevier, p. 63-114.

Bradley, R., 2023, Long Distance Connections Within Britain and Ireland: the Evidence of Insular Rock Art: Proceedings of the Prehistoric Society, v. 89, p. 249-271.

-, 2024, Beyond the bluestones: links between distant monuments in Late Neolithic Britain and Ireland: Antiquity, p. 1-8.

Bradley, R., and Edmonds, M., 2005, Interpreting the axe trade: production and exchange in Neolithic Britain, Cambridge University Press.

Cawood, P. A., Nemchin, A. A., Strachan, R., Prave, T., and Krabbendam, M., 2007, Sedimentary basin and detrital zircon record along East Laurentia and Baltica during assembly and breakup of Rodinia: Journal of the Geological Society, v. 164, no. 2, p. 257-275.

Clark, C. D., Ely, J. C., Hindmarsh, R. C. A., Bradley, S., Ignéczi, A., Fabel, D., Ó Cofaigh, C., Chiverrell, R. C., Scourse, J., Benetti, S., Bradwell, T., Evans, D. J. A., Roberts, D. H., Burke, M., Callard, S. L., Medialdea, A., Saher, M., Small, D., Smedley, R. K., Gasson, E., Gregoire, L., Gandy, N., Hughes, A. L. C., Ballantyne, C., Bateman, M. D., Bigg, G. R., Doole, J., Dove, D., Duller, G. A. T., Jenkins, G. T. H., Livingstone, S. L., McCarron, S., Moreton, S., Pollard, D., Praeg, D., Sejrup, H. P., Van Landeghem, K. J. J., and Wilson, P., 2022, Growth and retreat of the last British–Irish Ice Sheet, 31 000 to 15 000 years ago: the BRITICE-CHRONO reconstruction: Boreas, v. 51, no. 4, p. 699-758.

Dröllner, M., Barham, M., and Kirkland, C. L., 2023, Reorganization of continent-scale sediment routing based on detrital zircon and rutile multi-proxy analysis: Basin Research, v. 35, no. 1, p. 363-386.

Dröllner, M., Barham, M., Kirkland, C. L., and Ware, B., 2021, Every zircon deserves a date: selection bias in detrital geochronology: Geological Magazine, v. 158, no. 6, p. 1135-1142.

Evans, J. A., Chenery, C. A., and Fitzpatrick, A. P., 2006, Bronze Age childhood migration of individuals near Stonehenge, revealed by strontium and oxygen isotope tooth enamel analysis: Archaeometry, v. 48, no. 2, p. 309-321.

Evans, J. A., Pashley, V., Mee, K., Wagner, D., Parker Pearson, M., Fremondeau, D., Albarella, U., and Madgwick, R., 2022, Applying lead (Pb) isotopes to explore mobility in humans and animals: PLOS ONE, v. 17, no. 10, p. e0274831.

Fairey, B. J., Kerrison, A., Meere, P. A., Mulchrone, K. F., Hofmann, M., Gärtner, A., Sonntag, B.-L., Linnemann, U., Kuiper, K. F., Ennis, M., Mark, C., Cogné, N., and Chew, D., 2018, The provenance of the Devonian Old Red Sandstone of the Dingle Peninsula, SW Ireland; the earliest record of Laurentian and peri-Gondwanan sediment mixing in Ireland: Journal of the Geological Society, v. 175, no. 3, p. 411-424.

Fairweather, A. D., and Ralston, I. B. M., 1993, The Neolithic timber hall at Balbridie, Grampian Region, Scotland: the building, the date, the plant macrofossils: Antiquity, v. 67, no. 255, p. 313-323.

Fleischer, M., and Altschuler, Z. S., 1986, The lanthanides and yttrium in minerals of the apatite group-an analysis of the available data: Neues Jahrbuch für Mineralogie, Monatshefte, p. 467-480.

Gehrels, G., 2011, Detrital zircon U-Pb geochronology: Current methods and new opportunities: Tectonics of sedimentary basins: Recent advances, p. 45-62.

Gibbard, P. L., and Clark, C. D., 2011, Chapter 7 - Pleistocene Glaciation Limits in Great Britain, *in* Ehlers, J., Gibbard, P. L., and Hughes, P. D., eds., Developments in Quaternary Sciences, Volume 15, Elsevier, p. 75-93.

Gillespie, J., Glorie, S., Khudoley, A., and Collins, A. S., 2018, Detrital apatite U-Pb and trace element analysis as a provenance tool: Insights from the Yenisey Ridge (Siberia): Lithos, v. 314-315, p. 140-155.

Glorie, S., Gillespie, J., Simpson, A., Gilbert, S., Khudoley, A., Priyatkina, N., Hand, M., and Kirkland, C. L., 2022, Detrital apatite Lu–Hf and U–Pb geochronology applied to the southwestern Siberian margin: Terra Nova, v. 34, p. 201-209.

Glorie, S., Hand, M., Mulder, J., Simpson, A., Emo Robert, B., Kamber, B., Fernie, N., Nixon, A., and Gilbert, S., 2023, Robust laser ablation Lu–Hf dating of apatite: an empirical evaluation: Geological Society, London, Special Publications, v. 537, no. 1, p. SP537-2022-2205.

-, 2024, Robust laser ablation Lu–Hf dating of apatite: an empirical evaluation: Geological Society, London, Special Publications, v. 537, no. 1, p. SP537-2022-2205.

Godwin, H., 1975, History of the Natural Forests of Britain: Establishment, Dominance and Destruction: Philosophical Transactions of the Royal Society of London. Series B, Biological Sciences, v. 271, no. 911, p. 47-67.

Goodenough, K. M., Millar, I., Strachan, R. A., Krabbendam, M., and Evans, J. A., 2011, Timing of regional deformation and development of the Moine Thrust Zone in the

Scottish Caledonides: constraints from the U–Pb geochronology of alkaline intrusions: Journal of the Geological Society, v. 168, no. 1, p. 99-114.

Harff, J., Flemming, N. C., Groh, A., Hünicke, B., Lericolais, G., Meschede, M., Rosentau, A., Sakellariou, D., Uścinowicz, S., and Zhang, W., 2017, Sea level and climate, *in* Flemming, N. C., Harff, J., Moura, D., Burgess, A., and Bailey, G., eds., Submerged Landscapes of the European Continental Shelf: quaternary paleoenvironments, p. 11-49.

Ixer, R., Bevins, R., and Turner, P., 2019, Alternative Altar Stones? Carbonate-cemented micaceous sandstones from the Stonehenge Landscape: Wiltshire Archaeological and Natural History Magazine, v. 112, no. 1, p. 1-13.

Ixer, R., Bevins, R. E., Pirrie, D., Turner, P., and Power, M., 2020, No provenance is better than wrong provenance: Milford Haven and the Stonehenge sandstones: Wiltshire Archaeological and Natural History Magazine, v. 113, p. 1-15.

Ixer, R., and Turner, P., 2006, A detailed re-examination of the petrography of the Altar Stone and other non-sarsen sandstones from Stonehenge as a guide to their provenance: Wiltshire Archaeological and Natural History Magazine, v. 99, p. 1-9.

Ixer, R., Turner, P., Molyneux, S., and Bevins, R., 2017, The petrography, geological age and distribution of the Lower Palaeozoic Sandstone debitage from the Stonehenge landscape: Wiltshire Archaeological and Natural History Magazine, v. 110, p. 1-16.

Jackson, S. E., Pearson, N. J., Griffin, W. L., and Belousova, E. A., 2004, The application of laser ablation-inductively coupled plasma-mass spectrometry to in situ U–Pb zircon geochronology: Chemical Geology, v. 211, no. 1, p. 47-69.

Janousek, V., Farrow, C., and Erban, V., 2006, Interpretation of Whole-rock Geochemical Data in Igneous Geochemistry: Introducing Geochemical Data Toolkit (GCDkit): Journal of Petrology, v. 47, p. 1255-1259.

Jochum, K. P., Nohl, U., Herwig, K., Lammel, E., Stoll, B., and Hofmann, A. W., 2005, GeoReM: A New Geochemical Database for Reference Materials and Isotopic Standards: Geostandards and Geoanalytical Research, v. 29, no. 3, p. 333-338.

John, B., 2018, The Stonehenge Bluestones, Greencroft Books.

-, 2024, The Stonehenge bluestones did not come from Waun Mawn in West Wales: The Holocene, p. 09596836241236318.

Kelloway, S., Craven, S., Pecha, M., Dickinson, W., Gibbs, M., Ferguson, T., and Glascock, M., 2014, Sourcing Olive Jars Using U-Pb Ages of Detrital Zircons: A Study of 16th

Century Olive Jars Recovered from the Solomon Islands: Geoarchaeology, v. 29, p. 47-60.

Kendall, R. S., 2017, The Old Red Sandstone of Britain and Ireland — a review: Proceedings of the Geologists' Association, v. 128, no. 3, p. 409-421.

Kharkongor, M. B. K., Glorie, S., Mulder, J., Kirkland, C. L., Chew, D., Kohn, B., and Simpson, A., 2023, Apatite laser ablation Lu–Hf geochronology: A new tool to date mafic rocks: Chemical Geology, v. 636, p. 121630.

Kirkland, C. L., Yakymchuk, C., Szilas, K., Evans, N., Hollis, J., McDonald, B., and Gardiner, N. J., 2018, Apatite: a U-Pb thermochronometer or geochronometer?: Lithos, v. 318-319, p. 143-157.

Liebmann, J., Barham, M., and Kirkland, C. L., 2023, Rutile Ages and Thermometry Along a Grenville Anorthosite Pathway: Geochemistry, Geophysics, Geosystems, v. 24, no. 2, p. e2022GC010330.

Luvizotto, G., Zack, T., Meyer, H. P., Ludwig, T., Triebold, S., Kronz, A., Münker, C., Stockli, D., Prowatke, S., Klemme, S., Jacob, D., and Eynatten, H., 2009, Rutile crystals as potential trace element and isotope mineral standards for microanalysis: Chemical Geology, v. 261, p. 346-369.

Marsh, J. H., Jørgensen, T. R. C., Petrus, J. A., Hamilton, M. A., and Mole, D. R., 2019, U-Pb, trace element, and hafnium isotope composition of the Maniitsoq zircon: A potential new Archean zircon reference material, Goldschmidt: Barcalona.

Martínková, N., Barnett, R., Cucchi, T., Struchen, R., Pascal, M., Pascal, M., Fischer, M. C., Higham, T., Brace, S., Ho, S. Y. W., Quéré, J.-P., O'Higgins, P., Excoffier, L., Heckel, G., Rus Hoelzel, A., Dobney, K. M., and Searle, J. B., 2013, Divergent evolutionary processes associated with colonization of offshore islands: Molecular Ecology, v. 22, no. 20, p. 5205-5220.

McDowell, F., McIntosh, W., and Farley, K., 2005, A precise ^{40}Ar–^{39}Ar reference age for the Durango apatite (U–Th)/He and fission-track dating standard: Chemical Geology, v. 214, no. 3-4, p. 249-263.

McKellar, Z., Hartley, A. J., Morton, A. C., and Frei, D., 2019, A multidisciplinary approach to sediment provenance analysis of the late Silurian–Devonian Lower Old Red Sandstone succession, northern Midland Valley Basin, Scotland: Journal of the Geological Society, v. 177, no. 2, p. 297-314.

Morton, A., Hounslow, M. W., and Frei, D., 2013, Heavy-mineral, mineral-chemical and zircon-age constraints on the provenance of Triassic sandstones from the Devon coast, southern Britain: Geologos, v. 19, no. 1-2, p. 67-85.

Morton, A., Knox, R., and Frei, D., 2016, Heavy mineral and zircon age constraints on provenance of the Sherwood Sandstone Group (Triassic) in the eastern Wessex Basin, UK: Proceedings of the Geologists' Association, v. 127, no. 4, p. 514-526.

Morton, A., Waters, C., Fanning, M., Chisholm, I., and Brettle, M., 2015, Origin of Carboniferous sandstones fringing the northern margin of the Wales-Brabant Massif: insights from detrital zircon ages: Geological Journal, v. 50, no. 5, p. 553-574.

Morton, A. C., Chisholm, J. I., and Frei, D., 2021, Provenance of Carboniferous sandstones in the central and southern parts of the Pennine Basin, UK: evidence from detrital zircon ages: Proceedings of the Yorkshire Geological Society, v. 63, no. 3.

Nash, D. J., Ciborowski, T. J. R., Darvill, T., Parker Pearson, M., Ullyott, J. S., Damaschke, M., Evans, J. A., Goderis, S., Greaney, S., Huggett, J. M., Ixer, R. A., Pirrie, D., Power, M. R., Salge, T., and Wilkinson, N., 2021, Petrological and geochemical characterisation of the sarsen stones at Stonehenge: PLOS ONE, v. 16, no. 8, p. e0254760.

Nash, D. J., Ciborowski, T. J. R., Ullyott, J. S., Pearson, M. P., Darvill, T., Greaney, S., Maniatis, G., and Whitaker, K. A., 2020, Origins of the sarsen megaliths at Stonehenge: Science Advances, v. 6, no. 31.

Nebel, O., Morel, M. L. A., and Vroon, P. Z., 2009, Isotope Dilution Determinations of Lu, Hf, Zr, Ta and W, and Hf Isotope Compositions of NIST SRM 610 and 612 Glass Wafers: Geostandards and Geoanalytical Research, v. 33, no. 4, p. 487-499.

Nordsvan, A. R., Kirscher, U., Kirkland, C. L., Barham, M., and Brennan, D. T., 2020, Resampling (detrital) zircon age distributions for accurate multidimensional scaling solutions: Earth-Science Reviews, v. 204, p. 103149.

Norris, C., A., and Danyushevsky, L., Towards Estimating the Complete Uncertainty Budget of Quantified Results Measured by LA-ICP-MS, *in* Proceedings Goldschmidt, Boston, 2018.

O'Sullivan, G., Chew, D. M., Kenny, G., Henrichs, I., and Mulligan, D., 2020, The trace element composition of apatite and its application to detrital provenance studies: Earth-Science Reviews, v. 201.

Oliver, G., Wilde, S., and Wan, Y., 2008, Geochronology and geodynamics of Scottish granitoids from the late Neoproterozoic break-up of Rodinia to Palaeozoic collision: Journal of The Geological Society v. 165, p. 661-674.

Parker Pearson, M., Bevins, R., Ixer, R., Pollard, J., Richards, C., and Welham, K., 2020, Long-distance landscapes:: from quarries to monument at Stonehenge, *in* Bouventura, R., Metaloto, R., and Pereira, A., eds., Megaliths and Geology: Oxford, Archaeopress Publishing Ltd, p. 151-169.

Paton, C., Hellstrom, J. C., Paul, B., Woodhead, J. D., and Hergt, J. M., 2011, Iolite: Freeware for the visualisation and processing of mass spectrometric data: Journal of Analytical Atomic Spectrometry, v. 26, p. 2508-2518.

Peacock, D., Cutler, L., and Woodward, P., 2010, A Neolithic Voyage: International Journal of Nautical Archaeology, v. 39, no. 1, p. 116-124.

Pearson, M. P., Bevins, R., Ixer, R., Pollard, J., Richards, C., Welham, K., Chan, B., Edinborough, K., Hamilton, D., Macphail, R., Schlee, D., Schwenninger, J.-L., Simmons, E., and Smith, M., 2015a, Craig Rhos-y-felin: a Welsh bluestone megalith quarry for Stonehenge: Antiquity, v. 89, no. 348, p. 1331-1352.

Pearson, M. P., Pollard, J., Richards, C., Thomas, J., Tilley, C., and Welham, K., 2022, Stonehenge Stage 1: the Late Neolithic, *in* Pearson, M., Pollard, J., Richards, C., Thomas, J., Tilley, C., and Welham, K., eds., Stonehenge for the ancestors: Part 2: Synthesis, Sidestone Press, p. 47-75.

Pearson, M. P., Pollard, J., Richards, C., Thomas, J., and Welham, K., 2015b, Stonehenge: making sense of a prehistoric mystery, Council for British Archaeology.

Pearson, M. P., Pollard, J., Richards, C., Welham, K., Casswell, C., French, C., Schlee, D., Shaw, D., Simmons, E., Stanford, A., Bevins, R., and Ixer, R., 2019, Megalith quarries for Stonehenge's bluestones: Antiquity, v. 93, no. 367, p. 45-62.

Phillips, E. R., Smith, R. A., Stone, P., Pashley, V., and Horstwood, M., 2009, Zircon age constraints on the provenance of Llandovery to Wenlock sandstones from the Midland Valley terrane of the Scottish Caledonides: Scottish Journal of Geology, v. 45, no. 2, p. 131-146.

Pigière, F., and Smyth, J., 2023, First evidence for cattle traction in Middle Neolithic Ireland: A pivotal element for resource exploitation: PLOS ONE, v. 18, no. 1, p. e0279556.

Pinder, A. P., Panter, I., Abbott, G. D., and Keely, B. J., 2017, Deterioration of the Hanson Logboat: chemical and imaging assessment with removal of polyethylene glycol conserving agent: Scientific Reports, v. 7, no. 1, p. 13697.

Pitts, M. W., 2022, How to build Stonehenge, London, Thames & Hudson Ltd.

Schmitz, M. D., Bowring, S. A., and Ireland, T. R., 2003, Evaluation of Duluth Complex anorthositic series (AS3) zircon as a U-Pb geochronological standard: new high-precision isotope dilution thermal ionization mass spectrometry results: Geochimica et Cosmochimica Acta, v. 67, no. 19, p. 3665-3672.

Schoene, B., and Bowring, S., 2006, U-Pb systematics of the McClure Mountain syenite: Thermochronological constraints on the age of the $^{40}Ar/^{39}Ar$ standard MMhb: Contributions to Mineralogy and Petrology, v. 151, p. 615-630.

Shewan, L., O'Reilly, D., Armstrong, R., Toms, P., Webb, J., Beavan, N., Luangkhoth, T., Wood, J., Halcrow, S., Domett, K., Van Den Bergh, J., and Chang, N., 2021, Dating the megalithic culture of laos: Radiocarbon, optically stimulated luminescence and U/Pb zircon results: PLOS ONE, v. 16, no. 3.

Simpson, A., Gilbert, S., Tamblyn, R., Hand, M., Spandler, C., Gillespie, J., Nixon, A., and Glorie, S., 2021, In-situ Lu Hf geochronology of garnet, apatite and xenotime by LA ICP MS/MS: Chemical Geology, v. 577.

Sláma, J., Košler, J., Condon, D. J., Crowley, J. L., Gerdes, A., Hanchar, J. M., Horstwood, M. S. A., Morris, G. A., Nasdala, L., Norberg, N., Schaltegger, U., Schoene, B., Tubrett, M. N., and Whitehouse, M. J., 2008, Plešovice zircon — A new natural reference material for U–Pb and Hf isotopic microanalysis: Chemical Geology, v. 249, no. 1, p. 1-35.

Snoeck, C., Pouncett, J., Claeys, P., Goderis, S., Mattielli, N., Parker Pearson, M., Willis, C., Zazzo, A., Lee-Thorp, J. A., and Schulting, R. J., 2018, Strontium isotope analysis on cremated human remains from Stonehenge support links with west Wales: Scientific Reports, v. 8, no. 1, p. 10790.

Spencer, C. J., Kirkland, C. L., Roberts, N. M. W., Evans, N. J., and Liebmann, J., 2020, Strategies towards robust interpretations of in situ zircon Lu–Hf isotope analyses: Geoscience Frontiers, v. 11, no. 3, p. 843-853.

Stacey, J. S., and Kramers, J. D., 1975, Approximation of terrestrial lead isotope evolution by a two-stage model: Earth and Planetary Science Letters, v. 26, no. 2, p. 207-221.

Stern, R. A., Bodorkos, S., Kamo, S. L., Hickman, A. H., and Corfu, F., 2009, Measurement of SIMS Instrumental Mass Fractionation of Pb Isotopes During Zircon Dating: Geostandards and Geoanalytical Research, v. 33, no. 2, p. 145-168.

Stevens, T., and Baykal, Y., 2021, Detrital zircon U-Pb ages and source of the late Palaeocene Thanet Formation, Kent, SE England: Proceedings of the Geologists' Association, v. 132, no. 2, p. 240-248.

Strachan, R. A., Olierook, H. K. H., and Kirkland, C. L., 2021, Evidence from the U–Pb–Hf signatures of detrital zircons for a Baltican provenance for basal Old Red Sandstone successions, northern Scottish Caledonides: Journal of the Geological Society, v. 178, no. 4.

Thomas, H. H., 1923, The Source of the Stones of Stonehenge: The Antiquaries Journal, v. 3, no. 3, p. 239-260.

Thompson, J., Meffre, S., Maas, R., Kamenetsky, V., Kamenetsky, M., Goemann, K., Ehrig, K., and Danyushevsky, L., 2016, Matrix effects in Pb/U measurements during LA-ICP-MS analysis of the mineral apatite: Journal of Analytical Atomic Spectrometry, v. 31, no. 6, p. 1206-1215.

Thomson, S. N., Gehrels, G. E., Ruiz, J., and Buchwaldt, R., 2012, Routine low-damage apatite U-Pb dating using laser ablation–multicollector–ICPMS: Geochemistry, Geophysics, Geosystems, v. 13, no. 2.

Vermeesch, P., 2004, How many grains are needed for a provenance study?: Earth and Planetary Science Letters, v. 224, no. 3, p. 441-451.

-, 2018, IsoplotR: A free and open toolbox for geochronology: Geoscience Frontiers, v. 9, no. 5, p. 1479-1493.

Vermeesch, P., 2021, On the treatment of discordant detrital zircon U–Pb data: Geochronology, v. 3, no. 1, p. 247-257.

Viner, S., Evans, J., Albarella, U., and Pearson, M. P., 2010, Cattle mobility in prehistoric Britain: strontium isotope analysis of cattle teeth from Durrington Walls (Wiltshire, Britain): Journal of Archaeological Science, v. 37, no. 11, p. 2812-2820.

Wiedenbeck, M., Allé, P., Corfu, F., Griffin, W. L., Meier, M., Oberli, F., Quadt, A. V., Roddick, J. C., and Spiegel, W., 1995, Three natural zircon standards for U-Th-Pb, Lu-Hf, trace element and REE analyses: Geostandards Newsletter, v. 19, no. 1, p. 1-23.

Woodcock, N., Holdsworth, R. E., and Strachan, R. A., 2012, The Grampian Orogeny: Mid-Ordovician Arc–Continent Collision along the Laurentian Margin of Iapetus, *in* Woodcock, N., and Strachan, R. A., eds., Geological History of Britain and Ireland: Chichester, Wiley-Blackwell, p. 91-109.

Zack, T., and Kooijman, E., 2017, Petrology and Geochronology of Rutile: Reviews in Mineralogy and Geochemistry, v. 83, no. 1, p. 443-467.

Zack, T., Stockli, D., Luvizotto, G., Barth, M., Belousova, E., Wolfe, M., and Hinton, R., 2011, In situ U–Pb rutile dating by LA-ICP-MS: ^{208}Pb correction and prospects for geological applications: Contributions to Mineralogy and Petrology, v. 162, p. 515-530.

Zutterkirch, I. C., Kirkland, C. L., Barham, M., and Elders, C., 2021, Thin-section detrital zircon geochronology mitigates bias in provenance investigations: Journal of the Geological Society, v. 179.

6.13. Appendix E

6.13.1. Potential Source Terranes for the Altar Stone

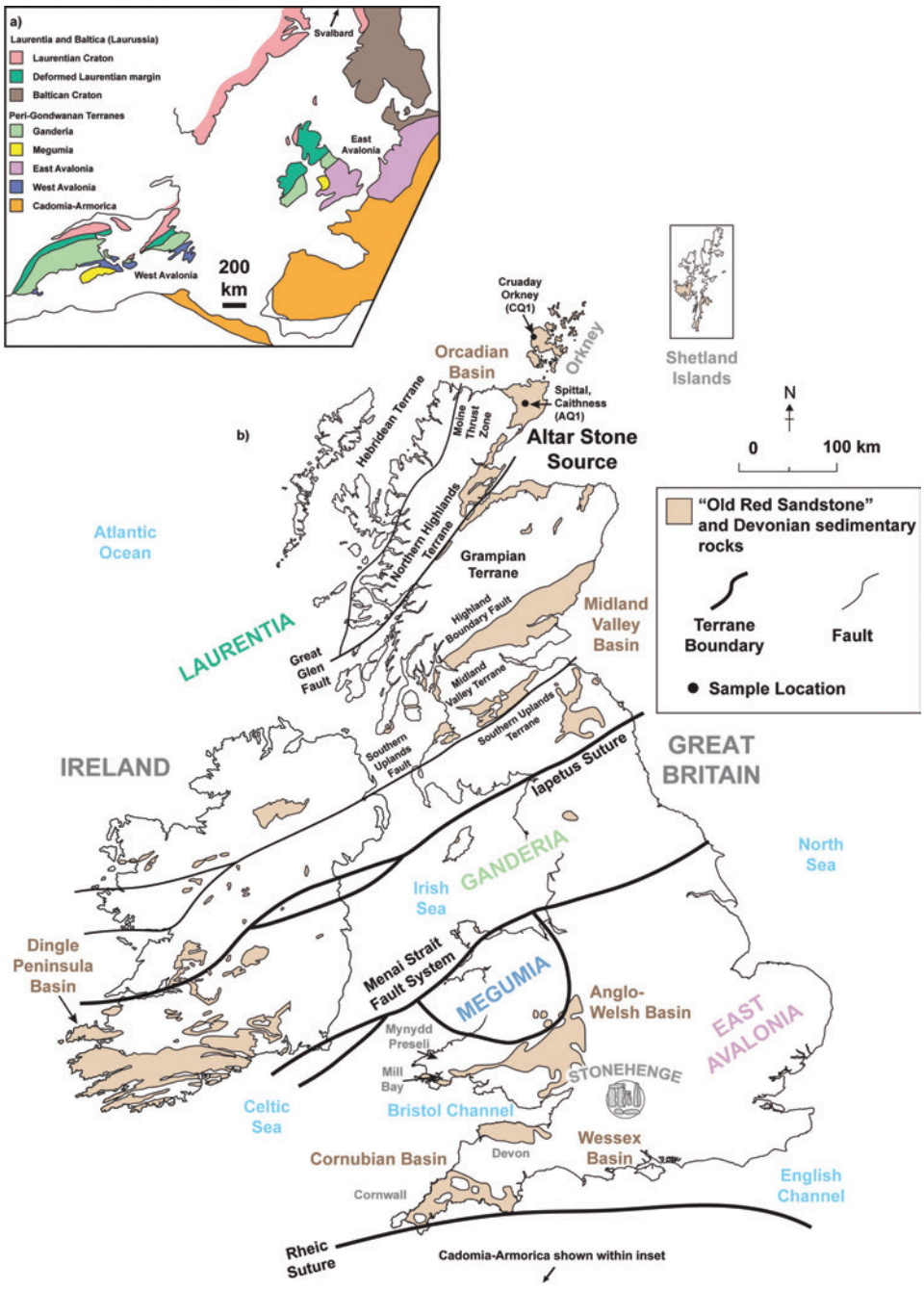

a) Schematic map of the North Atlantic region with the crystalline terranes in the Caledonian-Variscan orogens depicted prior to the opening of the North Atlantic, adapted after Landing et al. (2023). **b)** Schematic map of Britain and Ireland, showing outcrops of Old Red Sandstone, basement terranes, and major faults with reference to Stonehenge.

6.13.2. Altar Stone U–Pb Data

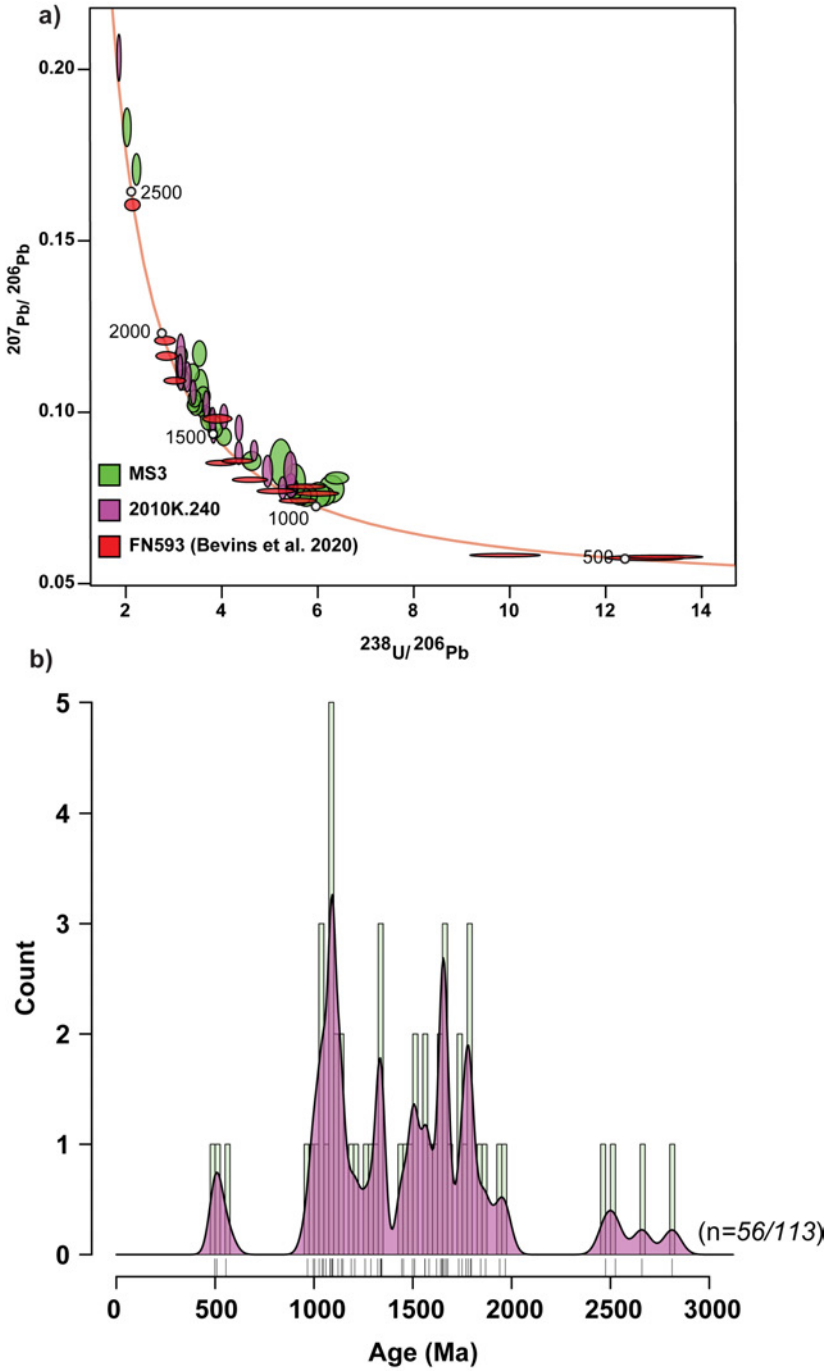

a) Tera-Wasserburg plot for all concordant (≤ 10 % discordant) zircon analyses reported from three samples of the Altar Stone. Discordance is defined using the concordia log % distance approach, and analytical ellipses are shown at the two-sigma uncertainty level. The ellipse colour denotes the sample. Replotted isotopic data for thin-section FN593 is from Bevins et al. (2020). **b)** Kernel density estimate for concordia U–Pb ages of concordant zircon from the Altar Stone, using a kernel and histogram bandwidth of 50 Ma. Fifty-six concordant analyses are shown from 113 measurements. A rug plot is given below the kernel density estimate, marking the age of each measurement

6.13.3. Comparative Kernel Density Estimates

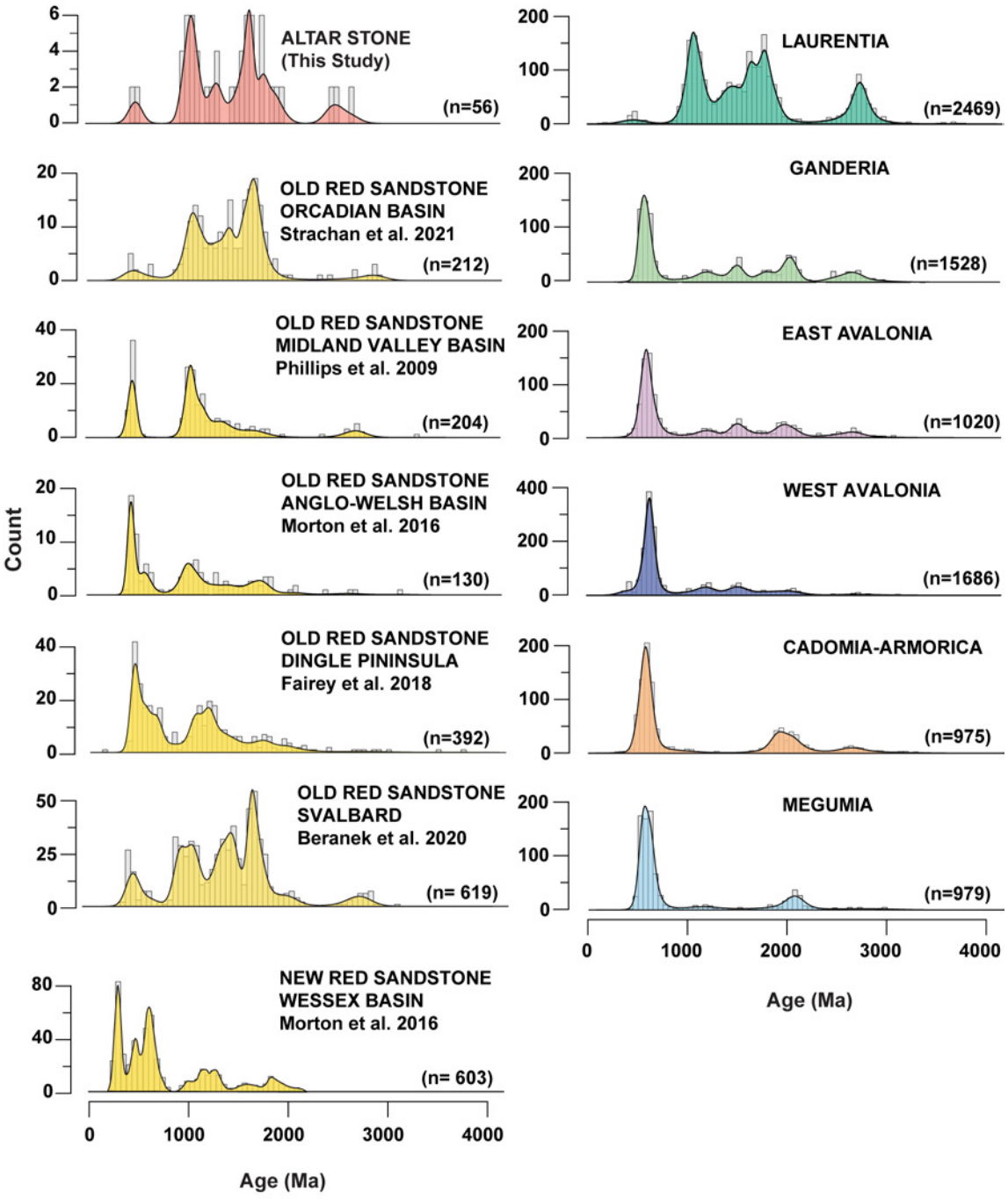

Comparative kernel density estimates of concordant zircon concordia ages from the Altar Stone, crystalline sources terranes, and comparative sedimentary rock successions. Each plot uses a kernel and histogram bandwidth of 50 Ma. Each comparative dataset's zircon U–Pb geochronology source is shown with their respective kernel density estimate. Zircon age data for basement terranes (right side of the plot) was sourced from Fairey et al. (2018) and Stevens and Baykal (2021).

6.13.4. Plots of Rutile U–Pb Ages

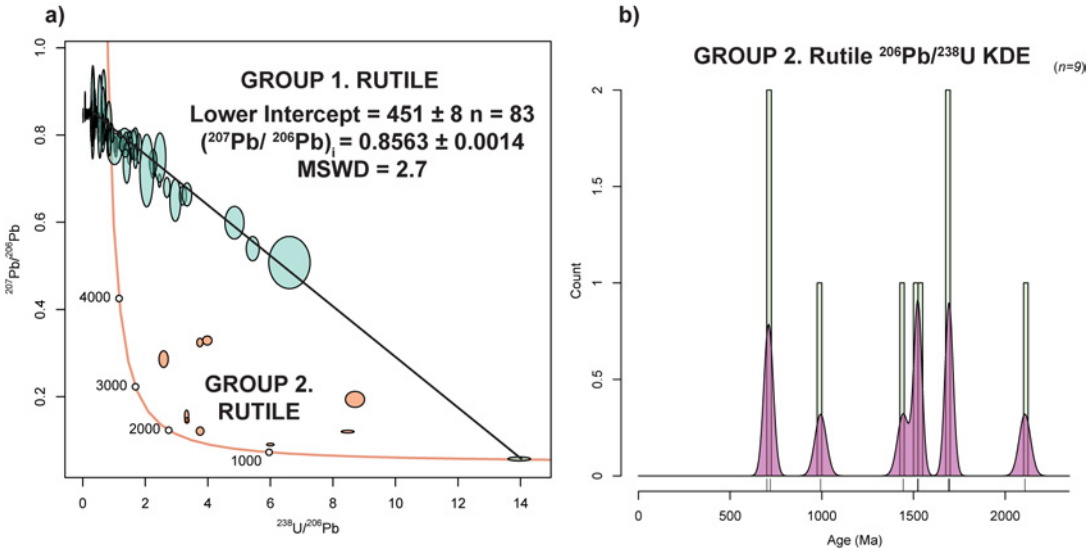

a) Tera-Wasserburg plot of rutile U–Pb analyses from the Altar Stone (thin-section MS3). Isotopic data is shown at the two-sigma uncertainty level. **b)** Kernel density estimate for Group 2 rutile ^{207}Pb corrected ^{206}Pb/^{238}U ages, using a kernel and histogram bandwidth of 25 Ma. The rug plot below the kernel density estimate marks the age for each measurement.

6.13.5. Apatite U–Pb Data for the Altar Stone and Orcadian Basin

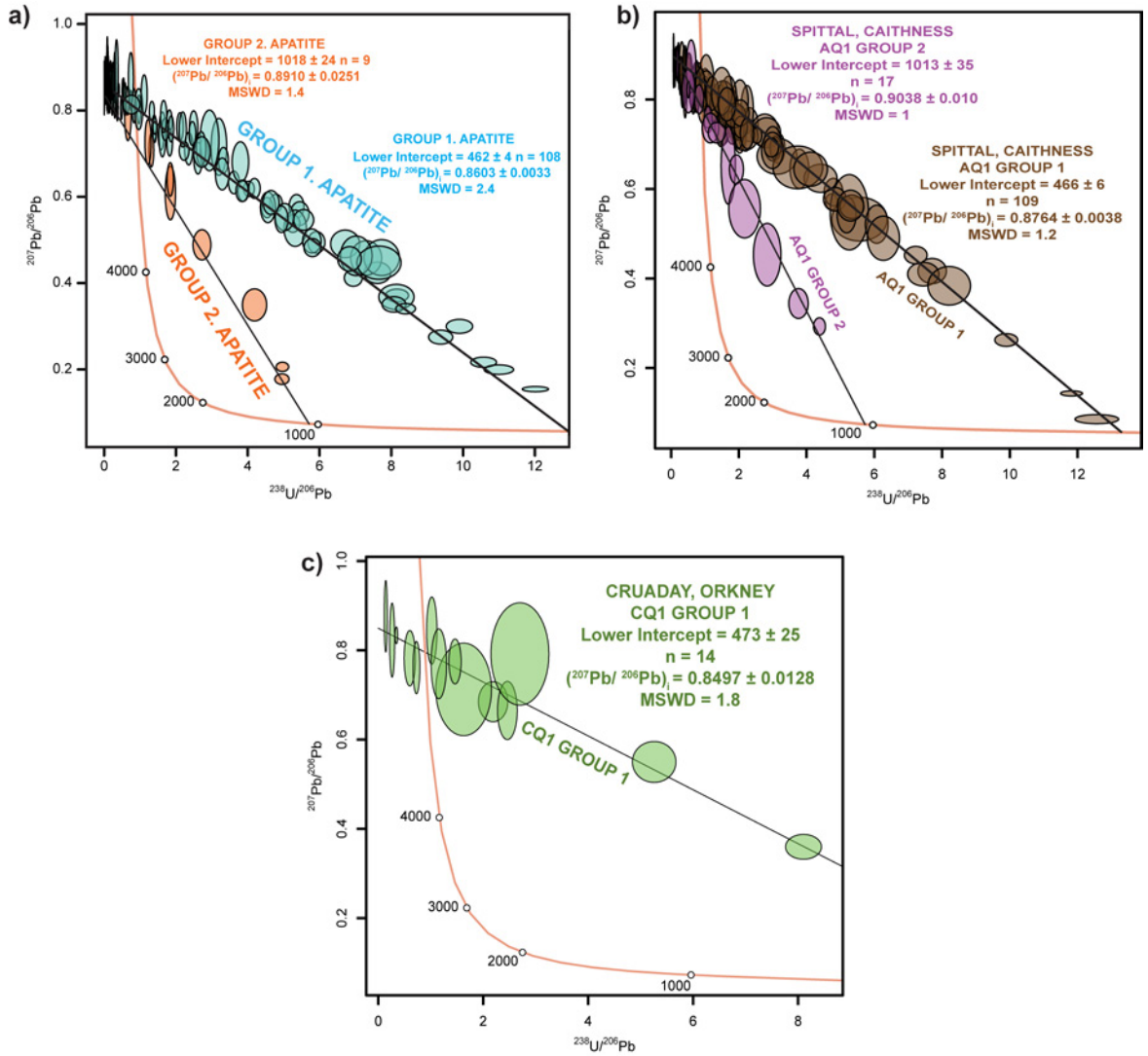

a) Altar Stone apatite U–Pb analyses from thin-section MS3. **b)** Orcadian Basin apatite U–Pb analyses from sample AQ1, Spittal, Caithness. **c)** Orcadian Basin apatite U–Pb analyses from sample CQ1, Cruaday, Orkney. All data is shown as ellipses at the two-sigma uncertainty level. Regressions through U–Pb data are unanchored.

6.13.6. Kernel Density Estimate and Histogram for Apatite Lu–Hf Ages from the Altar Stone

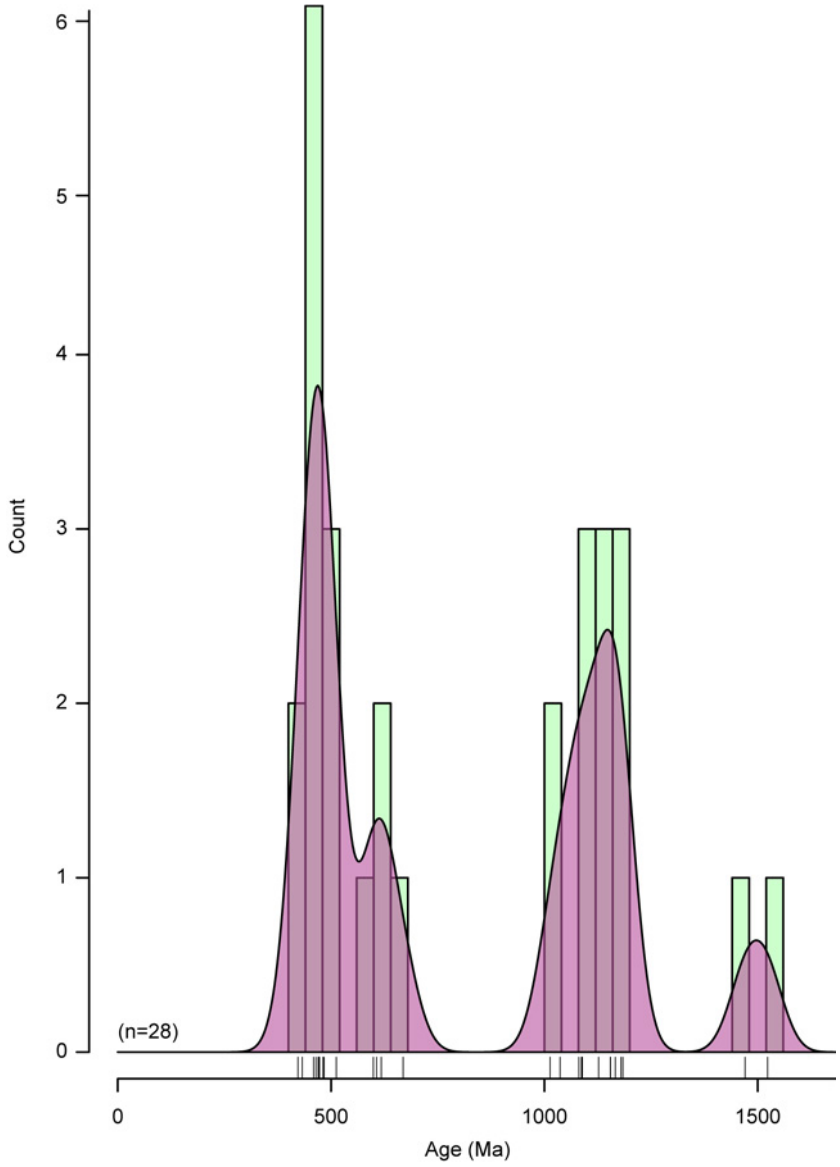

Combined kernel density estimate and histogram for apatite Lu–Hf single-grain ages from the Altar Stone. Lu–Hf apparent ages from thin-section 2010K.240. Kernel and histogram bandwidth of 50 Ma. The rug plot below the kernel density estimate marks each calculated age. Single spot ages are calculated assuming an initial average terrestrial $^{177}Hf/^{176}Hf$ composition.

6.13.7. Apatite Geochemistry for Altar Stone

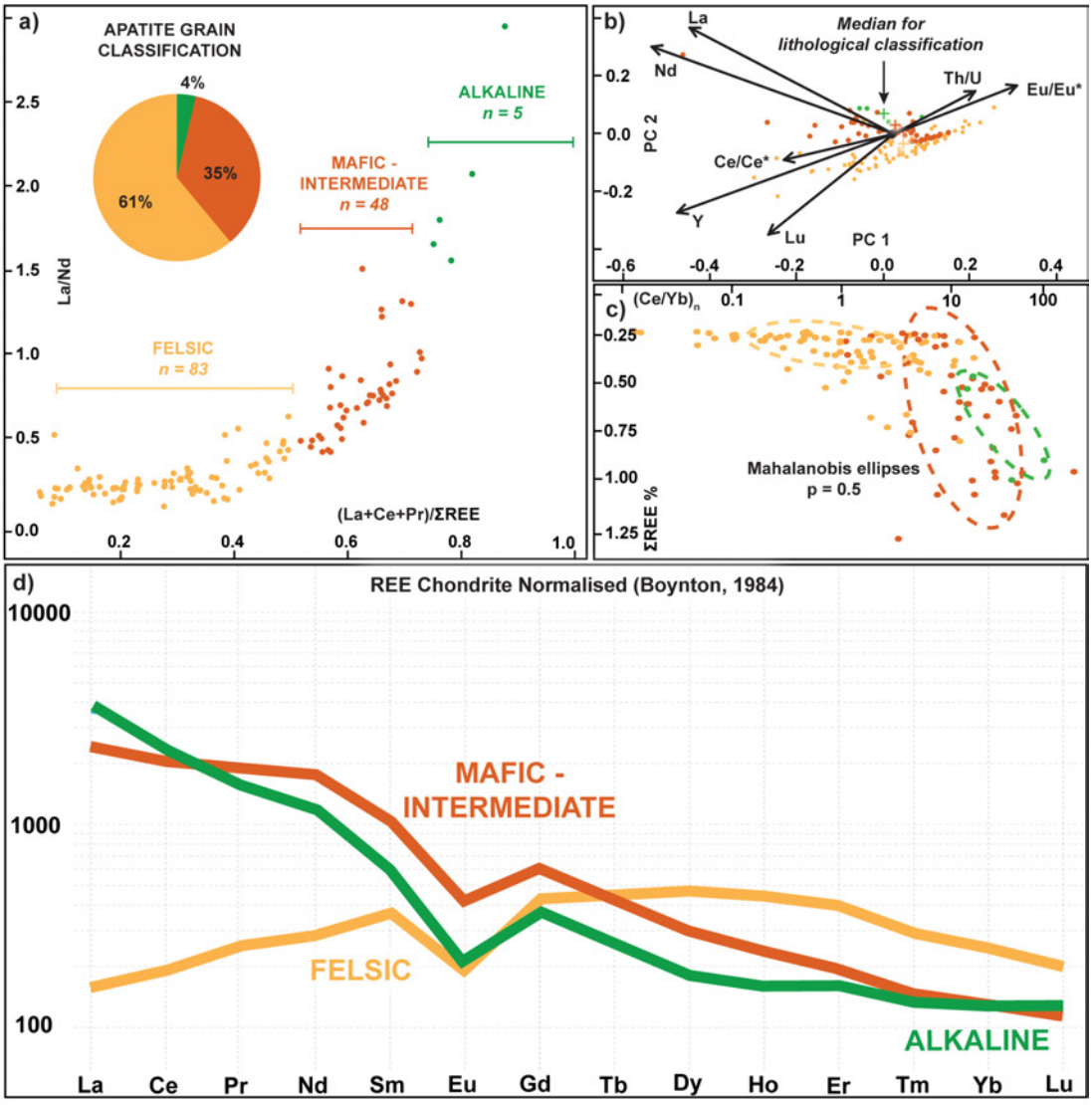

Colours for all plots follow the geochemical discrimination defined in A. **a)** Fleischer and Altschuler's (1986) classification plot for apatite with an inset pie chart depicting the compositional groupings based on these geochemical ratios**. b)** The principal component plot of geochemical data from apatite shows the main eigenvectors of geochemical dispersion, highlighting enhanced Nd and La in the distinguishing groups. Medians for each group are denoted with a cross. **c)** Plot of total REE (%) versus $(Ce/Yb)_n$ with Mahalanobis ellipses around compositional classification centroids. A P=0.5 in Mahalanobis distance analysis represents a two-sided probability, indicating that 50% of the probability mass of the chi-squared distribution for that compositional grouping is contained within the ellipse. This probability is calculated based on the cumulative distribution function of the chi-squared distribution. **d)** Chondrite normalised REE plot of median apatite values for each defined apatite classification type.

6.13.8. Comparative Cumulative Probability Density Plot

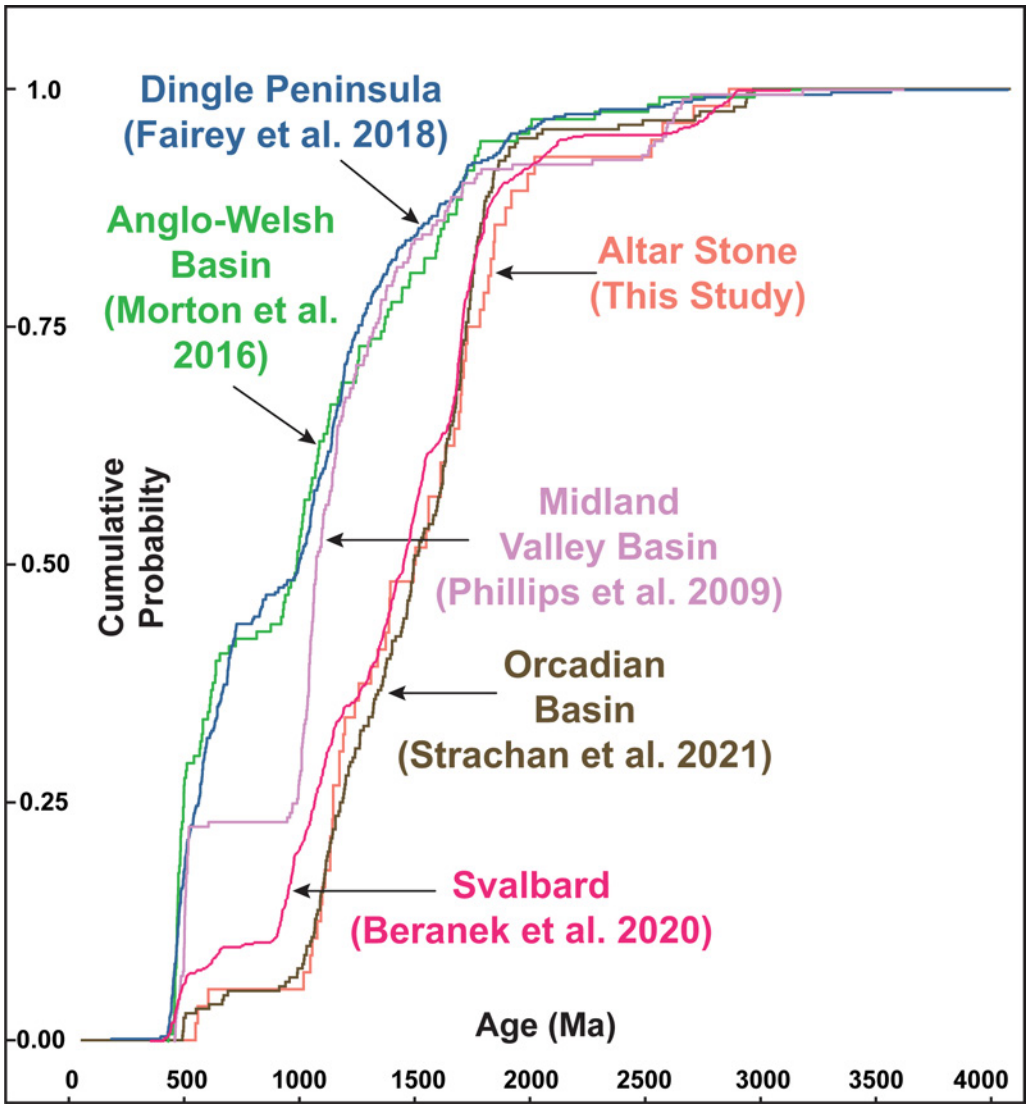

Cumulative probability density function plot of comparative Old Red Sandstone detrital zircon U–Pb datasets (concordant ages) versus the Altar Stone. Proximity between cumulative density probability lines implies similar detrital zircon age populations.

Chapter 7. Conclusions

Earth is the most geologically complex and dynamic planet we know of, yet our geochronometer of choice, zircon, may not sufficiently reflect the innate complexity of our planet. Hence, we may obtain a restricted insight into past processes by limiting our geochronological efforts to zircon alone. Although time is unidirectional (at least in the non-relativistic sense), a largely untapped arsenal of geochronometers present ways to travel back in geological time and give a unique window into Earth's myriad processes.

This research aimed to showcase how isotopic analyses from often underutilised or overlooked geochronometers can be integrated with zircon to constrain processes occurring at different locations within the continental crust throughout geological time (Figure 7.1). Chapters 2, 3, and 6 focused on fingerprinting geological material using isotopic signatures within detrital minerals, whilst Chapters 4 and 5 provided refined ages for poorly constrained or undated rocks. Although each chapter reached conclusions based on its associated dataset in this concluding chapter, findings from each research project are synthesised to address the broader thesis objectives.

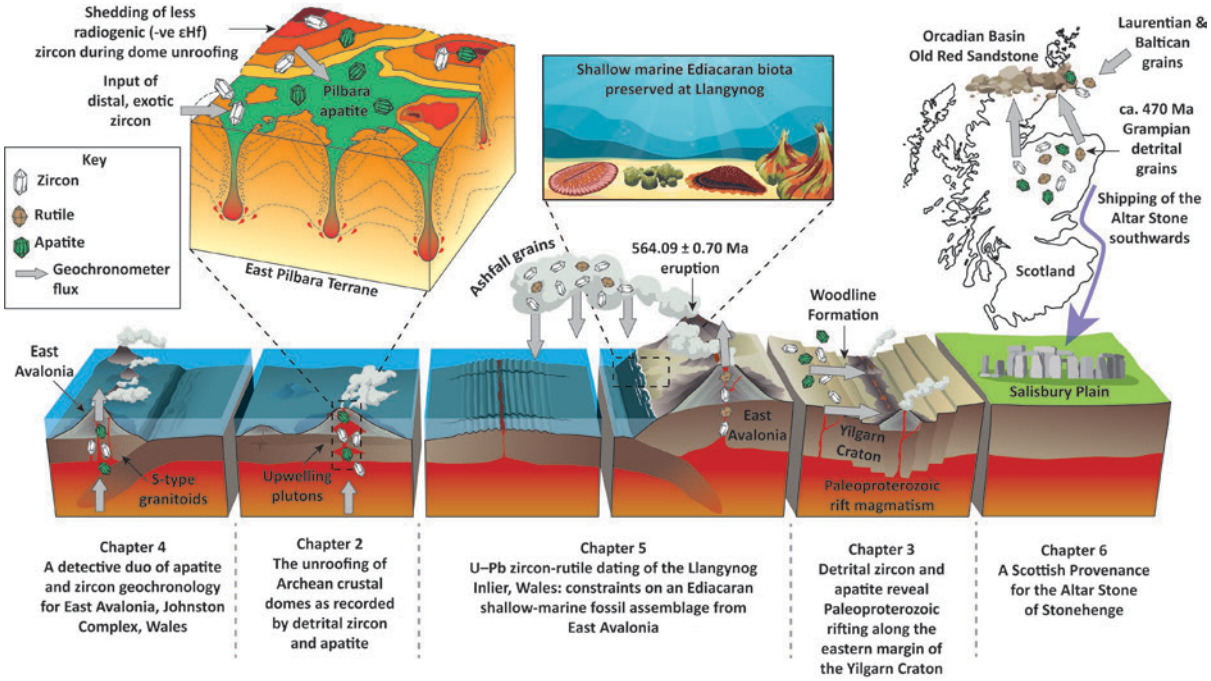

Figure 7.1. A schematic view of the diverse geological setting covered by each chapter of this thesis. Grey arrows indicate geochronometer (zircon, rutile and apatite) movement. Inset figures show models or locations explored within each chapter.

7.1 Can Compositional Biases in Detrital Zircon Datasets be Mitigated by Incorporating Apatite?

Detrital mineral studies strive for a representative insight into crystalline sources contributing to a basin yet typically rely on zircon U–Pb analyses alone, which are demonstrably biased towards source rocks formed via high-temperature felsic magmatism (Cawood et al., 2013; Dröllner et al., 2022; Moecher and Samson, 2006). Indeed, entire tectonomagmatic events can be missed by detrital zircon within a given catchment area (Krippner and Bahlburg, 2013), and mafic lithologies are underrepresented in the detrital archive throughout geological time (Malkowski et al., 2019; Roberts and Spencer, 2015). Furthermore, the tendency of zircon to remain within sedimentary systems throughout multiple sedimentary cycles complicates the identification of first versus multi-cycle detritus (Barham et al., 2021; Zutterkirch et al., 2023). These perceived biases of zircon were illustrated in Chapters 2 and 3. Moreover, many laboratory biases may render any sampled age components misleading (Andersen et al., 2019; Chew et al., 2020; Dröllner et al., 2021).

Chapters 2 and 3 analysed detrital grains from sand collected atop the West Australian Craton. Both these case studies reinforce these biases of zircon as the ages and Hf-isotopic signatures of detrital zircon from both datasets can be readily connected to known tectonomagmatic events throughout the West Australian Craton. Indeed, the oldest, 3586 Ma, and youngest, 221 Ma, zircon dated in this thesis are from unconsolidated regolith atop the East Pilbara Terrane – demonstrating the resilience of zircon to sedimentary reworking but highlighting the difficulty in discerning first versus multi-cycle detritus.

The widespread dissemination of detrital zircon throughout the West Australia Craton is remarkable. Chapter 2 revealed unconsolidated cover in the Pilbara Craton to contain zircon with ages and Hf-isotopic signatures consistent with an origin in the Albany-Fraser Orogen, some 1000 km to the southeast (Hartnady et al., 2019; Kirkland et al., 2015). Whereas Chapter 3 showed that regolith from the southwest margin of the Yilgarn Craton preserves detrital zircon with a provenance from the 700–500 Ma Pinjarra Orogen, ~700 km away from the opposing western flank of the West Australian Craton (Boger, 2011; Markwitz et al., 2017). U–Pb zircon ages of ca. 200–300 Ma with ƐHf signatures within reported values of -5.0 to +16.2 (Zhu et al., 2011) from sands of the East Pilbara Terrane are best correlated to the Lhasa Terrane now present in the Himalayas. These distal provenances demand a transportation mechanism such as that invoked by Morón et al. (2019), where continental-scale fluvial systems originating from the south of east Gondwana distributed detritus throughout Australia. Ultimately, detrital

zircon can readily track ultra-distal and local sources, with the caveat that when zircon enters the system, it stays in the system.

In Chapters 2 and 3, detrital zircon U–Pb analyses were undoubtedly a comprehensive record of granitic magmatism throughout the West Australian Craton. However, the source magmatism was biased towards high-temperature, felsic crystalline source rocks. Indeed, the dominant supply of zircon in Chapter 2 were the underlying granitoid domes of the East Pilbara Terrane, including the Callina Supersuite, a voluminous intrusion of tonalite–trondhjemite–granodiorite (TTG) magmas that partially occurs as a sheeted dyke complex in the North Shaw Suite (Van Kranendonk, 2008) and the Cleland and Emu Pool Supersuites. These magmatic sources contributed to the largest age peak at ca. 3300 Ma, and both suites predominantly comprise the Mount Edgar dome (Gardiner et al., 2017; Roberts and Tikoff, 2021). For Chapter 3, dominant contributions to the detrital zircon cargo of the Woodline Formation were granitoid suites within the adjacent Albany-Fraser Orogen, including the Recherche (1345–1260 Ma) and Esperance (1215–1140 Ma) Supersuites (Smithies et al., 2015; Spaggiari et al., 2015).

Both chapters on Australian geological questions were complemented by apatite U–Pb analyses. For Chapter 2, apatite U–Pb ages were more temporally restricted than zircon ages, with apatite ^{207}Pb corrected ages define a near unimodal population at ca. 2900 Ma, whilst the Sm–Nd isochron and inverse Lu–Hf isochron for the same apatite support an interpretation of a ca. 3200 Ma primary crystallisation age from the granitoid supersuites of the Mt. Edgar Dome. The U–Pb age population at 2900 Ma is interpreted as the time of thermal resetting due to heating from granitoids of the Split Rock Supersuite. Importantly, this record of thermal overprinting is absent from the detrital zircon record, whereas apatite in the Pilbara Craton offers important insights into thermal and fluid overprinting, which is poorly represented in the zircon record. In the case of areas with a protracted thermal history, the combined apatite-zircon approach can give more holistic insights into an area's thermochronology, accurately tracking the thermal pathway for a parcel of crust.

For Chapter 3, the Woodline Formation case study, the different resistances of zircon and apatite to prolonged chemical weathering proved to be a useful indicator rather than a hindrance. Apatite U–Pb analyses from the Woodline Formation yield a lower intercept date of 2062 ± 22 Ma, within the uncertainty of the ca. 2039 Ma zircon component. Compared to zircon, apatite is more labile and less likely to survive prolonged chemical weathering (Gillespie et al., 2018; O'Sullivan et al., 2020). Thus, apatite points towards a proximal

magmatic source, such as the recently defined Moonyoora Formation (Tucker et al., 2023), for the ca. 2030 Ma detrital component. Findings from Chapters 2 and 3 demonstrate that potential biases in zircon datasets can be mitigated by incorporating apatite, which gives insight into thermal resetting and sedimentary reworking absent from the zircon archive.

7.2 To What Extent Can Other Minerals, Such as Apatite and Rutile, Lead to Improved Age Determinations Compared to Zircon Alone?

Detrital studies aim to recognise the provenance and transport history of detritus to understand various geological processes, such as paleogeographic arrangements (Brennan et al., 2021), ancient tectonic settings (Barham et al., 2022; Olierook et al., 2019) and archaeological object provenance (Kelloway et al., 2014; Shewan et al., 2021). Zircon is a ubiquitous accessory mineral phase and, thus, the preferred geochronometer of the geological community.

However, in certain circumstances, age determinations from zircon alone may not be as robust as other minerals. Such was the case in Chapters 5 and 6, where little sample material (thin sections) led to limited zircon analyses. For Chapter 4, a 1–2 kg hand sample of quartz diorite was collected from the Johnston Complex. From this rock sample, a polished block and a fraction of zircon and apatite mounted onto an epoxy resin round were prepared. Therefore, to address potentially limited zircon *n*, alternative geochronometers such as apatite and rutile, which occurred in higher numbers than zircon in these samples, were also analysed.

In Chapter 4, zircon and apatite were analysed from the Johnston Complex, an intrusive suite of felsic plutons occurring within the crystalline basement of southern Britain. Apatite U–Pb data from an inland pluton of the Complex define a lower radiogenic intercept of 576 ± 11 Ma on a Tera-Wasserburg plot (MSWD = 1.2; $p[\chi^2] = 0.064$). From the same rock, zircon U–Pb analyses yield a concordia age of 569 ± 2 Ma (MSWD = 1.9; $p[\chi^2] = 0.079$). Nevertheless, despite the well-constrained age for the Complex, improved age determinations can be obtained using a multi-mineral approach. A weighted mean age calculation, using apatite and zircon, yields an age of 570 ± 3 Ma, similar to the zircon concordia age alone; however, with an MSWD = 1.1, $p[\chi^2] = 0.03$ and $n = 94$— an age assuredly more reliable to constrain the crystallisation of the Johnston Complex than zircon alone.

Obtaining primary crystallisation age constraints for S-type granitoids can be complicated by mineral inheritance, with difficulty identifying neoblastic mineral growth (Collins et al., 2021; Kelsey et al., 2022; Villaros et al., 2011). Due to the resilience of zircon

during magmatic processes, inheritance is a common issue; thus, S-type granitoids frequently contain multiple generations of zircon, each recording different geological events (Clemens et al., 2016; Zhu et al., 2020). Furthermore, high-grade metamorphic conditions can overprint original magmatic textures and reset U–Pb ratios, further complicating the identification of primary versus inherited grains and, thus, crystallisation ages. Lu–Hf analysis of zircon can help identify neoblastic growth by providing insights into the source and evolution of magmas, helping to distinguish between inherited and newly formed zircons (i.e. separate zircon populations).

Combined apatite-zircon U–Pb dating can remove some ambiguity when dating crystalline rocks with inherited geochronometers. Apatite is susceptible to dissolution in melts rich in SiO_2 and Al (felsic, S-type magmas); thus, xenocrystic apatite tends to dissolve out of felsic melts (Wolf and London, 1994). This solubility behaviour means that apatite within felsic rocks are more likely to have formed during the current magmatic event rather than being inherited from older magmatism. Therefore, the case of coeval zircon-apatite crystallisation in rock with minimal metamorphism (at least below the respective radiogenic Pb closure temperatures of zircon ≥900°C and apatite ≥350°C) strongly suggests coeval magmatic growth rather than inheritance.

Chapter 5 provided radiometric age constraints for a hitherto undated assemblage of Ediacaran fossils at the Llangynog Inlier, south Wales. Three zircon U–Pb analyses yielded a concordia age of 562.8 ± 7.7 Ma. Rutile U–Pb analyses yield a two-component mixing line between a common and radiogenic Pb component, with a lower intercept equal to an age of 558.0 ± 22.9 Ma. The combined lower intercept age calculated from an unanchored regression through both minerals is 563.1 ± 6.2 Ma, slightly older but 25% more precise than the zircon-only age. Despite the higher concentration of common to radiogenic Pb within rutile (Zack and Kooijman, 2017), this improvement in age determination demonstrates the benefit of incorporating rutile analyses from the same rock, where petrographic evidence demonstrates they can be considered cogenetic.

Moreover, the coeval zircon and rutile ages suggest rapid cooling through their respective closure temperatures (zircon ≥ 900°C, rutile ≥ 600°C). This rapid cooling scenario is consistent with minimal thermal overprinting of the Llangynog Inlier, which facilitated the preservation of macrofossils. As in Chapter 4, zircon inheritance in volcanic rocks can obscure age interpretations; however, more robust age determinations are obtained by incorporating

additional minerals, such as rutile, with varying melt solubilities (Ayers et al., 1997; Zack and Kooijman, 2017). In summary, the combined zircon-rutile approach enhances the precision of age determinations by providing additional mineral-specific constraints and aids in reconstructing a rock's thermal history. This methodology highlights the importance of integrating different mineral systems to obtain meaningful geological ages and understand processes in geologically complex settings.

7.2 Can a Multi-Mineral Approach Improve Provenance Interpretations?

The geological record of crystalline lithologies is fragmented; thus, any shed detritus is subject to further destruction and potential preservation biases. Therefore, detrital studies are inherently information-limited, continuously losing primary information as chemical systems homogenise in the crust. To mitigate against these difficulties in provenance studies, the more information that can be obtained from a sample, i.e. through a multi-mineral and isotopic system approach, the better any source interpretation will be.

To that end, Chapter 6 represented a culmination of techniques and geochronometers deployed throughout this thesis. Fundamentally, Chapter 6 was a classic geological problem — a sedimentary rock containing detrital grains with an unknown provenance. To address this problem, two polished 30 µm thin sections of the Altar Stone from Stonehenge were made available for analysis, thus necessitating the integration and leveraging of multiple minerals (zircon, apatite and rutile), isotopic systems (U–Pb, Lu–Hf) and trace element analysis to obtain a comprehensive, robust characterisation of the detrital assemblage.

Fifty-six zircon concordia U–Pb ages provided the basis for our provenance interpretations. Kolmogorov–Smirnov (KS) tests on zircon age spectra from the Altar Stone and the crystalline basement terranes of Britain (Fairey et al., 2018; Stevens and Baykal, 2021) gave a clear result. At a 95% confidence level, no distinction in provenance was evident between the Altar Stone detrital zircon U–Pb ages and those from the Laurentian basement and Old Red Sandstone from the Orcadian Basin of northeast Scotland and Svalbard. From the KS test, we cannot reject the null hypothesis that all samples were drawn from the same underlying age distribution. Indeed, detrital zircon age components, defined by ≥ 4 grains in the Altar Stone at 1047, 1091, 1577, 1663, and 1790 Ma correspond to tectonomagmatic sources within Laurentia and Baltica, including the Grenville (1095 – 980 Ma), Labrador (1690 – 1590 Ma), Gothian (1660 – 1520 Ma), and Svecokarellian (1920 – 1770 Ma) orogenies (Strachan et al., 2021). Thus, conventional zircon U–Pb analyses constrained the provenance of the Altar Stone

to the Orcadian Basin atop the Laurentian crystalline basement. However, from 56 concordant ages from 56 grains at > 95% certainty, the largest unmissed fraction was calculated at 9% of the entire detrital population (Vermeesch, 2004). Hence, provenance determinations for the Altar Stone can be bolstered by incorporating apatite (U–Pb and Lu–Hf) and rutile (U–Pb) analyses as these minerals respond dissimilarly during transport.

Apatite (U–Pb 462 ± 4 Ma and Lu–Hf 470 ± 28 Ma) and rutile (451 ± 8 Ma) detrital components within the Altar Stone reveal a dominant mid-Ordovician magmatic source. A crystalline source for these grains is corroborated by the igneous trace element signatures of apatite in the Altar Stone and the absence of metamorphic overgrowths, suggesting a magmatic origin. Zircon within the Altar Stone spanned 2812 – 498 Ma; thus, zircon did not record the mid-Ordovician detrital component. Based on apatite and rutile, the most appropriate source region for such mid-Ordovician grains within the Laurentian basement is the Grampian Terrane of northeast Scotland, which comprises Neoproterozoic to Lower Palaeozoic metasediments intruded by a compositionally diverse suite of Palaeozoic granitoids and gabbros (Oliver et al., 2008). Moreover, an additional apatite age component at 1018 ± 24 Ma is consistent with a Grenvillian source, the presence of which suggests direct derivation from the Laurentian basement, given that apatite breaks down during prolonged chemical weathering (Glorie et al., 2022; O'Sullivan et al., 2020).

Chapter 6 demonstrated that a multi-mineral approach can uncover complex provenance histories that might be missed when using zircon alone. As highly robust minerals, zircon and rutile persist through sedimentary recycling processes, thus providing insights into primary source regions, whilst apatite, albeit more susceptible to alteration and weathering, provides additional information on proximal sources, adding depth to provenance interpretations. By integrating multiple minerals and isotopic systems, provenance studies can achieve a more detailed and accurate reconstruction of sedimentary source regions. This approach reduces ambiguity that inevitably develops from relying on a single mineral or isotopic system, leading to enhanced provenance interpretations.

7.3 Future Work and Research Directions

This thesis analysed zircon, apatite, and rutile within diverse lithological settings throughout Earth's history to understand how accessory mineral geochronology can lead to more comprehensive insights into geological processes. In doing so, avenues for further work pertinent to each chapter have been created.

7.3.1 Chapter 2 – The unroofing of Archean crustal domes as recorded by detrital zircon and apatite

- This chapter presented a geological model whereby the evolved (less radiogenic, ƐHf -ve) cores of upwelling crustal domes are lost into the detrital archive due to preferentially erosion. This model accounts for trends in the oldest detrital zircon grains, which show a wider Hf compositional range and encompass less radiogenic (−ve) ƐHf values. Indeed, the interquartile ƐHf range for the 3.5–3.4 Ga time interval encompasses proportionally more negative ƐHf values than the contemporaneous crystalline basement. To that end, future detrital studies should examine detrital zircon atop other Archean granite-greenstone terranes to evaluate the applicability of the dome unroofing model. Potential case study areas could include the Superior Province and Slave Craton, Canada, which contain the Abitibi-Wabigoon greenstone and Yellowknife greenstone belts and associated granitoid plutons in an analogous arrangement to the East Pilbara Craton (Anhaeusser, 2014; Percival et al., 2012).
- To gain an insight into Archean crustal dynamics, less studied cratons should be examined using detrital zircon within unconsolidated sediment. The Singhbhum and Zimbabwe Cratons are both Paleo to Mesoarchean cratons that may contain vestiges of earlier continental crust (Anhaeusser, 2014; Dirks and Jelsma, 2002; Hofmann et al., 2022). Indeed, as this thesis demonstrated in Chapter 3, a detrital approach can effectively identify poorly exposed or now destroyed ancient continental crust.
- The isotopic systematics of detrital apatite within additional prospective case-study areas would be an informative research avenue. Does detrital apatite in other Archean granite-greenstone terranes preserve a thermally reset U–Pb age like the East Pilbara Terrane? Can apatite Sm–Nd and Lu–Hf analyses offer constraints on nascent continental crust formation?
- Zircon U–Pb age populations have a pronounced geographical influence. Samples collected atop granitoid domes have a unimodal age signature corresponding to the crystallisation age of the underlying dome, whilst samples collected from greenstone

regolith have more heterogeneous age components. This distribution raises an interesting question on how best to conduct detrital studies in an area of unknown geology. What is the most effective sampling strategy to understand regional geology from unconsolidated material? This question may soon require an answer. A stated goal of Mars sample return missions is to ensure that collected regolith samples are geologically diverse and amenable to geochronology (Grady, 2020; Grant et al., 2018). However, given the limited quantity of returned regolith and potentially low zircon *n*, considering geological biases to obtain representative age spectra is essential.

7.3.2 Chapter 3 – Detrital zircon and apatite reveal Paleoproterozoic rifting along the eastern margin of the Yilgarn Craton

- Like the Woodline Formation, enigmatic Paleoproterozoic detritus is found throughout the Barren Basin within the Stirling Range and Mount Barren Group (Hall et al., 2008; Spaggiari et al., 2015). The tandem zircon-apatite approach implemented here should be deployed to other basin sequences to further constrain the detritus from rift-related A-type magmatism. With additional analysis of detritus, the nature of the crystalline source area could be better constrained (e.g. a single crystalline source versus multiple magmatic sources, compositional evolution through time).
- The recently defined ca. 2030 Ma Moonyoora Suite (Tucker et al., 2023) represents a proximal and coeval source for some of the Paleoproterozoic detritus identified from the Woodline Formation. However, the Hf signatures of the Moonyoora Suite are distinctly more radiogenic than coeval zircon from the Woodline Formation. Thus, the ultimate source of Paleoproterozoic detritus likely remains concealed on the eastern margin of the Yilgarn Craton. Further drill core analysis (of widely available drill core fragments) and geophysical investigation, as implemented in Tucker et al. (2023), could help further elucidate Paleoproterozoic source rocks.

7.3.3 Chapter 4 – A detective duo of apatite and zircon geochronology for East Avalonia, Johnston Complex, Wales

- The relationship between the Johnston Complex and the adjacent Benton Volcanic Group is uncertain. Nonetheless, the entrainment of both inliers within the Johnston–Benton thrust zone, and their shared calc-alkaline chemistry (Thorpe 1972; Bevins et al. 1995) implies a common magmatic source for both units. Understanding the relationship between both inliers has important implications for the chronology of

subduction-related magmatism in East Avalonia during the Neoproterozoic, contributing to our understanding of Gondwanan continent assembly. The Benton Volcanic Group warrants zircon, apatite isotopic, and chemical analysis to determine its relationship to the Johnston Complex and broader geological context.

7.3.4 Chapter 5 – U–Pb zircon–rutile dating of the Llangynog Inlier, Wales: constraints on an Ediacaran shallow-marine fossil assemblage from East Avalonia

- This work presented a maximum age of 564.09 ± 0.70 Ma for Ediacaran biota contained within the hitherto undated Llangynog Inlier, Wales. However, other Neoproterozoic rocks in southern Britain that contain trace fossils remain less well-constrained. The Longmyndian Supergroup of the Anglo-Welsh border contains a range of microbially induced sedimentary structures, including '*Arumberia*' and small discoidal markings previously thought to be Ediacaran macrofossils (Longmyndian '*Intrites*,' '*Medusinites*' and '*Beltanelliformis*'). These trace fossils are now understood to be micro stromatolites and other features resulting from the response of microbial-mat-covered surfaces to small-scale fluid escape (Menon et al., 2017). Nevertheless, age constraints include two minor lapilli tuff layers within the Stretton Group of the Longmyndian Supergroup, dated to 566.6 ± 2.9 and 555.9 ± 3.5 Ma (Compston et al., 2002). High-precision age constraints for the Long Mynd would enhance biostratigraphic comparisons to Llangynog Inlier and other Ediacaran fossil assemblages within Avalonia.
- Due to sampling restrictions or an absence of datable grains (i.e., no associated volcanic rocks), the material available for dating fossils can be limited. The Llangynog Inlier chapter demonstrated that the precision of age determinations obtained from comparatively few *in-situ* zircon U–Pb ablations can be improved by incorporating rutile analyses (with higher common Pb contents) from the same rock. The 2σ uncertainty on the zircon concordia age of 562.8 ± 7.7 Ma ($n = 3$) improves by 25% to 563.1 ± 6.2 Ma ($n = 97$) when a regression through both rutile and zircon U–Pb analyses is calculated. Therefore, legacy samples stored within museum collections present exciting opportunities for refined ages for otherwise inaccessible fossil sites.

7.3.5 Chapter 6 – A Scottish Provenance for the Altar Stone of Stonehenge

- Now that the Altar Stone has been provenanced to the Orcadian Basin, a campaign of zircon, apatite, and rutile (U–Pb, Lu–Hf, Sm-Nd and trace elements) analyses should commence at the outcrop scale to determine the megalith's precise source. Indeed, split-stream U–Pb/Lu–Hf zircon analyses would offer an additional isotopic fingerprint that may remove some ambiguity when comparing coeval zircon age components between the Altar Stone and potential Orcadian Basin sources.
- An Orcadian Basin provenance for the Altar Stone raises intriguing questions about the connectivity and infrastructure of Neolithic Britain. Northeast Scotland, including Orkney, is rich in archaeological sites, including Skara Brae, the Rings of Brodgar, Maeshowe, Knap of Howar and Easter Aquhorthies (Bayliss et al., 2017; Fairweather and Ralston, 1993; Macsween et al., 2015). The sites' sophistication and geographical concentration demonstrate that northeast Scotland was a nexus of cultural and social activity during the Neolithic period. Constituent sandstone megaliths of Orcadian Basin Neolithic sites should be analysed using the multi-mineral approach implemented in Chapter 6 to ascertain if there are connections between these archaeological sites and the Altar Stone.
- Detrital zircon morphology holds increasing promise as a provenance tool (Markwitz and Kirkland, 2018; Scharf et al., 2023; Scharf et al., 2022). Geological factors such as cooling rate, metasomatism, and melt composition (SiO_2 concentration and the presence of co-crystallising phases) influence the shape of a zircon crystal, giving insight into holding clues about its parent rock. As no direct sampling of the Altar Stone is permitted, we are left to analyse thin sections prepared from historical fragments of the megalith. In Chapter 6, we analysed two samples of the Altar Stone, yet there are several more of varying authenticity. The semi-automated analysis of detrital zircon morphology using high-resolution photographs of Altar Stone detrital grains would enhance provenance interpretations through the characterisation of the crystalline sources of the sandstone. Indeed, individual plutons within the Grampian and Northern Highlands Terrane could be linked to the Altar Stone (Scharf et al., 2023). For unverified samples of the Altar Stone (Ixer et al., 2019), results similar to those of confirmed samples would help confirm the authenticity of purported samples.
- Were the bluestone megaliths of Stonehenge transported by humans or ice? Debate continues as some favour glacial transport (John, 2018) whilst others point towards

Neolithic quarrying sites on the Mynydd Preseli (Pearson et al., 2015; Pearson et al., 2019) in Wales. Further isotopic work might elucidate this problem. Cosmogenic nuclides are measurable isotopes produced in rocks on the Earth's surface by interactions between cosmic rays and target atoms. They accumulate over time and, through cosmogenic nuclide dating, can constrain total surface exposure. For a glacial transport mechanism, one would expect a surface exposure time approaching 500 Kya from the Anglian Stage glaciation (Gibbard and Clark, 2011; John, 2018), which reached as far south as Wiltshire. For anthropogenic transport, radiocarbon dating suggests that quarrying activities took place during the construction of Stonehenge, about five kya (Parker Pearson et al., 2020; Pearson et al., 2019). Cosmic nuclide analysis would help clarify the Stonehenge story, given the order of magnitude age difference between both estimates.

- Another investigation to address the glacial versus anthropogenic problem would be to conduct a campaign for detrital mineral analysis of unconsolidated regolith atop the Salisbury Plain. Chapters 2 and 3 illustrate that such endeavours can inform sediment transport and crystalline source regions. If sources are found that support the Irish Glacial stream in the local unconsolidated cover, then such a transport mechanism might have carried the stone.

7.4 References

Andersen, T., Elburg, M. A., and Magwaza, B. N., 2019, Sources of bias in detrital zircon geochronology: Discordance, concealed lead loss and common lead correction: Earth-Science Reviews, v. 197.

Anhaeusser, C. R., 2014, Archaean greenstone belts and associated granitic rocks – A review: Journal of African Earth Sciences, v. 100, p. 684-732.

Ayers, J. C., Watson, E. B., Tarney, J., Pickering, K. T., Knipe, R. J., and Dewey, J. F., 1997, Solubility of apatite, monazite, zircon, and rutile in supercritical aqueous fluids with implications for subduction zone geochemistry: Philosophical Transactions of the Royal Society of London. Series A: Physical and Engineering Sciences, v. 335, no. 1638, p. 365-375.

Barham, M., Kirkland, C. L., and Handoko, A. D., 2022, Understanding ancient tectonic settings through detrital zircon analysis: Earth and Planetary Science Letters, v. 583, p. 117425.

Barham, M., Kirkland, C. L., Hovikoski, J., Alsen, P., Hollis, J., and Tyrrell, S., 2021, Reduce or recycle? Revealing source to sink links through integrated zircon–feldspar provenance fingerprinting: Sedimentology, v. 68, no. 2, p. 531-556.

Bayliss, A., Marshall, P., Richards, C., and Whittle, A., 2017, Islands of history: the Late Neolithic timescape of Orkney: Antiquity, v. 91, no. 359, p. 1171-1188.

Boger, S. D., 2011, Antarctica — Before and after Gondwana: Gondwana Research, v. 19, no. 2, p. 335-371.

Brennan, D. T., Li, Z.-X., Rankenburg, K., Evans, N., Link, P. K., Nordsvan, A. R., Kirkland, C. L., Mahoney, J. B., Johnson, T., and McDonald, B. J., 2021, Recalibrating Rodinian rifting in the northwestern United States: Geology, v. 49, no. 6, p. 617-622.

Cawood, P. A., Hawkesworth, C. J., and Dhuime, B., 2013, The continental record and the generation of continental crust: GSA Bulletin, v. 125, no. 1-2, p. 14-32.

Chew, D., O'Sullivan, G., Caracciolo, L., Mark, C., and Tyrrell, S., 2020, Sourcing the sand: Accessory mineral fertility, analytical and other biases in detrital U-Pb provenance analysis: Earth-Science Reviews, v. 202, p. 103093.

Clemens, J. D., Buick, I. S., and Kisters, A. F. M., 2016, The Donkerhuk batholith, Namibia: A giant S-type granite emplaced in the mid crust, in a fore-arc setting: Journal of the Geological Society, v. 174, no. 1, p. 157-169.

Collins, W. J., Murphy, J. B., Blereau, E., and Huang, H. Q., 2021, Water availability controls crustal melting temperatures: Lithos, v. 402-403, p. 106351.

Compston, W., Wright, A. E., and Toghill, P., 2002, Dating the Late Precambrian volcanicity of England and Wales: Journal of the Geological Society, v. 159, no. 3, p. 323-339.

Dirks, P. H. G. M., and Jelsma, H. A., 2002, Crust–mantle decoupling and the growth of the Archaean Zimbabwe craton: Journal of African Earth Sciences, v. 34, no. 3, p. 157-166.

Dröllner, M., Barham, M., Kirkland, C. L., and Ware, B., 2021, Every zircon deserves a date: selection bias in detrital geochronology: Geological Magazine, v. 158, no. 6, p. 1135-1142.

Dröllner, M., Kirkland, C. L., Barham, M., Evans, N. J., and McDonald, B. J., 2022, A persistent Hadean–Eoarchean protocrust in the western Yilgarn Craton, Western Australia: Terra Nova, v. n/a, no. n/a.

Fairey, B. J., Kerrison, A., Meere, P. A., Mulchrone, K. F., Hofmann, M., Gärtner, A., Sonntag, B.-L., Linnemann, U., Kuiper, K. F., Ennis, M., Mark, C., Cogné, N., and Chew, D., 2018, The provenance of the Devonian Old Red Sandstone of the Dingle Peninsula, SW Ireland; the earliest record of Laurentian and peri-Gondwanan sediment mixing in Ireland: Journal of the Geological Society, v. 175, no. 3, p. 411-424.

Fairweather, A. D., and Ralston, I. B. M., 1993, The Neolithic timber hall at Balbridie, Grampian Region, Scotland: the building, the date, the plant macrofossils: Antiquity, v. 67, no. 255, p. 313-323.

Gardiner, N. J., Hickman, A. H., Kirkland, C. L., Lu, Y., Johnson, T., and Zhao, J.-X., 2017, Processes of crust formation in the early Earth imaged through Hf isotopes from the East Pilbara Terrane: Precambrian Research, v. 297, p. 56-76.

Gibbard, P. L., and Clark, C. D., 2011, Chapter 7 - Pleistocene Glaciation Limits in Great Britain, *in* Ehlers, J., Gibbard, P. L., and Hughes, P. D., eds., Developments in Quaternary Sciences, Volume 15, Elsevier, p. 75-93.

Gillespie, J., Glorie, S., Khudoley, A., and Collins, A. S., 2018, Detrital apatite U-Pb and trace element analysis as a provenance tool: Insights from the Yenisey Ridge (Siberia): Lithos, v. 314-315, p. 140-155.

Glorie, S., Gillespie, J., Simpson, A., Gilbert, S., Khudoley, A., Priyatkina, N., Hand, M., and Kirkland, C. L., 2022, Detrital apatite Lu–Hf and U–Pb geochronology applied to the southwestern Siberian margin: Terra Nova, v. 34, p. 201-209.

Grady, M. M., 2020, Exploring Mars with Returned Samples: Space Science Reviews, v. 216, no. 4, p. 51.

Grant, J. A., Golombek, M. P., Wilson, S. A., Farley, K. A., Williford, K. H., and Chen, A., 2018, The science process for selecting the landing site for the 2020 Mars rover: Planetary and Space Science, v. 164, p. 106-126.

Hall, C. E., Jones, S. A., and Bodorkos, S., 2008, Sedimentology, structure and SHRIMP zircon provenance of the Woodline Formation, Western Australia: Implications for the tectonic setting of the West Australian Craton during the Paleoproterozoic: Precambrian Research, v. 162, no. 3-4, p. 577-598.

Hartnady, M. I. H., Kirkland, C. L., Martin, L., Clark, C., Smithies, R. H., and Spaggiari, C. V., 2019, Zircon oxygen and hafnium isotope decoupling during regional metamorphism: implications for the generation of low $\delta^{18}O$ magmas: Contributions to Mineralogy and Petrology, v. 175, no. 1, p. 9.

Hofmann, A., Jodder, J., Xie, H., Bolhar, R., Whitehouse, M., and Elburg, M., 2022, The Archaean geological history of the Singhbhum Craton, India – a proposal for a consistent framework of craton evolution: Earth-Science Reviews, v. 228, p. 103994.

Ixer, R., Bevins, R., and Turner, P., 2019, Alternative Altar Stones? Carbonate-cemented micaceous sandstones from the Stonehenge Landscape: Wiltshire Archaeological and Natural History Magazine, v. 112, no. 1, p. 1-13.

John, B., 2018, The Stonehenge Bluestones, Greencroft Books.

Kelloway, S., Craven, S., Pecha, M., Dickinson, W., Gibbs, M., Ferguson, T., and Glascock, M., 2014, Sourcing Olive Jars Using U-Pb Ages of Detrital Zircons: A Study of 16th Century Olive Jars Recovered from the Solomon Islands: Geoarchaeology, v. 29, p. 47-60.

Kelsey, D. E., Wingate, M., Spaggiari, C. V., Smithies, R. H., Fielding, I. O. H., Lu, Y., Porter, J. K., and Finch, E. G., 2022, Crystalline basement beneath the eastern Canning Basin at the Top Up Rise prospect, Perth, Geological Survey of Western Australia, Accelerated Geoscience Program (AGP), 16 p.:

Kirkland, C. L., Spaggiari, C. V., Smithies, R. H., Wingate, M. T. D., Belousova, E. A., Gréau, Y., Sweetapple, M. T., Watkins, R., Tessalina, S., and Creaser, R., 2015, The affinity of Archean crust on the Yilgarn—Albany–Fraser Orogen boundary: Implications for gold mineralisation in the Tropicana Zone: Precambrian Research, v. 266, p. 260-281.

Krippner, A., and Bahlburg, H., 2013, Provenance of Pleistocene Rhine River Middle Terrace sands between the Swiss–German border and Cologne based on U–Pb detrital zircon ages: International Journal of Earth Sciences, v. 102, no. 3, p. 917-932.

Macsween, A., Hunter, J., Sheridan, A., Bond, J., Ramsey, C. B., Reimer, P., Bayliss, A., Griffiths, S., and Whittle, A., 2015, Refining the Chronology of the Neolithic Settlement at Pool, Sanday, Orkney: Implications for the Emergence and Development of Grooved Ware: Proceedings of the Prehistoric Society, v. 81, p. 283-310.

Malkowski, M., Sharman, G., Johnstone, S., Grove, M., Kimbrough, D., and Graham, S., 2019, Dilution and propagation of provenance trends in sand and mud: Geochemistry and detrital zircon geochronology of modern sediment from central California (U.S.A.): American Journal of Science, v. 319, p. 846-902.

Markwitz, V., and Kirkland, C. L., 2018, Source to sink zircon grain shape: Constraints on selective preservation and significance for Western Australian Proterozoic basin provenance: Geoscience Frontiers, v. 9, no. 2, p. 415-430.

Markwitz, V., Kirkland, C. L., and Evans, N. J., 2017, Early Cambrian metamorphic zircon in the northern Pinjarra Orogen: Implications for the structure of the West Australian Craton margin: Lithosphere, v. 9, no. 1, p. 3-13.

Menon, L. R., McIlroy, D., and Brasier, M. D., 2017, 'Intrites' from the Ediacaran Longmyndian Supergroup, UK: a new form of microbially-induced sedimentary structure (MISS), *in* Brasier, A. T., McIlroy, D., and McLoughlin, N., eds., Earth System Evolution and Early Life: A Celebration of the Work of Martin Brasier, Volume 448, Geological Society of London Special Publications, p. 271-283.

Moecher, D., and Samson, S., 2006, Differential zircon fertility of source terranes and natural bias in the detrital zircon record: Implications for sedimentary provenance analysis: Earth and Planetary Science Letters, v. 247, no. 3-4, p. 252-266.

Morón, S., Cawood, P. A., Haines, P. W., Gallagher, S. J., Zahirovic, S., Lewis, C. J., and Moresi, L., 2019, Long-lived transcontinental sediment transport pathways of East Gondwana: Geology, v. 47, no. 6, p. 513-516.

O'Sullivan, G., Chew, D. M., Kenny, G., Henrichs, I., and Mulligan, D., 2020, The trace element composition of apatite and its application to detrital provenance studies: Earth-Science Reviews, v. 201.

Olierook, H. K. H., Barham, M., Fitzsimons, I. C. W., Timms, N. E., Jiang, Q., Evans, N. J., and McDonald, B. J., 2019, Tectonic controls on sediment provenance evolution in rift basins: Detrital zircon U–Pb and Hf isotope analysis from the Perth Basin, Western Australia: Gondwana Research, v. 66, p. 126-142.

Oliver, G., Wilde, S., and Wan, Y., 2008, Geochronology and geodynamics of Scottish granitoids from the late Neoproterozoic break-up of Rodinia to Palaeozoic collision: Journal of The Geological Society v. 165, p. 661-674.

Parker Pearson, M., Bevins, R., Ixer, R., Pollard, J., Richards, C., and Welham, K., 2020, Long-distance landscapes:: from quarries to monument at Stonehenge, *in* Bouventura, R., Metaloto, R., and Pereira, A., eds., Megaliths and Geology: Oxford, Archaeopress Publishing Ltd, p. 151-169.

Pearson, M. P., Bevins, R., Ixer, R., Pollard, J., Richards, C., Welham, K., Chan, B., Edinborough, K., Hamilton, D., Macphail, R., Schlee, D., Schwenninger, J.-L., Simmons, E., and Smith, M., 2015, Craig Rhos-y-felin: a Welsh bluestone megalith quarry for Stonehenge: Antiquity, v. 89, no. 348, p. 1331-1352.

Pearson, M. P., Pollard, J., Richards, C., Welham, K., Casswell, C., French, C., Schlee, D., Shaw, D., Simmons, E., Stanford, A., Bevins, R., and Ixer, R., 2019, Megalith quarries for Stonehenge's bluestones: Antiquity, v. 93, no. 367, p. 45-62.

Percival, J., Skulski, T., Sanborn-Barrie, M., Stott, G., Leclair, A. D., Corkery, M. T., and Boily, M., 2012, Geology and tectonic evolution of the Superior Province, Canada: Geological Association of Canada Special Paper, v. 49, p. 321-378.

Roberts, N. M., and Tikoff, B., 2021, Internal structure of the Paleoarchean Mt Edgar dome, Pilbara Craton, Western Australia: Precambrian Research, v. 358.

Roberts, N. M. W., and Spencer, C. J., 2015, The zircon archive of continent formation through time: Geological Society, London, Special Publications, v. 389, no. 1, p. 197-225.

Scharf, T., Kirkland, C. L., Barham, M., Yakymchuk, C., and Puzyrev, V., 2023, Does Zircon Shape Retain Petrogenetic Information?: Geochemistry, Geophysics, Geosystems, v. 24, no. 10, p. e2023GC011018.

Scharf, T., Kirkland, C. L., Daggitt, M. L., Barham, M., and Puzyrev, V., 2022, AnalyZr: A Python application for zircon grain image segmentation and shape analysis: Computers & Geosciences, v. 162, p. 105057.

Shewan, L., O'Reilly, D., Armstrong, R., Toms, P., Webb, J., Beavan, N., Luangkhoth, T., Wood, J., Halcrow, S., Domett, K., Van Den Bergh, J., and Chang, N., 2021, Dating the megalithic culture of Laos: Radiocarbon, optically stimulated luminescence and U/Pb zircon results: PLOS ONE, v. 16, no. 3.

Smithies, R. H., Spaggiari, C., and Kirkland, C., 2015, Building the crust of the Albany-Fraser Orogen: Constraints from granite geochemistry.

Spaggiari, C. V., Kirkland, C. L., Smithies, R. H., Wingate, M. T. D., and Belousova, E. A., 2015, Transformation of an Archean craton margin during Proterozoic basin formation and magmatism: The Albany–Fraser Orogen, Western Australia: Precambrian Research, v. 266, p. 440-466.

Stevens, T., and Baykal, Y., 2021, Detrital zircon U-Pb ages and source of the late Palaeocene Thanet Formation, Kent, SE England: Proceedings of the Geologists' Association, v. 132, no. 2, p. 240-248.

Strachan, R. A., Olierook, H. K. H., and Kirkland, C. L., 2021, Evidence from the U–Pb–Hf signatures of detrital zircons for a Baltican provenance for basal Old Red Sandstone successions, northern Scottish Caledonides: Journal of the Geological Society, v. 178, no. 4.

Tucker, N. M., Payne, J. L., Kemp, A. I., Kirkland, C. L., Smyth, A., Tunmer, W., Harvey, S., Stinear, M., Machuca, A., Rangel Suarez, S., and De Waele, B., 2023, A newly discovered 2030–2010 Ma magmatic suite records the dawn of Proterozoic extension on the southern margin of the Yilgarn Craton: Precambrian Research, v. 397, p. 107192.

Van Kranendonk, M. J., 2008, Structural geology of the central part of the Lalla Rookh – Western Shaw structural corridor, Pilbara Craton,: Geological Suvery of Western Australia.

Vermeesch, P., 2004, How many grains are needed for a provenance study?: Earth and Planetary Science Letters, v. 224, no. 3, p. 441-451.

Villaros, A., Buick, I., and Stevens, G., 2011, Isotopic variations in S-type granites: An inheritance from a heterogeneous source?: Contributions to Mineralogy and Petrology, v. 163, p. 243-257.

Wolf, M. B., and London, D., 1994, Apatite dissolution into peraluminous haplogranitic melts: An experimental study of solubilities and mechanisms: Geochimica et Cosmochimica Acta, v. 58, no. 19, p. 4127-4145.

Zack, T., and Kooijman, E., 2017, Petrology and Geochronology of Rutile: Reviews in Mineralogy and Geochemistry, v. 83, no. 1, p. 443-467.

Zhu, D. C., Zhao, Z. D., Niu, Y., Mo, X. X., Chung, S. L., Hou, Z., Wang, L. Q., and Wu, F. Y., 2011, The Lhasa Terrane: Record of a microcontinent and its histories of drift and growth: Earth and Planetary Science Letters, v. 301, p. 241-255.

Zhu, Z., Campbell, I. H., Allen, C. M., and Burnham, A. D., 2020, S-type granites: Their origin and distribution through time as determined from detrital zircons: Earth and Planetary Science Letters, v. 536, p. 116140.

Zutterkirch, I. C., Barham, M., Kirkland, C. L., and Elders, C., 2023, Contrasting Detrital Feldspar Pb Isotope Ratios and Zircon Geochronology to Distinguish Proximal versus Distal Transport: The Journal of Geology, v. 131, no. 1, p. 25-73.